PROCEEDINGS

UK acm

UK Association for Computational Mechanics

2024

10-12 April 2024

Department of Engineering, Durham University

Proceedings of the 2024 UK Association for Computational Mechanics Conference
Durham, UK, 10-12 April 2024.
https://doi.org/10.62512/conf.ukacm2024

UK Association for Computational Mechanics

Edited by

William M. Coombs
Department of Engineering, Durham University, Durham, UK.

Conference sponsors

COMSOL is a global provider of simulation software for product design and research to technical enterprises, research labs, and universities. Its COMSOL Multiphysics® product is an integrated software environment for creating physics-based models and simulation applications. A particular strength is its ability to account for coupled or multiphysics phenomena. Add-on products expand the simulation platform for electromagnetics, structural, acoustics, fluid flow, heat transfer, and chemical applications. Interfacing tools enable the integration of COMSOL Multiphysics® simulations with all major technical computing and CAD tools on the CAE market.

It is the mission of River Publishers to become an influential market player in the publishing and distribution of state-of-the-art, peer-reviewed, English language academic and professional content in specific STM fields; books and journals written by academics and engineers for the institutional and professional markets. River Publishers supports the UKACM conference prizes and works with UKACM on special issues associated with the European Journal of Computational Mechanics.

Table of Contents

Conference papers organised by Technical Session

Conference papers organised by Paper ID

Preface

The proceedings present 52 scientific papers written for the 32nd conference of the UK Association for Computational Mechanics (UKACM). The organisation was founded in 1992 with the aim of promoting research in computational mechanics and various engineering applications and establishing formal links with similar organisations in Europe and the International Association of Computational Mechanics (IACM). The conference was held in the Department of Engineering at Durham University, Durham, UK, between the 11th and 12th April 2024, with the 2024 UKACM School being held on the 10th April 2024. In total 72 technical presentations were delivered as part of the conference, in addition to four plenary lectures and three introductory UKACM School lectures.

Numerous people have contributed to the delivery of this event, but in particular the organising committee would like to thank Professor Charles Augarde, Head of the Department of Engineering, Durham University, UK, for his unwavering support. The event would not have been possible without the support of members of Durham University's Computational Mechanics Research Node, who provided scientific oversight of the submitted contributions, and the administrative support provided by Durham University's Department of Engineering and Event Durham. We would also like to thank Professor David Emerson (Science and Technology Facilities Council, UK), Professor Jon Trevelyan (Durham University, UK), Professor Xiaoying Zhuang (Leibniz University Hannover, Germany) and Dr Tim Hageman (Roger Owen Prize 2022 winner, University of Oxford, UK) who kindly accepted the invitation to deliver plenary lectures; and the three lecturers of the UKACM School, Professor Charles Augarde, Dr Robert Bird and Professor Jon Trevelyan who gave up their time to provide introductory lectures to the material point method, discontinuous Galerkin finite element methods and the boundary element method, respectively.

The papers submitted to UKACM 2024 cover the breadth of computational mechanics research within the UK and beyond. The proceedings are organised in the following sections, linked to the technical sessions of the conference:

- Advances in Bio-inspired Computational Modelling for Engineering Applications
- Advances in Finite Element Modelling
- Computational Innovations in Fluid Dynamics and Material Behaviour
- Computational Methods in Heat Transfer and Hydro-Mechanical Modelling
- Computational Modelling for Material Processing and Multi-scale Analysis
- Computational Modelling of Stress Concentration and Constitutive Relations
- Cutting-Edge Applications in Computational Engineering and Design
- Finite Element and Meshless Methods in Deformation Analysis
- Geotechnical Modelling 1: Pile Jacking to Rainfall-Induced Landslides
- Geotechnical Modelling 2: Rock Failure and Structural Interaction
- Geotechnical Modelling 3: MPM, PFEM and Soil-Structural Interaction
- Innovative Computational Approaches in Composite Material Analysis
- Machine Learning Applications in Engineering
- Phase-Field Modelling for Predicting Fracture and Degradation in Materials
- Structural Analysis and Optimisation: Modelling, Characterisation, and Response

The editor would like to thank the authors for their contributions and their willingness to consider the comments of the scientific committee when preparing their conference papers.

Will Coombs
UKACM 2024 Conference Chair, April 2024

Scientific Committee

Chair

Professor Will Coombs

Durham University members

Professor Charles Augarde
Dr Robert Bird
Dr Stefano Giani
Dr Marti Lloret-Cabot
Professor Simon Mathias
Dr Bartolomeo Panto
Dr Alexandros Petalas
Dr Mohammed Seaid
Dr Stefan Szyniszewski
Dr Wangcheng Zhang

2024 UKACM School

It is traditional for the UKACM Conference to be preceded by a UKACM School, with the aim of introducing different areas of computational mechanics to early careerer researchers. The 2024 School is focused on different methods for analysing problems in solid mechanics (and beyond).

Introduction to the boundary element method

Professor Jon Trevelyan, Durham University

The Boundary Element Method (BEM) is one of the numerical methods available for finding an approximate solution to Partial Differential Equations. In comparison with the FEM, it offers some advantages and some disadvantages. The principal disadvantage lies in the much greater versatility that FEM offers engineers working in the whole range of non-linear, time dependent, multiphysics problems. This has meant that FEM has been far more successful than BEM in a commercial sense within the global engineering industry. On the other hand, there are some problems for which the BEM offers advantages, sometimes very considerable ones, in accuracy and computational efficiency. For this reason, the method has continued its appeal to researchers in computational mechanics. Further, with the advent of isogeometric formulations, there is reason to be optimistic about the future for BEM since its boundary-only philosophy is a natural fit to the NURBS boundary representations used by CAD systems. In this lecture, Jon Trevelyan will provide an introduction to the BEM aimed at early-career researchers who have some awareness of numerical methods in engineering (e.g. FEM) but may be new to the BEM. We will see that, although the meshing is confined to the boundary, our outer surface/perimeter of the object being analysed, the numerical implementation involves some complications not found in FEM. However, once those are overcome we have a method able to deliver highly accurate solutions from a mesh that is entirely restricted to the boundary of the object.

About the speaker: Prof. Jon Trevelyan is Emeritus Professor of Engineering at Durham University. After obtaining his PhD in Civil Engineering from Bristol (studying the dynamics of double curvature arch dams) he worked for over a decade in industry. The majority of this period was spent with the Computational Mechanics Group, developers of the BEASY software, and included seven years running the North American operations of the Group. On his return to the UK, Jon made a career change into academia, first spending one year at the University of Brighton, and then in 1996 being appointed to a lectureship at Durham, where he spent the remainder of his career. His early years at Durham working alongside Professor Peter Bettess were formative ones, particularly in together developing enriched BEM formulations for acoustics problems. The idea of using non-standard basis functions, removing the adherence to piecewise polynomial elements, has been a continuing unifying theme in his research since then, and has led to promising developments in enriched BEM schemes for fracture mechanics and to isogeometric BEM approaches. Jon's BEM software has been used for over twenty years in the aerospace sector. He is a Fellow of the Institution of Mechanical Engineers, and has also served a four-year term as Head of the (then) School of Engineering and Computing Sciences in Durham. Jon formally retired in 2023 but has retained Emeritus Professor status so he can still access Matlab.

An introduction to material point methods for solid mechanics

Professor Charles Augarde, Durham University

The purpose of this presentation is to introduce you to the Material Point Method (MPM) for solids, which is closely related to the standard finite element method (FEM) but with major advantages for modelling problems with large deformations. There is considerable interest in MPMs in disparate areas, e.g. geotechnics and computer graphics, and strong proponents of various types, e.g. implicit or explicit, single or multiphase, which makes the topic an interesting area of computational mechanics in which to work. After explaining the approach, the presentation will focus on key issues with MPMs that are the topic of current research and could be taken forward by interested researchers. The presentation will assume a reasonable knowledge of the standard FEM for solids.

About the speaker: Prof. Charles Augarde is Head of Department and Professor of Civil Engineering in the Department of Engineering at Durham University. He has been an academic at Durham since 2001, being promoted

to Professor in 2013. Prior to Durham he spent six years in industry, working for Manchester City Engineer's Dept on road, bridge and sewer design and construction, achieving Chartered Engineer (CEng) status in the process, then returned to academia to do a PhD on finite element analysis of tunnelling at Oxford University. After his PhD, and a brief period as a lecturer in structural engineering at the University of Westminster, he returned to Oxford as a Departmental Lecturer in Engineering Science where he stayed until 2001. Charles's research interests lie in development of numerical methods aimed mainly at problems in geotechnics, but with a substantial presence in the field of computational fracture mechanics, and a totally separate interest in earthen construction methods and materials.

Discontinuous Galerkin Methods: from basic to advanced techniques

Dr Robert Bird, Durham University

The aim of this lecture is to introduce discontinuous Galerkin (DG) methods as a tool to solve engineering problems. Several applications of DG methods are presented. This lecture starts by describing some of the characteristics of DG methods that set them apart from standard conforming methods. DG methods are particularly suitable for mesh adaptivity. Therefore, some of the most common automatic adaptivity techniques are presented in detail together with applications. In the last part of the lecture, advanced techniques are discussed. The aim is to make this lecture suitable for anyone with experience with FEMs.

About the speaker: Dr Robert Bird is a Post-Doctoral Research Associate (PDRA) at Durham University, UK. He obtained his PhD in 2019 from Durham University researching hp-adaptive finite element methods for accurate crack propagation. After his PhD he accepted a PDRA position at Imperial College London. At Imperial he developed methods to model, and quantitatively define, fracture intensity (P32) from subsurface blast shock waves in rocks. He also developed analytical methods to analyse the reflection of pulse-waves impinging on fractures. Currently at Durham he uses the material point method (MPM) for modelling rigid bodies interacting with non-linear materials. Much of this work is focused on formulations for frictional contact and imposition of boundary conditions due to the lack of defined material boundary with the MPM. His other focus is on crack propagation, both discrete and phase-field type fracture, combined with residual based a posteriori error estimation for hp-adaptivity with the discontinuous Galerkin finite element method. They key aim with this research is to allow computational trackable simulations with no a priori knowledge of where cracks will propagate. During Robert's PhD he won two prizes for his distinguished research, the 2016 ACME Conference Award for Best Post-Graduate Research Student and the 2020 UKACM Roger Owen Award for the best PhD thesis. Additionally, he was a finalist in 2021 for the international ECCOMAS best PhD thesis and the 11th ECCOMAS PhD Olympiad.

Advances in Bio-inspired Computational Modelling for Engineering Applications

UKACM 2024 Conference, 10-12 April 2024, Durham University, Durham, UK
https://doi.org/10.62512/conf.ukacm2024.008

INVERSE DESIGN OF SPINODOID CELLULAR STRUCTURES WITH TAILORED MECHANICAL-HYDRO-THERMAL PERFORMANCES

Jinlong Fu, Hirak Kansara, Wei Tan*

School of Engineering and Materials Science, Queen Mary University of London, E1 4NS, UK.
Presenter: jinlong.fu@qmul.ac.uk; *Corresponding author: wei.tan@qmul.ac.uk

Abstract. In this study, a data-driven computational framework is developed for multi-objective inverse design of spinodoid cellular metamaterials with desired anisotropic properties, which enables us to simultaneously tailor the mechanical deformation, fluid transport and heat transfer performances. Cellular structures with various spinodal topologies are generated within the full design space, and multiple physical properties, including mechanical stiffness, hydraulic permeability and thermal conductivity tensors, are numerically evaluated via finite element analysis and computational fluid dynamics respectively. After having a sufficiently large database, regressional conditional generative adversarial network (cGAN) is used to construct the one-to-many mapping to represent inverse structure-property relations, from which multiple cellular structures can be generated by inputting the target mechanical-hydro-thermal properties. The preliminary results demonstrate that this new computational design framework is an effective tool to deal with stiffness-permeability-diffusivity synergy, expand the tunable scope of multi-physical performances, and tailor spinodoid cellular metamaterials with the desired multi-functionality.

Key words: *Spinodoid cellular metamaterials; Inverse simulation-aided design; Data-driven modelling; Regressional cGAN; Multi-physical properties*

1 Introduction

The vast design space of multi-functional metamaterials has motivated the need for inverse design [1] to identify the optimal structural topology that satisfies the requirement of multi-physical properties. However, this challenging problem has not been properly solved due to several primary reasons [2, 3]: (i) The "curse of dimension" problem due to the vast array of structural topologies and material constituents; (ii) Different physical properties are often strongly coupled, even conflicting, which makes it difficult to simultaneously optimise and independently adjust them; (iii) Mapping physical properties to structural topology space is an ill-posed problem, because multiple topologies can have the same effective properties. Herein, we propose a data-driven computational framework for efficient inverse design of spinodoid cellular metamaterials to achieve the desired mechanical-hydro-thermal performances.

2 Methodology

Conditional generative adversarial network (cGAN) [4], consisting of a generator and a discriminator, can generate a set of designs satisfying the predefined conditions by feeding a set of random noise. In this study, the conditions are physical properties of spinodoid cellular metamaterials, including stiffness, permeability and thermal conductivity tensors. And cGAN is applied to learn an one-to-many mapping from multi-physical properties to the design variables that characterise the spinodal topology of cellular structures. As illustrated in Figure 1, a property regressor is newly added to the standard cGAN, aiming to greatly enhance its capability in learning the inverse structure-property relationships. It is a new practice to use regressional cGAN for multi-objective inverse design of spinodoid cellular metamaterials

to achieve tailored mechanical-hydro-thermal performances. Compared to conventional feedforward neural networks [2], the regressional cGAN is able to generate non-unique designs given the same input, and these designs are statistically equivalent in aspects of the conditions (physical properties).

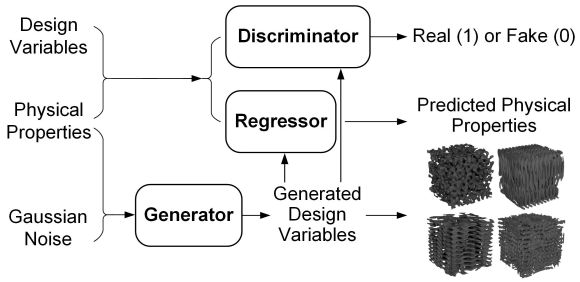

Figure 1: The workflow of regressional cGAN for multi-objective inverse design of spinodoid cellular metamaterials by learning the inverse structure-property mapping.

3 Data preparation

As an emerging class of metamaterials, spinodoid cellular structures [2, 5] not only enable enormous anisotropic design spaces with mechanical resilience, but can also biomimick diverse microstructural features of natural materials. Spinodoid topologies with nearly zero mean curvature are engineered to minimise localised junction failure and enhance pore network connectivity. The procedure for generating spinodoid structures is briefly explained in Figure 2. There are four design parameters describing the unique topology of a spinodoid structure, which are the relative density $\bar{\rho}$ and three angles $(\theta_1, \theta_2, \theta_3)$. Here, a wide range of design parameters is randomly sampled from the full design space, based on which a set of 3D spinodoid structures of representative size are generated.

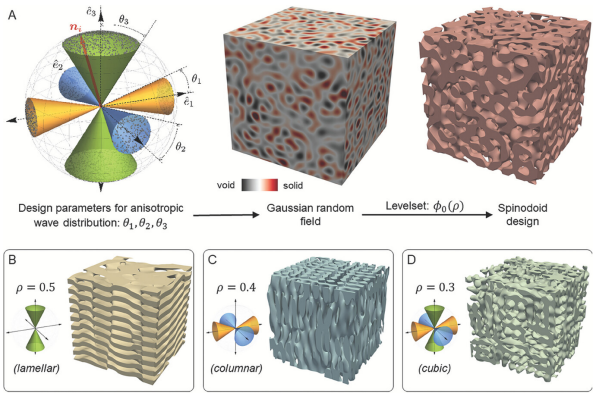

Figure 2: Illustration of generating spinodoid celluler structures [5].

For each spinodoid structure sample, the finite element method (FEM) is used to evaluate the effective stiffness tensor E via computational homogenisation. The lattice Boltzmann method (LBM) and finite volume method (FVM) are carried out for numerical simulations of fluid flow and heat transfer, from which the permeability tensor κ and thermal conductivity tensor λ can be computed respectively. The

obtained database, consisting of physical properties $C = [E, \kappa, \lambda]$ and design parameters $\chi = [\bar{\rho}, \theta_1, \theta_2, \theta_3]$, will be used to train a regressional cGAN model to accurately establish a one-to-many mapping from multi-physical properties C to design variables χ. The properly trained regressional cGAN model will then be used to generate design variables by inputting the target physical properties.

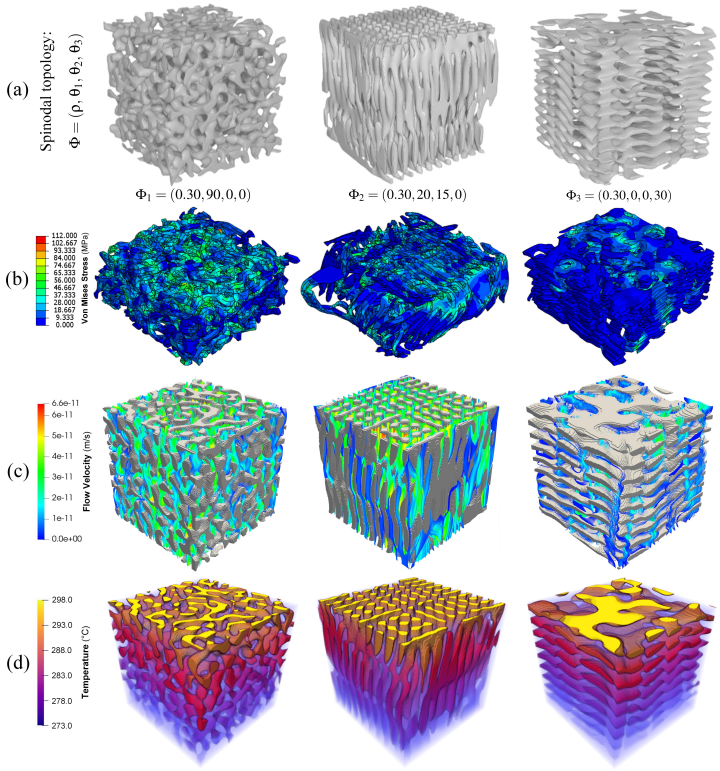

Figure 3: Constructing a sufficiently large database for data-driven inverse design: (a) Generating various spinodoid cellular structures with different design variables; (b) Evaluating stiffness tensors using the FEM to simulate compression deformation; (c) Evaluating permeability tensors using the LBM for pore-scale flow simulation; and (d) Evaluating thermal conductivity tensors using the FVM to simulate heat transfer.

4 Preliminary results and future works

At the current stage, we are still generating more data via high-fidelity numerical simulations for constructing the data-driven models that represent the inverse structure-property relationships of spinodoid cellular metamaterials. Therefore, only some preliminary results are shown in this section to demonstrate the potential/effectiveness of the proposed computational inverse design tool. Different regressional cGAN models are separately trained by using the available data, and the inverse design results are shown in Figure 4 and 5. Obviously, the morphological similarity between the real/reference and generated structures can be easily seen via visual inspection. For quantitative assessment, the physical properties of generated spinodoid cellular structures will be numerically evaluated, and the results will be compared with the reference values at the next step. After a sufficiently large database is constructed, we will use it to train a new regressional cGAN model for multi-objective inverse design of spinodoid

cellular strictures with tailored mechanical-hydro-thermal performances.

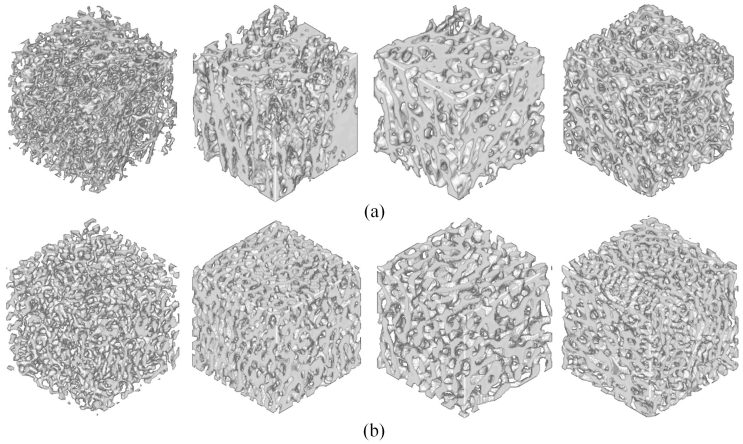

Figure 4: (a) Real bone structures obtained from micro-CT scanner; (b) Spinodoid cellular strictures generated from the regressional cGAN model, which are statistically equivalent to the real bone structures in terms of mechanical stiffness E.

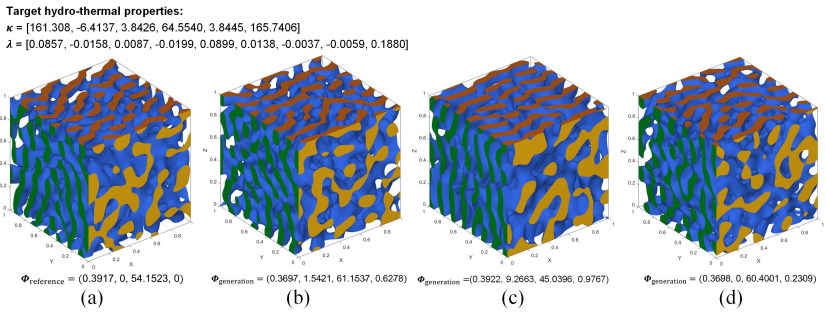

Figure 5: (a) The reference spinodoid cellular stricture; (b), (c) and (d) Multiple structures generated from the regressional cGAN model, which are statistically equivalent to the reference structure in terms of permeability E and thermal conductivity λ tensors.

Acknowledgments: We acknowledge the financial support from the EPSRC [EP/V049259/1].

References

[1] Kansara H, Liu M, He Y, et al. Inverse design and additive manufacturing of shape-morphing structures based on functionally graded composites [J]. *Journal of the Mechanics and Physics of Solids*, 2023, 180: 105382.

[2] Kumar S, Tan S, Zheng L, et al. Inverse-designed spinodoid metamaterials [J]. *npj Computational Materials*, 2020, 6(1): 73.

[3] Zhang L, Song B, Choi S K, et al. Anisotropy-inspired, simulation-guided design and 3D printing of microlattice metamaterials with tailored mechanical-transport performances [J]. *Composites Part B: Engineering*, 2022, 236: 109837.

[4] Dong Y, Li D, Zhang C, et al. Inverse design of two-dimensional graphene/h-BN hybrids by a regressional and conditional GAN[J]. *Carbon*, 2020, 169: 9-16.

[5] Deng W, Kumar S, Vallone A, et al. AI-Enabled Materials Design of Non-Periodic 3D Architectures With Predictable Direction-Dependent Elastic Properties [J]. *Advanced Materials*, 2024: 2308149.

UKACM 2024 Conference, April 11-12, 2024, The University of Durham, Durham, UK
https://doi.org/10.62512/conf.ukacm2024.024

Mechanics of 3D printed bioresorbable stents: A virtual testbed assessment.

Michael I. Okereke[1*], Atabak G. Tabriz[2], Roxanne Khalaj[2], Dennis Douroumis[2]

[1] Mathematical Modelling for Engineering Research Group, Department of Engineering Science., University of Greenwich. m.i.okereke@gre.ac.uk

[2] Centre for Innovation in Process Engineering and Research (CIPER), Department of Pharmaceutical, Chemical and Environmental Sciences, University of Greenwich, United Kingdom.

Abstract

Next-generation stents are expected to be manufactured from fully bioresorbable materials. Such stents can achieve the restoration of patency of occluded atherosclerotic arteries, before hydrolysing in the body following healing. There has been a sustained growth of research in the development of new biomaterials and manufacturing methods for such stents. Three-dimensional printing is one of the exciting fields for the manufacture of coronary BRS. Here, we show a virtual testing approach for the development of 3D printable coronary artery stents based on bioresorbable polymeric biomaterials. In the study, the authors designed 10 novel 3D printable stents and manufactured them using Fused Deposition Modelling (FDM) 3D-printing technology. Also, a virtual testing approach based on finite element methods was used to characterize the in vivo structural response of the stents with a view to assessing the suitability of the stent designs for use in the restoration of patency for occluded coronary arteries. The approach presented here can represent a future preoperative management tool for interventional cardiologists to assess the structural performance of bespoke patient-specific 3D printable stent designs prior to manufacture and implantation at the occluded site. **Key words:** *stent, virtual testing*

1. Introduction

Intravascular stents are widely used for restoration of patency of atherosclerotic coronary arteries. Although majority of stents used in clinical practice are metallic stents, there is a growing interest in biodegradable and bioreabsorbable stents. In the last decade, drug-eluting biodegradable stents have emerged as alternative to bare metal stents. Most recently, polymeric stents have also emerged as probable alternatives to bare metal stents. Innovations in polymer manufacture have led to development of biocompatible, bioreabsorbable, and high modulus polymers as PLA, PLLA and polydiaxanone which can be used in manufacture of cardiovascular (polymeric) stents. The advances made in 3D printing technologies have led to deployment of such techniques in manufacture of bespoke patient-specific complex-geometry stents [1,2] . The expectation is that such stents can be printed on demand specifically for a given patient right beside the operating table. Although there is a significant number of studies based on computational modelling of the behaviour of bare metal and polymercoated stents, there is just a few initial studies investigating 3D printable polymeric stents.

2. Problem description

This paper aims to develop a virtual testbed for investigating the structural response of 3D printable polymeric stents in coronary angioplasty. Such stents are typically small to fit the arteries. The proposed virtual testbed is analogous to a laboratory testing scheme ranging from representative virtual domain, appropriate material design, to selection of adequate loading scheme (boundary conditions) and subsequent post-test batch analysis (post-processing tasks) [3,4].

The virtual testbed presented here (see Figure 1) uses the finite element modelling scheme as a computing engine for the structural analysis of candidate designs of the polymeric stents. The virtual domain consists of a multi-fold hyperelastic balloon material, elasto-plastic stent material, hyperelastic behaviour of the arterial walls and atherosclerotic plaque, and finally multi-step loading scheme (capturing multi-fold mechanism of balloon and pressurization of arterial walls simulating blood flow).

Ten designs of 3D-printable stents were created and used in this study. The set of these ten designs are shown in Figure 1. The designs were distinguished by the size and shapes of the cells in each stent. These range from racetrack, curved diamond, diamond, and skewed parallelogram designs. Each stent design was subjected to a

virtual testbed assessment to determine its mechanics in view of ranking according to an expected mechanics of stent, damage assessment and structural performance.

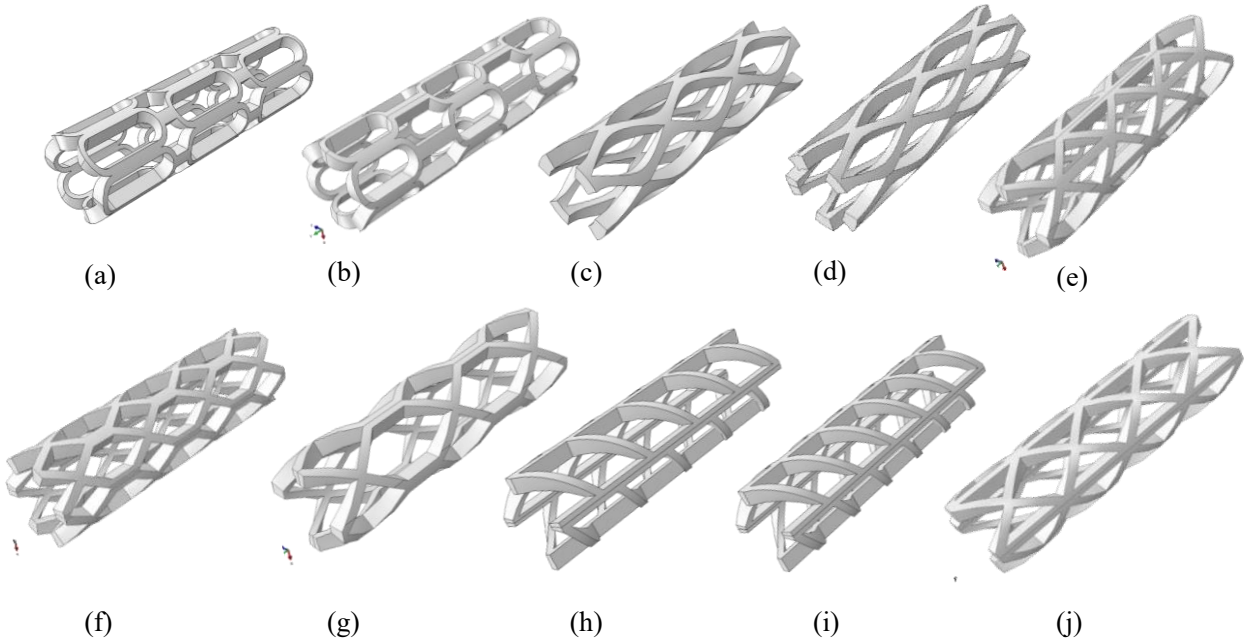

Figure 1: Geometric Designs of 3D printable stents showing ten different stent designs which include the following stent's geometric cell shapes: **Racetrack** (a) RA (b) RB; **Curved diamond** (c) CDA (d) CDB; **Diamond** (e) DA (f) DB (g) DC; and **Skewed parallelograms** (h) SPA (i) SPB and (j) SPC.

3. Numerical results

The study reports on such structural parameters as: radial recoil index, longitudinal retraction index, foreshortening percentage, dogboning index, as well as maximum diametral strain. The result from this study is significant as it offers developers of polymeric stents a virtual platform to assess the structural performance of candidate designs of stents before their eventual printing. This is essential since the use of patient-specific data will drive design of different designs of stents, hence leading to different structural responses. As a result, the use of the proposed virtual testbed will provide instant feedback on the behaviour of such bespoke 3D printable stent designs before investing further resources for their 3D printing. Also, outputs from such testbed will provide the surgeon a first-hand assessment of the structural scaffolding response of the stent before the deployment within the patient. Each variant shows a distinct stent mechanics and will be quantified numerically as shown in Figure 2.

Table 1: Results of structural parameters derived for the virtual testbed.

Stent cell shape group	**Stent label**	R_{rec} (%)	L_{ret} (%)	F_{sh} (%)	*DAI* (-)	*SMA* (-)	Ranking (-)
Racetrack	RA	13.2	-16.93	8.83	Intact	Pass	3rd
	RB	6.94	-34.41	5.64	Intact	Pass	1st
Curved diamond	CDA	5.46	-53.75	14.34	Damaged	Pass	(-)
	CDB	20.68	-27.28	15.55	Intact	Pass	5th
Diamond	DA	4.62	-26.22	7.12	Intact	Fail	(-)
	DB	8.04	-35.47	13.08	Intact	Pass	4th
	DC	3.25	-54.03	14.31	Intact	Pass	2nd
Skewed parallelogram	SPA	12.70	-47.09	14.53	Damaged	Fail	(-)
	SPB	6.12	-42.76	12.29	Damaged	Fail	(-)
	SPC	4.61	-53.13	8.10	Intact	Fail	(-)

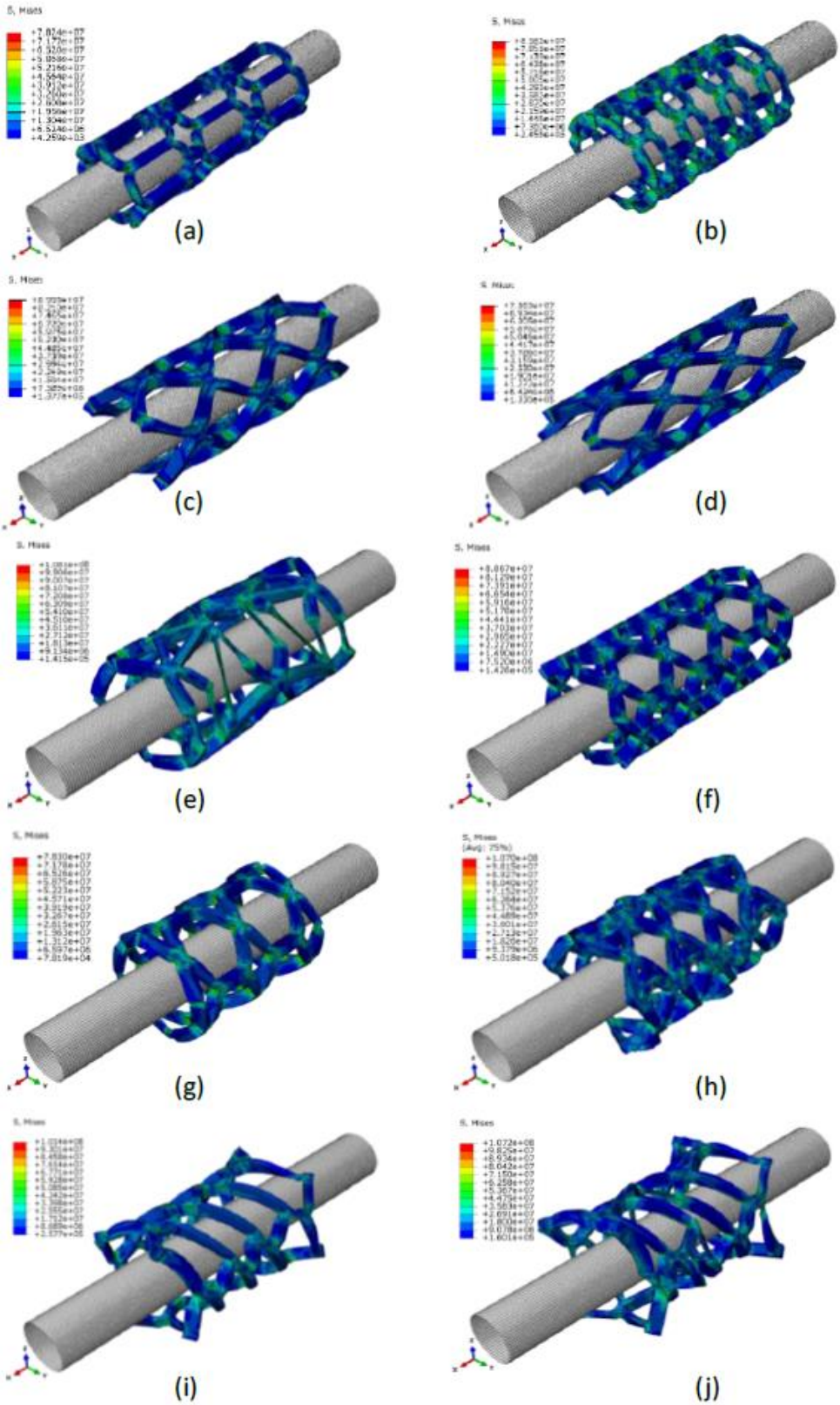

Figure 1. The contour plot showing the structural response for the following 3D-printable bioresorbable stents with the following cell shapes: **racetrack**: (a) RA, and, (b) RB; **curved diamonds**: (c) CDA, and, (d) CDB; **diamonds**: (e) DA, and, (f) DB; (g) DC, and**,** **skewed parallelogram** (h) SPC (i) SPA and (j) SPB.

4. Conclusions

Next-generation coronary stents are expected to be based on bioresorbable materials which following restoration of patency of the occluded artery will hydrolyse preventing current permanent caging of the arteries as seen in metallic stents. Already, several metal-based bioresorbable stents have been developed and have undergone clinical trials with comparable success as fully metallic stents [5–8]. However, these bioresorbable stents can either degrade quickly (e.g. Magnesium-based stents) or too slowly (e.g. Iron-based stents). These undesirable degradation timeframes mean that they either cannot support the artery wall for the required healing period, or they remain in the artery for longer than required. As a result, they are fraught with neointimal restenosis and late-stage thrombosis: the same issues seen in metallic stents.

The study has used the virtual testbed to rank 10 designs of 3D-printable coronary stents and determined the structural parameters commonly used for objective assessment of the viability of a stent for use in coronary angioplasty. The study has also investigated the damage and stent mechanics assessments to ensure that the chosen stent will not fail during the stent deployment process. This study is the first attempt in pushing existing FDM-type 3D printing technology to create coronary stents with strut thicknesses of 150-500 μm. We have therefore shown an ambitious approach for manufacturing homogeneous 3D printed bioresorbable stents as well as virtual assessment of their *in vivo* mechanics. With sustained collaborative research from material science and additive manufacturing fields, we envision a future where 3D printed bioresorbable (polymeric) coronary stents can become common in clinical settings.

Acknowledgments

This project has received funding from the *Interreg 2 Seas* programme 2014-2020 co-funded by the *European Regional Development Fund* under subsidy contract No. **2S01-059 IMODE**.

References

[1] S. McMahon, N. Bertollo, E.D.O. Cearbhaill, J. Salber, L. Pierucci, P. Duffy, T. Dürig, V. Bi, W. Wang, Bioresorbable polymer stents: a review of material progress and prospects, Prog. Polym. Sci. 83 (2018) 79–96. https://doi.org/10.1016/J.PROGPOLYMSCI.2018.05.002.

[2] R. Khalaj, A.G. Tabriz, M.I. Okereke, D. Douroumis, 3D printing advances in the development of stents, Int. J. Pharm. 609 (2021) 121153. https://doi.org/10.1016/J.IJPHARM.2021.121153.

[3] M.I. Okereke, A.I. Akpoyomare, M.S. Bingley, Virtual testing of advanced composites, cellular materials and biomaterials: A review, Compos. Part B Eng. (2014). https://doi.org/10.1016/j.compositesb.2014.01.007.

[4] M.I. Okereke, R. Khalaj, A.G. Tabriz, D. Douroumis, Development of 3D printable bioresorbable coronary artery stents: A virtual testing approach, Mech. Mater. 163 (2021) 104092. https://doi.org/10.1016/J.MECHMAT.2021.104092.

[5] H.Y. Ang, H. Bulluck, P. Wong, S.S. Venkatraman, Y. Huang, N. Foin, Bioresorbable stents: Current and upcoming bioresorbable technologies, Int. J. Cardiol. 228 (2017) 931–939. https://doi.org/10.1016/J.IJCARD.2016.11.258.

[6] W. Schmidt, P. Behrens, C. Brandt-Wunderlich, S. Siewert, N. Grabow, K.P. Schmitz, In vitro performance investigation of bioresorbable scaffolds – Standard tests for vascular stents and beyond, Cardiovasc. Revascularization Med. 17 (2016) 375–383. https://doi.org/10.1016/J.CARREV.2016.05.001.

[7] D.W.Y. Toong, J.C.K. Ng, Y. Huang, P.E.H. Wong, H.L. Leo, S.S. Venkatraman, H.Y. Ang, Bioresorbable metals in cardiovascular stents: Material insights and progress, Materialia. 12 (2020) 100727. https://doi.org/10.1016/J.MTLA.2020.100727.

[8] J.Y. Kim, S. Park, P. Serrao, Effect of over/under-expanding on the mechanical behavior in provisional stenting using bioresorbable scaffold, J. Mech. Sci. Technol. 2020 346. 34 (2020) 2371–2376. https://doi.org/10.1007/S12206-020-0514-8.

Advances in Finite Element Modelling

UKACM 2024 Conference, 10-12 April 2024, Durham University, Durham, UK
https://doi.org/10.62512/conf.ukacm2024.001

Geometric Optimization and Mechanical Analysis of Multilayer Graphene Platelet Films: A Finite Element Approach

Penghao Qi[1], Xindong Chen[1,2], Hanxing Zhu[1*]

[1] Department of Engineering, Cardiff University, Cardiff, CF24 3AA, UK.
QiP@cardiff.ac.uk
[2] Institute of Biomechanics and Medical Engineering, AML, Department of Engineering Mechanics, Tsinghua University, Beijing 100084, China
chenxin7@tsinghua.edu.cn, ZhuH3@cardiff.ac.uk

Abstract

Monolayer graphene exhibits remarkable strength and stiffness. However, the large-scale fabrication of flawless monolayer graphene films remains challenging due to the prevalence of imperfections, such as additional layers, wrinkles, or folds. These imperfections significantly compromise the performance of monolayer graphene across diverse applications. In contrast, the fabrication of large-size multilayer graphene platelet films (MGPFs) with commendable mechanical properties is comparatively more attainable and holds considerable promise for widespread applications in modern industries. It is imperative to systematically investigate the dependences of the mechanical properties of multilayer graphene platelet films on their geometric structures and to optimize the structural design of MGPFs. To address these objectives, this paper employs finite element methods to construct a 3D macroscopic multilayer graphene representative volume element model with each layer being a 2D periodic random Voronoi platelet structure. The ensuing investigation aims to explore the influences of geometrical features, encompassing graphene platelet size, and area fraction, on the elastic modulus of MGPFs. The findings indicate a significant positive correlation between the elastic modulus of MGPFs and the size of its graphene microplates. This observation proves that the characteristic parameters of graphene platelets play a crucial role in influencing the macroscopic mechanical properties of the materials.

Key words: *Multilayer graphene platelet; Finite element; Elastic properties;*

1 Introduction

Monolayer graphene, particularly highlighted since its synthesis by Novoselov and Geim et al. [1] in 2004, has garnered widespread attention owing to its promising applications in the fields of electrical, mechanical, electronic, optical, and biomedical engineering [2]. Although, there has been an exponential rise in studies of graphene materials, the remarkable properties of monolayer graphene are still only presented in a few laboratories and cutting-edge devices. This is due to the lack of efficient and low-cost methods for the preparation of defect-free monolayer graphene in the prior technology [3–6]. Whereas the layer-by-layer hierarchical structure of multilayer graphene platelet films (MGPFs) similar to the nacre materials can combine intralayer strong sp^2 bonds and interlayer crosslinks for efficient load transfer [7]. Their multilayer structures can reduce the impact of stress concentrations on materials dimensions. Hence, fewer or more layers of graphene can be relatively easy to synthesis and have been employed in some materials, such as graphene aerogels and graphene-based composite materials. Prvious studies have indicated that the mechanical properties of MGPFs are affected to various degrees by their geometric parameters of graphene sheet. Hence, it is valuable to discuss how the mechanical properties of MGPFs depend on their geometrical structures and how to optimize the structural/geometrical design of multilayer graphene platelet films to enable the desired combination of their mechanical properties and to enhance their functions in practical applications.

Liu et al. [7] analogised multilayered graphene platelet films to lamellar structured materials such as pearl nacre and established that the overall mechanical properties of such materials were analysed using idealized 2D continuum dielectric mechanics and investigated how these properties depended on the mechanical properties of monolayered graphene platelets and their dimensions. Zhang et al. [8] investigated the impact of randomly staggered platelet distribution on the mechanical properties of unidirectional nanocomposites, revealing its significant role alongside volume fraction, platelet shape, and orientation. However, their 2D geometrical models [8] are very different from the actual structure of MGPFs. Here, inspired by some

work [9,10] and the morphological structure of nacre, this research introduced the random Voronoi platelets into the representative volume element (RVE) model in the work of Tang et al. [11] to explore how the mechanical properties of the random Voronoi platelets affect the mechanical properties of the nacre. As the mechanical properties of multilayer graphene platelet films (MGPFs) are obviously in-plane isotropic and MGPFs have three orthogonal planes of elastic symmetry, they have five independent elastic constants to be determined [12]. If the gaps between the intralayer graphene platelets are relatively large and their intralayer interaction force can reasonably be ignored, the individual platelets in the MGPFs are held together only by the interlayer van der Waals force between the staggered graphene platelets. This study introduces, for the first time, periodic 3D multilayer random Voronoi graphene platelet models to obtain the five independent elastic constants through finite element simulations. It aims to investigate the impact of geometrical properties, such as graphene platelet size, regularity degree, and area fraction, as well as the number of graphene platelet layers, on the five independent elastic constants of MGPFs.

2 Problem description

Three-dimensional periodic representative volume elements (RVE) models, featuring nacre-like structures (Fig. 1c), are systematically constructed to simulate the elastic characteristics of multilayer graphene platelet films (MGPFs). Each layer of the MGPFs within the RVE model is represented by a periodic two-dimensional square random Voronoi platelet structure containing $\boldsymbol{N}$ complete graphene platelets, as depicted in Figure 1b, with solid lines demarcating the boundaries (or inter-platelet gaps) within intralayer configurations. In previous simulation studies, graphene layers were modeled as thin layers composed of shell elements, with the thickness of the graphene layer reduced by a factor of 10 to 100 to represent the model's thickness, allowing for the assumption of infinite out-of-plane stiffness of the graphene layer [1]. The out-of-plane Poisson's ratio is thus assumed to be 0.0. The Young's modulus $\boldsymbol{E_G}$ of the thin layer was accordingly increased by the corresponding factor to ensure accurate representation of material parameters such as in-plane Young's modulus and tensile stiffness. Additionally, the in-plane Poisson's ratio was set to $\boldsymbol{v_G}$ =0.178. Considering the considerable reduction in the interlayer shear modulus of multilayer graphene due to van der Waals interactions, which is several orders of magnitude lower than its in-plane Young's modulus. Hence, the interaction between staggered neighboring graphene platelets in the RVE model is approximated by a uniform layer of equivalent isotropic linear elastic material with a thickness of 0.34 nm, a Young's modulus of 10 GPa and a Poisson's ratio of 0.001. Moreover, the regularity of the model [9,10] is constrained within the range of 0.6 ± 0.025, and periodic boundary conditions are applied along the in-plane boundaries of the model to extend the simulation scale of the material.

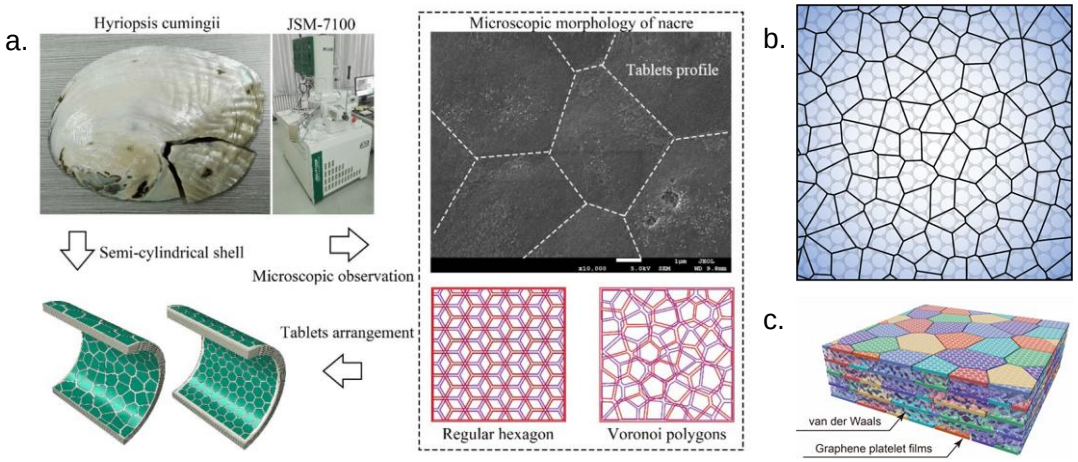

Fig.1 (a) Microscopic tablets structure of nacre [13], (b) the nacre structure-like random irregular Voronoi graphene platelet model with 100 complete platelets and degrees of regularity $\boldsymbol{\alpha}$ = 0.6. (c) Finite element RVE model of MGPFs in Abaqus.

3 Numerical results

The elastic properties of random irregular Voronoi honeycombs are found to be in-plane isotropic [10]. Intuitively, the elastic properties of the MGPFs composed of multilayer random Voronoi graphene platelets are also in-plane isotropic. Moreover, MGPFs have three orthogonal planes of elastic symmetry and thus have only five independent elastic constants [14] to be determined: E_1, v_{12}, E_3, G_{13} and v_{13}. And in order to

ensure that the in-plane elastic properties of the MGPF are isotropic. The number of intact Voronoi graphene particles N in each layer of the calculated RVE model is set to 100 for the following simulations.

When the MGPFs are in-plane stretched, the applied tensile force is transmitted via the interlayer shear stress resulted from the van der Waals interaction between the staggered graphene platelets [7,8,15]. Liu et al.[7] analysed the unidirectional mechanical properties of MGPFs based on a 2D tension-shear chain model in which the graphene platelets are represented by one dimensional bars of the same length $\boldsymbol{l}$, and all the overlaps between the regularly staggered graphene platelets are assumed to be the same as $\boldsymbol{l}/2$. A characteristic platelet length [7,8] is obtained as $\boldsymbol{L_0} = \sqrt{Dh_0/(4G)} = 2.407nm$, where $\boldsymbol{D}$ is the in-plane tensile stiffness of the graphene platelets (i.e. the one dimensional bars in the 2D model), $\boldsymbol{h_0}$ is the interlayer distance between the staggered graphene platelets, and $\boldsymbol{G}$ is the shear modulus (i.e. 5 GPa) of the equivalent solid material between the regularly staggered graphene platelets. The unidirectional mechanical properties [7] are found to be significantly dependent on the size $\boldsymbol{l}$ of the graphene platelets if $\boldsymbol{l}$ is close to $\boldsymbol{L_0}$ or smaller, and become less dependent on the size of the graphene platelets if $\boldsymbol{l}$ is several times larger than $\boldsymbol{L_0}$.

As the multilayer graphene platelet films (MGPFs) are three-dimensional structures, as shown in Figure 1c, the 2D tension-shear chain models [7,8,16] are difficult to correctly represent their actual geometrical structure and accurately reflect the overlaps between the staggered graphene platelets. For MGPFs with five graphene layers, the RVE models were applied to study the effects of the mean size (diameter $\boldsymbol{d}$) of graphene platelets on the five independent elastic properties and the results are presented in Figure 1c, where $\boldsymbol{d_0}$ is the mean diameter of the graphene platelets and $\boldsymbol{L_0}$. It is noted that the results in Figure 2 are obtained from random RVE models with a fixed graphene platelet area fraction of $\boldsymbol{F_A} = 0.997$, tensile strain is around 0.001 and a fixed regularity degree of $\boldsymbol{\alpha} = 0.6$.

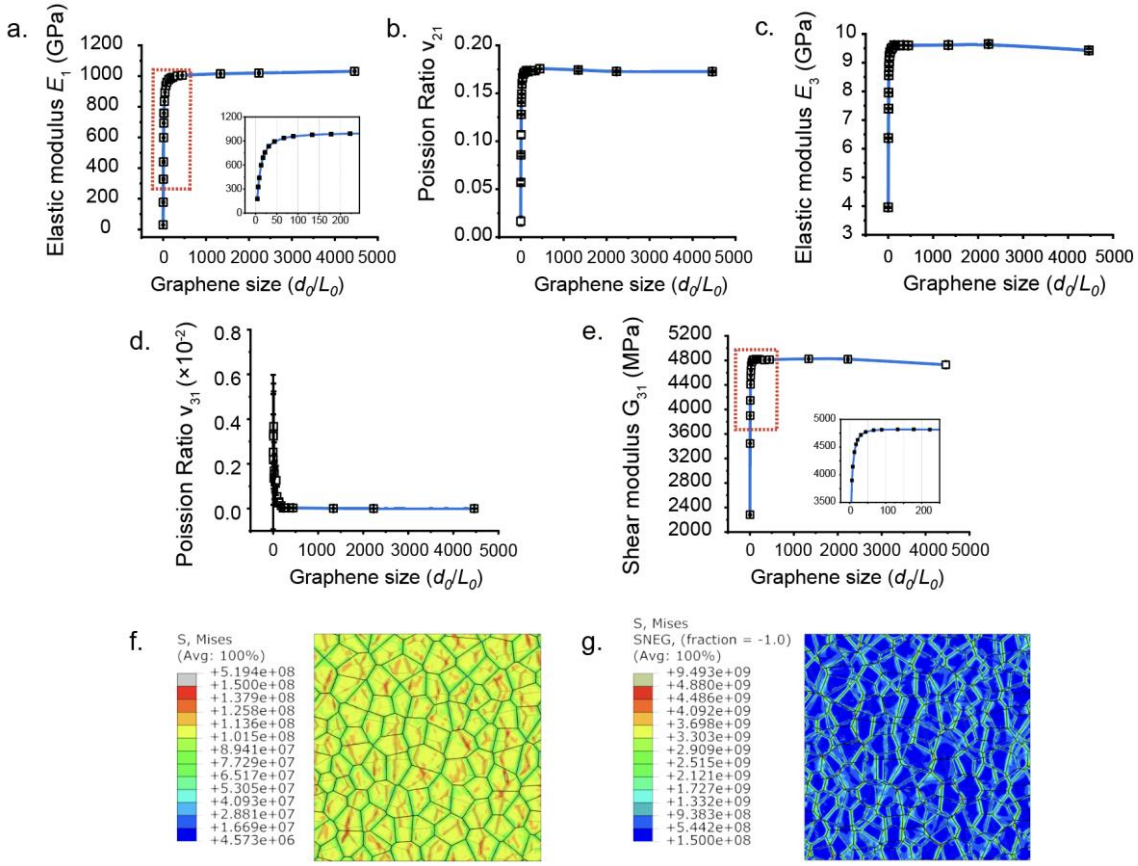

Fig.2 Effects of graphene platelet size (d_0/L_0)) on the elastic properties of MGPFs with $F_A = 0.99$, graphene layers M=5 and regularity degree α=0.6. a) The in-plane Young's modulus, b) the in-plane Poisson's ratio, c) the out-of-plane Young's modulus, d) the Poisson's ratio v_{13}, e) the shear modulus G_{13}, f) the von Mises stress contour in the equivalent solid plates of the staggered graphene platelets and g) in the equivalent solid plates of the van der Waals interaction between the staggered graphene platelets when the film is in-plane stretched in the horizontal direction ($\boldsymbol{d_0}/\boldsymbol{L_0} = 44.64$).

4 Conclusions

As the individual graphene platelets in the RVE model MGPFs are held together by the van der Waals interaction forces between the staggered graphene platelets, both the in-plane stiffness (E1 in Fig. 2a) and the out-of-plane stiffnesses (E_3 in Fig. 2c and G_{31} in Fig. 2e) of the MGPFs are all very sensitive to the mean size (i.e., d_0/L_0) of the graphene platelets when it is small. The stress concentration near the edges of the overlap areas of the staggered graphene platelets is also presented by the stress contours in Fig. 2f and Fig. 2g. The results in Fig. 2a and Fig. 2c show that both the in-plane and out-of-plane Young's moduli of the MGPFs increase rapidly with the increase of d_0/L_0 when the dimensionless mean size d_0/L_0 of graphene platelets in the 3D RVE model is smaller than 20, and their increases become slow-down with the further increase of d_0/L_0. Obviously, if the mean size (i.e., d_0/L_0) of the graphene platelets tends to infinite, the predicted in-plane stiffnesses based on either our 3D model or the other 2D models [7,8] would all increase to their maximum values.

Acknowledgments

The authors would like to thank the Chinese Scholarship Council and Cardiff University for providing financial support to this project

References

[1] K. S. Novoselov, V. I. Fal′ko, L. Colombo, P. R. Gellert, M. G. Schwab, and K. Kim, *A Roadmap for Graphene*, Nature **490**, 192 (2012).

[2] C. Lee, X. Wei, J. W. Kysar, and J. Hone, *Measurement of the Elastic Properties and Intrinsic Strength of Monolayer Graphene*, Science **321**, 385 (2008).

[3] M. Wang, D. Luo, B. Wang, and R. S. Ruoff, *Synthesis of Large-Area Single-Crystal Graphene*, Trends Chem. **3**, 15 (2021).

[4] B. Wang et al., *Camphor-Enabled Transfer and Mechanical Testing of Centimeter-Scale Ultrathin Films*, Adv. Mater. **30**, 1800888 (2018).

[5] W. Zhu, T. Low, V. Perebeinos, A. A. Bol, Y. Zhu, H. Yan, J. Tersoff, and P. Avouris, *Structure and Electronic Transport in Graphene Wrinkles*, Nano Lett. **12**, 3431 (2012).

[6] J. Peng and Q. Cheng, *High-Performance Nanocomposites Inspired by Nature*, Adv. Mater. **29**, 1702959 (2017).

[7] Y. Liu, B. Xie, Z. Zhang, Q. Zheng, and Z. Xu, *Mechanical Properties of Graphene Papers*, J. Mech. Phys. Solids **60**, 591 (2012).

[8] Z. Q. Zhang, B. Liu, Y. Huang, K. C. Hwang, and H. Gao, *Mechanical Properties of Unidirectional Nanocomposites with Non-Uniformly or Randomly Staggered Platelet Distribution*, J. Mech. Phys. Solids **58**, 1646 (2010).

[9] H. X. Zhu, S. M. Thorpe, and A. H. Windle, *The Geometrical Properties of Irregular Two-Dimensional Voronoi Tessellations*, Philos. Mag. A **81**, 2765 (2001).

[10] H. X. Zhu, J. R. Hobdell, and A. H. Windle, *Effects of Cell Irregularity on the Elastic Properties of 2D Voronoi Honeycombs*, J. Mech. Phys. Solids **49**, 857 (2001).

[11] H. Tang, F. Barthelat, and H. D. Espinosa, *An Elasto-Viscoplastic Interface Model for Investigating the Constitutive Behavior of Nacre*, J. Mech. Phys. Solids **55**, 1410 (2007).

[12] H. X. Zhu, T. X. Fan, and D. Zhang, *On the Optimal Mechanical Properties of Hierarchical Biomaterials*, in *Hierarchically Structured Porous Materials*, edited by B.-L. Su, C. Sanchez, and X.-Y. Yang (Wiley-VCH Verlag GmbH & Co. KGaA, Weinheim, Germany, 2011), pp. 621–631.

[13] H. Yang, D. Gao, P. Chen, and G. Lu, *Numerical Investigation on the Ballistic Performance of Semi-Cylindrical Nacre-like Composite Shells under High-Velocity Impact*, Materials **16**, 10 (2023).

[14] H. X. Zhu, H. C. Zhang, J. F. You, D. Kennedy, Z. B. Wang, T. X. Fan, and D. Zhang, *The Elastic and Geometrical Properties of Micro- and Nano-Structured Hierarchical Random Irregular Honeycombs*, J. Mater. Sci. **49**, 5690 (2014).

[15] A. Crisafulli, A. Khodayari, S. Mohammadnejad, and M. Fasano, *Sliding Dynamics of Parallel Graphene Sheets: Effect of Geometry and Van Der Waals Interactions on Nano-Spring Behavior*, Crystals **8**, 4 (2018).

[16] Q. Peng, C. Liang, W. Ji, and S. De, *A Theoretical Analysis of the Effect of the Hydrogenation of Graphene to Graphane on Its Mechanical Properties*, Phys. Chem. Chem. Phys. **15**, 2003 (2013).

UKACM 2024 Conference, 10-12 April 2024, Durham University, Durham, UK
https://doi/org/10.62512/conf.ukacm2024.013

TOWARDS SIMULATION OF MAGNET QUENCH USING *HP*-FEM

S. Miah[1*], P.D. Ledger[1], A.J. Gil[2], M. Mallet[3], T.-Q. Ye[3]

[1] School of Computer Science and Mathematics, Keele University, ST5 5BG, UK.
m.s.miah@keele.ac.uk, p.d.ledger@keele.ac.uk
[2]Zienkiewicz Institute for Modelling, Data and AI, Faculty of Science and Engineering,
Swansea University, SA1 8EN, UK.
a.j.gil@swansea.ac.uk
[3]Siemens Healthineers, MR Magnet Technology, OX29 4BP, UK.
michael.mallett@siemens-healthineers.com, tian-qing.ye@siemens-healthineers.com

Abstract. Magnetic Resonance Imaging (MRI) scanners rely on superconducting magnets consisting of coils of superconducting material to produce a strong magnetic field across the bore of the magnet as part of the imaging process. To maintain superconductivity, the material needs to be kept very cold in a bath of liquid helium. However, sometimes problems can occur during a process called quench leading to heating of the material and the loss of superconductivity. This work is concerned with predicting quench by solving a coupled system of transient Thermal, Maxwell and Circuit equations.

Key words: *Magnetic Resonance Imaging; Electromagnetics; Coupling; Finite Element Methods; Quench; Circuit*

1 Introduction

The use of Magnetic Resonance Imaging (MRI) has been an essential tool in modern medical diagnosis being used for the examination of the brain and spinal cord for tumours to internal organs such as the liver or the prostate gland. Our group's previous work involved the simulation of a coupled 3D magneto mechanical problem to predict resonance effects associated with vibrations induced by eddy currents in conducting components (see [5] and references therein). The present work focuses on the modelling of superconducting materials used to produce the strong static magnetic field and how they transition to become conducting. During normal operation of an MRI scanner, the coils of superconducting material are kept cool in a bath of liquid helium so that they conduct electricity without resistance. However, sometimes undesirable effects can lead to heating of the coil so that the material becomes normal conducting and resistive. This process is called magnet quench. The heating of the coil boils-off the liquid helium, which is costly to replace. To better understand magnet quench, and predict when it is likely to occur, the solution of a highly non-linear coupled multi-physics problem involving electromagnetic, thermal and mechanical effects is required. We will investigate transient electro-thermal coupling within rotationally symmetric scanners, in addition to coupling with a circuit model to describe other components.

2 Problem Description

Somewhat surprisingly, it is not good conductors (e.g copper) that make the best superconducting materials. An example of a material that makes a good superconductor are strands of Nb-Ti (Niobium-Titanium), which, whilst under normal conditions, is resistive and not a particularly good conductor, becomes superconducting, without resistance to electricity, under certain conditions. This material will only be superconducting if the combination of temperature T, magnitude of magnetic flux density $|\boldsymbol{B}|$

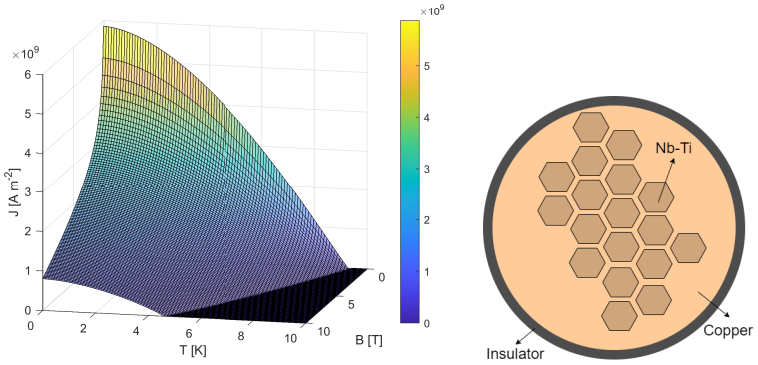

(a) Critical surface (b) MRI cable cross section

Figure 1: (a) An illustration of the critical surface for Nb-Ti and (b) the cross section of a typical MRI cable.

and current I is below a critical surface [4] (Figure 1(a)). However, when a superconductor is above the critical surface, it will remain normal conducting and resistance will be generated leading to heating effects.

MRI cables are made up of filaments which is a fine or very thin thread or fibre of material where as a strand is a series of filaments twisted together. A Rutherford cable, which is a particular wire bundle comprising of multiple strands of wire, with these strands being bound together and includes part copper, part superconducting medium Nb-Ti and part insulator, is commonly used in a typical MRI main magnet coil and these cables form our stranded coil Ω_s (Figure 1(b)). The small scale features of the MRI cables mean that the modelling of the strands (and filaments) is not possible and instead a homogenised model [2] is used to describe the materials properties of Ω_s and are used to relate the field quantities to the circuit quantities. One such homogenised model is the stranded model [2], which relates the external volume current density $\boldsymbol{J}^{ext}(t)$ field to the circuit current $I(t)$ through

$$\boldsymbol{J}^{ext}(t) = I(t)\boldsymbol{\chi}, \tag{1}$$

where $\boldsymbol{\chi}$ is a winding function that is characteristic of the type of conducting cable. In the simplest case, $|\boldsymbol{\chi}|$ is set to be the ratio of the number of turns in the wire and the cross sectional area so that $\boldsymbol{\chi} = (N_{turns}/A_{cross})\boldsymbol{e}_\phi$, where $\boldsymbol{e}_\phi$ is a unit vector in the azimuthal direction. The following material properties are also homogenised: resistivity ρ^e, thermal conductivity κ and volumetric heat capacity ρc with non-linear constitutive models (based on experimental measurements) being available for the component materials [4]. The (circuit) resistance of the coil being

$$R(t) = \int_{\Omega_s} \boldsymbol{\chi}^T \rho^e \boldsymbol{\chi} \mathrm{d}\Omega, \tag{2}$$

and for the present situation constant inductance L is assumed. A circuit model is used to describe how the different coil components of the MRI scanner are joined together. In addition to the coils, the domain of interest can also include conducting shields Ω_c with conductivity γ and magnetic permeability μ_0. The coils and other conducting bodies are surrounding by a non-conducting region and thermal bath Ω_{bath}. The electromagnetic fields are computed from the eddy current model of Maxwell's equations where

the homogenised treatment of Ω_s simplifies the treatment of this region. We adopt the vector potential $\boldsymbol{A}(t)$ field formulation of the eddy current model. The thermal equations for the temperature $T(t)$ in $\Omega_s \cup \Omega_c$ and the helium bath Ω_{bath} are described by energy balance [6] and include different loss terms that are associated with different effects. The losses include an Ohmic loss term $P^{Ohmic} = \gamma |\partial \boldsymbol{A}/\partial t|^2$, that describes the dissipation of energy through Ohmic heating, a Joule heating term $P^{Joule} = \rho^e I(t)^2 |\boldsymbol{\chi}|^2$, which describes the conducting effects in the stranded coil Ω_s, and lastly, a dynamic loss term $P^{Dyn} = \mu_0^{-1} \tau_{eq} |\mathrm{curl}\, \partial \boldsymbol{A}/\partial t|^2$, where τ_{eq} is a time constant that is dependent on the type of filament in the cable. The latter term is associated with the variation of the magnetic energy density function [1] caused by the inter-filament coupling and a form of this is also present in the electromagnetic equations for Ω_s. Initially, all parts of the coil are superconducting until a quench is initiated by forcing part of the coil to be normal conducting. One possible magneto-thermal-circuit coupled model is: Find $\boldsymbol{A}(t) \in \mathbb{R}^3(0, t_{max}]$, $I(t) \in C^1(0, t_{max}], T(t) \in \mathbb{R}(0, t_{max}]$ such that

$$\mathrm{curl}\, \mu_0^{-1} \mathrm{curl}\, \boldsymbol{A} + \mathrm{curl}\, \mu_0^{-1} \tau_{eq} \mathrm{curl}\, \frac{\partial \boldsymbol{A}}{\partial t} = I(t) \boldsymbol{\chi} \qquad \text{in } \Omega_s, \tag{3a}$$

$$\mathrm{curl}\, \mu_0^{-1} \mathrm{curl}\, \boldsymbol{A} + \gamma \frac{\partial \boldsymbol{A}}{\partial t} = \boldsymbol{0} \qquad \text{in } \Omega_c, \tag{3b}$$

$$\mathrm{curl}\, \mu_0^{-1} \mathrm{curl}\, \boldsymbol{A} = \boldsymbol{0} \qquad \text{in } \Omega_{bath}, \tag{3c}$$

$$\mathrm{div}\, \boldsymbol{A} = 0 \qquad \text{in } \Omega_{bath} \cup \Omega_s, \tag{3d}$$

$$-L \frac{\mathrm{d}I}{\mathrm{d}t} + IR = \int_{\Omega_s} \boldsymbol{\chi} \cdot \frac{\partial \boldsymbol{A}}{\partial t} \mathrm{d}\Omega + IR = 0 \tag{3e}$$

$$(\rho c) \frac{\partial T}{\partial t} - \mathrm{div}(\kappa\, \mathrm{grad}\, T) - P^{Dyn} - P^{Joule} - P^{Ohmic} = 0 \qquad \text{in } \Omega_s, \tag{3f}$$

$$\rho c \frac{\partial T}{\partial t} - \mathrm{div}(\kappa\, \mathrm{grad}\, T) - P^{Ohmic} = 0 \qquad \text{in } \Omega_c, \tag{3g}$$

$$\rho c \frac{\partial T}{\partial t} - \mathrm{div}(\kappa\, \mathrm{grad}\, T) = 0 \qquad \text{in } \Omega_{bath}, \tag{3h}$$

to which interfaces and initial conditions must also be added. The above (3e) is presented for the situation of a single coil, but can be extended to more complex configurations.

2.1 Computational Methodology

The coupled equations involved in quench simulation cannot be solved analytically and, hence, an approximate numerical simulation is performed using the Finite Element Method (FEM) to obtain the spatially and temporally varying fields. Additionally, rather than solving the problem in 3D, we solve in cylindrical coordinates and assume rotational symmetry to the equations to an axisymmetric formulation. We are developing an approach based on hp–finite element discretisation of the fields, implicit time integration and a fixed point iteration for the coupled system. We are able to then compute the fields of interest through post-processing.

3 Numerical results

A sample of single physics benchmark images taken from [3] and for details of these problems see this reference. This reference also shows that we can accurately compute solutions for each of the physics

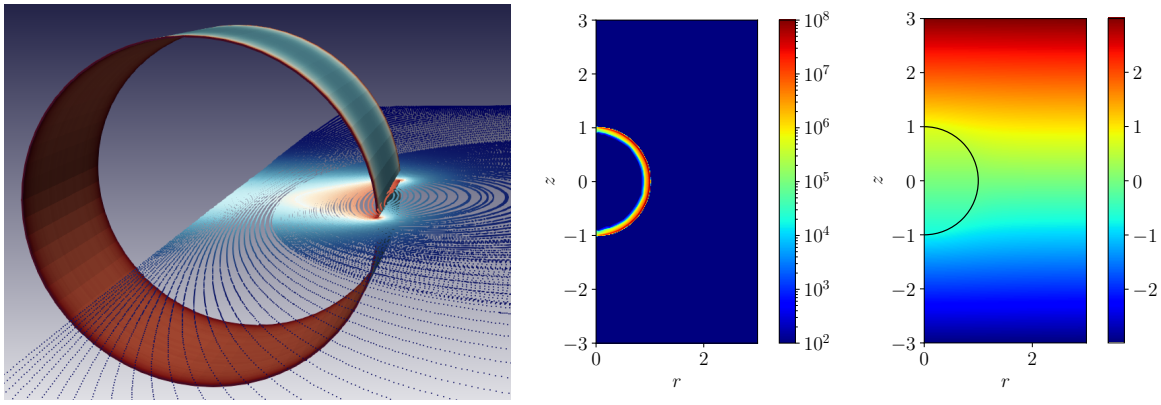

(a) Cylindrical coil (b) Conducting sphere (c) Thermal sphere

Figure 2: (a) Magnetostatic solution for a cylindrical coil in free space: Streamline plot of the $\boldsymbol{B}$ obtain by Paraview. Contours show the $|\boldsymbol{B}|$. (b) Time harmonic conducting sphere in constant amplitude time varying field: Contour plot with logarithmic scaled color bars of the eddy current field $|\mathcal{J}^e_\phi|$ for $\omega = 2\pi[500]$ rad/s. (c) Thermally conducting sphere in a uniform temperature gradient: Contour plot of the static T field.

separately.

4 Conclusion

The presentation will include presentation of the algorithm employed and a selection of results for the fully coupled magneto-thermal-circuit quench problem.

Acknowledgments

S. Miah is grateful for the financial support received from an EPSRC CASE Award Studentship in partnership with Siemens Healthineers.

REFERENCES

[1] L. Bortot, A. Auchmann, I. C. Garcia, A. F. Navarro, M. Maciejewski, M. Prioli, S. Schoöps, and A. Verweij. A 2D finite element model for electro-thermal transients in accelerator magnets. *IEEE Transactions on Magnetics*, 54:7000404, 2017.

[2] I. Cortes Garcia. *Mathematical Analysis and Simulation of Field Models in Accelerator Circuits*. PhD thesis, Technische Univerität Darmstadt, 2020.

[3] S. Miah. PhD thesis, Keele University, UK, In Progress.

[4] S. Russenschuck. *Field Computation for Accelerator Magnets: Analytical and Numerical Methods for Electromagnetic Design and Optimization*. John Wiley & Sons, Weinheim, Germany, 2011.

[5] M. Seoane, P. D. Ledger, A. J. Gil, and M. Mallett. An accurate and efficient three-dimensional high-order finite element methodology for the simulation of magneto-mechanical coupling in MRI scanners. *International Journal for Numerical Methods in Engineering*, 119:1185–1215, 2019.

[6] M. N. Wilson. *Superconducting Magnets*. Clarendon Press, United Kingdom, 1983.

Computational Innovations in Fluid Dynamics and Material Behaviour

UKACM 2024 Conference, 10-12 April 2024, Durham University, Durham, UK
https://doi.org/10.62512/conf.ukacm2024.029

MODELLING THE LIQUID DROPLET IMPACT BEHAVIOUR OF POLYMER MATERIALS

Luke J. Webb, Wei Tan[1]

[1] School of Engineering and Materials Science, Queen Mary University of London, E1 4NS, UK.
wei.tan@qmul.ac.uk

Abstract. In this study, we propose a multi-physics phase field model to predict the material degradation of polymer materials under liquid droplet impact. This model employs the Arbitrary Lagrangian-Eulerian (ALE) technique in conjunction with a predefined multiphysics interface for Two-Phase Flow and Phase Field. The ALE method captures the dynamics of the deforming geometry and evolving boundaries through a moving grid. The boundary between water and air is tracked using the phase-field method. Meanwhile, the deformable solid is modelled using a variety of constitutive models, including linear elastic, Von Mises plasticity, and continuum damage mechanics. The computational model is subsequently validated against the experimental results. The displacement, strain distribution, and strain wave history from both modelling and experiment are compared. Our model demonstrates good qualitative agreement with the experimental results. The plasticity model or fracture model also provides insights into the failure mechanisms. This preliminary work opens a new avenue to model the degradation of polymer materials under extreme conditions.

Key words: *Liquid-solid Impact; Phase field methods; Polymer materials*

1 Introduction

The pursuit of ambitious net-zero goals, coupled with the ongoing energy crisis, has generated a heightened demand for lightweight polymer materials extensively utilised in the transport and energy sectors. Despite their widespread use, these polymers are vulnerable to extreme conditions, including environmental ageing and dynamic liquid-solid impact (LSI). The contact between a high-velocity liquid mass and a solid surface initiates transient stress waves, which may interact at interfaces and with successive impacts to results in significant damage. This multiphysics phenomenon is not only prevalent in natural events like coastal erosion but also poses a substantial threat to critical sectors such as energy and transportation. Anecdotal evidence has emphasised the growing danger of liquid impact erosion on wind/steam turbine blades and aircraft leading edges, and its reduction of the system's efficiency [1]. Effectively addressing the challenges of material degradation associated with LSI necessitates a thorough understanding of the underlying damage mechanisms, particularly in the context of polymer materials. In this work, we proposed a multiphysics computational model to analyse the mechanics throughout the process of a polymer undergoing liquid-solid impact.

2 Methods

The Arbitrary Lagrangian-Eulerian (ALE) framework is used for the modelling of fluid-solid interaction. For the solid domain, we utilise various constitutive models for polymer materials, including linear elastic, elastoplastic, and viscoelastic models. For the fluid domain, we employ the phase field method for the multiphase laminar flow (water and air).

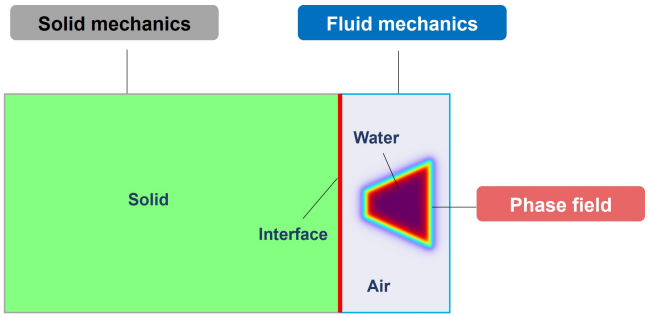

Figure 1: Various models employed across different domains.

2.1 Phase field method for multiphase flow

The phase field method offers an attractive alternative to more established methods for solving multiphase flow problems. For instance, in the liquid-solid impact phenomenon, the two-phase flow consists of water and air. Instead of directly tracking the interface between two fluids, the interfacial layer is governed by a phase field variable. The surface tension force is added to the Navier-Stokes equations as a body force by multiplying the chemical potential of the system by the gradient of the phase field variable.

The free energy of a system of two immiscible fluids consists of mixing, bulk distortion, and anchoring energy. For simple two-phase flows, only the mixing energy is retained, which results in a rather simple expression for the free energy.

$$F(\phi,\nabla\phi,T) = \int (\frac{1}{2}l^2|\nabla\phi|^2 + f(\phi,T))dV = \int f_{tot}dV \tag{1}$$

where l is a measure of the interface thickness.

The evolution of the phase field variable is governed by the Cahn-Hilliard equation, which is a 4th-order PDE. The Phase Field interface decomposes the Cahn-Hilliard equation into two second-order PDEs.

$$\frac{\partial\phi}{\partial t} + \mathbf{u}\cdot\nabla\phi = \nabla\cdot\frac{\gamma\lambda}{l^2}\nabla\psi \tag{2}$$

$$\psi = -\nabla\cdot l^2\nabla\phi + (\phi^2-1)\phi \tag{3}$$

where ϕ is the dimensionless phase field variable, λ the mixing energy density, l phase field length that scales with the thickness of the interface.

3 Numerical results

3.1 Validation of the global impact response

The experimental results [2] of the PMMA's full-field displacement were captured via Digital Image Correlation, using filters $\pm 4\mu$m and $\pm 2\mu$m for the x and y displacement values, respectively. Fig. 2 displays these results (denoted by 'Exp') during the initial stages of impact, compared against the model (denoted by 'FE') using the same filter.

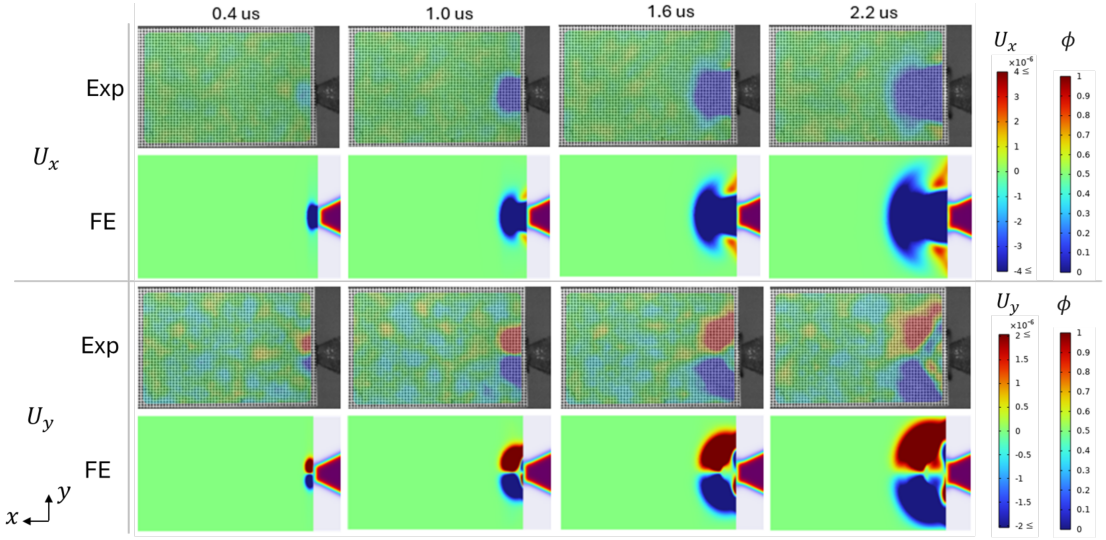

Figure 2: Model validation through the comparison of experimental and numerical displacement results.

The displacement contours formed during the analysed stages showed good correlation between the experiment and model in both the x and y fields. Of note was the model's capability to generate the parabolic front in the x displacement field and the multiple, separated fronts in the y displacement field. Considering the front propagation, the model displayed a similar rate of dispersion. This likeness suggested to the potential of the proposed method to accurately model the process of high-velocity liquid-solid impact.

3.2 Influence of the material model

As established by Burson-Thomas et. al [2], the PMMA substrate was not perfectly elastic in reality, hence a more complex material model was needed in order to better represent the its response. To quantify this, the x-displacement at a point 2mm below the surface of the initial contact point was analysed, comparing the experimental results to the numerical model with considerations for plasticity, viscoelasticity, and strain rate hardening, displayed in Fig. 3.

As expected, the elastic model over-predicted the deformation, showing results around 10 times higher than that seen in the experiment. In attempting to correct this, the plastic model continued to display excessive deformation, even when hardened. The viscoelastic model introduced a damping effect into the response, replicating the oscillatory nature of the experimental results and lowering the displacement to a realistic magnitude, indicating the viability of the material model. The strain rate hardened elastic model showed similar potential, with generally slightly lower displacement results than the viscoelastic model. While the strain rate hardened model assumed an equivalent increase in elastic modulus by a factor of 10, the speed with which the impact event occurred suggested to the possibly large influence of strain rate, and so the material model was also considered further development.

Analysing the latter stages of the impact, after 1μs, all the numerical models showed a general diminishing trend. None were able to capture the latter increase in displacement seen in the experiment or the abrupt return to equilibrium. Potentially a more complex material description may replicate this.

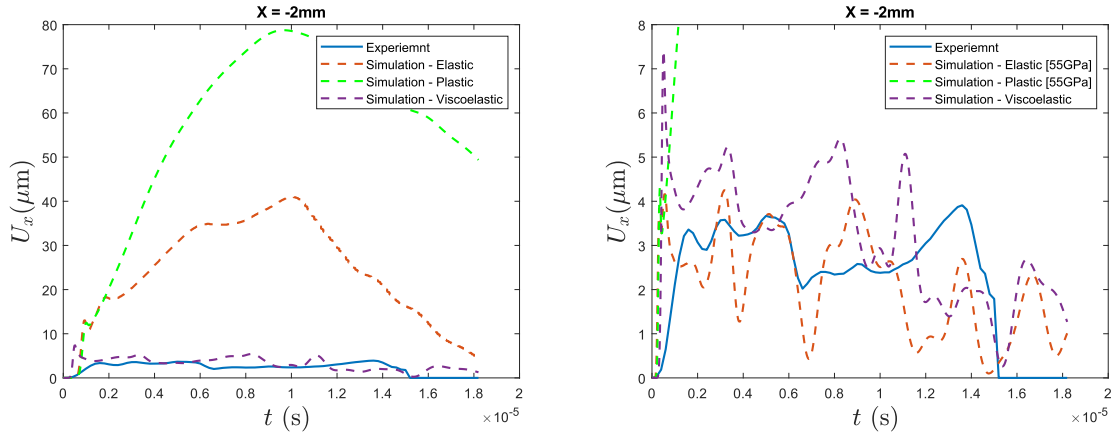

(a) (b)

Figure 3: Internal point (X=-2mm) x displacement comparison between experimental and numerical results, varying the material model: (a) Simple material models; (b) Consideration of strain rate hardening.

4 Conclusions

A methodology for modelling the response of a solid substrate to high-velocity liquid droplet impact has been presented using the ALE technique to capture the FSI and a phase-field to track the water-air boundary. The method was shown to replicate the full-field displacement contours recorded in a water-PMMA impact experiment, displaying a good qualitative correlation. The initial elastic material model over-predicted the x displacement results by a factor of about 10. However, a viscoelastic and a strain rate hardened elastic model were proposed to better capture the PMMA's behaviour, showing significantly more realistic results. The capability for this method to improve understanding of material response and degradation to fluid impact, throughout the event, is noteworthy and has the potential to provide guidance on developing more resilient materials. Future work will focus on continuing to improve the PMMA material model and introducing multi-material interfaces to capture polymer behaviour.

Acknowledgments

W. Tan acknowledges the support from UKRI Frontier Research/ERC Starting Grant [EP/Y037103/1] and Royal Society [RGS/R1/231417].

REFERENCES

[1] Mishnaevsky, L., Hasager, C.B., Bak, C., Tilg, A.M., Bech, J.I., Rad, S.D. and Fæster, S. Leading edge erosion of wind turbine blades: Understanding, prevention and protection. *Renewable Energy* (2021) **169**, doi: 10.1016/j.renene.2021.01.044.

[2] Burson-Thomas, C. B., Harvey, T.J., Fletcher, L., Wellman, R., Pierron, F. and Wood, R.J.K. Investigating high-speed liquid impingement with full-field measurements. *Proc. R. Soc. A.* (2023) **479**:2277, doi: 10.1098/RSPA.2023.0023.

UKACM 2024 Conference, 10-12 April 2024, Durham University, Durham, UK
https://doi.org/10.62512/conf.ukacm2024.033

A numerical flume with enhanced momentum conservation for the two-phase flow simulation

Xin Wang[1*], Dominic E Reeve[1], Min Luo[2,] Harshinie Karunarathna[1], Jose M. Horrillo-Caraballo[1]

[1] Faculty of Science and Engineering, Swansea University, Swansea, SA1 8EN, UK
xin.wang2@swansea.ac.uk
[2] Ocean College, Zhejiang University, Zhoushan, 316021, China
d.e.reeve@swansea.ac.uk, min.luo@zju.edu.cn, h.u.karunarathna@swansea.ac.uk, j.m.horrillo-caraballo@swansea.ac.uk

Abstract

The numerical simulation of two-phase flow with Navier-Stokes equations is often hampered by the instabilities rises across the interface of the different fluids. The interfacial gradient of velocity and density leads to the unphysical momentum change, resulting in an ill-defined velocity field and twisted interface. To deal with this problem, we developed an interfacial treatment which enhances the interfacial continuity of momentum (EMC treatment) [1]. Charactered by a momentum-based velocity reconstruction process and a strong coupling scheme between the N-S equation solving and interface capturing, the proposed EMC treatment can mitigate the interfacial instability and improve the accuracy and smoothness of the interface. An FDM-based flume with the EMC treatment is established based on the open-source REEF3D code [2]. Cases have been simulated for validation of EMC treatment, including pure numerical cases with idealised settings, as well as the experiments with highly deformed breaking wave [3], to demonstrate its effectiveness.

Key words: *two-phase flow; momentum conservation; N-S equation; breaking wave; numerical simulation; REEF3D*

1 Introduction

Two-phase flow is a frequently seen phenomenon in the real world, involving the interaction between different fluids. Numerical simulation is an effective way to study two-phase flow, but the accuracy and stability of numerical simulation are often hampered by the large density ratio between the fluids (e.g., water and air). In the numerical simulation, the large gradient across the water-air interface would introduce unphysical momentum to the water or air phase, resulting in the numerical error and instability. As a result, accurate simulation of this problem is still challenging.

Regarding this issue, we proposed an interfacial treatment to deal with the interfacial instability, and established a numerical flume based on an open-source FDM code. The numerical algorithm includes the momentum-based velocity reconstruction and strong time-coupling between flow field resolving and interface capturing. Validation is performed to check the accuracy of the established algorithm, including an idealized case of a falling dense and inviscid droplet, and an experimental case of freak wave impact on a box structure. The performance of the algorithm is then discussed.

2 Numerical algorithm

An open-source model (REEF3D) is adopted in the study [2], which is based on incompressible NS equation as shown in Eqs. (1) and (2), and the water-air interface is defiend by Level Set method [4].

$$\frac{\partial u_i}{\partial x_i} = 0 \tag{1}$$

$$\frac{\partial u_i}{\partial t} + u_j \frac{\partial u_i}{\partial x_j} = -\frac{1}{\rho}\frac{\partial p}{\partial x_i} + \nu[\frac{\partial}{\partial x_j}\left(\frac{\partial u_i}{\partial x_j} + \frac{\partial u_j}{\partial x_i}\right)] + g_i \tag{2}$$

For a better momentum conservation, we choose the advection of momentum and mass instead of the advection of velocity (Eqs. (3) and (4)), and the advected velocity field is re-constructed by Eq. (5):

$$\frac{\partial M_i}{\partial t} + u_j \frac{\partial M_i}{\partial x_j} = 0 \tag{3}$$

$$\frac{\partial \rho}{\partial t} + u_j \frac{\partial \rho}{\partial x_j} = 0 \tag{4}$$

$$u_i^* = \frac{M_i^*}{\rho^*} \tag{5}$$

in which M, u and ρ stands for the momentum, velocity and density. The calculation sequence of solving NS equation and surface capturing is also modified to provide a strong coupling between them, to achieve a good synchronization of the variables, for a detailed introduction of the proposed algorithm, the reader is referred to (Wang et al., 2023). For comparison, the original REEF3D code was labelled FDM, and the version with the modified algorithm was labelled FDM-EMC.

3 Numerical results

3.1 Simulation of a falling inviscid dense fluid droplet

The first validation case is an idealized case, and the settings are shown in Figure 1(a). The computational domain was 0.5 m × 2 m. A droplet with 0.15 m radius, 1.4 m height was initially located at the horizontal centre. The densities of the droplet and surrounding fluid were 10^6 kg/m^3 and 1 kg/m^3, respectively. Both fluids were set to be inviscid, hence the flow field depended solely on the convection and gravity. Due to the extreme density ratio, the influence of the lighter fluid on the heavier fluid should be negligible and in the falling process the droplet should stay its initial disk shape. Three mesh systems with different transition area sizes and mesh sizes were adopted in the numerical simulation. They were labelled with Case 1-1, Case 1-2 and Case 1-3, as shown in Table 1. Open boundary condition was applied on each side of the domain.

Table 1. The grid settings of the three cases.

Case	transition area size (ϵ)	Mesh size (Δx)
Case 1-1	2.1 Δx	0.01 m
Case 1-2	2.1 Δx	0.005 m
Case 1-3	1.05 Δx	0.005 m

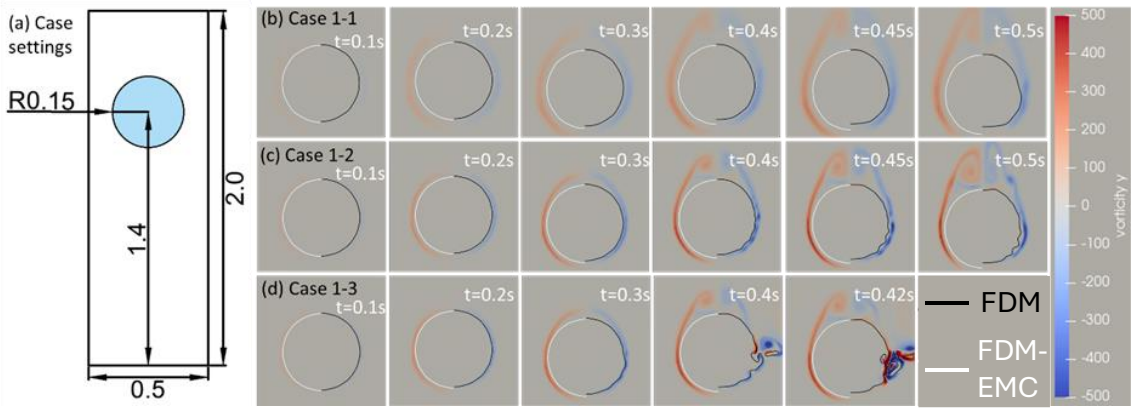

Figure 1: The water-air interfaces and vorticity fields during the falling of the three cases

Figure 1(b), (c) and (d) present the water-air interface profiles and the vorticity fields of the three cases simulated by the original FDM model and FDM-EMC model. With the increase of the falling speed, the vorticity field kept developing and vortices were generated above the droplet, and the difference on the

interface became more and more obvious. FDM-EMC preserved the smoothness of the vorticity and interface, and the disk shape of the droplet remained very well. However, the original FDM model generated a twisted surface shape with spurious current on the water-air interface, and the vorticity contour became more and more vibrated. The difference on the vertical length of the droplet could be observed clearly after t=0.3s.

Comparing Cases 1-1, 1-2 and 1-3, it was found when simulated by the original FDM model, shortening the grid spacing and transition area size resulted in a lower stability, more extreme surface twisting and spurious current, as the original code crashed at 0.42 s in case 1-3 while the FDM-EMC can still provide a smooth surface and satisfying round shape. Although grid refining and surface sharpening may reduce the stability, the FDM-EMC made it possible to adopt a shorter transition area and mesh refining.

3.2 Simulation of a freak wave impact on a box structure

A 2D numerical wave flume, as sketched in Figure 2, was established to reproduce the experimental settings presented in [3]. The two sides of the platform were equipped by a numerical paddle and wave absorber, respectively. Three wave gauges are located in the flume. A box with 0.12 m height and 0.5 m length was set to be 12.557 m away from the paddle and 0.049 m above the still water level (0.7 m). 2 pressure sensors were located on the front face of the box with 0.035 m and 0.08 m from the deck bottom, and 2 more pressure sensors were located on the bottom face with 0.035 m and 0.205 m away from the front border. Four mesh sizes were adopted in the study, as shown in Table 2. No-slip boundary was applied on the bottom of the computational domain, and the displacement of the numerical wave paddle followed the paddle movement history in the laboratory experiment.

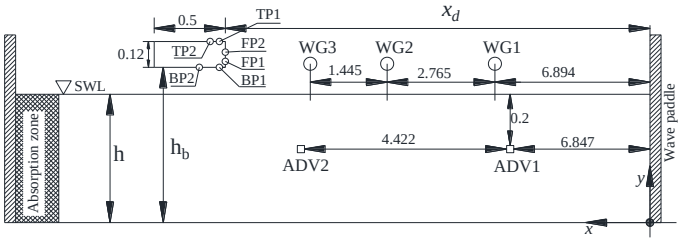

Figure 2: The settings of the experiment of freak wave impact on a box structure.

Table 2. The mesh settings of the simulation of freak wave impact.

Mesh	Mesh size (Δx)
Mesh A	0.02 m
Mesh B	0.01 m
Mesh C	0.0075 m
Mesh D	0.005 m

Figure 3 shows the profile of the freak wave at t = 18.60 s under four mesh sizes. The original FDM model did not reproduce the overturning tongue in all four mesh sizes, and twisted free surface shapes were already observed at Meshes B and C. The simulation with the finest mesh, i.e. Mesh D, crashed at t = 18.55 s due to the interfacial instability. In contrast, the highly deformed overturning tongues were well reproduced by FDM-EMC model for Meshes B, C and D. It was evident that the predicted wave profile by FDM-EMC approached to the experimental one with mesh refinement, and Mesh D achieved the best agreement with the experiment snapshot. In all four mesh systems, the free surface profiles kept their smoothness, and were much less influenced by the numerical instability. This implied the necessity of the EMC treatment in modelling breaking waves involving large deformation of fluid interface. A good mesh size convergence of the developed FDM-EMC model was demonstrated. Figure 4 presents the normalized pressure (P_N) at the six pressure sensors. It can be seen the FDM-EMC model achieved a higher accuracy than the simulation with SPH method in (Sun et al., 2019), especially the front wall (FP1 and FP2).

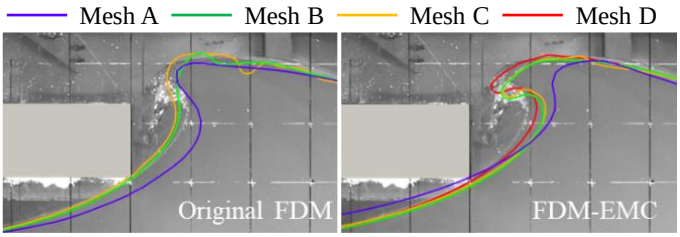

Figure 3: Comparison of the water-air interface profiles upon the wave impact

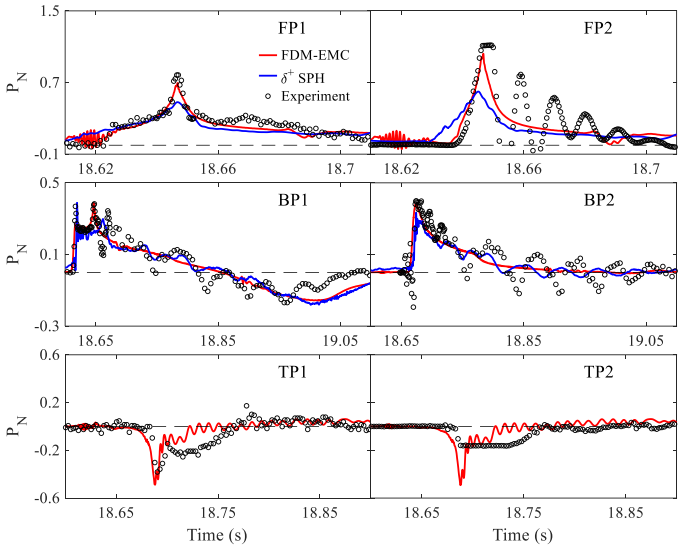

Figure 4: Validation of the pressure histories at the six wave gauges.

4 Conclusions

The large density ratio is one of the main reasons of the interfacial stability and accuracy. By applying momentum-based velocity reconstruction and strong temporal coupling of flow field resolving and surface capturing, EMC treatment significantly improved the performance of FDM simulation of two-phase flow.

Acknowledgments

The presenting author would like to thank the Centenary Scholarship from the Faculty of Science and Engineering of Swansea University.

References

[1] Wang, X., Luo, M., Karunarathna, H., & Reeve, D. E. (2023). An enhanced momentum conservation treatment for FDM simulation of two-phase flows with large density ratio. Journal of Computational Physics, 111949.

[2] Bihs, H., Kamath, A., Chella, M. A., Aggarwal, A., & Arntsen, Ø. A. (2016). A new level set numerical wave tank with improved density interpolation for complex wave hydrodynamics. Computers & Fluids, 140, 191-208.

[3] Sun, P. N., Luo, M., Le Touzé, D., & Zhang, A. M. (2019). The suction effect during freak wave slamming on a fixed platform deck: Smoothed particle hydrodynamics simulation and experimental study. Physics of Fluids, 31(11), 117108.

[4] Osher, S., & Sethian, J. A. (1988). Fronts propagating with curvature-dependent speed: Algorithms based on Hamilton-Jacobi formulations. Journal of Computational Physics, 79(1), 12-49.

UKACM 2024 Conference, 10-12 April 2024, Durham University, Durham, UK
https://doi.org/10.62512/conf.ukacm2024.037

Validation of Open-source CFD Solvers for Rotating Detonation

Reuben Hann, Enric Grustan-Gutierrez
School of Aerospace, Transport and Manufacturing, Cranfield University, Cranfield, MK43 0AL, UK.
reuben.hann@cranfield.ac.uk

Abstract

Computational Fluid Dynamics (CFD) are a core aspect of research into Rotating Detonation Engines (RDEs). However, barriers to entry to conduct RDE CFD simulations, such as pay-walled and closed-source solvers hinder the ability of researchers to recreate, validate and build on past work in the RDE research field. As such, we test an open-source alternative solver, RYrhoCentralFoam, a multi-phase, multi-component, compressible and reacting flow OpenFOAM solver developed by the National University of Singapore's Computational Combustion and Energy Group. We validate and test the solver by simulating a hydrogen-air small annular RDE across a range of mass flow rates. Using this solver, we were able to achieve rotating detonation in a simulated small RDE, at mass flow rates ≥40 g/s with stoichiometric mixtures. The detonation velocity was within 90-94% of the Chapman–Jouguet detonation velocity, this being higher than the typical 60-80% range for annular RDEs. This is due to the inviscid flow conditions assumed in the RDE chosen to limit the computational cost of the simulation.

Keywords: *OpenFOAM; Rotating Detonation Engine; RYrhoCentralFoam; CFD;*

1 Introduction

The two distinct types of combustion, deflagration and detonation, are primarily differentiated by the velocity a flame expands in a mixture of reactants or flame speed. Deflagration has subsonic flame speeds, typically between 1-100 m/s whilst detonation has supersonic flame speeds in the region of 1500-2500 m/s [1]. This supersonic flame speed leads to the detonation wave comprising a leading shockwave and an attached combustion region behind it. The leading shockwave compresses the reactants before being burnt, allowing the combustion to occur at a higher pressure and temperature than if the reactants were deflagrated, improving the combustion system efficiency [2]. If fully realised, this could allow there to be a pressure gain over the combustor, as opposed to a pressure loss typically found in jet and rocket engine combustors and an improvement in the overall efficiency of the engine. Using detonation in combustion engines in the form of rotating detonation has so far empirically shown a 5-7% reduction in specific fuel consumption in gas turbines and a 6-8% higher specific impulse in rocket engines though no total pressure gain over the combustor has yet been achieved [3]. RDEs operate by adding directionality to detonation allowing for continuous detonation combustion. By injecting a detonation wave tangentially into an annular or cylindrical combustion chamber the detonation wave will then continuously rotate around the inside wall of the chamber. This process is then sustained by injecting reactants along the axis of the combustion chamber in an annular injection area. The combusted products are then ejected out of the other end along the axis of the chamber into a turbine or a nozzle to generate thrust and energy.

Though RDEs were first discovered and tested in the 1960s [4] research in the field had to wait until the 2000s to gain traction [5], due to several different factors. Firstly, there is now a greater need for new approaches to improve the efficiency of propulsive and energy generation systems due to the greater prevalence of climate change as an existential issue compared to the mid-1960s. Secondly is the current availability of Computational Fluid Dynamics (CFD) and the computational power to run such simulations. CFD has been a core foundation of research into RDEs and an irreplaceable asset to modelling and understanding the flow inside RDEs. Given the intense heat, shock and pressure conditions within the engine, it can be difficult to gather direct empirical data. As such other approaches are necessary, for instance, CFD simulations help us understand the flow within RDEs, and as such any barriers to entry to conducting these simulations may hinder the research field and make it difficult for new researchers to enter.

2 Problem description

As CFD is a core aspect of RDE research, the accessibility of CFD software and solvers is necessary to continue conducting research and expanding the base of researchers in the field. Currently, barriers to entry such as pay-walled CFD solvers like Ansys Fluent [6], [7], and studies where only the equations have been listed but not the solver code, requiring other researchers to rebuild the solver [8], provide unnecessary barriers to entry for other researchers to validate, recreate and build on previous work, hindering progress in the field. Therefore, in this paper, we test an open-source alternative to conducting RDE CFD simulations that is openly available and free. We test to see if this solver can achieve rotating detonation and document our experience with it.

3 Numerical results

The solver used was RYrhoCentralFoam on OpenFOAM 8, a compressible, density-based, multi-component, reactive solver developed from the standard rhoCentralFoam OpenFOAM solver by the National University of Singapore's Computational Combustion and Energy Group [9], [10]. A 19 reaction, 9 species H2-Air combustion mechanism was used [11] by a laminar combustion model. RDEs can be very computationally expensive and time-consuming to run given their large, highly refined mesh sizes, large reaction mechanisms, and short time steps. Therefore, in this paper, the simulation setup needed to balance the computational cost against the simulation accuracy. As viscous forces and turbulence can have minimal effect on detonation waves an inviscid simulation setup and laminar combustion model were deemed appropriate for the task of simulating a rotating detonation wave as they allow for the lowest computational cost to simulate detonation with the limited compute available [12].

The numerical schemes, solution and algorithm control setup were adopted from the H2+NH2/Air detonation setup used by R. Zhu and X. Fang et al. [13]. The numerical flux was solved using the Kurganov, Noelle, and Petrova (KNP) method and corrected using the Van Leer limiter approach. Convective terms for energy and species were solved with a total variation diminishing scheme. Diffusive terms were calculated with a second-order central differencing scheme and a semi-implicit second-order scheme was used for time discretisation. The Euler Implicit chemistry integration solver was used based on Z. Huang et al. [9] testing of different chemistry solvers in RYrhoCentralFoam, in which it was found that the Euler Implicit solver provided the best balance of accuracy and computational cost. Species JANAF tables were sourced from OpenFOAM 6 validated by O. A. Marzouk [14]. The Courant number was kept to 0.05 to produce a time step of around 1e-9s. To validate the simulation setup and reaction mechanism, a 1D detonation velocity study was conducted. A 0.5m long 1-D domain was filled with stoichiometric hydrogen and air at 1 bar and 300 K and initiated by patching 1 cell on the left side of the domain with a pressure of 70 bar and 2000 K. Using pressure outlet boundary conditions on both ends of the domain ensured no reflected waves interfering with the detonation wave. The simulation was run for 0.0002s so that the simulation stopped just before the detonation wave reached the right side of the domain and the detonation wave had reached a steady state velocity. The mesh study showed that a cell size of 0.02 mm allowed for mesh independence, as shown in Figure 1. Therefore, a cell size of 0.02 mm was used in the validation study.

The simulated detonation velocity results were all within 10% and typically within 2% of the NASA Chemical Equilibrium with Applications (CEA) results, which calculated the Chapman-Jouguet (CJ) idealised detonation velocities. However, the simulated detonation wave tended to overestimate the CEA detonation velocity. Compared to the empirical results which tested the detonation velocity in detonation tubes over a range of blockage ratios (BR) and different diameters (Ø), only the stochiometric condition reasonably approximated the empirical value with a difference of 7.13%. However, the empirical data in Figure *1* shows some of the issues and reasons why the idealised detonation velocity is primarily used as the reference point instead of empirical results. Detonation tube experimental results are the primary method for empirically determining detonation velocities but are limited by the tube's diameter. Inside the detonation tube, the detonation wave acts as a 2-D cross-sectional plane travelling axially along the tube filled with reactants. The velocity of the detonation wave will be proportional to the total energy of the wave, which will be proportional to the cross-sectional area and therefore amount of reactants it can consume. Wall friction and heat transfer will reduce the amount of energy the detonation wave has. These losses will be proportional to the circumference of the wave. As the diameter is increased the total energy of the detonation wave will increase more than the friction and heat transfer losses, increasing the velocity of the detonation wave. As the diameter of the tube approaches infinity, the detonation wave velocity will approach the CJ

velocity. Therefore, as seen within the research field, the idealised CJ results are used as the primary reference point for detonation velocity [3], [9], [12], [13].

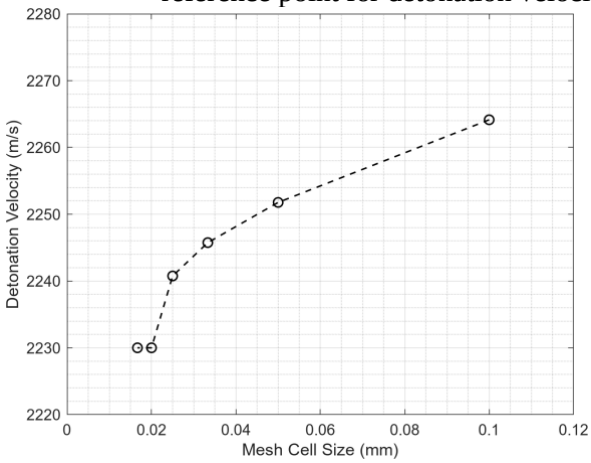

Figure 1: 1-D detonation velocity mesh study

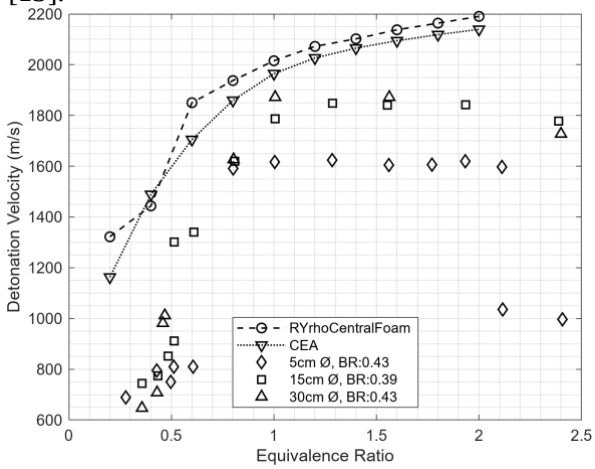

Figure 2: 1-D validation study testing the simulated detonation velocity over a range of equivalence ratios plotted against both the Idealised detonation velocity i.e., CEA and the empirical results from detonation tube experiments of different diameters (Ø) and blockage ratios (BR) [1]

As the 1-D detonation tube results showed the best alignment between the CFD and the empirical results at an equivalence ratio of 1, a stochiometric mixture was used throughout the subsequent annular RDE CFD simulations. With the CFD setup validated, a small annular RDE was simulated, inspired by the design by the US Air Force Institute of Technology [15]. The annular RDE had an outer diameter of 36mm, an inner diameter of 32mm and a height of 30mm. As seen in Figure 3 the RDE had a mass flow inlet on the bottom, with a mass flow rate range between 20-80 g/s with a total temperature of 300K, adiabatic no-slip inner and outer walls and a static pressure outlet with a pressure of 1 atm.

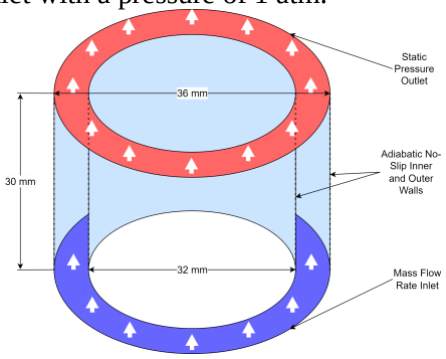

Figure 3: RDE geometry and boundary conditions

The simulation was initiated in two stages, first a blocking wall was placed between the outer and inner walls stopping any full rotation of any detonation waves. The initial conditions are the RDE being filled with a stochiometric mixture of air and hydrogen, at 1 atm, and 300K. A small region by the blocking wall is then set to a pressure of 30 bar and 1500K to initiate the detonation wave. The simulation is run for 5e-5s, with the detonation wave being forced to travel in one direction around the chamber by the blocking wall, giving directionality to the detonation wave. The simulation is stopped before the detonation wave reaches the other side of the blocking wall and is reflected. The blocking wall is then removed, and the simulation is continued for a total simulation time of 0.0005s. The detonation velocity was calculated by measuring the location of the detonation wave pressure peak over time and then calculating the instantaneous velocity and averaging it once it reached a steady state. A mesh study was conducted to determine the correct cell size for mesh independence, of which a cell size of 0.25 mm was found to meet that criterion as seen in Figure *4*.

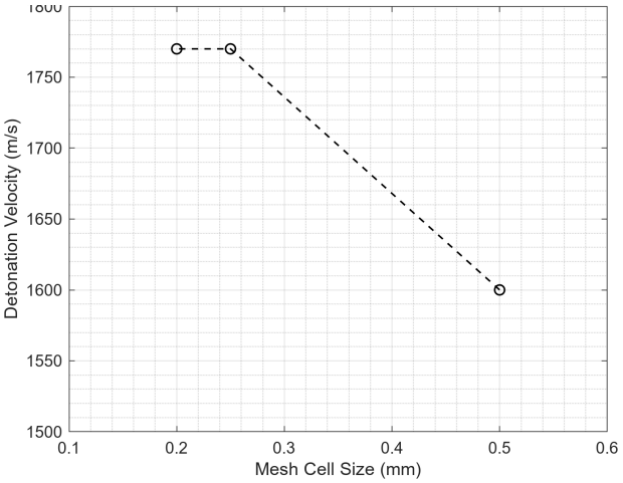

Figure 4: RDE detonation velocity mesh study

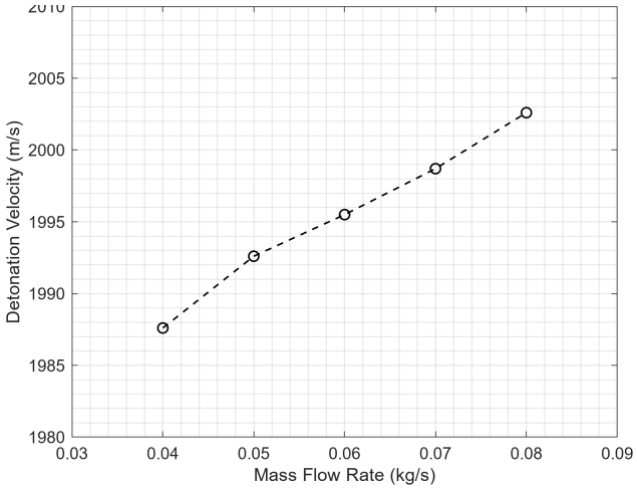

Figure 5: RDE detonation velocity across mass flow rate range

Simulating the RDE across the mass flow rate range, it was found that the RDE successfully reached sustained steady-state rotating detonation, at mass flow rates of 40 g/s and higher. At lower mass flow rates, the detonation wave would fail and dwindle into deflagration occurring at the inlet. As seen in Figure *5* as the mass flow rate increased the detonation velocity increased, this is due to higher mass flow rates improving the availability of reactants for the detonation wave to consume. It was found that the detonation velocities were within 90-94% of the CJ detonation velocity. This is significantly higher than most empirical annular RDEs, which typically are around 60-80% CJ detonation velocities [3]. The setup used in this series of simulations ignored viscous forces, which meant boundary layers were not accounted for, which can induce significant losses on rotating detonation waves operating in small combustion chambers [16]. However, successful rotating detonation only occurring at higher mass flow rates and increasing detonation velocity of the single detonation wave as the mass flow rate increased both match the general performance characteristics of empirical RDEs validating this setup for studying the general characteristics of RDEs [3]. Further research should test RYrhoCentralFoam with solvers that include viscous forces and boundary layer effects such as Reynolds-averaged Navier–Stokes (RANS) and Large-Eddy Simulation (LES) CFD setups.

Though the solver was able to successfully reproduce the rotating detonation phenomenon, and whilst being a free and openly accessible solver, there were issues using the solver. Such as when testing the reaction mechanism used throughout this study for purely H2/O2 reactions with no N2 present, the solver failed to run no matter the setup or settings. The use of an older OpenFOAM version also presented some challenges running on newer hardware and operating systems. These problems are also likely due to the fact the solver is the project of a small team that does not have the resources to continually update and fix bugs within the solver, rather than that of a large commercial software provider e.g. ANSYS. The solver was provided as is without any tutorial, documentation, or test cases, which though common for open-source projects, can result in a steep entry level to the use of the solver. This could be solved by simply supplying a small number of simple test cases showing off the different aspects of the solver, which would provide a benefit for researchers using the solver in the future. Additionally, providing some notes on best practices for the solver and other researchers' experiences could also improve the ability of future researchers to use this solver. As such, the data and files for this study will be available on request for use as a tutorial case.

4 Conclusions

In conclusion, the solver was able to recreate the rotating detonation phenomenon, proving this solver can be used to simulate RDEs, though the inviscid solver setup used throughout this study significantly overestimated the detonation velocities compared to typical empirical results. Further testing is required to test the solver with RANS and LES simulation setups which simulate and model boundary layer and viscous forces effects on the detonation wave and its detonation velocity. However, RYrhoCentralFoam was able to recreate the general characteristics of empirical RDEs, with rotating detonation only successfully initiating at

higher mass flow rates, and the detonation velocity of the single detonation wave increasing as the mass flow rate increased.

Acknowledgements

The authors would like to thank Xiaohang Fang for providing help with the simulation setup and Huangwei Zhang for providing access to the solver.

References

[1] C. M. Guirao, R. Knystautas, J. H. Lee, and U. Jer, "A Summary of Hydrogen-Air Detonation Elxperiments."

[2] Y. B. Zeldovich, "To the question of energy use of detonation combustion," *Journal of Propulsion and Power*, vol. 22, no. 3. American Inst. Aeronautics and Astronautics Inc., pp. 588–592, 2006. doi: 10.2514/1.22705.

[3] V. Anand and E. Gutmark, "Rotating detonation combustors and their similarities to rocket instabilities," *Progress in Energy and Combustion Science*, vol. 73. Elsevier Ltd, pp. 182–234, Jul. 01, 2019. doi: 10.1016/j.pecs.2019.04.001.

[4] J. A. Nicholls, R. E. Cullen, and K. W. Ragland, "Feasibility studies of a rotating detonation wave rocket motor," *J Spacecr Rockets*, vol. 3, no. 6, pp. 893–898, 1966, doi: 10.2514/3.28557.

[5] B. Wang and J. P. Wang, "Introduction to the special section on recent progress on rotating detonation and its application," *AIAA Journal*, vol. 58, no. 12, pp. 4974–4975, 2020, doi: 10.2514/1.J060144.

[6] W. jie Fan, W. dong Liu, H. yang Peng, S. jie Liu, and J. Sun, "Numerical study on ethylene-air continuous rotating detonation in annular combustors with different widths," *Journal of Zhejiang University: Science A*, vol. 23, no. 5, pp. 388–404, May 2022, doi: 10.1631/jzus.A2100448.

[7] V. F. Nikitin and E. V. Mikhalchenko, "Safety of a rotating detonation engine fed by acetylene – oxygen mixture launching stage," *Acta Astronaut*, vol. 194, pp. 496–503, May 2022, doi: 10.1016/j.actaastro.2021.11.035.

[8] Q. Li, P. Liu, and H. Zhang, "Further investigations on the interface instability between fresh injections and burnt products in 2-D rotating detonation," *Comput Fluids*, vol. 170, pp. 261–272, Jul. 2018, doi: 10.1016/j.compfluid.2018.05.005.

[9] Z. Huang, M. Zhao, Y. Xu, G. Li, and H. Zhang, "Eulerian-Lagrangian modelling of detonative combustion in two-phase gas-droplet mixtures with OpenFOAM: Validations and verifications," *Fuel*, vol. 286, Feb. 2021, doi: 10.1016/j.fuel.2020.119402.

[10] H. Zhang, M. Zhao, and Z. Huang, "Large eddy simulation of turbulent supersonic hydrogen flames with OpenFOAM," *Fuel*, vol. 282, Dec. 2020, doi: 10.1016/j.fuel.2020.118812.

[11] J. Y. Choi, I. S. Jeung, and Y. Yoon, "Computational fluid dynamics algorithms for unsteady shock-induced combustion, Part 1: validation," *AIAA journal*, vol. 38, no. 7, pp. 1179–1187, 2000, doi: 10.2514/2.1112.

[12] L. F. Gutiérrez Marcantoni, J. Tamagno, and S. Elaskar, "Two-dimensional numerical simulations of detonation cellular structures in H2–O2–Ar mixtures with OpenFOAM®," *Int J Hydrogen Energy*, vol. 42, no. 41, pp. 26102–26113, Oct. 2017, doi: 10.1016/j.ijhydene.2017.08.188.

[13] R. Zhu, X. Fang, C. Xu, M. Zhao, H. Zhang, and M. Davy, "Pulsating one-dimensional detonation in ammonia-hydrogen-air mixtures," *Int J Hydrogen Energy*, vol. 47, no. 50, pp. 21517–21536, Jun. 2022, doi: 10.1016/j.ijhydene.2022.04.265.

[14] Osama A. Marzouk., "Assessment of Three Databases for the NASA Seven-Coefficient Polynomial Fits for Calculating Thermodynamic Properties of Individual Species Assessment of Three Databases for the NASA Seven-Coefficient Polynomial Fits for Calculating Thermodynamic Properties of Individual Species," *Int J Aero-nautics Aerospace Res*, vol. 5, no. 1, pp. 150–163, 2018, [Online]. Available: http://garfield.chem.elte.hu/Burcat/

[15] N. T. Fiorino, "Improving the Stability and Operability of a Small-Scale Rotating Improving the Stability and Operability of a Small-Scale Rotating Detonation Engine Detonation

Engine," Air Force Institute of Technology, 2021. [Online]. Available: https://scholar.afit.edu/etd/5067

[16] R. Yokoo *et al.*, "Propulsion performance of cylindrical rotating detonation engine," *AIAA Journal*, vol. 58, no. 12, pp. 5107–5116, 2020, doi: 10.2514/1.J058322.

UKACM 2024 Conference, 10-12 April 2024, Durham University, Durham, UK
https://doi.org/10.62512/conf.ukacm2024.056

REDUCING AERODYNAMIC DRAG ON FLATBED TRAILERS FOR PASSENGER VEHICLES USING NOVEL APPENDABLE DEVICESE

Michael Gerard Connolly[1*], **Malachy J. O'Rourke**[1], **Alojz Ivankovic**[1]

[1] School of Mechanical and Materials Engineering, University College Dublin, D04 PR94 Dublin, Ireland
michael.connolly@ucdconnect.ie

Abstract. This article presents a study on the aerodynamic drag of a generic dual-axle flatbed trailer and explores ways to reduce the drag using appendable drag-reducing devices. The primary sources of drag originated from the van and trailer's rear, along with the trailer's wheels. The most-effective initial device for reducing drag was a full trailer underside cover, which offered a 7% drag reduction. Additionally, ladder racks, dropsides, and rear gates were studied, and it was found that protruding ladder racks significantly increased drag. Rear gates added large amounts of drag and should be removed and stored when not needed. The study also explored novel mid-section devices that increased the van's base pressure and reduced drag. An axle test revealed that drag for single-, dual-, and triple-axle trailers was very similar in direct flow, but different in yawed flow. A drawbar length test showed a near-linear relationship between drawbar length and drag, manifesting as a 1.7% change in drag per 250 mm change in drawbar length. Several novel modifications were made to the trailer, including fitting six unique appendable devices, which offered a total 7.3% drag reduction. A novel rear van device known as the multi-stage converging cavity was introduced, which reduced drag by nearly 18%. When all the devices were used together, a total 25% drag reduction was observed for the van–trailer combination.

Key words: *drag reduction; CFD; flatbed trailer aerodynamics; appendable devices; fuel savings*

1 Introduction

As of Q2 2023, a considerable knowledge gap exists within the literature on van–trailer aerodynamics. With a global effort under way to transition the world's transport sector to electric vehicles, it is ever more important to understand the aerodynamics of van–trailer combinations and explore options for novel drag reduction as fears mount within the consumer market that electric vehicles are not suitable for towing due significant range detriment. The Irish government under their ambitious 2021 climate action plan aim to half Greenhouse Gas (GHG) emissions by 2030 and achieve net zero by 2050 [Gov.ie (2021)]. As of 2021, the Irish transport sector accounts for approximately 20% of the country's GHG emissions [Gov.ie (2021)], highlighting the need for continued work on and research into drag reduction technology. Aerodynamic drag is the most-dominant resistance force opposing a ground vehicle's motion when travelling at speeds above 80 km/h [Wood and Bauer(2003)]. In general, four forces oppose a ground vehicle in motion, namely acceleration resistance, gradient resistance, rolling resistance, and air resistance. Vehicles with large drag coefficients are particularly affected when travelling at highway and motorway speeds ranging from 80–120 km/h. EU law requires that vehicles towing a trailer are to restrict their speeds to 80 km/h or less. When a van and trailer are travelling at 80 km/h, or above, the resistance due to aerodynamic drag is well above half the vehicle's total resistance. Drag reduction through the application of appendable devices can play a key role in reducing fuel consumption and improving driving range for electric vehicles, particularly when towing a trailer. As a general rule of thumb, a 20% drag reduc-

tion would materialise as a 10% fuel savings when travelling at highway speeds [Ekman et al.(2016)]. Flatbed trailers are used to transport a variety of large or irregularly sized cargo and usually consist of a large bed supported by one to three axles. It is also common for flatbeds to be fitted with drop sides, rear gates, and front faces with mounting/tying bars. While the aerodynamics of these trailers largely depend on their cargo, theoretically, they may spend half their time unloaded while returning to their starting location. Few studies exist within the literature outlining the aerodynamics of this type of trailer when towed by vans, and none detail how their drag can be reduced through the application of appendable devices.

2 Problem description

The airflow over ground vehicles can be effectively modelled using a continuum approach as only the macroscopic interactions are of interest, with any given fluid element being the average of a large number of fluid particles in both space and time. Air was modelled as an isothermal Newtonian fluid with constant viscosity and density. The constant density assumption was justified as the investigated flows had Mach numbers below 0.3, minimising compressibility effects. The governing equations that form the basis for CFD simulations are the Navier–Stokes equations (Equations (1) and (2)), which are derived from the principles of mass and momentum conservation.

$$\frac{\partial \rho}{\partial t} + \frac{\partial (\rho u_i)}{\partial x_i} = 0 \tag{1}$$

$$\rho \frac{\partial u_i}{\partial t} + \rho \frac{\partial (u_i u_j)}{\partial x_j} = -\frac{\partial P}{\partial x_i} + \frac{\partial \tau_{ij}}{\partial x_i} + \rho f_i \tag{2}$$

The CFD results detailed throughout this article were realised using ANSYS Fluent, which solves the Reynolds-Averaged Navier–Stokes (RANS) equations detailed below in Equations (3) and (4) with the help of turbulence models such as the $k-\omega$ SST model [Menter(1993)], where k is the turbulent kinetic energy and ω is the specific rate of dissipation in this two-equation turbulence model.

$$\frac{\partial \overline{u_i}}{\partial x_i} = 0 \tag{3}$$

$$\rho \frac{\partial \overline{u_i u_j}}{\partial x_j} = -\frac{\partial P}{\partial x_i} + \frac{\partial}{\partial x_j}\left(\mu \frac{\partial \overline{u_i}}{\partial x_j} - \rho \overline{u_i' u_j'}\right) \tag{4}$$

3 Numerical results

3.1 Flatbed Trailer 1.0

To effectively investigate the aerodynamics of flatbed trailers, a generic model for a flatbed trailer was established that closely represented the majority of flatbeds in operation in Ireland and the U.K. Flatbed Trailer 1.0 (FBT1) was a twin-axle, torsion suspension trailer with a 3.7 m $\times$ 1.92 m bed raised 670 mm off the ground. The trailer was attached to a generic electric van model. Note that the wheels of both the trailer and van use slick tires with alloy covers to improve aerodynamics and to remove the requirement for sliding mesh or moving reference frame modelling. The aerodynamic results for FBT1 are outlined

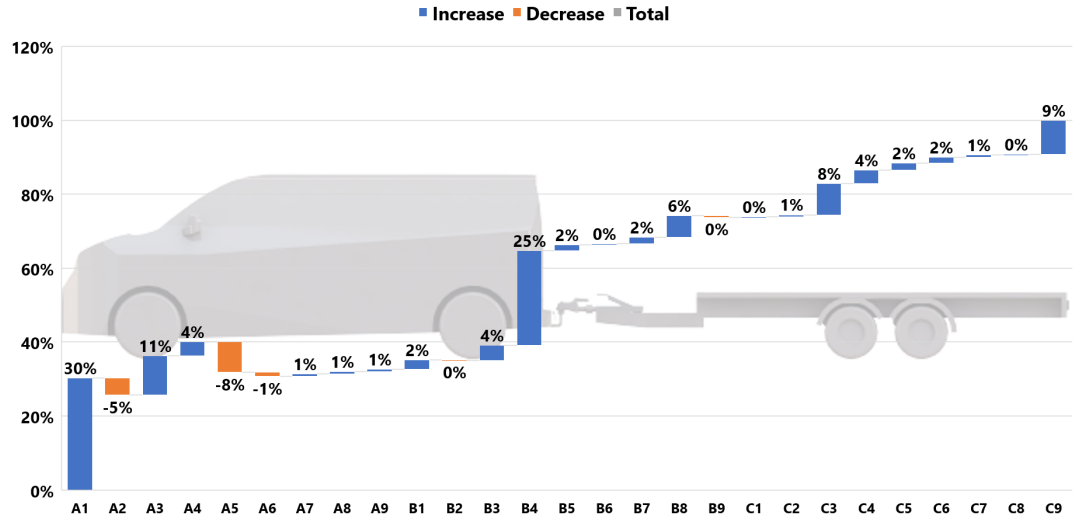

Figure 1: Accumulated drag distribution for FBT1.

in Table 1. For reference, the standalone van had a drag coefficient of 0.331 and a lift coefficient of -0.323. Note that the frontal area for the van–trailer combination was approximately equal to that of the standalone van, which was the case for all configurations to follow unless stated otherwise. Therefore, all drag reductions will be discussed explicitly in terms of % C_D reduction and not drag area (C_DA). When attached, the trailer increases the body's drag by 40.79%. ,

Table 1: FBT1's drag and lift coefficient

Simulation Name	Drag Coefficient	Lift Coefficient
FBT1	0.466	-0.116

To help understand the increase in drag, Figure 1 is presented, which shows the drag force accumulation along the combination's length. As expected, there was a large contribution from the van's front; however, the rear surfaces of both the van and trailer were shown to have similarly substantial contributions, with the van rear carrying 25% and the trailer rear 9% of the total drag. This observation highlights the need for appendable drag-reduction devices on all rear surfaces. Other areas suited for drag reduction devices include the trailer's drawbar and face, along with the trailer's wheels and axle package. The primary cause of drag on the rear surfaces is the under-pressured wake that follows them.

3.2 Final Design

To conclude the Results Section, a final design that incorporated both the van and trailer fitted devices was created and is shown in Figure 2. The final design reported a drag coefficient of 0.352, which amounts to a near 25% drag reduction on the baseline FBT1 (Table 2). For reference, the standalone van had a drag coefficient of 0.331, which highlights that, when both the van and trailer utilised a wide range of appendable devices, the added drag due to the trailer can be heavily mitigated and brought close to

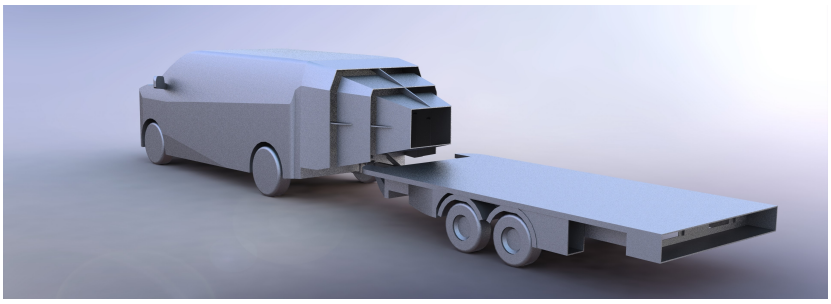

Figure 2: Rendered image of FBT1—final design fit with both van and trailer devices.

full negation.

Table 2: Aerodynamic coefficients for FBT1—final design.

Simulation Name	C_D	C_D **% Change**
FBT1—Final Design	0.352	−24.46%

4 Conclusions

In conclusion, a generic dual-axle flatbed trailer was studied to find ways to reduce drag using appendable devices. The initial work revealed that the majority of the drag originated from the back of the van, with notable contributions from the trailer's wheels. Following some initial geometry modifications, a full trailer undertray was shown to offer a near 7% drag reduction. A study into the drag effects of ladder racks, dropsides, and rear gates was conducted in which large drag increases for ladder racks protruding from the van were observed, while ladder racks that shadowed the van performed better. It was demonstrated that a solid face rack could outperform a hollow rack due to the interference effects between the rack's face and the van's wake. Rear gates were found to add large amounts of drag and should be removed and stored when not needed. An axle test was performed to compare C_D for single-, dual-, and triple-axle trailers. Interestingly, the C_D for all versions was found near identical in direct flow, but differed in yawed flow. In direct flow, the single-axle variant had the highest C_D. Additional geometry modifications included a full-size skirt system, which did not reduce drag noticeably, as it prevented the flow exiting from the wheel wells. A better design would include a partial side skirt system, in which breaks at the wheels are inserted to allow the flow to vent out. An alternate bed texture was used to see if it would affect the drag coefficient of the trailer, but no noticeable C_D reduction was observed. The most-interesting modification was the use of mesh sides and mesh gates on the trailer, in which the drag increased by a substantial 41%, highlighting that, if possible, mesh sides should be detached and stored away when not needed. A drawbar length test was conducted in which a near-linear relationship between the drawbar length and drag was observed. A C_D change of approximately 1.7% per 250 mm change in length was noted. Six unique appendable devices were fit to the flatbed trailer, which together offered a 7.3% drag reduction. To reduce the drag on the rear of the van, a new novel device known as the Multi-Stage Converging Cavity was introduced to reduce drag by nearly 18%. To finish, a final design using a combination of both the van and trailer devices was made that offered a 25% drag reduction, which nearly fully negated the drag additions associated with adding the flatbed trailer to the van.

Acknowledgments

This research was funded by The Irish Research Council Grant Number EPSPG/2022/213 and Science Foundation Ireland Grant Number 22/NCF/EI/11277.

REFERENCES

[Gov.ie (2021)] Ireland—Climate Action Plan. 2021. Available online: https://www.gov.ie/en/publication/6223e-climate-action-plan-2021/ (accessed on 20 October 2023).

[Wood and Bauer(2003)] Wood, R.M.; Bauer, S.X.S. Simple and Low-Cost Aerodynamic Drag Reduction Devices for Tractor-Trailer Trucks. *SAE Trans.* **2003**, *112*, 143–160. https://doi.org/10.4271/2003-01-3377.

[Ekman et al.(2016)] Ekman, P.; Gardhagen, R.; Virdung, T.; Karlsson, M. *Aerodynamic Drag Reduction of a Light Truck—From Conceptual Design to Full Scale Road Tests*; 2016; SAE International p. 2016-01-1594. https://doi.org/10.4271/2016-01-1594.

[Menter(1993)] Menter, F. Zonal Two Equation k-w Turbulence Models For Aerodynamic Flows. In Proceedings of the 23rd Fluid Dynamics, Plasmadynamics, and Lasers Conference, Orlando, FL, USA, 6–9 July 1993. https://doi.org/10.2514/6.1993-2906.

UKACM 2024 Conference, 10-12 April 2024, Durham University, Durham, UK
https://doi.org/10.62512/conf.ukacm2024.074

Accounting for Particle Morphology in CFD-DEM Modelling

Sadaf Maramizonouz, Sadegh Nadimi
School of Engineering, Newcastle University, Newcastle upon Tyne, NE1 7RU, UK.
sadaf.maramizonouz@newcastle.ac.uk
sadegh.nadimi-shahraki@newcastle.ac.uk

Abstract

In this study, the drag force acting on real irregular particles with various morphologies belonging to the four shape categories of the Zingg chart is estimated using the empirical models proposed in literature and the results are compared to the drag force obtained through computational fluid dynamics (CFD). Then, the chosen drag models are utilised to numerically simulate the flow of irregular particles through air along a cylindrical pipe, their exit at the nozzle, and their entrainment at a certain spot. The dynamics of the particulate material is simulated using discrete element method (DEM) modelling that is one-way coupled to CFD simulations via the drag force exerted on the particles. It is observed that particle morphology significantly influences the particle flow dynamics.

Key words: *Computational Fluid Dynamics (CFD), Discrete Element Modelling (DEM), Drag Force, Drag Coefficient, Particle Shape, Non-spherical Particle.*

1. Introduction

Particulate materials and their interaction with the fluid media around them dominate many natural and industrial processes [1, 2]. The fluid-particle interactions generate forces and moments highly dependent on particles' morphology affecting their movement. The drag force the particles experience can in many applications be considered the dominant force, dictating the dynamics of particles' motion [3, 4]. In literature, various models have been proposed to estimate the drag force acting on irregular particles. These models utilise several shape characteristics to account for the irregularities in particles' morphology. It was shown that each empirical drag model is efficient for particles belonging to a particular shape category of the Zingg chart [5], namely, compact, bladed, elongated, and flat particles [6].

In order to investigate the effects of different particle morphologies and their drag force on the particles' dynamics as they move through air, the particles' flow along a cylindrical pipe, their exit at the nozzle, and their entrainment at a certain spot [7] is numerically studied using a DEM model which is one-way coupled to a CFD simulation.

2. Numerical Simulation

2.1 Discrete Element Modelling

The dynamic behaviour of the rigid and discrete particles are modelled through Newton's law of translational and Euler's law of rotational motion [8]:

$$m_i \, {d\boldsymbol{U}_{p_i}}/{dt} = \sum \boldsymbol{F}_{c_i} + m_i \boldsymbol{g} \tag{1}$$

$$d(\boldsymbol{I}_i \cdot \boldsymbol{\omega}_i)/{dt} = \boldsymbol{R}_i \cdot \sum \boldsymbol{M}_{c_i} \tag{2}$$

Hertz-Mindlin contact model [8] is used to model the inter-particle and particle-geometry interactions.

2.2 Computational Fluid Dynamics

The dynamics of the fluid flow is modelled using the Navier-Stokes equations [3]:

$$\boldsymbol{\nabla}.\left(\boldsymbol{U}_f\right) = 0 \tag{3}$$

$$\rho_f\left(\frac{\partial \boldsymbol{U}_f}{\partial t} + \left(\boldsymbol{U}_f \cdot \boldsymbol{\nabla}\right)\boldsymbol{U}_f\right) = -\boldsymbol{\nabla}P + \mu_f\left(\boldsymbol{\nabla^2}\boldsymbol{U}_f\right) \tag{4}$$

2.3 CFD-DEM Coupling

The CFD simulation is one-way coupled to the DEM modelling. This means that the fluid dynamics affect the particle dynamics but not vice-versa. The one-way CFD-DEM coupling is implemented using the velocity field of the fluid resulted from the CFD simulation which is imported to the DEM simulation. This velocity field is then used to calculate the drag force acting on the particles at each time step [3, 4]:

$$F_D = \frac{1}{2}\rho_f C_D A\left|\boldsymbol{U}_p - \boldsymbol{U}_f\right|\left(\boldsymbol{U}_p - \boldsymbol{U}_f\right) \tag{5}$$

The drag coefficient is a function of the Reynolds number and the morphology of the particle. To account for the particle morphology, particles' sphericity defined by Wadell [9] as the ratio of surface area of the volume equivalent sphere to the particle surface area is incorporated in the drag model proposed by Ganser [10] (Equations *(6)-(9)*):

$$C_D = \frac{24K_S}{Re}\left(1 + 0.1118\left(ReK_N/K_S\right)^{0.6567}\right) + \left(0.4305K_N/\left(1 + \frac{3305}{\left(ReK_N/K_S\right)}\right)\right) \tag{6}$$

$$Re = \rho_f\left|\boldsymbol{U}_p - \boldsymbol{U}_f\right|d/\mu_f \tag{7}$$

$$K_N = 10^{1.8148\left(-log\Phi_W\right)^{0.5743}} \tag{8}$$

$$K_S = (1/3) + \left((2/3)\sqrt{\Phi_W}\right) \tag{9}$$

Table 1 summarises all the symbols used in the above equations and their definitions.

Table 1. All symbols used in the paper.

Symbol	Definition	Symbol	Definition
A	Particle reference area	m	Particle mass
C_D	Particle drag coefficient	$\boldsymbol{R}$	Particle rotation matrix
d	Particle reference length	Re	Particle Reynolds number
$\boldsymbol{F}_C$	Particle contact force	t	Time
$\boldsymbol{F}_D$	Particle drag force	$\boldsymbol{U}_f$	Fluid translational velocity
$\boldsymbol{g}$	Gravitational acceleration	$\boldsymbol{U}_p$	Particle's translational velocity
$\boldsymbol{I}$	Particle moment of inertia	μ_f	Fluid viscosity
i	Particle number indicator	ρ_f	Fluid density
K_N	Newton's drag correction	Φ_W	Particle sphericity by Wadell [9]
K_S	Stoke's drag correction	$\boldsymbol{\omega}$	Particle rotational velocity
$\boldsymbol{M}_C$	Contact torque		

3. Results and Discussions

Four different particle morphologies shown in **Figure 1** are used in DEM simulations to investigate the effects of particle shape on and their dynamic behaviour.

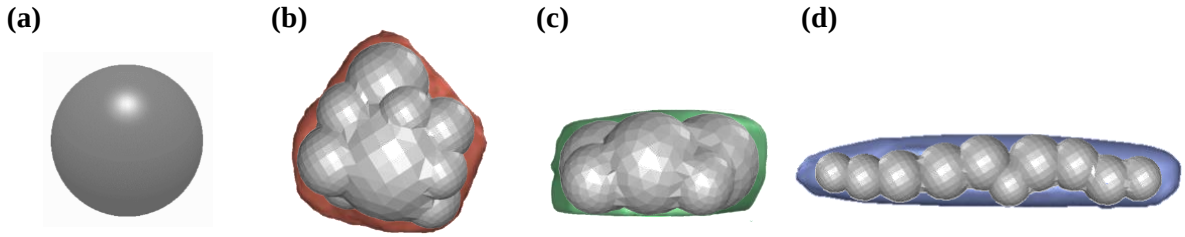

Figure 1. Four different particle morphologies used in the DEM model: **(a)** spherical, **(b)** compact, **(c)** flat, and **(d)** elongated particles all with the same size of ~1.2 mm.

The snapshots of the DEM modelling are presented in **Figure 2(a)** to **(d)** for **(a)** spherical, **(b)** compact, **(c)** flat, and **(d)** elongated particle with one-way CFD coupling and Ganser drag force [10] to capture the effect of adding the drag force acting on the particles due to the airflow inside the nozzle.

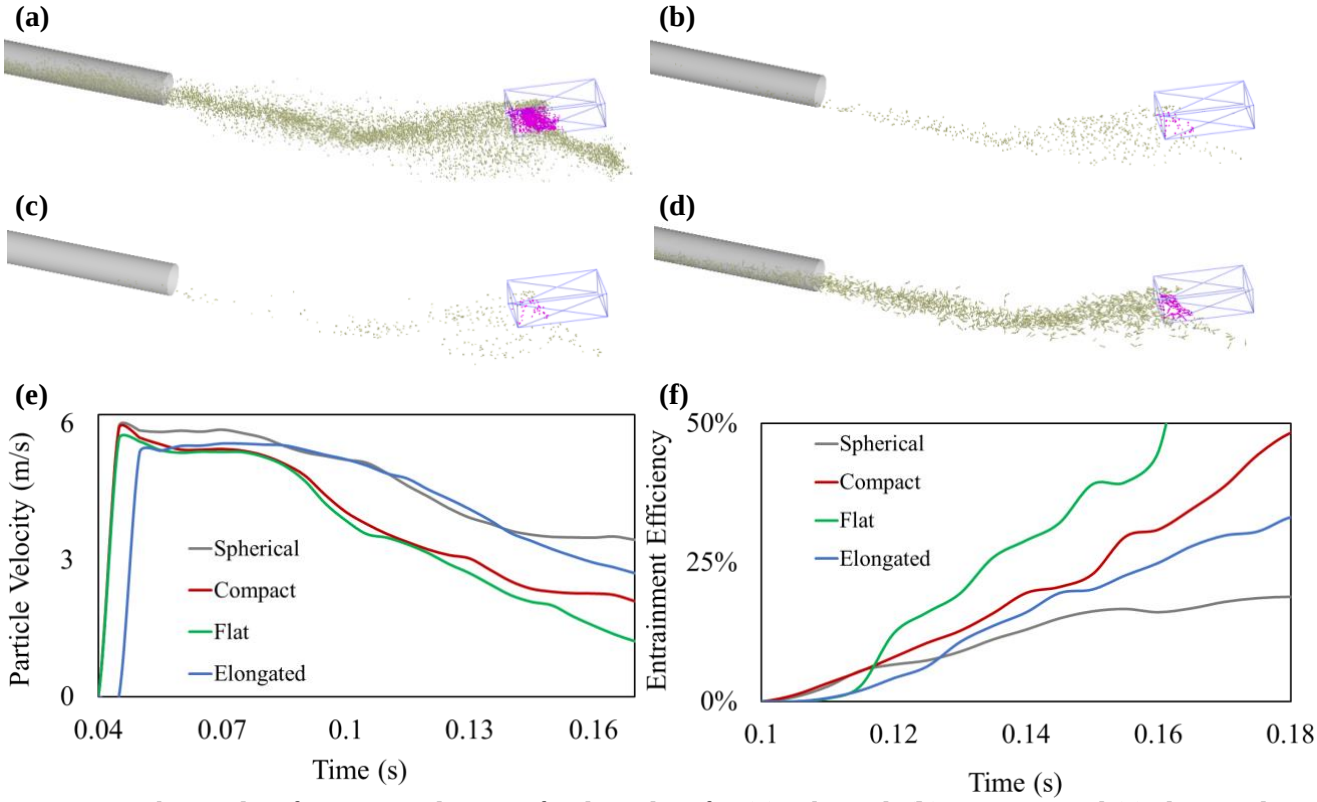

Figure 2. The results of DEM simulations of rail-sanding for **(a)** spherical, **(b)** compact, and **(c)** elongated sand grains **(1)** without CFD coupling and drag force, and **(2)** one-way CFD coupling with drag force; Comparison of the **(e)** average particle velocity and **(f)** entrainment efficiency versus time for spherical, compact, flat, and elongated particles.

Figure 2(e) shows the average velocity of the particles during their flow through the cylinder versus time for spherical, compact, flat, and elongated particles. It can be seen that particles' morphology influences their velocities as the spherical and elongated particles show the highest

value for the average velocity while for compact and flat particles, the velocity values are lower.

Figure 2(f) presents the efficiency of the particles' entrainment at a certain spot (the box outlined in blue in **Figure 2(a)** to **(d)**) versus time for spherical, compact, flat, and elongated particles. It is shown that the entrainment efficiency is the highest for flat particles and decreases for compact, elongated, and spherical particles.

4. Conclusions

In this research, the effects of particle shape on the drag force it experiences, and its dynamic behaviour was investigated through DEM simulation one-way coupled to CFD via the drag force dictating the particles' flow due to the airflow inside the nozzle. It was concluded that the particles' shape and geometry influence their drag force and thus their dynamics. As the particles' sphericity increases and their shape moves from elongated to compact and then spherical, their velocity also increases.

Acknowledgements

This work was funded by the UK Engineering and Physical Sciences Research Council (EPSRC) grant No. EP/V053655/1 RAILSANDING - Modelling Particle Behaviour in the Wheel-Rail Interface.

References

[1] S. J. Blott and K. Pye, "Particle Shape: A Review and New Methods of Characterization and Classification," *Sedimentology*, vol. 55, no. 1, pp. 31-63, 2008.

[2] V. Angelidakis, S. Nadimi, and S. Utili, "SHape Analyser for Particle Engineering (SHAPE): Seamless Characterisation and Simplification of Particle Morphology from Imaging Data," *Computer Physics Communications*, vol. 265, p. 107983, 2021, doi: 10.1016/j.cpc.2021.107983.

[3] F. M. White, *Fluid Mechanics*. Tata McGraw-Hill Education, 1979.

[4] C. T. Crowe and E. E. Michaelides, *Multiphase Flow Handbook*. Taylor & Francis, 2006.

[5] T. Zingg, "Beitrag zur Schotteranalyse," ETH Zurich, 1935.

[6] S. Maramizonouz and S. Nadimi, "Drag Force Acting on Ellipsoidal Particles with Different Shape Characteristics," *Powder Technology*, vol. 412, p. 117964, 2022, doi: 10.1016/j.powtec.2022.117964.

[7] W. Skipper, S. Nadimi, M. Watson, A. Chalisey, and R. Lewis, "Quantifying the Effect of Particle Characteristics on Wheel/Rail Adhesion & Damage through High Pressure Torsion Testing," *Tribology International*, p. 108190, 2023.

[8] C. Thornton, "Granular Dynamics, Contact Mechanics and Particle System Simulations," *A DEM study. Particle Technology Series*, vol. 24, 2015.

[9] H. Wadell, "Volume, Shape, and Roundness of Rock Particles," *The Journal of Geology*, vol. 40, no. 5, pp. 443-451, 1932.

[10] G. H. Ganser, "A Rational Approach to Drag Prediction of Spherical and Nonspherical Particles," *Powder Technology*, vol. 77, no. 2, pp. 143-152, 1993.

Computational Methods in Heat Transfer and Hydro-Mechanical Modelling

UKACM 2024 Conference, 10-12 April 2024, Durham University, Durham, UK
https://doi.org/10.62512/conf.ukacm2024.028

OVERLAPPING IMPROVED ELEMENT-FREE GALERKIN AND FINITE ELEMENT METHODS FOR THE SOLUTION OF NON-LINEAR TRANSIENT HEAT CONDUCTION PROBLEMS WITH CONCENTRATED MOVING HEAT SOURCES

Juan C. Álvarez-Hostos[1], **Zahur Ullah**[2*]

[1]Centro de Investigación y Transferencia (CIT) Rafaela, Universidad Nacional de Rafaela (UNRaf)/Consejo Nacional de Investigaciones Científicas y Técnicas (CONICET), Rafaela/Argentina.
[2] Advanced Composites Research Group (ACRG), School of Mechanical and Aerospace Engineering (SMAE), Queen's University Belfast (QUB), Ashby Building, Belfast BT9 5AH, UK.
z.ullah@qub.ac.uk

Abstract. A novel overlapping approach, termed the Overset IEFG-FE method (Ov-IEFG-FEM), is proposed for solving transient heat conduction problems with concentrated moving heat sources. This mesh-less/mesh-based chimera-type method combines improved element-free Galerkin (IEFG) and finite element (FE) methods. The Ov-IEFG-FEM uses a coarse FE mesh to discretise the problem geometry, while a set of overlapping patch nodes moves with the heat source, enhancing accuracy via the IEFG technique to capture marked thermal gradients. In regions outside the heat source area where accuracy requirements are lower, the thermal problem is solved using the FE method (FEM). The method involves solving the problem over these two overlapping domains and transferring numerical information between the approximations performed on both. The Ov-IEFG-FEM aims to provide an enriched solution by coupling temperature fields computed on the patch nodes and the coarse background mesh using IEFG and FE methods, respectively. Numerical experiments demonstrate the method potential in accurately and efficiently solving transient heat conduction problems with concentrated moving heat sources, including marked non-linear aspects related to temperature-dependent properties and phase change phenomena.

Key words: *Heat conduction, Moving heat sources, Overset, Element-free Galerkin, Finite element*

1 Introduction

Most numerical solutions reported in the literature for transient heat conduction problems with moving heat sources are based on mesh-based discretisation techniques such as the finite element method or the finite volume method, often requiring significant refinements along the scanning path to achieve an appropriate capture of high temperatures and marked thermal gradients. It is also well-known that performing mesh refinements along the heat source path or adaptive re-meshing techniques can be very cumbersome, and sometimes even unfeasible in problems involving heat sources following curved scanning paths in complex 3-D geometries[1–3]. Mesh-less or mesh-free methods have a emerged as an interesting alternative to the most commonly used mesh-based techniques due to two main reasons[4]: (i) the capability of easily attain higher-order approximations with continuous derivatives, and (ii) the enhanced flexibility of adding or removing nodes during adaptive local refinements. Such versatility of mesh-less methods has also enabled the implementation of such numerical techniques in the solution of both linear and non-linear applied problems involving concentrated moving heat sources[1,2]. Although the potential of mesh-less methods, these numerical techniques still pose noteworthy challenges in terms of computational efficiency, which primarily arise from the need for identifying neighbouring nodes that

define the support domain for numerical approximations and the construction of shape functions via more computationally expensive unconventional procedures[1,2,4]. The emergence of hybrid mesh-less/mesh-based approaches has introduced very interesting alternatives that combine the strengths of mesh-less methods with the less computationally demanding approximations usually involved in standard mesh-based techniques[5]. The mesh-less element-free Galerkin (EFG) method shares similarities with FEM, notwithstanding differences in the construction of shape functions and assembly of the algebraic system of equations. These analogies primarily arise from both numerical techniques being developed in a weak formulation of the governing equations, promoting the development of hybrid EFG-FEM-based approaches[5]. These techniques improve computational efficiency by using EFG methods only in regions demanding high numerical accuracy[5], and the less computationally expensive FEM is used in the rest of the problem domain. Although hybrid EFG-FEM approaches have provided excellent results in scenarios demanding high accuracy[5], these techniques commonly require well defined coupling boundaries where EFG and FEM regions share common nodes. Implementing these approaches in transient heat conduction with concentrated moving heat sources might pose challenges due to the need of redefining the EFG-FEM coupling boundaries at each time step, such EFG computations are performed only near the moving heat source location. This communication aims to highlight the potential of a recently developed chimera-type scheme based on the Improved EFG (IEFG) and the FEM to overcome these challenges. The proposed Overset IEFG-FEM (Ov-IEFG-FEM) offers an enriched accurate solution, smoothly transitioning from EFG to FEM regions dispensing with predefined topological relationship.

2 Governing equations and problem description

The Ov-IEFG-FEM will be used to solve a problem emulating the thermal conditions of the direct metal laser sintering (DMLS) of AlSi10Mg alloys, with the geometric features depicted in Fig. 1. The enriched solution is obtained solving the governing equations of transient heat conduction in the domain Ω_{FEM} with boundaries $\Gamma_{\text{FEM}} = \Gamma_D \cup \Gamma_N$ and the domain Ω_{IEFG} with boundaries Γ_{IEFG}, and performing an appropriate coupling via a reciprocal transfer of information. The thermal problem in Ω_{FEM} is:

$$\begin{gathered} \rho c_p \frac{\partial T}{\partial t} = \nabla.(k\nabla T) + \dot{Q} \qquad \text{in} \quad \Omega_{\text{FEM}} \times [0,t_f], \\ T = T_D \qquad \text{on} \quad \Gamma_D \times [0,t_f], \quad \text{and} \qquad k\nabla T \cdot \hat{n} = q_N \qquad \text{on} \quad \Gamma_N \times [0,t_f], \end{gathered} \tag{1}$$

whereas the thermal problem in Ω_{IEFG} is:

$$\begin{gathered} \rho c_p \left(\frac{\partial T}{\partial t} - \vec{v} \cdot \nabla T \right) = \nabla.(k\nabla T) + \dot{Q} + \rho H_f \left(\frac{\partial f_s}{\partial t} - \vec{v} \cdot \nabla f_s \right) \qquad \text{in} \quad \Omega_{\text{IEFG}} \times [0,t_f], \\ T = \tilde{T}_{\text{FEM}} \qquad \text{on} \quad \Gamma_{\text{IEFG}} \times [0,t_f]. \end{gathered} \tag{2}$$

It is important to note that the effect of the moving heat source can be incorporated either through the volumetric term $\dot{Q}$ or as a concentrated surface heat flux via a Neumann condition. The choice depends on the specific model used for the moving heat source, as discussed in [1,2]. Phase change terms, dependent on f_s and H_f, are exclusively incorporated within Ω_{IEFG} since melting/solidification only occurs in proximity to the moving heat source represented by the surface Gaussian distribution $q_N = 2\eta\dot{Q}_T/(\pi r_0^2) e^{-2\left[(x-||v||\times t)^2+y^2\right]/r_0^2}$. The temperature fields in the weak formulation of Eqs. (1) and (2) are approximated using standard linear interpolating finite element basis functions $\varphi_{\text{FEM}}^{(I)}(\vec{x})$ and improved moving least squares (IMLS) approximations $\varphi_{\text{IEFG}}^{(I)}(\vec{x})$, respectively:

$$T_{\text{FEM}}(\vec{x}) = \sum_{I=1}^{n_{\text{FEM}}} \varphi_{\text{FEM}}^{(I)}(\vec{x}) \hat{T}_{\text{FEM}}^{(I)} \quad \text{for all } \vec{x} \in \Omega_{\text{FEM}}, \qquad T_{\text{IEFG}}(\vec{x}) = \sum_{I=1}^{n_{\text{IEFG}}} \varphi_{\text{IEFG}}^{(I)}(\vec{x}) \hat{T}_{\text{IEFG}}^{(I)} \quad \text{for all } \vec{x} \in \Omega_{\text{IEFG}}. \tag{3}$$

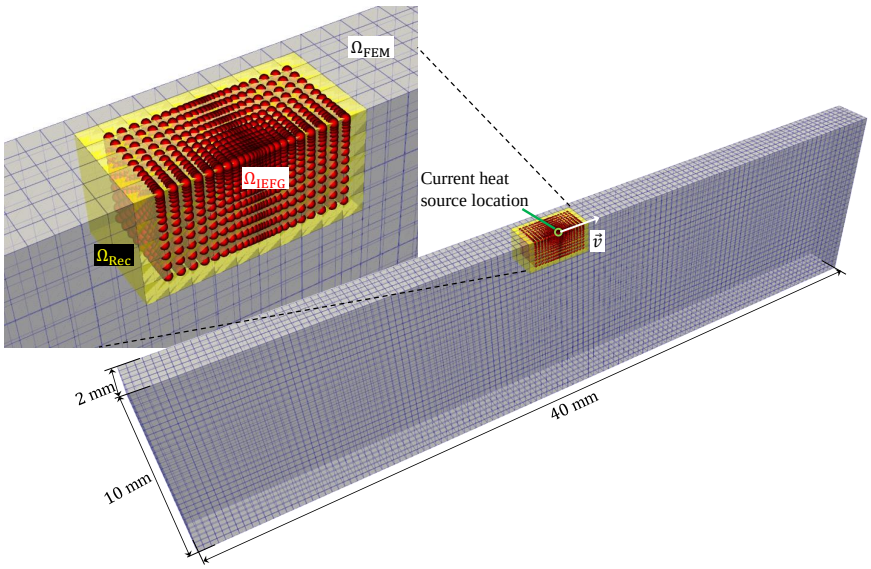

Figure 1: Detail on the discretisation of Ω_{FEM} and representation of Ω_{IEFG}. The nodes representing Ω_{IEFG} constantly moves tracking the scanning path, according to the the heat source velocity $\vec{v}$. This movement ensures that, at every time step, the heat source remains precisely centered within the arrangement of nodes.

Substituting the approximations given in (3) into the weak formulation of Eqs. (1) and (2) gives rise to the following systems of equations:

$$\begin{aligned} \mathbf{C}_{\text{FEM}}\dot{\hat{\mathbf{T}}}_{\text{FEM}} + \mathbf{K}_{\text{FEM}}\hat{\mathbf{T}}_{\text{FEM}} &= \mathbf{Q}^{(T)}_{\text{FEM}} \qquad \text{in} \quad \Omega_{\text{FEM}} \\ \mathbf{C}_{\text{IEFG}}\dot{\hat{\mathbf{T}}}_{\text{IEFG}} + \left(\mathbf{K}_{\text{IEFG}} - \mathbf{A}_{\text{IEFG}} + \mathbf{K}^{(p)}_{\text{IEFG}}\right)\hat{\mathbf{T}}_{\text{IEFG}} &= \mathbf{Q}^{(T)}_{\text{IEFG}} + \mathbf{Q}^{(p)}_{\text{IEFG}} \qquad \text{in} \quad \Omega_{\text{IEFG}} \end{aligned} \tag{4}$$

The Dirichlet condition $\tilde{T}_{\text{FEM}}$ on the immersed boundaries Γ_{IEFG} is obtained through local reconstruction of FEM-based results via IMLS approximations over the sub-domain $\Omega_{\text{Rec}} \in \Omega_{\text{FEM}}$ (yellow region in Fig. 1). This allows the transfer of information from Ω_{FEM} to Ω_{IEFG} using the penalty matrix $\mathbf{K}^{(p)}_{\text{IEFG}}$ and vector $\mathbf{Q}^{(p)}_{\text{IEFG}}$ in the system of equations for Ω_{IEFG}. Numerical information from IEFG-based results is reciprocally transferred to the FE mesh using IMLS approximations $T_{\text{IEFG}}(\vec{x})$ to compute temperatures at FE mesh nodes within Ω_{IEFG}. These nodal values are then prescribed in the system of equations for Ω_{FEM}. The iterative procedure continues until convergence is achieved in the coupling along Γ_{IEFG} and with respect to non-linearities related to phase change and temperature-dependent thermal properties.

3 Numerical results

The Ov-IEFG-FEM simulations for the thermal problem have been performed with laser power absorptivity $\eta = 0.95$ and heat source effective radius $r_0 = 100,\mu$m. Results for total heat source power $\dot{Q}_T = 150$ W with scanning speed $||\vec{v}|| = 500$ mm/s are shown in Fig. 2 (a), with a sensitivity analysis on melt pool depth to variations in these parameters presented in Fig. 2 (b). The outcomes demonstrate seamless coupling along Γ_{IEFG} and accurate capture of thermal gradients near the heat source. This indicates an appropriate information transfer between overlapping domains and solution of non-linearities. The sensitivity analysis on melt pool depth to variations in $\dot{Q}_T$ and $||\vec{v}||$ suggests a consistent thermal

model as it behaves as expected in a wide range process parameters. Solving the phase change effects as a heat source term improves the convergence during the non-linear thermal problem numerical solution.

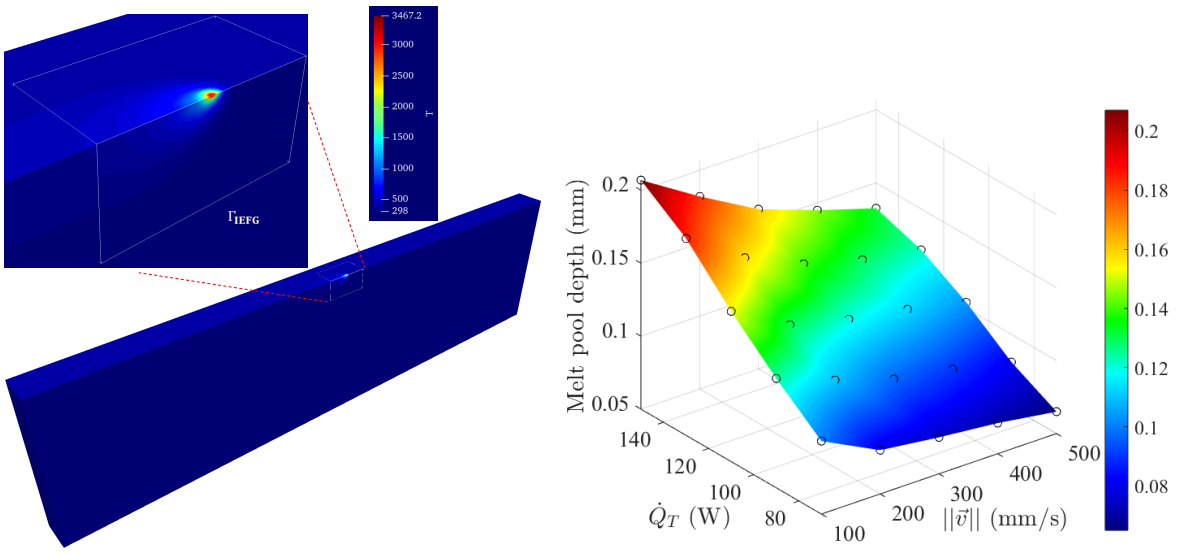

(a) Temperature field

(b) Dependence of melt pool depth with $\dot{Q}_T$ and $||\vec{v}||$.

Figure 2: Numerical solution for the DMLS thermal problem, via the Ov-IEFG-FEM.

4 Conclusions

The Ov-IEFG-FEM introduces a novel approach to solving non-linear transient heat conduction problems with concentrated moving heat sources. By using a coarse FE mesh and overlapping patch nodes for IEFG computations, the method achieves enhanced accuracy, seamlessly coupling temperature fields and capturing thermal gradients. The sensitivity analysis confirms stability across a wide range of process parameters, and incorporating phase change effects as a heat source term has improved convergence in the numerical solution of material non-linearities.

REFERENCES

[1] Juan C. Álvarez Hostos, Bruno Storti, Benjamín A. Tourn, and Víctor D. Fachinotti. Solving heat conduction problems with a moving heat source in arc welding processes via an overlapping nodes scheme based on the improved element-free Galerkin method. *International Journal of Heat and Mass Transfer*, 192:122940, 2022.

[2] Juan C. Álvarez Hostos, Zahur Ullah, Bruno A. Storti, Benjamín A. Tourn, and Javier A. Zambrano-Carrillo. An overset improved element-free Galerkin-finite element method for the solution of transient heat conduction problems with concentrated moving heat sources. *Comp. Meth. in App. Mech. and Eng.*, 418:116574, 2024.

[3] Bruno A. Storti, Alejandro E. Albanesi, Ignacio Peralta, Mario A. Storti, and Víctor D. Fachinotti. On the performance of a Chimera-FEM implementation to treat moving heat sources and moving boundaries in time-dependent problems. *Finite Elements in Analysis and Design*, 208:103789, 2022.

[4] G. R. Liu. *Meshfree Methods: Moving Beyond the Finite Element Method.* CRC Press, 2009.

[5] Zahur Ullah, Will Coombs, and C. Augarde. Parallel computations in nonlinear solid mechanics using adaptive finite element and meshless methods. *Engineering Computations*, 33(4):1161–1191, 2016.

UKACM 2024 Conference, 10-12 April 2024, Durham University, Durham, UK
https://doi.org/10.62512/conf.ukacm2024.032

STOCHASTIC MODELLING OF UNSTABLE PREFERENTIAL FLOW IN SPATIALLY VARYING WATER REPELLENT SOILS

Evan John Ricketts[1*], Peter Cleall[1], Anthony Jefferson[1*], Pierre Kerfriden[2], Paul Lyons[3]

[1] School of Engineering, Cardiff University, Cardiff, CF24 3AA, UK
rickettse1@cardiff.ac.uk, cleall@cardiff.ac.uk, jeffersonad@cardiff.ac.uk
[2] Centre de Matériaux, Mines Paris /PSL University, Evry, France
pierre.kerfriden@minesparis.psl.eu
[3] LUSAS, Surrey, UK
paul.lyons@lusas.com

Abstract. It has been established that material variability can lead to distinct unstable hydraulic behaviour, and is prominent in soils due to their large spatial heterogeneity. This behaviour is amplified when the wettability of the medium is non-uniform, specifically if the soil becomes hydrophobic. When soil is naturally water repellent (WR), there is often spatial variability of wettability, such that a network of preferential flow paths is created. As water infiltrates, the water repellent regions will impede flow, resulting in preferential wetting pathways. This leads to highly preferential fingered flow, and can result in rapid movement of contaminants, or induce localised erosion. The WR properties of soil can be induced artificially through the addition of chemicals, via contamination, and as the consequence of natural processes such as wildfire. In this study, an investigation into the modelling of hydrophobic soil is presented. Local spatial variations in material parameters are accounted for using Gaussian random fields as part of a stochastic finite element model. This is then employed to replicate field scale experiments. A key component of the model is the relationship used to represent the saturation-capillary pressure relationship responsible for defining water entry pressures. For wettable soil, this can be achieved with the standard van Genuchten relation. For hydrophobic soil, this is not applicable; thus, an alternative is employed. Results from numerical simulations are presented, which are based on a set of published experimental data.

Key words: *Finite element methods; Stochastics; Unsaturated soil; Hydrophobic soil; Preferential flow*

1 Introduction

Material variability in soils, especially due to spatial heterogeneity, can cause unstable hydraulic behaviour, often exaggerated in water repellent (WR) soils, leading to preferential flow paths and fingered flow. Modelling approaches for soil often assume the soil to be fully wettable and homogeneous, highlighting the need to represent soil hydrophobicity and its heterogeneity more appropriately. Previous studies have investigated fingered flow in water repellent soils, considering hysteresis and heterogeneity as key factors influencing the persistence and formation of flow paths [1]. Here, local spatial variations in material parameters are represented through Gaussian random fields in a stochastic finite element model, aiming to more accurately replicate in situ conditions. The developed model is then employed to replicate field scale experiments by Lipsius & Mooney (2006) [2]. The approach utilises the van Genuchten relation for wettable layers present in the soil and an alternative relation for hydrophobic soils, whose parameters -in both cases- are spatially varying. Results from simulations based on experimental data are then presented, offering insights into the model's effectiveness in capturing soil water dynamics under

these conditions.

2 Theoretical and numerical formulation

The soil is assumed to be composed of liquid water and solid mass phases, where neglecting the gaseous phase allows the volumetric water content θ to be solely dependent on the liquid phase. The liquid pressure u_l is considered to be the primary variable. A mass balance equation depending on the degree of saturation and porosity is used to represent the volumetric water content such that

$$\frac{\partial(\rho_l n S_l)}{\partial t} + \rho_l \nabla \cdot v_l = 0 \tag{1}$$

where ρ_l is the liquid density, n the porosity, S_l the degree of saturation of pore water, and v_l the liquid velocity. The flow is driven by gradients of total head, accounted for by Darcy's Law. By combining Darcy's Law with the mass conservation equation, the governing equation for flow can be formulated as

$$-n\rho_l \frac{\partial S_l}{\partial s}\frac{\partial u_l}{\partial t} - \nabla\left(\frac{\rho_l K_l}{\gamma_l}\nabla u_l\right) = \rho_l \nabla(K_l \nabla \mathrm{z}) \tag{2}$$

where γ_l the unit weight of liquid, z the elevation, and K_l the unsaturated hydraulic conductivity. The Finite Element Method is used to solve (2), where the associated discretised equation are derived using the Gauss-Green divergence theorem, and time discretisation is achieved through an implicit Euler backward difference scheme.

To represent spatial variability of the material, Gaussian random fields are generated based on the solution of stochastic PDEs [4], such that the stationary field and its resulting correlation structure can be represented by the Matérn autocorrelation function. The length-scale parameter $l > 0$ controls the resulting structure of the correlated fields. The autocorrelation function is posed as a stochastic PDE, the solution of which will be our Gaussian random field. Once more, a Finite Element approximation with usual Galerkin choice is made, leading to a matrix equation the can be solved using standard finite element routines. The form of the matrix equation shares similarities with standard components of the wider FE process, allowing for the method to be easily integrated into existing FE codes. In solving this equation, we are left with a Gaussian random field that can be used to introduce spatial variability into our numerical framework in terms of material properties, initial conditions, or problem geometries. For full details, see Ricketts et al. (2023) [3].

3 Application: hydrophobic soil

Often, the saturation-capillary pressure relationship used in unsaturated soil models is the standard van Genuchten relation. Whilst this is suitable for considering wettable unsaturated soil, the behaviour of hydrophobic soil may not be so well represented. For hydrophobic soil, the water entry pressures needed for infiltration can be in the positive pore-water pressure range (i.e. negative suction). The van Genuchten relation cannot account for the positive pore-water pressures that are characteristic of WR soil, suggesting the need for an alternative. Foroughi et al., (2022) proposed a new saturation-capillary pressure relationship for porous media of varying wettabilities, which proved to be more flexible and accurate than existing relationships [5]. This relationship can be written as

$$S_l = \left(\frac{1}{\pi}\left(\frac{\pi}{2} - \tan^{-1}\left(\frac{s-A}{B}\right)\right)\right)^{\frac{1}{C}} \tag{3}$$

where A is an indicator of wettability, B is the curvature index, and C is the saturation exponent. Whilst there is no fundamental basis for the functional form, the given parameters of the function can be interpreted physically. The most important in this study is A, where $A > 0$ indicates a wettable or hydrophilic medium, $A < 0$ indicates hydrophobicity, and $A \approx 0$ suggests a mixed-wettable medium where locally the medium could be hydrophobic or hydrophilic.

As in Ricketts et al. (2023) [3], Gaussian random fields were chosen to directly represent the saturated conductivity K_s, and the van Genuchten parameters α_{vg} and n_{vg}, leading to spatial variation in the SWRC and conductivity relations amongst other constitutive components. Foroughi et al.'s, (2022) [5] relationship is adopted in WR regions, and spatial variation in the water retention function is accounted for by varying the parameters A, B, and C. A transition between layers was also considered. This assumed a localised mixture of wettable and WR regions being present within a representative elementary volume, with the ratio of each fraction varying with depth. As the model considers discrete water retention functions in each layer, by interpolating between them based on the depth in a predefined transition zone, a combined water retention function can be calculated.

The domain was discretised by regular hexahedral elements of element length 2 cm (with appropriate convergence checks undertaken), where a rainfall flux boundary condition of 25 mm irrigation over 2.5 hours was applied. After this, the moisture was allowed to redistribute for 24 hours. In the experiment, a tracer was also applied to the surface to allow for imaging of the infiltration profiles, and is tracked numerically based on an assumed degree of saturation that the tracer would be active. The numerical domain is seen in Figure 1, where the top part of the soil is assumed fully hydrophobic, and the bottom section assumed wettable. The size of the water repellent and transition layers were based on the top 10 cm of the experimental plots displaying signs of heterogeneous water repellency. Slices were taken from the domain to compare with the experimental images based on the dye coverage percentage and the spatial distribution of the fingered shapes, as are seen in Figure 1. It is clear that the response seen experimentally is well represented by the numerical results. This is in terms of the spatial distribution of tracer activation and dye coverage percentages. The less conductive regions see a larger build-up of water as it struggles to pass through, suggesting the increased chance that the tracer will be active in said region. Conversely, the more conductive regions allow for faster passage of the wetting front, taking the tracer with it. Whilst a single instance is shown here, many realisations were considered to ensure convergence in the response.

4 Conclusion

The introduction of an alternative SWRC plays a crucial role in the wetting response, enabling the simulation of water entry pressures typical of water repellent soils. This adjustment allows for the simulation of surface pore water pressure build-up, mirroring the infiltration resistance observed in WR soils. The variability in water entry pressure further influences the soil's flow behaviour, leading to unstable fingered flow within the hydrophobic and transition zones, which becomes more diffuse upon reaching wettable layers.

The observed flow patterns within the non-wettable layers effectively capture the hydraulic behaviour of WR soils, showcasing the model's proficiency in simulating complex flow phenomena. The accuracy of the model is validated through dye coverage analysis of soil profiles, aligning closely with experimental findings.

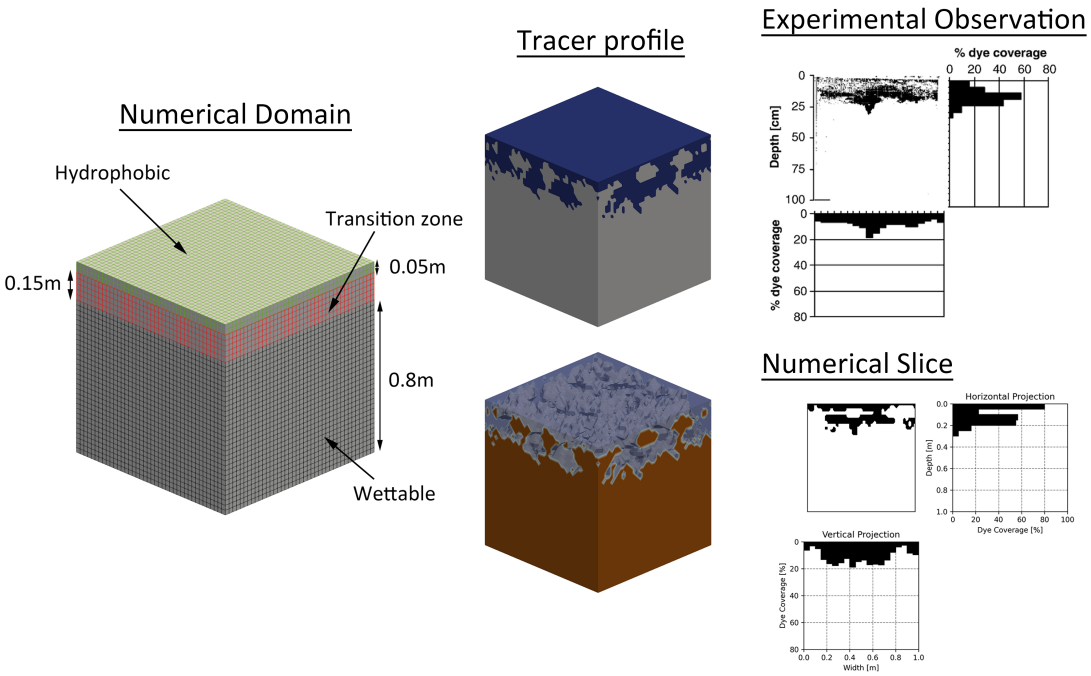

Figure 1: Illustrations of the numerical domain, resulting tracer infiltration profiles after 24 hours of redistribution time, and comparison with experimental observations of dye coverge.

Acknowledgments

Financial support from the finite element company LUSAS (www.lusas.com), is gratefully acknowledged.

REFERENCES

[1] Ritsema, C.J., Dekker, L.W., Nieber, J.L. and Steenhuis, T.S. Modeling and field evidence of finger formation and finger recurrence in a water repellent sandy soil. *Water Resources Research* (1998) **34**:555–567. doi: 10.1029/97WR02407.

[2] Lipsius, K. and Mooney, S.J. Using image analysis of tracer staining to examine the infiltration patterns in a water repellent contaminated sandy soil. *Geoderma* (2006) **136**:865—875. doi: 10.1016/j.geoderma.2006.06.005.

[3] Ricketts, E.J., Cleall, P.J., Jefferson, T., Kerfriden, P., Lyons, P. Representation of three-dimensional unsaturated flow in heterogeneous soil through tractable Gaussian random fields. *Géotechnique*. (2023) 1–13. https://doi.org/10.1680/jgeot.22.00316

[4] Lindgren, F., Rue, H., and Lindström, J. An explicit link between Gaussian fields and Gaussian Markov random fields: the stochastic partial differential equation approach. *In J. R. Statist. Soc. B*. (2011) **73**.

[5] Foroughi, S., Bijeljic, B. and Blunt, M.J. A Closed-Form Equation for Capillary Pressure in Porous Media for All Wettabilities. *Transport in Porous Media*. (2022) doi: 10.1007/s11242-022-01868-3.

UKACM 2024 Conference, 10-12 April 2024, Durham University, Durham, UK
https://doi.org/10.62512/conf.ukacm2024.079

MATHEMATICAL MODELLING OF PRESSURE INDUCED FREEZING POINT DEPRESSION WITHIN SOILS EXHIBITING STRONG CAPILLARY PRESSURE EFFECT

Ekaterina Lgotina[1*], Simon Mathias[1], Marti Lloret-Cabot[1], Andrew Ireson[2]

[1] Department of Engineering, Durham University, Durham, UK.
ekaterina.v.lgotina@durham.ac.uk, s.a.mathias@durham.ac.uk, marti.lloret-cabot@durham.ac.uk
[2] School of Environment and Sustainability, University of Saskatchewan, Saskatoon, Canada.
andrew.ireson@usask.ca

Abstract. Many geotechnical applications are affected by the melting and formation of ice in soils. Current state of practice involves incorporating the presence of ice within hydrological models for unsaturated soils using the so-called generalised Clapeyron equation [1]. This represents a modification of the conventional Clapeyron equation by allowing for the pressure in ice and liquid to be different at an ice-liquid interface. Such an idea has come about due to the effects of surface tension, which become important within the pores of porous materials such as soil and rock. However, a common assumption when using the generalised Clapeyron equation is that the ice pressure remains constant [2], which leads to unrealistic behaviour in the presence of significant pore-water pressure changes. Here we develop a new mathematical modelling framework to explore the impact of pressure induced freezing point depression within soils exhibiting strong capillary pressure effect. We solve the coupled mass and energy conservation problem using method of lines (e.g., [3]) with pressure and enthalpy as the primary dependent variables. Strong non-linear coupling develops through the chemical potential equation accounting for coexistence of ice and water in the presence of surface tension [5]. We present a sensitivity analysis showing how freezing point depression evolves within a porous block subject to temperature surface boundary cooling and varied capillary pressures.

Key words: *Ice; Clapeyron equation; Porous media; Enthalpy; Surface tension; Method of lines*

1 Problem description

In this work we develop the necessary equations for studying pressure induced freezing point depression in porous materials with capillary pressure effects. We construct the coupled mass and energy conservation problem that takes into account the heat conduction in the heterogeneous (partly frozen) porous material together with the latent heat of fusion, which is deposited at the freezing boundary layer. It is assumed that there is no convection as it is prevented by the low permeability of the material considered, which greatly simplifies the problem. The solid grains that comprise the porous material are assumed to be in thermal equilibrium with the water and ice contained within the pore-space. We also assume that in the same volume, there is always the same mass of solid grains.

Let us consider a horizontal porous column of length, L [L], with fully saturated pores, which are initially set at a uniform temperature, T_I [Θ], and pressure, p_I [$\mathrm{ML^{-1}T^{-2}}$], respectively (see Fig. 1). One of the boundaries is then treated as adiabatic whilst the other boundary is fixed at temperature, T_0 [Θ]. The boundary temperature is chosen to be less than the freezing-point temperature associated with the initial conditions. The coefficients of isothermal compressibility, α_T [$\mathrm{M^{-1}LT^2}$], and isobaric thermal expansivity, β_P [Θ^{-1}], are assumed to be constant, and the relationship between the freezing point temperature,

$T_c(p)$ [Θ], and pressure, p, is determined through a chemical potential equation accounting for the co-existence of ice and water in the presence of a surface tension. The ice is considered to be compressible and subjected to thermal expansion. The total mass of water component does not change over time due to there being zero permeability and no evaporation.

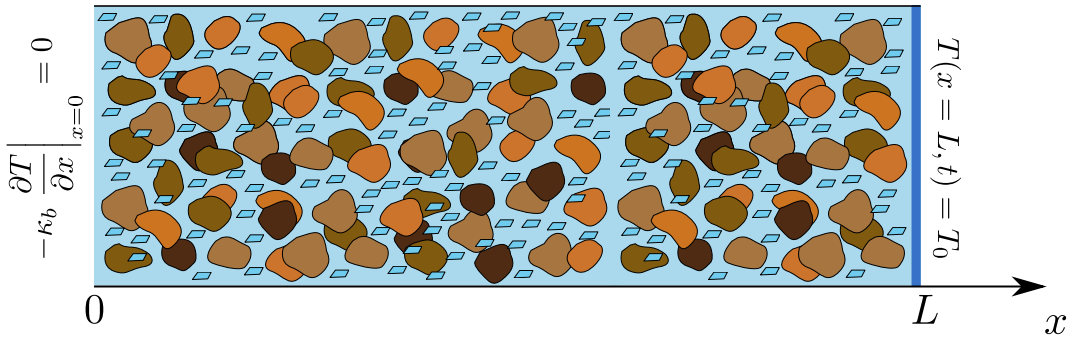

Figure 1: Schematic diagram of conceptual model.

The heat conduction problem takes the following form

$$\frac{\partial U}{\partial t} = \frac{\partial}{\partial x}\left(\kappa \frac{\partial T}{\partial x}\right), \quad T(x,0) = T_I(x), \quad T(x=L,t) = T_0, \quad -\kappa \left.\frac{\partial T}{\partial x}\right|_{x=0,t} = 0. \tag{1}$$

where x [L] is distance, T [Θ] is temperature, U [$\mathrm{ML^{-1}T^{-2}}$] is internal energy density and κ [$\mathrm{MLT^{-3}\Theta^{-1}}$] is thermal conductivity.

Let G_m [$\mathrm{ML^{-3}}$] be the mass of water per unit volume of porous material found from

$$G_w = \phi\left[S_w \rho_w + (1 - S_w)\rho_i\right], \tag{2}$$

where ϕ [–] is the porosity, S_w [–] is the saturation degree of water, ρ_w [$\mathrm{ML^{-3}}$] is the the mass density of liquid water and ρ_i [$\mathrm{ML^{-3}}$] is the mass density of ice.

By taking the full differential of G_w and choosing the pressure and enthalpy density, H [$\mathrm{ML^{-1}T^{-2}}$], as the primary dependent variables ($G_w = G_w(H, p)$), we get

$$dG_w = \frac{\partial G_w}{\partial H} dH + \frac{\partial G_w}{\partial p} dp. \tag{3}$$

Differentiating G_w from Eq. (2) with respect to p and H gives

$$\frac{\partial G_w}{\partial p} = G_w \frac{(1-\phi)}{\phi}\alpha_r + \phi\left[S_w \rho_w \alpha_w + (1 - S_w)\rho_i \alpha_i\right] + \phi(\rho_w - \rho_i)\frac{\partial S_w}{\partial p}, \tag{4}$$

and

$$\frac{\partial G_w}{\partial H} = -\left\{G_w \frac{(1-\phi)}{\phi}\beta_r + \phi\left[S_w \rho_w \beta_w + (1 - S_w)\rho_i \beta_i\right]\right\}\frac{\partial T}{\partial H} + \phi(\rho_w - \rho_i)\frac{\partial S_w}{\partial H}. \tag{5}$$

The evolution of G_w in time can be obtained by considering the time-derivative form of Eq. (3)

$$\frac{\partial G_w}{\partial t} = \frac{\partial G_w}{\partial H}\frac{\partial H}{\partial t} + \frac{\partial G_w}{\partial p}\frac{\partial p}{\partial t}. \tag{6}$$

Note that because of the absence of any convection (due to the zero permeability assumption), the mass is conserved, i.e. $\partial G_w/\partial t = 0$.

The constructed coupled mass and energy conservation problem is solved using the *method of lines*. For the numerical solution, we use one of the ordinary differential equations solvers available in MATLAB — `ode15s` — a variable-step, variable-order solver based on the numerical differentiation formulas of orders 1 to 5 [4].

The strong non-linear coupling develops through the chemical potential equation accounting for the coexistence of ice and water in the presence of surface tension:

$$\frac{dp}{dT_c} = \frac{L_f}{T_c(\bar{v}_w - \bar{v}_i)} + \frac{\bar{v}_i}{\bar{v}_w - \bar{v}_i}\frac{dp_c}{dT_c}, \tag{7}$$

where L_f [$\mathrm{L^2T^{-2}}$] is the latent heat of fusion, p_c [$\mathrm{ML^{-1}T^{-2}}$] is the capillary pressure, $\bar{v}_w$ [$\mathrm{L^3M^{-1}}$] is the specific volume of liquid water and $\bar{v}_i$ [$\mathrm{L^3M^{-1}}$] is the specific volume of ice.

2 Numerical results

In the following simulation cases we compared the curves of freezing point temperature, $T_c(x,t)$, and water degree of saturation, $S_w(x,t)$, obtained with ($p_c =$ some constant) and without ($p_c = 0$) the influence of capillary pressure.

Figs. 2 and 3 compare results, at different times for when the capillary pressure is zero and $p_c = 5$ MPa (lower magnitudes showed negligible effect). Increasing the capillary pressure leads to the soil freezing at a lower temperature (see Fig. 2). The water saturation distribution during the freezing period (see Fig. 3) becomes higher when capillary pressure is introduced because of the capillary forces that prevent liquid water from freezing.

Figs. 4 and 5 shows how the response of our model, after one day, is affected by a wider variation in capillary pressure, from 1450 Pa (almost no influence) to 10 MPa (strong influence). The influence of capillary pressure, in this context, is found to be negligible for values < 1 MPa. The freezing point temperature in Fig. 4 is lowered by the high capillary pressure due to the surface tension effects as expected. Fig. 5 shows that the slope of the water saturation curve (for region where $S_w < 1$) looks similar for all values of capillary pressure, and this effect needs to be studied further.

3 Conclusions

Our preliminary results demonstrate important aspects concerning the effect of water freezing on the temperature of porous material. A series of numerical experiments regarding the capillarity effect was conducted to demonstrate how freezing point depression and water saturation evolve within a porous block subject to temperature surface boundary cooling and varied capillary pressures. The proposed study intends to form a basis for the development of a liquid water–vapour–heat transfer model in unsaturated freezing soils to help better understand porous materials processes taking place in climate change–induced hydrological and ecological changes to frozen regions.

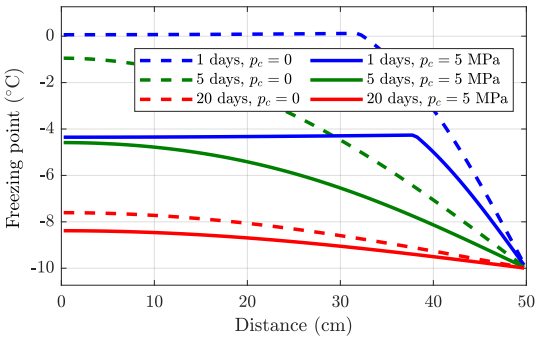

Figure 2: Plots of freezing point temperature for various times and p_c values as indicated in the legend.

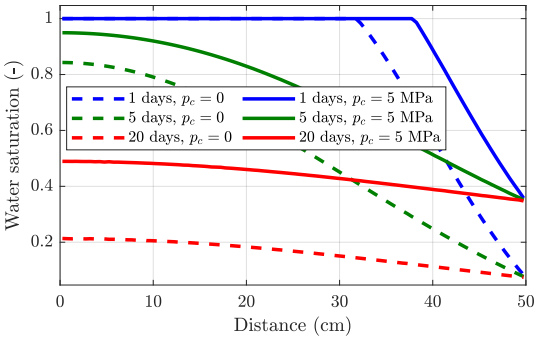

Figure 3: Plots of water saturation for various times and p_c values as indicated in the legend.

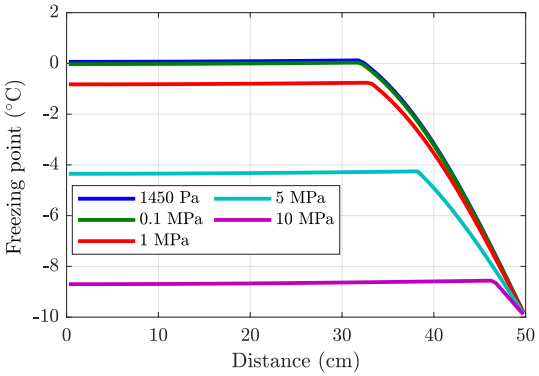

Figure 4: Plots of freezing point temperature after 1 day with various p_c values as indicated in the legend.

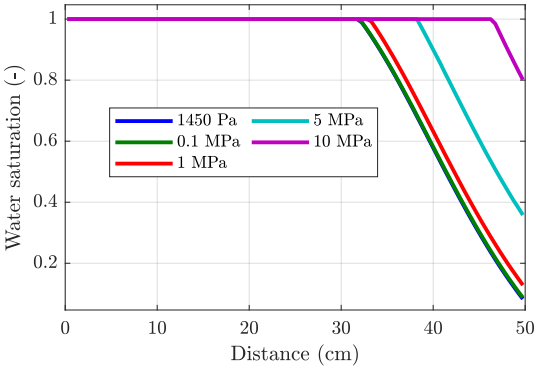

Figure 5: Plots of water saturation after 1 day with various p_c values as indicated in the legend.

REFERENCES

[1] Zhou, J., Wei, C., et al. *Application of the generalized Clapeyron equation to freezing point depression and unfrozen water content*. Water Resour. Res. 54(11) (2018): 9412–9431.

[2] Zheng, C., Šimůnek, J., et al. *Development of the Hydrus-1D freezing module and its application in simulating the coupled movement of water, vapor, and heat*. J. Hydrol. 598 (2021): 126250.

[3] Goudarzi, S., Mathias, S., Gluyas, J. G. *Simulation of three-component two-phase flow in porous media using method of lines*. Transp. Por. Med. 112(1) (2016): 1-19.

[4] Shampine, L. F., Reichelt, M. W. *The matlab ode suite*. SIAM J. Sci. Comp. 18(1) (1997): 1-22.

[5] Loch, J., Gustav, P. *Thermodynamic equilibrium between ice and water in porous media*. Soil Sci. 126 (1978): 77–80.

Hydro-mechanical Modeling of CO_2 Injection in Deformable Porous Media

F. Ghalamzan Esfahani[1*], G. Alfano[1], H. Bahai[1]

[1] Department of Mechanical and Aerospace Engineering, Brunel University London, Uxbridge, UK
Farzaneh.GhalamzanEsfahani@brunel.ac.uk, Giulio.Alfano@brunel.ac.uk, Hamid.Bahai@brunel.ac.uk

Abstract

Storing CO_2 in deep saline aquifers is a key strategy for carbon capture and storage, an essential technology in the global effort to mitigate greenhouse gas emissions. Several mathematical and computational models have been proposed to simulate CO_2 storage in geological formations [1-3]. These models aim to comprehensively capture the intricate interactions between fluids, gases, and geological media. In this study, we propose a novel quadrilateral finite element designed to simulate the flow of CO_2 and water in an isothermal deformable porous medium. This element has been developed in user element subroutine (UEL) of Abaqus. The balance equations include momentum balance, as well as the mass balance of CO_2 and water as outlined in prior research [2]. The proposed element is used to simulate certain tests, and preliminary results are presented.

Key words: *Finite Element Modeling (FEM), CO_2 Sequestration, Multiphase Flow, Hydromechanics*

1 Introduction

Carbon capture and storage has emerged as a critical technology in mitigating the adverse effects of greenhouse gas emissions, particularly CO_2, on the global climate. Among the various storage options, injecting CO_2 into deep saline aquifers offers a promising solution due to their abundance, widespread distribution, and potential for long-term storage. To facilitate effective CO_2 storage, it is necessary to develop accurate computational models capable of simulating the complex interactions between CO_2, water, and geological formations within these aquifers.

In recent years, significant research efforts have been directed towards the development of such models, aiming to comprehensively capture the intricate processes involved in CO_2 storage in geological formations [1-3]. These models encompass a range of aspects, including, geomechanical behavior [2], chemical reactions [5], thermal effects [6], and multiphase interactions [7]. By simulating CO_2 storage scenarios, these models provide insights into the behavior of CO_2 within geological reservoirs, enabling better-informed decision-making regarding site selection, injection strategies, and overall storage performance.

This study presents a novel quadrilateral element specifically designed to simulate the diffusion of CO_2 and water flow within deformable porous media. This element is developed within the user element subroutine (UEL) of Abaqus. Incorporating momentum and mass balance equations derived from prior studies [8], the proposed quadrilateral element is utilized to conduct numerical simulations illustrating the pore pressure changes in a consolidation problem where the porous medium is saturated, and the behavior of the solid skeleton is elastic. Additionally, we evaluate the coupling between CO_2 pressure and the degree of water saturation using this newly proposed element.

2 Problem description

In a porous medium containing two immiscible fluid phases, water and CO_2, the governing equations consist of mass balance equations for each fluid phase and a momentum balance equation for the entire mixture. This study assumes an isothermal environment, non-reactive chemical behavior between phases, no mutual dissolution between CO_2 and water, constant density and viscosity for CO_2, and unaffected mechanical properties of the solid skeleton due to the CO_2 sequestration process. The momentum balance equation is expressed as follows:

$$\nabla \boldsymbol{\sigma} + \boldsymbol{b} = 0 \tag{1}$$

Where $\boldsymbol{\sigma}$ is the total stress and b is the body force. Based on the modified effective stress concept, for a partially saturated porous medium, the total stress is computed as:

$$\boldsymbol{\sigma} = \boldsymbol{\sigma}' - \boldsymbol{I}\alpha p \tag{2}$$

In which $\boldsymbol{\sigma}'$ is the effective stress, $\boldsymbol{I}$ is the identity vector and α is Biot's constant representing the compressibility of solid grain and p is the mean pore pressure which is computed based on the averaging technique as $\mathrm{p} = (S_w p_w + S_g p_g)$. Where S_w and S_g are degrees of saturation of water and CO_2 respectively, p_w and p_g are water and CO_2 pressure respectively. The mass balance equation for water phase is [8]:

$$\left(\frac{\alpha-\varphi}{K_s}S_w^2+\frac{\varphi S_w}{K_w}\right)\frac{\partial p_w}{\partial t}+\frac{\alpha-\varphi}{K_s}S_w S_g\frac{\partial p_g}{\partial t}+\alpha S_w\frac{\partial \boldsymbol{\epsilon}}{\partial t}+\left(\frac{\alpha-\varphi}{K_s}S_w p_w-\frac{\alpha-\varphi}{K_s}S_w p_g+\varphi\right)\frac{\partial S_w}{\partial t}+\frac{1}{\rho_w}\nabla(\varphi\, S_w\rho_w\boldsymbol{v}_w)-Q_w=0 \tag{3}$$

The mass balance equation for CO_2 phase is [8]:

$$\left(\frac{\alpha-\varphi}{K_s}S_w S_g\right)\frac{\partial p_w}{\partial t}+\left(\frac{\alpha-\varphi}{K_s}S_g^2+\frac{\varphi S_g}{K_g}\right)\frac{\partial p_g}{\partial t}+\alpha S_g\frac{\partial \boldsymbol{\epsilon}}{\partial t}-\left(\frac{\alpha-\varphi}{K_s}S_g(p_g-p_w)+\varphi\right)\frac{\partial S_w}{\partial t}+\frac{1}{\rho_g}\nabla(\varphi\, S_g\rho_g\boldsymbol{v}_g)-Q_g=0 \tag{4}$$

in which φ porosity, K_s, K_{w} and K_{g} are the bulk modulus of the solid, water, and CO_2, respectively; $\mathbf{v}_w$ and $\mathbf{v}_{\mathrm{g}}$ are water and CO_2 relative velocities to the solid phase; Q_{w} and Q_g are source or sink terms. Darcy's law is considered for fluid velocity as:

$$\varphi\, S_\theta\boldsymbol{v}_\theta=\frac{\boldsymbol{k}k_{r\theta}}{\mu_\theta}(-\nabla p_\theta+\rho_\theta\boldsymbol{g}) \tag{5}$$

In which $\boldsymbol{g}$ is the gravitational acceleration vector**,** $\mathbf{k}$ is intrinsic permeability tensor, $k_{r\theta}, \mu_\theta, p_\theta, \rho_\theta$ are relative permeability, dynamic viscosity, pressure, and intrinsic averaged density of phase θ, respectively. The water and CO_2 pressure are related by capillary pressure $p_{\mathrm{c}}(\mathrm{S_w}) = p_g - p_w$. The capillary pressure-saturation relation is defined based on the equation proposed by [4] as:

$$p_c(S_w)=\frac{p_b}{(S_e)^{\frac{1}{\lambda}}}\qquad p_c\le p_b \tag{6}$$

Where p_b and λ are characteristic constants of the medium and $S_e=\frac{S_w-S_{wr}}{1-S_{wr}-S_{gr}}$ is the effective saturation, S_{wr} and S_{gr} are the residual water and CO_2 saturation. We consider the pressure-saturation formulation due to its ability to decouple the governing equations into a concise set. The finite element formulation of the governing equations is derived using the weighted residual method, where the fundamental variables are considered as displacements, CO_2 pressure, and the degree of water saturation. A two-dimensional quadrilateral element, with 8 nodes, is proposed in this study. The corner nodes encompass 4 degrees of freedom, representing displacements, CO_2 pressure, and the degree of water saturation, while the middle nodes are solely associated with displacements. This element is implemented through a user-defined subroutine (UEL) in ABAQUS [9].

3 Numerical results

To validate the model, a 1D column of 1m with 50 elements is considered. A saturated porous medium is assumed, with the water saturation degree set to one. Horizontal displacement of all nodes is constrained, while vertical displacement is constrained at the bottom of the column. The pore pressure is set equal to zero at the top surface of the column. The permeability is equal to 0.46×10^{-11} m/s, dynamic viscosity of water is equal to 0.001, Elastic modulus and Poisson's ratio are equal to 6 MPa and 0.4, respectively and $p_b = 0$. Figure 1(a) shows the boundary condition of the 1D column. Given that the saturation degree of water equals 1 and the capillary pressure is 0, the CO_2 pressure degree of freedom corresponds to the pore water pressure ($p_g = p_w$). A vertical stress equal to 10 kPa is applied on the top surface of the column instantaneously. As a result of this applied load, the column underwent consolidation in the vertical direction, characterized by an increase in vertical displacement accompanied by changes in pore pressure. During the consolidation process, we closely monitored the evolution of pore pressure and vertical displacement. As depicted in Fig. 1(b), the pore pressure gradually dissipates over the consolidation period. Figure 1(c) illustrates the progressive increase in vertical displacement as consolidation proceeds.

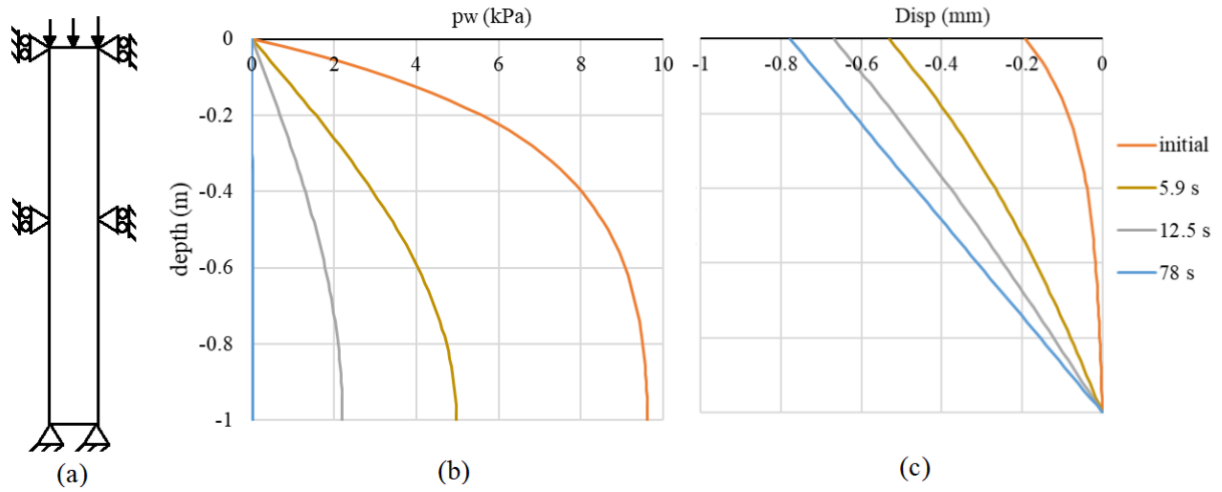

Figure 1: consolidation of a 1D column a) boundary condition, b) distribution of pore pressure and c) vertical displacement by time.

To evaluate the interaction between CO_2 pressure and water saturation, we analyze a 1D column with 1 m depth with 50 elements. All node displacements are constrained along both horizontal and vertical axes, as depicted in Figure 1(a). The permeability is equal to 0.46×10^{-11} m/s, dynamic viscosity of water is equal to 0.001, the residual water saturation is 0.397, and $p_b = 225$ kPa. Initially, the water saturation is 0.52, the CO_2 pressure is 102 kPa. The CO_2 pressure (p_g) at the top of the column is increased to 210 kPa in 100 seconds. Figure 2(b) illustrates the CO_2 pressure increase along the column over time, while Figure 2(c) shows the variation in degree of water saturation along the column during the CO_2 pressure increase. After 4900 seconds, the CO_2 pressure reaches 210 kPa across the entire column depth, with the water saturation degree (S_w) reaching 0.86. The changes in pore water pressure and degree of CO_2 saturation can be computed using the capillary pressure-saturation relation.

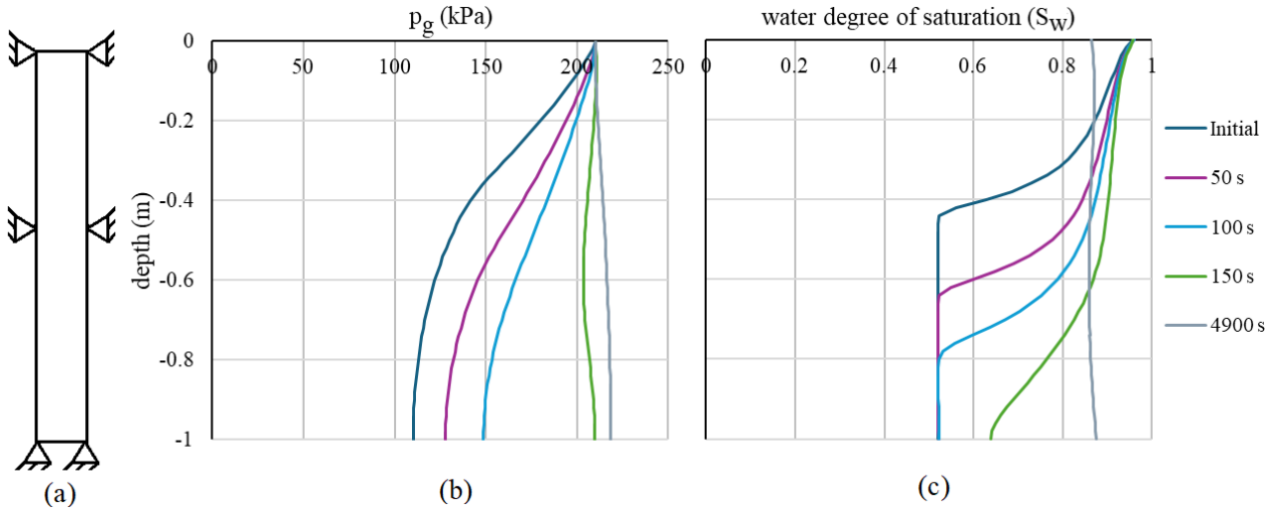

Figure 2: Coupling between water saturation and CO_2 pressure a) boundary condition, b) propagation of CO_2 pressure and c) distribution of degree of water saturation.

4 Conclusions

The storage of CO_2 in deep saline aquifers presents a promising method for mitigating greenhouse gas emissions. To comprehensively understand the long-term implications and environmental effects of such storage, it is imperative to develop accurate models. Finite Element Method (FEM) stands out as a viable approach for simulating CO_2 diffusion within storage reservoirs. In this study, we introduced a novel 2D element designed to incorporate the flow of CO_2 alongside water in a deformable porous medium. Our model

is based on momentum and mass balance equations for water and CO_2. The preliminary results encompass simple simulations, yet our ongoing efforts are directed towards enhancing our model to tackle more complex scenarios involving the injection of CO_2 into the storage reservoir.

Acknowledgments

The authors would like to thank the Engineering and Physical Sciences Research Council (EPSRC) [EP/T033940/1] for their financial support, which has facilitated this project.

References

[1] A. R. Khoei, R. Ehsani, N. Hosseini. (2022) An Extended-FEM Model for CO_2 Leakage Through a Naturally Fractured Cap-Rock During Carbon Dioxide Sequestration. *Transp Porous Med*, 145, 175–195.
[2] M. Talebian · R. Al-Khoury · L. J. Sluys. (2013) Coupled Electrokinetic–Hydromechanic Model for CO_2 Sequestration in Porous Media. *Transp Porous Med*, 98, 287–321.
[3] C. Ladubec, R. Gracie, and J. Craig. (2015) An extended finite element method model for carbon sequestration. *Int. J. Numer. Meth. Engng*, 102, 316–331.
[4] Brooks, R.H., Corey, A.T. (1964) Hydraulic properties of porous media. Hydrol. Pap., Colo. State Univ.
[5] Shi, Y. et al. (2023) Geochemical reaction of compressed CO_2 energy storage using saline aquifer, *Alex. Eng. J.*, 64, 679-689
[6] Andersen, O., Nilsen, H. M. (2018) 'Investigating simplified modeling choices for numerical simulation of CO_2 storage with thermal effects, *Int. J. Greenhouse Gas Control*, 72, 49-64,
[7] Saaltink, M. W. et al (2013), A method for incorporating equilibrium chemical reactions into multiphase flow models for CO_2 storage, *Adv Water Resour*, 62, 431-441,
[8] Lewis, R.W., Schrefler, B.A. (1998) The Finite Element Method in the Static and Dynamic Deformation and Consolidation of Porous Media, 2nd edn. Wiley, New York.
[9] Hibbitt, Karlsson, Sorensen, (2009). Abaqus: Abaqus/Standard. Theory Manual 1172.

Computational Modelling for Material Processing and Multi-scale Analysis

UKACM 2024 Conference, 10-12 April 2024, Durham University, Durham, UK
https://doi.org/10.62512/conf.ukacm2024.077

COMPUTATIONAL MULTI-SCALE MODELLING AND INVERSE DESIGN OF FLEXOELECTRIC METAMATERIALS

Xiaoying Zhuang*, Han Hu, S.S. Nanthakumar

Department of Mathematics and Physics, Leibniz University Hannover, Hannover, 30167, Germany.
zhuang@iop.uni-hannover.de
hanhu@iop.uni-hannover.de
nanthakumar@iop.uni-hannover.de

Abstract. In this work, we present machine learning-assisted flexoelectric materials characterization and apply topological optimization for flexoelectric structures across atomistic to continuum scales. New formulations for nonlinear topological optimization of flexoelectric structures, accounting for nonlocal stress and large deformation processes, will be presented. A robust machine-learning interatomic potentials-based tool is developed for designing advanced energy harvesters in micro scale and interesting phenomena of optimized structures in macro scale will be presented.

Key words: *Flexoelectricity; Machine learning; Topological optimization; Metamaterials; Energy harvesting*

1 Introduction

Flexoelectricity is the mechanical deformation subjected to an electric gradient (converse-flexo). It is a more general phenomenon than the piezoelectric effect, existing in a wider range of centrosymmetric materials, especially non-toxic materials useful for biomedical applications. Flexoelectricity grows dominantly in energy density when the scale is reduced to submicro or nano, signaling the promise of enabling self-powered nano devices such as body implants and small-scale wireless sensors. The study of this flexoelectricity is divided into two main theoretical frameworks: microscopic and macroscopic theories. The microscopic approach examines atomic-scale interactions to calculate material flexoelectric outputs, leveraging computational methods [2] and machine learning [1] for material design and simulation. Conversely, the macroscopic theory applies a thermodynamic perspective, treating materials as continuous media for the design of flexoelectric devices using finite element analysis and topology optimization [4, 5], streamlining the creation of devices with enhanced performance.

2 Flexoelectricity in 2D Van der Waals bilayers: a machine learning-based approach

Two-dimensional (2D) materials, such as transition metal dichalcogenides (TMDCs),exhibit significant electromechanical properties through bending flexoelectricity [2, 3]. Among various theoretical approaches, density functional theory (DFT) calculations are prominently used to investigate flexoelectricity in 2D materials. The development of 2D van der Waals (vdW) materials introduces complex variables such as layer number dependency, stack sequencing, and the potential for stacking different materials, highlighting new research avenues and challenges. Flexoelectricity in vdW layers faces issues like nonperiodic vertical alignments and diverse stacking configurations, which are not fully addressable by DFT simulations alone. We propose an AI-assisted molecular dynamics (MD) approach to tackle these challenges, utilizing accurate interatomic potentials derived from first-principles simulations. Specifically, this study leverages machine learning-based interatomic potential (MLIP) parameters for predicting mechanical and thermal properties of monolayer 2D materials, applying MLIP for short-range and deriving

long-range interaction parameters from DFT.

The methodology unfolds in three stages: (1) Generating inter-atomic potential parameters: Data sets for vdW bilayers at various temperatures are used to obtain MLIP parameters via machine learning. Lennard-Jones (LJ) and charge-dipole (CD) potentials are matched with DFT measurements of interlayer energy, see Fig.1(b), and polarizability, see Fig.1(c). (2) Validating potential parameters: Initial tests compare mechanical and piezoelectric properties with literature data and DFT simulations to validate the parameters. (3) Bending under compression: Compression tests on bilayer systems using developed parameters extract flexoelectric coefficients from atomic data.

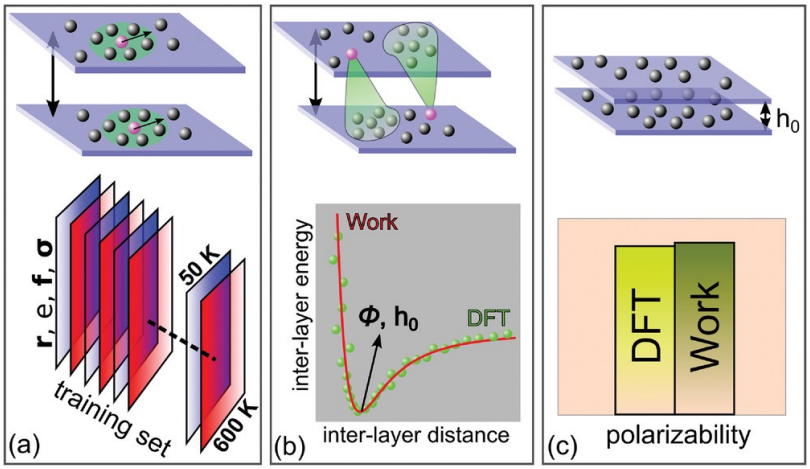

Figure 1: a) Schematic bilayer configuration with neighbor atom selection for short-range interactions. b) Highlighting the neighbor atom selection that accounting the vdW interactions in a bilayer configuration. The comparison between calculated (work) and DFT predicted inter-layer energy ϕ and interlayer distance h. c) Illustrating the bilayer configuration with minimum energetic separation used to calculate the atomic polarizability. Establishing the matching between the polarizability from CD model (work) and from DFT calculations to predict the CD model parameter that accounting the long-range charge-dipole interactions.

Findings reveal that bilayer TMDCs can have flexoelectric coefficients 2–7 times larger than monolayer forms, with increases up to 20 times for Janus diamane and fluorinated boron-nitrogen diamane derivatives. These insights enhance understanding of flexoelectric effects in vdW heterostructures and offer a robust MLIP-based tool for designing advanced energy harvesting devices.

3 Topology optimization of linear/nonlinear flexoelectric structures

A critical gap in current research is the underutilization of flexoelectric principles for the development of engineering structures with superior piezoelectric strength and electromechanical coupling capabilities. The primary challenge lies in the computational complexity associated with discretizing and solving fourth order partial differential equations, limiting the availability of computational tools, e.g. the governing equations for flexoelectricity in the linear context shown as follows,

$$\nabla \cdot (\sigma - \nabla \cdot \tau) + f^{\text{ext}} = 0 \qquad \text{in}\,\Omega \tag{1}$$

$$\nabla \cdot (\varepsilon_0 \mathbf{E} + \mathbf{P}) - q = 0 \qquad \text{in}\,\Omega, \tag{2}$$

where σ and τ are stress and higher order stress terms, $\mathbf{E}$ is the electric field and $\mathbf{P}$ is polarization. f^{ext} and q are body force and body charge, respectively. Moreover, despite the existence of finite element (FE) based topology optimization methods for piezoelectric materials, similar advancements for flexoelectric materials are notably scarce. Addressing this gap, we have developed computational models designed for the topology optimization of flexoelectric structures for both linear and nonlinear scenarios [4, 5]. This model aims to maximize the intrinsic material performance, focusing on enhancing the energy conversion efficiency of flexoelectric nanostructures. With regards to the energy conversion factor (ECF) k, the optimization problem can be mathematically defined as

$$\min \quad F = \frac{1}{k^2} = \frac{\Pi_e}{\Pi_m} \tag{3}$$

$$\text{Subject to} \quad \int_\Omega \mathrm{d}\Omega = \bar{\mathrm{V}} \tag{4}$$

$$\text{and} \quad \delta\Pi = 0, \tag{5}$$

where Π, Π_e and Π_m indicate the total free energy, electrical energy and mechanical energy, respectively, and $\bar{V}$ is the user-defined volume constraint. The optimization problem is solved iteratively and the trial topology is obtained based on the level set method for linear flexoelectricity [4] or Solid Isotropic Material with Penalization (SIMP) method for the nonlinear case [5]. The first example showcases the

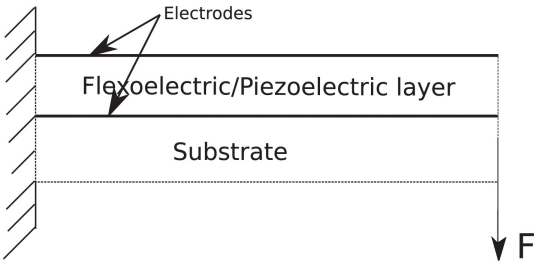

Figure 2: A cantilever type energy harvester with piezoelectric/flexoelectric layer placed over a substrate.

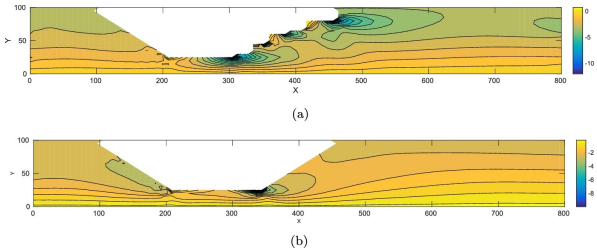

Figure 3: (a) The optimal topology for maximizing energy conversion of a flexoelectric layer in a cantilever energy harvester (ECF = 0.15) (b) An example topology with smooth surfaces (ECF = 0.06).

enhancement of ECF of linear flexoelectric cantilever energy harvester, where a substrate with a piezoelectric or flexoelectric layer as shown in Fig.2(a). The study demonstrates that topology optimization significantly enhances the energy conversion efficiency (ECF) in barium titanate (BTO) nanobeams. It reveals an eightfold increase in ECF for 100 nm thick flexoelectric nanobeams, in contrast to only a 5% increase for piezoelectric and surface piezoelectric effects. This distinction highlights the unique advantages of topology optimization, which, in flexoelectric beams, not only redistributes material but also leverages stress singularities from sharp corners to enhance ECF through increased local polarization. Fig.3 illustrates this by comparing the optimal topology, featuring beneficial corrugations, with a smoother example topology, showcasing how non-smooth surfaces can significantly boost ECF from 0.06 to 0.15.

The second example concerns a double clamped beam, as shown in Fig.4, optimized by the nonlinear framework. Fig.5 illustrates the differences between nonlinear and linear topology optimization formulations, highlighting that the nonlinear model achieves a superior conversion factor of 61.6%, compared to

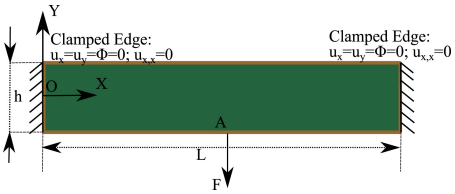

Figure 4: A two-side clamped beam under central load.

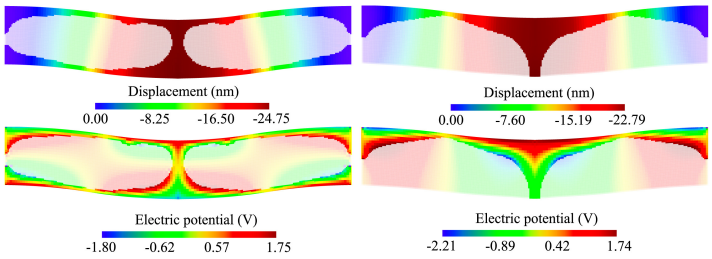

Figure 5: Obtained optimized structure from the nonlinear (left column Figures, ECF = 0.61) and linear (right column Figures, ECF = 0.55) topology formulations.

54.8% for the linear model. This suggests that conversion efficiency is inversely related to elastic energy, resulting in greater compliance in structures with higher conversion factors. Accordingly, the maximum vertical displacement values observed are 24.7 nm for the nonlinear model and 22.8 nm for the linear model, further emphasizing the enhanced performance of nonlinear optimization in ECF.

4 Conclusions

This work has successfully demonstrated the integration of machine learning and topological optimization in the characterization and design of flexoelectric materials and structures. Through atomistic simulations and continuum-scale models, we have provided new insights into the flexoelectric phenomena including 2D Van der Waals bilayers and linear/nonlinear flexoelectric structures. Our findings reveal that machine learning-assisted methodologies can significantly enhance the prediction and understanding of flexoelectric effects, offering a robust tool for the design of advanced energy harvesting devices. Furthermore, the developed topological optimization formulations have proven effective in enhancing the energy conversion efficiency of flexoelectric structures, outperforming traditional designs.

REFERENCES

[1] Javvaji, B., Zhuang, X., Rabczuk, T., & Mortazavi, B. (2022). Machine-Learning-Based Exploration of Bending Flexoelectricity in Novel 2D Van der Waals Bilayers. *Adv. Energy Mater.*, 12(32), 2201370.

[2] Javvaji, B., Zhang, R., Zhuang, X., & Park, H. S. (2021). Flexoelectric electricity generation by crumpling graphene. *J. Appl. Phys*, 129(22).

[3] Zhuang, X., He, B., Javvaji, B., & Park, H. S. (2019). Intrinsic bending flexoelectric constants in two-dimensional materials. *Phys. Rev. B*, 99(5), 054105.

[4] Nanthakumar, S. S., Zhuang, X., Park, H. S., & Rabczuk, T. (2017). Topology optimization of flexoelectric structures. *J. Mech. Phys. Solids*, 105, 217-234.

[5] Zhuang, X., Thai, T. Q., & Rabczuk, T. (2023). Topology optimization of nonlinear flexoelectric structures. *J. Mech. Phys. Solids*, 171, 105117.

UKACM 2024 Conference, 10-12 April 2024, Durham University, Durham, UK
https://doi.org/10.62512/conf.ukacm2024.080

Numerical Simulation of Nanomachining: Exploring Meshless and Finite Element Techniques for Material Removal Modelling

Rahul Yadav[1*], Sivakumar Kulasegaram[1], Emmanuel Brousseau[1], Sahar Alimohammadi[2], Dan Read[2,3]

[1]School of Engineering, Cardiff University, Cardiff CF24 3AA, UK.
[*]YadavR2@cardiff.ac.uk, BrousseauE@cardiff.ac.uk, KulasegaramS@cardiff.ac.uk
[2] School of Physics and Astronomy, Cardiff University, Cardiff CF24 3AA, UK
AlimohammadiS1@cardiff.ac.uk
[3]Department of Electrical and Computer Engineering, University of California Santa Barbara, Santa Barbara, CA 93106, USA
ReadDE@cardiff.ac.uk

Abstract

Mechanical nano machining involves the precise removal of material at the nanoscale under the action of a cutting tool, enabling the creation of intricate structures and devices in various sectors, including semiconductors, optics, and manufacturing of medical devices. Nano-machining simulation offers advantages, providing cost-effective, time-efficient exploration of nanoscale material removal. When the nano-machining process is conducted on Atomic Force Microscopy (AFM) instruments, the AFM probe, which is employed as the cutting tool, can be affected by substantial wear of the probe tip. As the tool operates at the nanoscale, the AFM tip experiences significant stress and friction, leading to tip wear that diminishes precision, and impacts the quality of machined surfaces. The present study proposed a simulation framework for nano-scale machining of OFHC-Cu material using a mesh-free technique developed by in-house Lagrangian smooth particle hydrodynamics (SPH) code and finite element method (FEM) employing the dynamic explicit algorithm. The influence of the tip radius as a result of tool wear on the cutting mechanism is analysed. The study found that the cutting mechanism shifted from shearing to ploughing as the tip radius increased to 3.3 times the scratching depth for OFHC copper material. Further, the study explores the impact of scratching depth, rake angle, and tip radius on cutting forces, groove dimensions, and deformed thickness. Increased tip radius results in intense material deformation, indicated by higher cutting forces. The prevalence of normal forces over cutting forces suggested the extrusion of material near the tip radius under significant contact pressure. The ploughing mechanism was also shown to be a more likely processing phenomenon at an increased negative rake angle.

Key words: *Nano-scratching, SPH, FEM, Ploughing, Cutting, Deformation*

1 Introduction

Nano-machining, an advanced manufacturing technique, operates at the nanoscale to precisely shape materials for diverse applications like electronics, medicine, and materials science. AFM tip-based scratching, a precise nanofabrication technique, utilises atomic force microscopy tips to create controlled nanostructures such as nano-scale grooves, slots, and channels [1]. In AFM based nano-machining, the phenomenon of tip wear, involving the gradual erosion of tip at the nanoscale, presents a critical challenge. The understating and monitoring of tip wear is pivotal for sustaining precision and efficiency, essential in advancing nanofabrication processes [2].

The experimental exploration of nano-scale machining is associated with limitations attributed to challenges in nano-scale measurements and comprehension of physical phenomena. Numerical models can provide insights into complex interactions, such as material removal and tool wear, aiding in optimising processes. Molecular dynamics (MD) simulation is a commonly used technique to study nano-scale machining processes. MD simulates the interactions among individual atoms and molecules over time and provides valuable insights into the processes of removing material [3, 4]. Smoothed Particle Hydrodynamics (SPH) models has some advantages over MD simulations for nano-scratching, efficiently managing large deformations in solids and seamlessly scaling to macroscopic systems for enhanced efficiency. For example, SPH algorithms have been

developed to simulate the nano-scale scratching of annealed oxygen-free high conductivity (OFHC) copper using a rigid spherical indenter [5, 6].

The current study focuses on utilising two modelling approaches, namely a mesh-less in-house developed SPH program and the finite element method (FEM), to replicate the physical processes of nano-scale material removal. The proposed research centres on examining how tooltip wear affects the scratching process, with a particular emphasis on understanding the transition from cutting to ploughing phenomena.

2 Problem description

This section details the approach used to simulate nano-scale scratching through SPH and FEM, covering the contact and material models employed. The computational method employed relied on SPH, representing a continuum domain with a set of particles. In a Lagrangian-based approach, field variables are tracked at SPH particles, following material deformation. SPH formulations use a kernel function to approximate field properties of each particle. This involves replacing the integral representation of field functions with a summation over neighbouring particles as follows [7, 8]:

$$f(\boldsymbol{x}) = \sum_{b=1}^{M} f_b W_b(\boldsymbol{x} - \boldsymbol{x_b}, h_b)\ V_b \tag{1}$$

where, *h* represents the smoothing length, and V_b is the volume of neighbouring particle b. The leap-frog time integration is employed to update the positions and velocities of particles.

In the current modelling SPH approach, the Hertz contact model is adopted for computing the forces on the tool particles due to the workpiece particles during the nano-scratching process. The Johnson-Cook model is introduced to predict plastic behaviour. This is a widely employed constitutive model that characterises the strain-rate and temperature-dependent deformation of materials mentioned in equation 2 [9, 10]. In the nano-cutting process carried out using AFM instruments, the heat generated from plastic deformation and friction is typically minimal due to the relatively slow processing speeds. Therefore, in the current study, only the mechanical effects are considered.

$$\boldsymbol{\sigma} = (A + B\epsilon^n)\left[1 + C.ln\left(\frac{\dot{\varepsilon}}{\dot{\varepsilon}_0}\right)\right]\left[1 - \left(\frac{T - T_{ref}}{T_m - T_{ref}}\right)^m\right] \tag{2}$$

Coulomb friction was used in the FE model during the scratching process with friction coefficient of 0.15 used between the diamond tool material and the copper workpiece. The cutting parameters employed in the investigation are specified in Table 1. The properties were considered for OFHC-Cu workpiece material from the literature for simulation [11].

Table 1. The parameters employed for cutting in the investigation

Cutting parameters	Values
Scratching depth	100 nm
Tip radius	20 nm, 50 nm, and 100 nm
Rake angle	− 60°

3 Numerical results

This section begins by presenting the simulation outcomes for various tip radii. Figure 1(a) illustrates the simulated nano-grooves using both SPH and FE approaches for tip radii of 100 nm and 100 nm at a scratching depth. The corresponding force variation over time is depicted in Figure 1(b). Initially, the normal forces are higher due to the tip indentation into the workpiece, subsequently decreasing during the initial stages of cutting. The magnitude of the normal force exceeded the cutting forces, a result of the negative tool rake angle of (−)60°. The FE results exhibit greater force fluctuation, attributed to the utilisation of the element deletion

criterion for the material separation. The force trend and the average force values fall within acceptable limits for both simulation methodologies as compared to experimental results reported in [12].

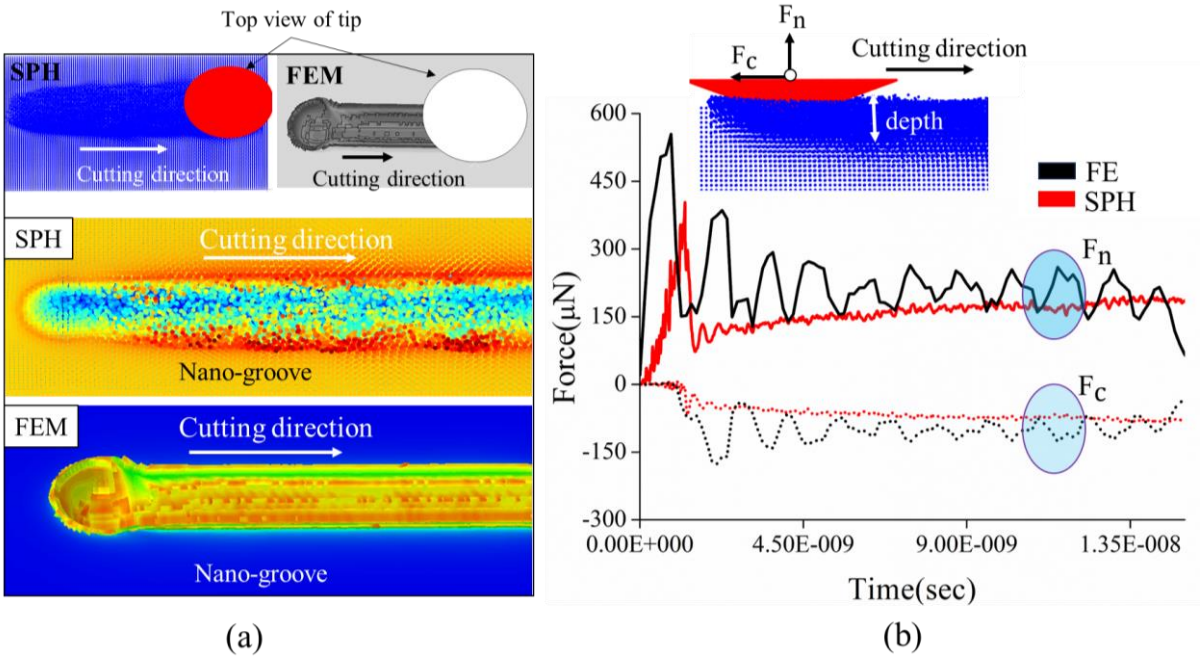

Figure 1: Simulation outcomes from SPH and FEM algorithms are presented as follows: **(a)** Nano-grooves generated by a conical tool with a tip radius of 100 nm and a scratching depth of 100 nm, and **(b)** The force fluctuation over time during both indentation and cutting processes.

The cutting mechanisms are influenced as the sharpness of the probe tip deteriorates over the cutting time. Figure 2(a) illustrates the relationship between the normal force and cutting force ratios across various scalar ratios of scratching depth to tip radius. As tip wear intensifies, the force ratio rises because the normal force surpasses the cutting forces. This occurs because a larger tip radius induces material ploughing rather than cutting. Once the scalar ratio reaches a critical limit of 0.3 (i.e. the tip radius increased to 3.3 times the scratching depth) for OFHC copper material, the cutting mechanism ceases and the force ratio increased in a nonlinear fashion. Within this range, the material is solely ploughed, resulting in a degradation of the surface finish on the workpiece. The force magnitude increased with a rise in tip radius as depicted in Figure 2(b). This can be ascribed to a larger contact area between the tip and the surface, leading to increased friction and ploughing effects, thereby contributing to an overall force increase.

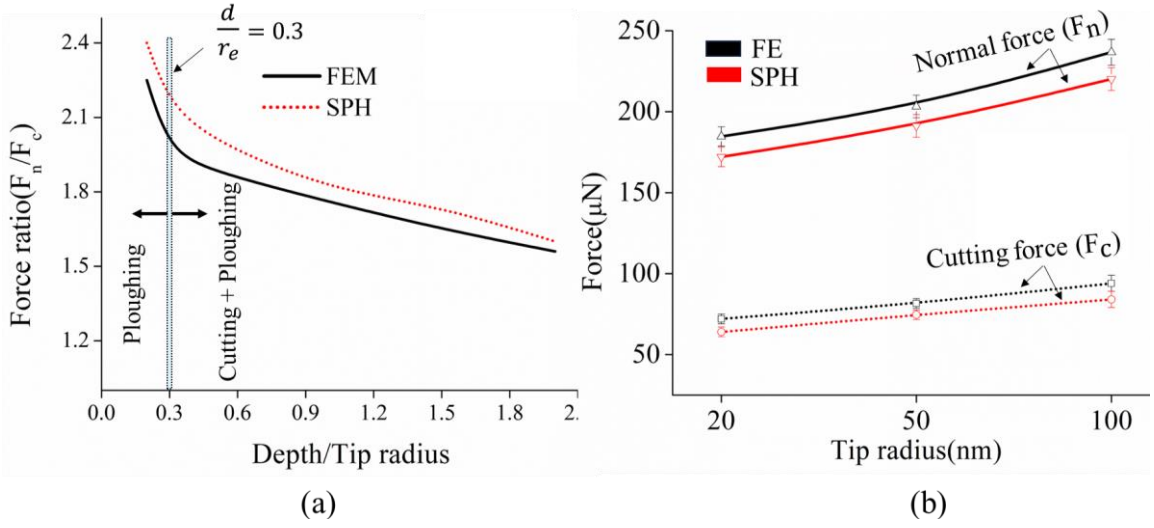

Figure 2: (a) The variation of force ratio ($\frac{F_n}{F_c}$) with scalar ratio of scratching depth to tip radius **(b)** Variation of normal and cutting force concerning the tip radius of the probe.

4 Conclusions

This research implemented the mesh-free Smooth Particle Hydrodynamics (SPH) and Finite Element Method (FEM) approaches for simulating nano-scale scratching on OFHC-Cu using conical tools with a negative rake angle. The study explored the impact of tooltip radius on contact forces and surface topography. Notably, it revealed that tip wear caused a shift from a cutting to a ploughing regime, when the tip radius reached 3.3 times that of the scratching depth on the OFHC-Cu work material. The proposed modelling methods can be effectively applied to capture the physics involved in nano-scale cutting.

The current study could be expanded by incorporating the size effect by introducing the strain gradient in the constitutive model. Additionally, the deflection of the cantilever beam inducing dynamic instability, affecting the precision of cuts and surface finish, could be considered in future studies.

Acknowledgments

The reported research was funded by the Engineering and Physical Sciences Research Council (EPSRC) under the grant EP/T01489X/1. We would like to thank Supercomputing Wales for allowing us to run our code efficiently in the HAWK supercomputing system.

References

[1] Yongda Yan, Yanquan Geng, Zhenjiang Hu, 2015. Recent Advances in AFM Tip-Based Nanomechanical Machining. Int. J. Mach. Tools Manuf., 99, pp. 1–18.

[2] Xiangcheng Kong, Jia Deng, Jingyan Dong, Paul H. Cohen, 2020. Study of tip wear for AFM-based vibration-assisted nanomachining process, Journal of Manufacturing Processes,Vol. 50, 47-56.

[3] Chen Jian-Hao, Zheng Qiu-Yang, Zhou Zhen-Yu, Ding Cong, Piao Zhong-Yu, 2021. Molecular dynamics simulation of monocrystalline copper nano-scratch process under the excitation of ultrasonic vibration, Mater. Res. Express. Vol. 8, 046507.

[4] Wan Wang, Dongpeng Hua, Dawei Luo, Qing Zhou, Shuo Li, Junqin Shi, Haifeng Wang, 2022. Molecular dynamics simulation of deformation mechanism of CoCrNi medium entropy alloy during nanoscratching, Comput. Mater. Sci. Vol. 203,111085.

[5] R. A. Gingold, J. J. Monaghan, 1977. Smoothed particle hydrodynamics: theory and application to non-spherical stars, Mon. Not. R. Astron. Soc. Vol. 181, 375–389.

[6] S. Leroch, M. Varga, S.J. Eder, A. Vernes, M.R. Ripoll, G. Ganzenmüller, 2016. Smooth particle hydrodynamics simulation of damage induced by a spherical indenter scratching a viscoplastic material, Int. J. Solids Struct. Vol. 81, 188–202.

[7] Anuj Sharma, Sivakumar Kulasegaram, Emmanuel Brousseau, Kane Esien, Dan Read, 2023. Investigation of Nanoscale Scratching on Copper with Conical Tools Using Particle-Based Simulation. Nanomanufacturing and Metrology, Vol.6(1).

[8] M. Takaffoli, M. Papini, 2012. Material deformation and removal due to single particle impacts on ductile materials using smoothed particle hydrodynamics, Wear, Vol. 274–275, 50-59.

[9] Rahul Yadav, Nilanjan Das Chakladar, Soumitra Paul, 2024. Tailoring of residual stress by ultrasonic vibration-assisted abrasive peening in liquid cavitation of metallic alloys. Int. J. Mach. Tools Manuf. Vol. 194, 104100.

[10] Rahul Yadav, Nilanjan Das Chakladar, Soumitra Paul, 2023. Effects of tailored residual stress on micro - end milling : numerical modelling and validation. *Int. J. Adv. Manuf. Technol.* 0123456789.

[11] Jun Zhang, Xiang Xu, Jose Outeiro, Hongguang Liu, Wanhua Zhao, 2020. Simulation of Grain Refinement Induced by High-Speed Machining of OFHC Copper Using Cellular Automata Method. Journal of Manufacturing Science and Engineering, Transactions of the ASME, Vol. 142(9), 91006

[12] Sumaiya Islam, Raafat Ibrahim, Raj Das, Tim Fagan, 2012. Novel approach for modelling of nanomachining using a mesh-less method. Appl. Math. Model. Vol. 36, 5589–5602.

Computational Modelling of Stress Concentration and Constitutive Relations

UKACM 2024 Conference, 10-12 April 2024, Durham University, Durham, UK
https://doi.org/10.62512/conf.ukacm2024.025

METAMATERIALS GENOME: PROGRESS TOWARDS A COMMUNITY TOOLBOX FOR AI METAMATERIALS DISCOVERY

Jacob Earnshaw[1], Nicholas Syrotiuk[1], Oliver Duncan[2], Lukasz Kaczmarczyk[3], Fabrizio Scarpa[4], Stefan Szyniszewski[1*]

[1] Department of Engineering, Durham University, Durham, DH1 3LE, UK.
stefan.t.szyniszewski@durham.ac.uk
[2] Manchester Metropolitan University
[3] University of Glasgow
[4] University of Bristol

Abstract. Understanding the limits of the design space is a key aspect in optimising complex hierarchical structures and is vital for exploring and designing novel Metamaterials. Simultaneously, abundant data (mostly text, images, and location) aggregated by multinational corporations accelerated the development of machine learning and artificial intelligence technologies. Although increasingly conceptually advanced, the origins of machine learning can be traced back to traditional statistical methods and data-centric analysis. These techniques have been used in fields where establishing relationships and using differential equations or closed-form descriptions have been challenging due to the systems' complexity. However, well-established and validated physics-based modelling tools offer direct solutions for various physical domains relevant to metamaterials. What is the right place for the emerging machine learning techniques in that context?

Key words: *metamaterials; open research commons, ai, machine learning, mechanical, optimisation*

1 Introduction

Fundamentally, numerous research groups and companies repeatedly carry out physics-based calculations, all employing the same fundamental equations such as Maxwell equations or wave or dynamic equations of motion. Therefore, one can recognise a potential for a large collection of results, which are, however, currently scattered across various research groups and frequently guarded in private data silos. In many instances, the results are discarded at the completion of specific projects or archived for a limited time. As recognised by several US federal agencies [1], [2], [3], creating an open research commons and appropriate standards and infrastructure for sharing and reusing as well as recycling existing data and computational tools can accelerate the development of novel materials, reduce effort duplication among different stakeholders, and accelerate the overall progress of the discipline as a whole.

2 Current and Future Challenges and Opportunities

In order to create knowledge graphs that can integrate multiple physical domains like mechanical, optical, electromagnetic, etc., it is necessary to establish common data standards [4]. This requires input and agreement from both academic and industrial groups. Moreover, these standards may change over time. Therefore, it is essential to establish methods for migrating and adapting data.

Shared repositories of knowledge require the trust of all stakeholders [5], sustainable funding, and a transparent governance structure. To achieve satisfactory cyber security resiliency, such a repository

might require distributed storage across academic and industrial stakeholders as well as specialist cybersecurity support. Shared repositories of knowledge require the trust of all stakeholders, sustainable funding, and a transparent governance structure. Low barriers for adaptation and usage should facilitate broader benefits and adaptation of the start knowledge by the widest possible group of stakeholders. To achieve satisfactory cyber security resiliency, such a repository might require distributed storage across academic and industrial stakeholders.

Optimising the process of organising and utilising data that already exists can save time and resources for all stakeholders. Additionally, the establishment of a shared open research commons can lead to improved collaboration and knowledge mapping by linking research groups based on similarity and proximity metrics of the structures they produce. By enabling search engines for specific required properties, manufacturers and industrial stakeholders can quickly identify the key research groups and technology suppliers in the design space.

Shared data from 'adjacent' problems can be used to inform and suggest solutions for the problem being studied (also in different physical domains). Since Metamaterial problems solve a limited number of physical laws, transfer learning provides significant benefits in this area and suggests good starting points for developing Metamaterials with specific properties. This can be achieved by leveraging prior iterations and the experience of other academic groups and stakeholders. Transverse learning can be facilitated by using approximate surrogate models that are trained on prior data. Such fast-running surrogate models are also vital for optimisation and can underpin AI generative design, which could suggest promising areas for novel material discoveries.

An example of an unsolved problem in the field is the development of a compact topology parametrisation that is compatible with machine learning tools. Such encoding should be able to generate any suitable Metamaterial topologies without being restricted to a specific subclass of structures. Another challenge is to incorporate manufacturability, cost and sustainability aspects into the optimisation process and generative capabilities of the shared open research commons.

3 Advances in Methods and Techniques to Meet Challenges

The National Institute of Standards and Technologies (NIST) has developed an open-source platform called the Configurable Data Curation System (CDCS) [6] that can curate complex data structures. This platform is designed with cybersecurity in mind and is continuously updated and supported by NIST. We have used this platform to create a prototype of a shared database of metamaterials, which is accessible online at www.meta-genome.org. The database can handle complex hierarchical XML data structures, including topology information in discrete voxel formats and more parametric, vector-like descriptions such as step formats. The open-source code can also be cloned, and independent repositories can be created while still leveraging shared data standards and programmatic developments in toolkits for working and processing vast amounts of data. This is particularly relevant in the context of recent developments in the computer science community, where tools like VQGAN [7] are being used to describe topologies. These tools hold promise in establishing critical links between physical information in the Metamaterials community and rapidly developing AI toolboxes with impressive generative capabilities demonstrated for other material domains [8]. AI generative demonstrations have already been demonstrated in the context of mechanical metamaterials [9], [10].

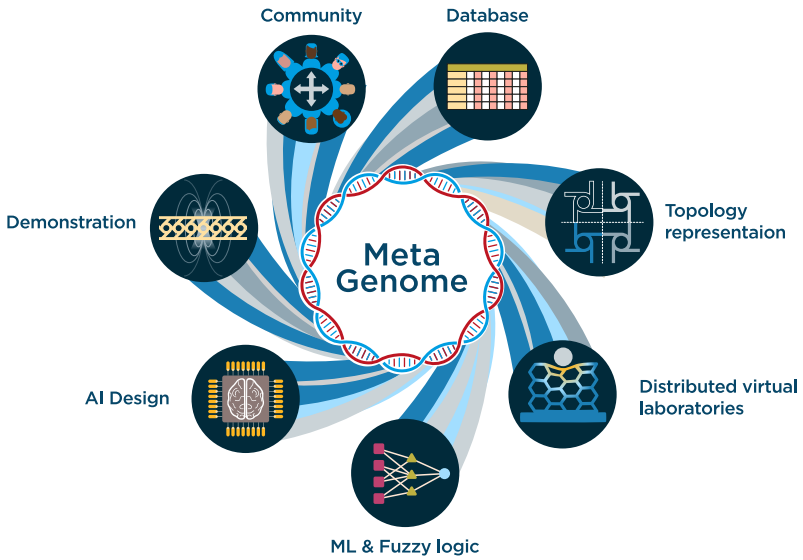

Figure 1: Synergy between physics-based simulations, data-centric analysis, community and developers is depicted as a circular concept.

4 Conclusions

Through the establishment of a shared open research commons, collaboration and knowledge mapping can be improved by utilising property-based norms and metrics. This will enable the community to quickly identify key research groups, manufacturers, and industrial stakeholders in the design space by searching for specific required properties. Secondly, it will enable researchers to focus on the most interesting and high-value activities, minimising duplication of effort and leveraging prior material discoveries. Thirdly, a standardised shared data platform lays the foundation for experimentation with and development of generative AI platforms to augment and enhance future meta-material discoveries.

Acknowledgments

We would like to acknowledge financial support from the Royce Institute for the Mechanical Meta-Materials Database (MCAP068) project, funded under the Materials Challenge Accelerator Programme (MCAP).

REFERENCES

[1] P. E. Bourne et al., Playing catch-up in building an open research commons, *Science*, vol. 377, **6603**:256-–258, Jul. 2022.

[2] A. Dima et al., 'Informatics Infrastructure for the Materials Genome Initiative', *JOM*, vol. 68, **8**:2053-–2064, Aug. 2016, doi: 10.1007/s11837-016-2000-4.

[3] National Science and Technology Council and Committee on Technology Subcommiitee on the Materials Genome Initiative, 'Materials Genome Initiative Strategic Plan', Department of Defence, National Science Foundation, Office of Science and Technology Policy and National Insti-

tute of Standards and Technology. https://www.mgi.gov/sites/default/files/documents/MGI-2021-Strategic-Plan.pdf

[4] Henry Royce Institute, 'Materials 4.0: A role for standards', Mar. 2021. Accessed: Aug. 24, 2022. https://www.royce.ac.uk/content/uploads/2021/06/Materials-4.0-A-Role-for-Standards.pdf

[5] Henry Royce Institute, 'Enabling Trust in Data Exchange for Materials 4.0', Jul. 2021. Accessed: Aug. 24, 2022. https://www.royce.ac.uk/content/uploads/2021/06/Materials-4.0-Enabling-Trust-in-Data-Exchange-Materials.pdf

[6] NIST, 'Configurable Data Curation System (CDCS)'. Accessed: Mar. 06, 2024. https://www.nist.gov/programs-projects/configurable-data-curation-system-cdcs

[7] J. Yu et al., 'Vector-quantized Image Modeling with Improved VQGAN'. *arXiv*, Jun. 04, 2022. doi: 10.48550/arXiv.2110.04627.

[8] B. A. Koscher et al., 'Autonomous, multiproperty-driven molecular discovery: From predictions to measurements and back', *Science*, vol. 382, no. 6677, p. eadi1407, Dec. 2023, doi: 10.1126/science.adi1407.

[9] A. J. Lew and M. J. Buehler, 'Single-shot forward and inverse hierarchical architected materials design for nonlinear mechanical properties using an Attention-Diffusion model', *Mater. Today*, **64**:10-–20, Apr. 2023, doi: 10.1016/j.mattod.2023.03.007.

[10] J.-H. Bastek and D. M. Kochmann, 'Inverse-design of nonlinear mechanical metamaterials via video denoising diffusion models'. *arXiv*, May 31, 2023. Accessed: Jun. 03, 2023. http://arxiv.org/abs/2305.19836

UKACM 2024 Conference, 10-12 April 2024, Durham University, Durham, UK
https://doi.org/10.62512/conf.ukacm2024.081

SENT Specimen Ductile-Failure Modelling via Damage Mechanics

Asif Ali[1*], Marius Gintalas[1], Giulio Alfano[1]

[1] Department of Mechanical and Aerospace Engineering, Brunel University London, Uxbridge, UB8 3PH
Asif.Ali@brunel.ac.uk
Marius.Gintalas@brunel.ac.uk, Giulio.Alfano@brunel.ac.uk

Abstract

Ductile fracture in metals has been intensively studied over at least 8 decades and a number of relatively well-established methods have been developed to characterise the fracture resistance of metal components in terms of critical fracture toughness parameter(s). The most widely used 'fitness-for-service' industry standards concerning evaluation of cracks or crack-like-flaws provides correlations to determine critical values of the stress intensity factor or the J integral as a function of temperature and component thickness (or crack front length). The most challenging aspect is how to take into account that the fracture toughness of metals can significantly depend on the degree of constraint characterised by stress triaxiality. On the other hand, damage mechanics is an alternative way of modelling progressive failure in materials. Depending on the damage model used, typically one or more damage variables are introduced at each material point, which range between 0 and 1, with 0 normally representing the undamaged state and 1 representing complete damage, which essentially means that a macro crack has formed or has propagated to the point. In this article, we will present and discuss the results of some finite element simulations conducted for a Single Edge Notched Tension (SENT) specimen using an explicit-dynamics solution procedure and a material model that accounts for ductile damage and plasticity. Due to the very refined mesh at the crack front, mass scaling is used to increase the minimum time increment ensuring stability and the effect of different choices of mass-scaling parameters are discussed.

Key words: *fracture toughness; crack front constraints; stress triaxiality; progressive ductile damage; shear damage; finite element analysis, fitness-for-service (FFS)*

1 Introduction

Cracks result in local stress concentration inside the material and may affect the load carrying capacity of the structure [1-9]. The degree of severity of a crack, for given values of the applied loads, is determined through one or more suitable parameters, such as the stress intensity factor, K, the energy release rate, G, the crack tip opening displacement (CTOD) or the J integral J. The concepts of stress intensity factor, K, and energy release rate, G, are in general applicable to brittle materials or ductile materials for cases which exhibit limited plastic zone at the crack tip i.e., cases for which the small-scale yielding assumption can be considered valid. CTOD [10] and J integral [11], on the other hand, are parameters that can be used for more general materials including ductile materials with considerably large plastic zones at the crack tip. The resistance of a material against fracture is measured through the critical value of one of the fracture mechanics parameters (i.e. K, G, CTOD or J) determined through fracture toughness testing on laboratory specimens.

Common fitness-for-service assessment standards [1, 2] utilise a Failure Assessment Diagram (FAD), which is a two-parameter approach to estimate the safety factor with respect to failure of a structural material in a range of material behaviour from linear elastic (brittle fracture) to fully plastic (ductile fracture). One of the two parameters considered in a FAD is the ratio between the stress intensity factor or the elastic-plastic J integral and their critical values leading to failure. The second parameter is the ratio of the applied load to the plastic collapse load.

Damage mechanics is an alternative framework to fracture mechanics to analyse the severity of a crack, particularly for 3-dimensional problems with complex geometries [5, 12, 13]. In damage mechanics, crack growth occurs once the material at crack front fails based on pre-defined failure criteria. Two widely used approaches account for the two phenomena of ductile damage due to nucleation, growth, and coalescence of voids and shear damage due to shear band localisation [9, 12]. Typically, ductile damage criteria assume that the equivalent plastic strain at failure, $\bar{\varepsilon}_D^{pl}$, is a function of the stress triaxiality factor, η. Instead, shear damage

criteria are based on the assumption that the equivalent plastic strain at failure (shear damage), $\bar{\varepsilon}_s^{pl}$, is a function of the shear stress ratio, θ_s. With this approach, failure occurs under shear damage at low stress triaxialities and through ductile damage at relatively higher stress triaxialities [14].

2 Problem description

This paper focuses on addressing issues that arise during modelling of crack growth in ductile materials such as those generally employed in pressure retaining equipment and structures, as a step towards formulating accurate and efficent crack-analysis procedures using FEA and damage mechanics. Data from experiments performed by Yizhe et. al. [3] has been used to calibrate material properties in the finite element analysis (FEA). Yizhe et. al. performed an experimental investigation of out-of-plane constraint effects on fracture toughness of Single Edge Notch Tension (SE(T)) specimens. They tested various sets of specimens, made from API X90 Pipeline Steel, with nominal thicknesses ranging from 9 mm to 108 mm, in 9 mm intervals. They measured the Crack Mouth Opening Displacement (CMOD) for various crack sizes using the double-clip gauge method, with the SE(T) specimen being subjected to tensile loading. The stress-strain curve for API X90 Steel specimens as determined by Yizhe et. al. is shown in Figure 1. The ultimate tensile strenght of the steel was found to be equal to 792 MPa and the average yield strenght equal to 640 MPa.

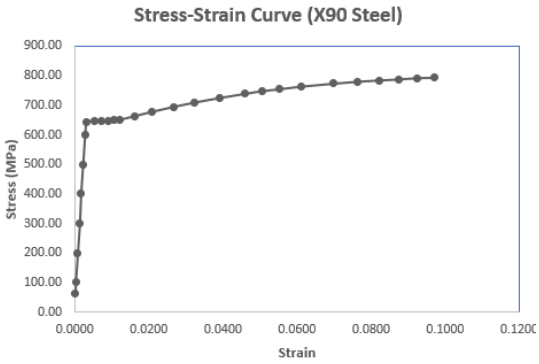

Figure 1: Stress-Strain curve for X90 Steel as used in the FE model (as reported by Yizhe et. al [3]).

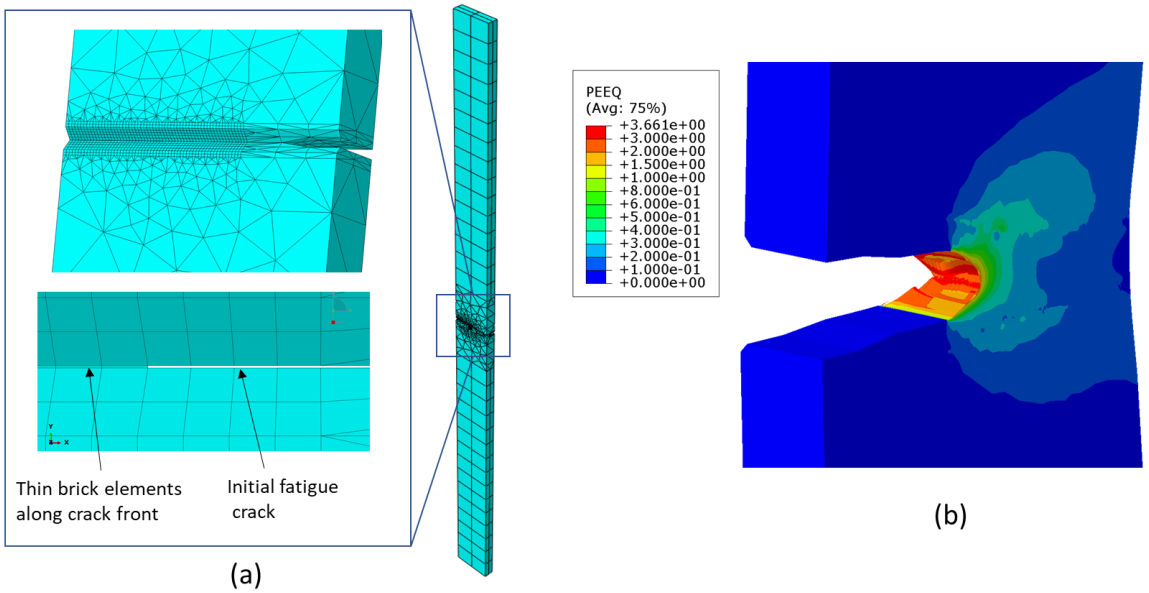

Figure 2: SENT specimen model: (a) mesh at crack front; (b) contour plot of the equivalent plastic strain.

Finite element modelling has been performed using the general purpose commercial code ABAQUS. The geometric model, material description and FE mesh was generated by coding Python scripts for better repeatability of the analysis with various specimen thicknesses and model parameters. By exploiting

symmetry, only half of the SENT specimen has been modelled as shown in Figure 2. An initial fatigue crack has been modelled as a 10-micron wide notch.

In order to capture the crack growth without remeshing, a refined mesh has been used in a rectangular cell along the anticipated crack growth path. This approach is similar to the method used by Brown et. al. [13]. The refined mesh at the crack front comprises of 8-node fully-integrated brick elements (named C3D8 in ABAQUS). A coarser mech consisting of the same elements have been used away from the crack. The transition region between fine and coarse mesh has been meshed with 10-node tetrahedral elements (C3D10). The FE mesh is as shown in Figure 2. Crack growth has been simulated through deletion of elements along the crack front once a pre-defined damage criteria is reached.

The explicit-dynamics solver in Abaqus has been used for better computational efficiency since the analysis involves large strains and an extremely discontinuous process such as crack propagation [12]. It is well known that the algorithm is conditionally stable and the time increment is a function of the smallest element size in the mesh. The computational time however can be reduced using 'mass scaling', which consists of using an artificial high material density to increase the minimum time increment that ensures stability of the algorithmic. Mass scaling can effectively reduce the analysis time as long as the errors introduced in the inertia forces do not significantly affect the solution. One way to obtain that is to apply mass scaling selectively, with different changes in density depending on the size of the elements.

For dependence of the damage model on the stress triaxiality. For these results, a suitable relationship has been chosen, whose details will be addressed in a forthcoming paper. This paper focuses on the effect of mass scaling and mesh size, because they significantly affect the time needed to conduct the simulations.

3 Numerical results

A contour plot of relation between the applied load and the CMOD predicted by the FE simulations have been plotted in Figures 3 and 4 against the experimental data.

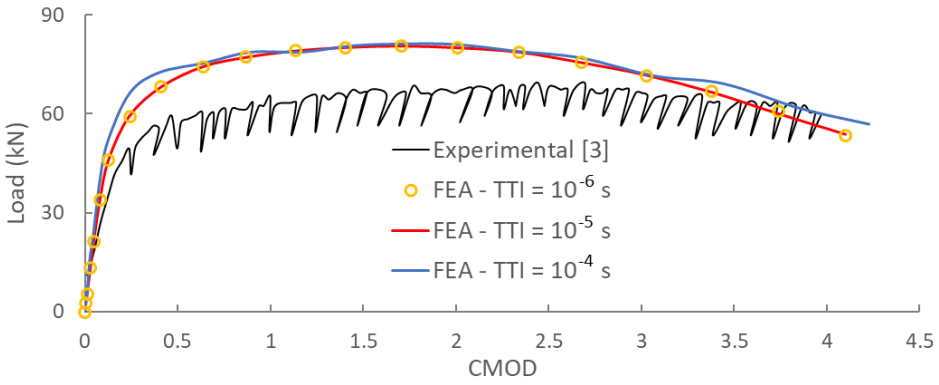

Figure 3: Load vs CMOD for three levels of mass scaling to achieve pre-set minimum target time increment (TTI) reported in the legend.

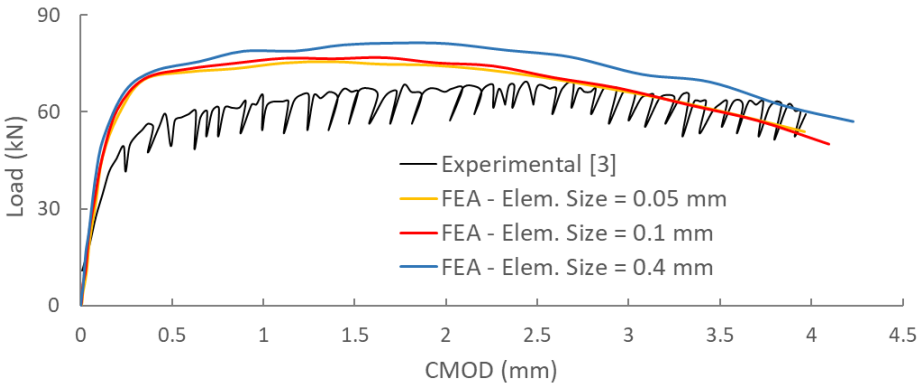

Figure 4: Load vs CMOD for three mesh refinement levels in term of element size at the crack front.

Mass scaling can be introduced in the solution procedure by choosing a 'target' time increment (TTI), so that the density of the relevant elements is increased automatically, if needed, to ensure that minimum stable time increment is not lower than the target one. Therefore, the chosen mass scaling parameters used are reported here in terms of TTI used in the simulations.

Figure 3 shows FE results obtained with a constant mesh size of 0.4 mm at crack tip, for three levels of mass scaling expressed in terms of TTI. Results for TTIs equal to 10^{-5} and 10^{-6} closely match. Further increase in TTI results noticeable differences, whereby 10^{-5} can be considered an optimum TTI for this simulation. Figure 4 reports FE results for three levels of mesh refinement at crack front with the same mass scaling and shows that 0.1 mm is an optimal mesh size as evident, because further refinement did not affect the results in any noticeable way. Figures 3 and 4 also reveal that the FE simulations capture the initial stiffness but overestimate the experimental results in terms of predicted load. On the other hand, the overall ductility predicted by the FEA conducted is in line with the experimental data.

4 Conclusions

Some preliminary results have been presented for a project that aims at developing accurate and efficient crack analysis procedure using damage mechanics and FEA. An explicit-dynamics solution procedure has been employed, and the effect of mass scaling and mesh refinement have been studied. Although the overall ductility and the qualitative trend of the load-CMOD curve are well captured, the load predicted by the FE simulations overestimates the experimental measurements of about 25%. It should be remarked that the stress-strain curve reported by Yizhe et al. [3], and employed in the simulation, does not include information on the scatter of results and refers to the reported curve as a 'typical stress-strain curve'. Further work is required to investigate whether possible scatter in the stress-strain curve could be explain the discrepancy found.

References

[1] British Standards Institution. *Guide on methods for assessing the acceptability of flaws in metallic structures.* BS 7910:2019.

[2] American Petroleum Institute. *Fitness-for-service.* API 579-1/ ASME FFS-1:2021.

[3] L. Yizhe et. al., (2017). Experimental investigation of out-of-plane constraint effect on fracture toughness of the SE(T) specimens, *International Journal of Mechanical Sciences*, Vol. 128–129, Pages 644-651.

[4] X. Zhu, (2016). Review of fracture toughness test methods for ductile materials in low-constraint conditions, *International Journal of Pressure Vessels and Piping*, Vol. 139–140, Pages 173-183.

[5] H. Hooputra et. al., (2004). A comprehensive failure model for crashworthiness simulation of aluminium extrusions, *International Journal of Crashworthiness*, Vol. 9:5, Pages 449-464.

[6] K. Konstantinos et. al., (2021). Validation of BS 7910 fracture assessment procedures; wide plates and cylinders. *International Journal of Pressure Vessels and Piping*, Vol. 190 (2021) 104309

[7] N.O. Larrosa et. al. (2017). 'Mind the gap' in fitness-for-service assessment procedures-review and summary of a recent workshop. *International Journal of Pressure Vessels and Piping*. Volume 158, December 2017, Pages 1-19.

[8] A.T. Zehnder (2009). Lecture Notes on Fracture Mechanics. New York: Cornell University.

[9] Anderson, T.L. (2017). Fracture Mechanics – Fundamentals and Applications. 4th Edition. Boca Raton: CRC Press.

[10] R.H. Subramanian et. al. (2019), A Critical Assessment of J-Integral and CTOD as Fracture Parameters. Advances in Interdisciplinary Engineering. Lecture Notes in Mechanical Engineering. Springer, Singapore. https://doi.org/10.1007/978-981-13-6577-5_41

[11] Rice, J.R. (1968). A Path Independent Integral and Approximate Analysis of Strain Concentrations by Notches and Cracks. *Journal of Applied Mechanics*, 35, pp. 379–386.

[12] Abaqus/CAE User's Manual, ver. 2023. Dassault Systèmes Simulia Corp.

[13] G.W. Brown et. al. (2016). Evaluation of groove radius assessment criteria based on brittle and ductile local failure models. Proceedings of the ASME 2016 Pressure Vessel and Piping Conference, American Society of Mechanical Engineers, Vancouver, British Columbia, July 2016.

[14] Yin, et. al. (2022). A New Micromechanical Criterion for Ductile Fracture of G20Mn5QT Cast Steels Under Shear Stress. *International Journal of Steel Structures* (2022) 22(5):1306–1321

Cutting-Edge Applications in Computational Engineering and Design

UKACM 2024 Conference, 10-12 April 2024, Durham University, Durham, UK
https://doi.org/10.62512/conf.ukacm2024.021

DEVELOPMENT OF A NUMERICAL FRAMEWORK FOR SIMULATION OF AQUACULTURE SYSTEMS

Shuo Mi[1*], **Eldad Jitzchak Avital**[2]

[1] School of Engineering and Materials Science, Queen Mary University of London UK.
s.mi@qmul.ac.uk
[2] School of Engineering and Materials Science, Queen Mary University of London UK.
e.avital@qmul.ac.uk

Abstract. A new integrated numerical framework is developed for simulating the fluid-structure interaction of aquaculture systems. The framework is based on our previous OpenFOAM formulation [1], while being coupled with a lumped mass-mooring model, MoorDyn [2], and a finite-element structural solver, EndoBeams [3]. Turbulent flow effects are dealt with using an incompressible fluid solver with a volume of fluid surface capturing method. The motion and deformation of the flexible nets are calculated using the screen and mass-spring methods. MoorDyn is used for simulating mooring lines while EndoBeams are used to calculate the deformation of other components of the aquaculture system, such as collars and frames. The coupling of all the components follows a loose-coupling method. The immersed boundary method is employed for the interactions between the fluid and all components of the aquaculture system. Fluid particle dynamics is also modelled using the Eulerian-Lagrangian to simulate fish disease waterborne transmission within aquaculture system area. The framework has been validated with extensive experimental data from the literature and is demonstrated as a robust tool to simulate the complex fluid-structure-particle dynamics of aquaculture systems.

Key words: *OpenFOAM; Aquaculture; Flexible nets; Mooring dynamics; Immersed boundary method; Fluid-structure interaction;*

1 Introduction

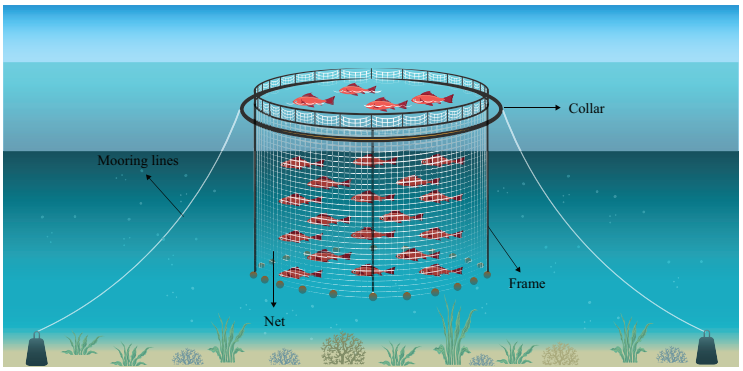

Figure 1: Sketch of a aquaculture system.

Aquaculture is important in global food security due to the increasing food demand. To improve the farming efficiency and reduce environmental impacts, traditional aquaculture is moving from nearshore to deep-sea areas for healthier fish stock and larger available space [4]. However, the deep-sea environ-

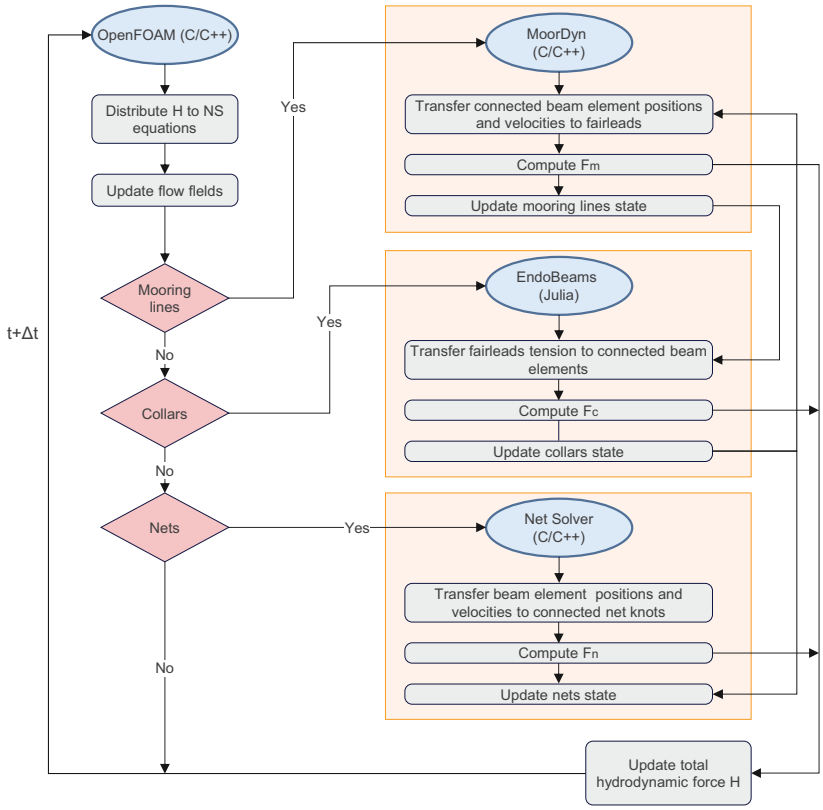

Figure 2: Flow chart of solving the coupled numerical framework.

ment is variable, extreme sea conditions can cause significant damage to aquaculture equipment. This requires more comprehensive study for deep-sea aquaculture structures design.

2 Problem description

Numerical simulation is promising to help design deep-sea aquaculture structures. However, a comprehensive model that captures the motion and deformation of each component within the entire system, as well as considers the interactions among components and the influences between the components and the fluid, is still lacking due to its complexity.

An typical aquaculture system includes multiple components that work together to raise fish or other sea life. As shown in in Figure 1, the net, as the main structure, encloses a space for raising and protecting fish. Collars can help maintain the net floating, while frames provide stability. Mooring lines allow for the movement of the system to absorb the energy of waves and currents while keeping the system within designated area. We developed a complete, high-fidelity and two-way coupled numerical frame to simulate the dynamic response of the aquaculture system in fluid. The development of this numerical model is based on our previously code for fluid-net interaction simulation [1], utilizing the open-source com-

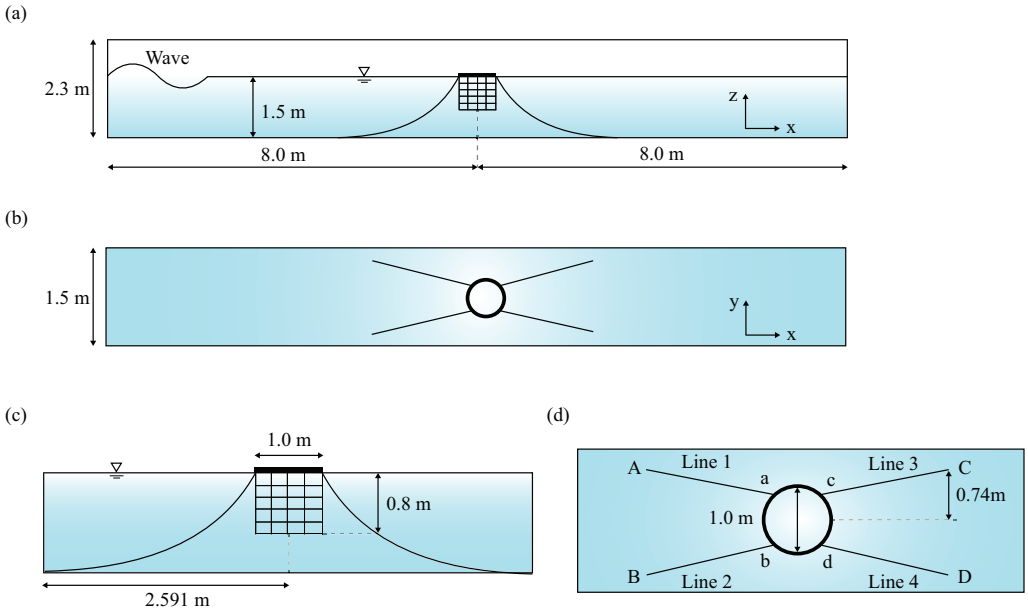

Figure 3: Numerical setup for the aquaculture system in regular waves. (a) Side view of the numerical flume; (b) Plan view of the numerical flume; (c) and (d) Details of side and plan view of the floating collar, net and mooring lines.

putational fluid dynamics (CFD) code, OpenFOAM [5]. We employed the immersed boundary method [6] to capture the interactions between the net structures and fluid, and used an implicit method to solve the motion equations of the net structure. Building on this foundation, we developed the nemerical framework, that is coupled with a mooring dynamics model, MoorDyn [2], and a finite element package, EndoBeams [3]. This model establishes elastic constraints among all components of one aquaculture system, such as mooring lines, net structures, and collars or frames to achieve comprehensive coupling. Figure 2 illustrates the flow chart of solving the coupled numerical framework.

3 Numerical results

A aquaculture system in regular waves is simulated using the current numerical framework. The computational domain of the numerical flume and details of floating collar, net and mooring lines are shown in Figure 3. The wave height and wave period are 0.5 m and 2 s, respectively. Figure 4 shows the snapshots over one wave period of the instantaneous free surface and the deformation of floating collar, net and mooring lines. The floating collar can be propelled above the water surface due to the impact of the waves. The net oscillates along the wave crest and gradually regains its shape under the influence of wave troughs. Mooring lines serve to maintain the operational range of the aquaculture system.

4 Conclusions

This study integrated a lumped-mass based mooring dynamics model, MoorDyn and a finite-element structural solver, EndoBeams with our previous developed OpenFOAM formulation to simulate the complex dynamic response of aquaculture systems in flow. A series of validations have confirmed the ac-

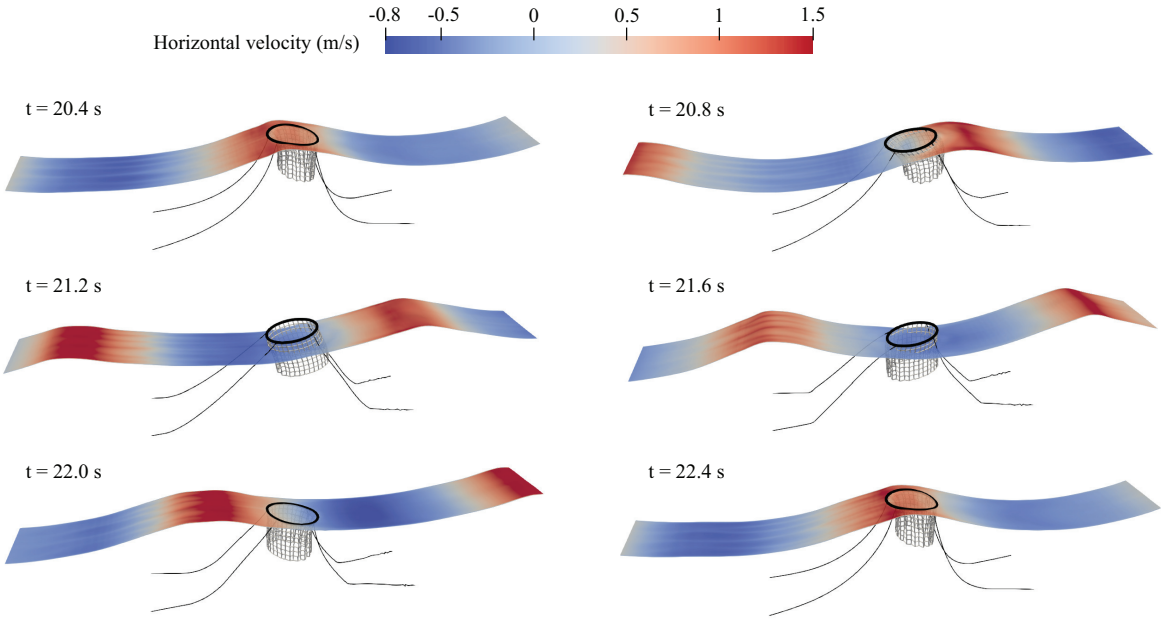

Figure 4: Sketch of a aquaculture system.

curacy of the current numerical framework. The present numerical framework can serve as a suitable tool for investigating the motion and deformation of various components within aquaculture systems under different wave or current conditions, and it can be used to help improve the design of deep-sea aquaculture structures.

Acknowledgments

The first author thanks CSC and QMUL for supporting his Ph.D. studentship.

REFERENCES

[1] Mi, Shuo, et al. An implicit Eulerian–Lagrangian model for flow-net interaction using immersed boundary method in OpenFOAM. *Ocean Engineering*. 264 (2022): 112843.

[2] Hall, Matthew, et al. Validation of a lumped-mass mooring line model with DeepCwind semisubmersible model test data. *Ocean Engineering*. 104 (2015): 590-603.

[3] Bisighini, Beatrice, et al. EndoBeams. jl: A Julia finite element package for beam-to-surface contact problems in cardiovascular mechanics. *Advances in Engineering Software*. 171 (2022): 103173.

[4] Cardia, F., Lovatelli, A., 2015. Aquaculture operations in floating hdpe cages. *Rome: FAO and Ministry of Agriculture of the Kingdom of Saudi Arabia*.

[5] Weller, H.G., Tabor, G., Jasak, H., Fureby, C., 1998. A tensorial approach to computational continuum mechanics using object-oriented techniques. *Computers in physics*. 12, 620–631.

[6] Uhlmann, M., 2005. An immersed boundary method with direct forcing for the simulation of particulate flows. *Journal of computational physics*. 209, 448–476

UKACM 2024 Conference, 10-12 April 2024, Durham University, Durham, UK
https://doi.org/10.62512/conf.ukacm2024.078

ISOGEOMETRIC ANALYSIS FOR BIM-BASED DESIGN AND SIMULATION OF SUB-RECTANGULAR TUNNEL

Hoang-Giang Bui[1*], Tai-Tien Nguyen[3], Van-Vi Pham[3], Ngoc-Anh Do[3], Ba-Trung Cao[4], Jelena Ninić[2*]

[1] Institute of Material Systems Modeling, Helmholtz-Zentrum Hereon, Germany.
giang.bui@hereon.de
[2] School of Engineering, University of Birmingham, UK.
Corresponing author: j.ninic@bham.ac.uk
[3] Department of Underground and Mining Construction, Faculty of Civil Engineering, Hanoi University of Mining and Geology, Hanoi, Vietnam.
nado1977bb@gmail.com
[4] Insitute of Structural Mechanics, Ruhr University Bochum, Germany.
ba.cao@rub.de

Abstract. The design and analysis of segmental tunnel lining is today often based on empirical solutions with simplified assumptions. This work showcases the application of Isogeometric Analysis (IGA) for computationally efficient simulations of tunnel linings [1, 2]. In our past research, we developed a design-through-analysis procedure that consists of i) parametric modeling of the segmented tunnel lining; ii) development of an IGA computational framework, iii) reconstruction of the BIM lining model for IGA analysis, and iv) simulation model for lining including a reconstructed IGA model, contact interfaces between the joints, and a non-linear soil-structure interaction model based on the Variational Hyperstatic Reaction Method (VHRM) [3].In this paper, we extend our method for the analysis of sub-rectangular tunnel linings and demonstrate its efficiency using the example of the Shanghai express tunnel. The advantage of our novel method is the flexibility in adapting the tunnel alignment with the help of NURBS/CAD technology. Employing the high-order geometry definition, convergence of the mesh refinement procedure can be obtained with much faster rate. As a result, the modelling effort and computational time are reduced significantly. Moreover, this approach allows to capture the bending moment with better regularity. The combination with an existing BIM modelling approach via geometry reconstruction leads to a very efficient framework for tunnel lining analysis and design.

Key words: *Sub-rectangular Tunnel Linings; Isogeometric Analysis; BIM*

1 Introduction

With a continuously increasing population, urban planners require novel approaches to address societal problems such as congestion, noise, and polution; and underground transportation systems are an optimal solution in terms of carbon emissions, energy consumption, and noise levels. In the last decades, the design and assessment of the stability and robustness of the tunnel structure has been one of the key tasks to ensure a safe and durable underground infrastcture design to withstand demanding use for up to 100 years. Since both planning and design phase require analysis, modelling, visualization, and numerical analysis, different tools such as Building Information Modelling (BIM) and numerical analysis software are used to perform these tasks. However, in current engineering practice, there are no systematic solutions for the exchange between design and analysis models, and these tasks usually involve manual and error-prone model generation in different tools.

To address these shortcomings, we developed a BIM-based approach that connects a user-friendly industry-standard BIM software with effective simulation tools for high-performance computing [2, 1]. A fully automatized design-through-analysis workflow solution for segmented tunnel lining is developed based on a fully parametric design model realized as a Revit plugin and an isogeometric B-Rep analysis software (IBRA), connected through an interface implemented with the Revit plugin Dynamo (see Figure 1). In our approach, the fully parametric design model for 3D segmented tunnel lining for arbitrary tunnel alignments is developed based on the so-called universal ring approach. Moreover, we devised a higher-order finite element method based on isogeometric analysis (IGA) and employed it to analyse the forces in the lining segment with high resolution. Finally, we created a robust interface from the design model to the analysis tool for i) the reconstruction of NURBS with trivariate representation suitable for IGA analysis from the original boundary representation using the trimmed NURBS model of the lining segment, and ii) generation of the simulation script based on semantic data extracted from the BIM model (e.g. tunnel depth, material parameters, water level, etc.) and automatic execution of the analysis.

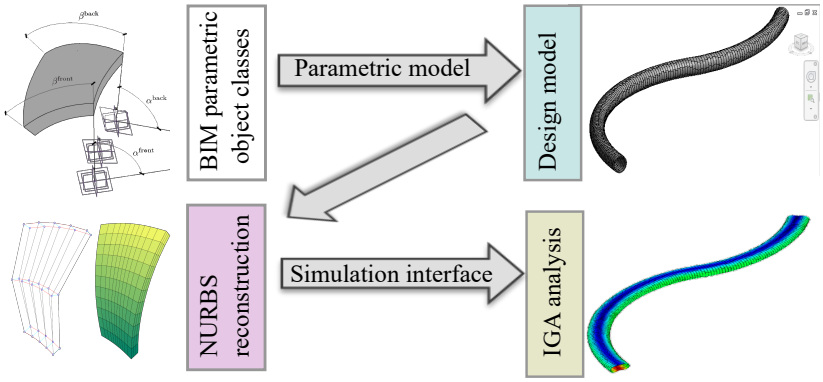

Figure 1: Design-through-analysis workflow for BIM-IGA assessment of the tunnel lining.

In this work, we extend our BIM-IGA approach to investigate the performance of IGA-VHRM for the analysis of sub-rectangular tunnel. We aim to simulate the interaction between the tunnel and surrounding soils under dynamics loading condition, i.e. seismic analysis. In the first step, the geometry of the tunnel is constructed using NURBS volumes. In the analysis phase, we employ the Isogeometric Analysis (IGA) concept in combination with the Variationally Hyperstatic Reaction Method (VHRM) approach to obtain higher computing performance and accuracy. This approach is first validated with statics analysis, in which the typical vertical geotechnical loading condition based on K_0 is assumed. For dynamics analysis, we perform validation using a simplified loading scheme based on [4].

2 Problem description

The (V-)HRM approach characterizes the interaction between the underground structure, i.e. tunnel and surrounding soils using nonlinear springs applied on the soil-structure interface. The internal forces on the springs are

$$\begin{aligned} r_n &= \chi p_{n,lim} \ln(p_{n,lim} + \eta_{n,0}\delta_n), \\ r_s &= \chi p_{s,lim} \ln(p_{s,lim} + \eta_{s,0}\delta_s), \\ r_t &= \chi p_{t,lim} \ln(p_{t,lim} + \eta_{t,0}\delta_t). \end{aligned} \tag{1}$$

In Eq. (1), the factor χ facilitates the calibration of the interaction against various factors, e.g. constitutive relationship. Moreover, it allows to match the results with classical HRM based on fixed-point iteration. The consistent linearization of the springs forces enables quadratic convergence when the Newton-Raphson iteration is used [3].

The structure and design of the sub-rectangular tunnel, including the boundary condition under statics loading condition, are presented in Fig. 2 (a). The sub-rectangular structure is characterized by segmental arcs, connected at the joints. The profile of the curve is of C_1 continuity.

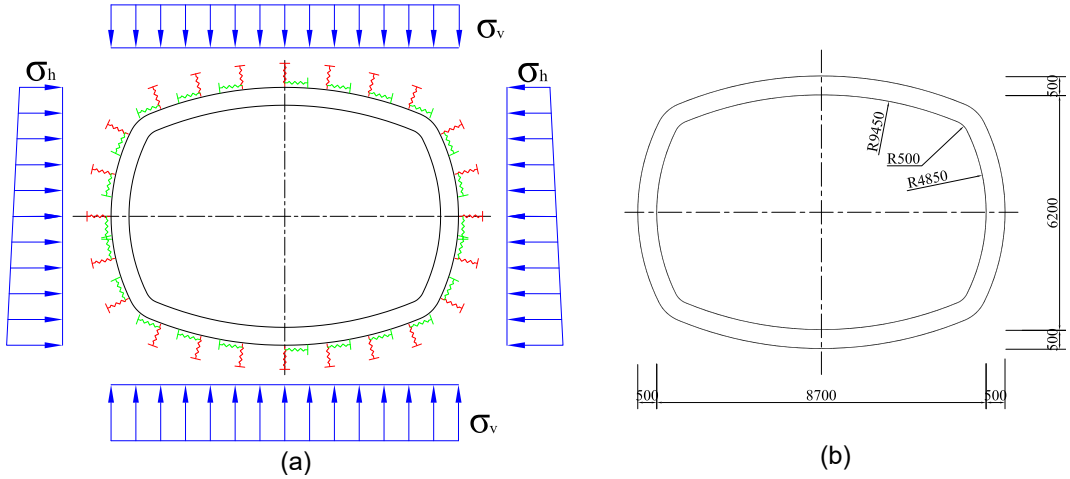

Figure 2: (a) Geometry and loading condition of sub-rectangular tunnel (b) Dimensions of the Shanghai express tunnel.

The geometry of the tunnel is constructed using NURBS volumes. The advantage of this approach is twofold: Firstly, the geometrical arcs of the sub-rectangular structure can be constructed precisely using quadratic NURBS. Secondly, the refinement of the control mesh is straightforward and does not alter the geometry; meanwhile, it improves the accuracy of the finite element solution. The NURBS volume is an extension of B-splines volume, which reads

$$\mathbf{V}(\xi_1,\xi_2,\xi_3) = \sum_{i=0}^{n}\sum_{j=0}^{m}\sum_{k=0}^{l} N_i^p(\xi_1)\,N_j^q(\xi_2)\,N_k^r(\xi_3)\,\mathbf{P}_{ijk} \tag{2}$$

in which N_i^p are the B-splines basis functions and $\mathbf{P}_{ijk}$ are the control points in Cartesian coordinates. A NURBS volume is obtained by using homogeneous coordinates for $\mathbf{P}_{ijk}$ [1].

3 Numerical results

The computational approach is used to analyse the deformation of the Shanghai express tunnel [4] under static loading condition. The dimensions of the tunnel are depicted in Fig. 2 (b).

The analysis results are shown in Fig. 3 (right). We note that due to the special design of the tunnel, there is a high degree of stress concentration at the corners. Nevertheless, the structure of the tunnel allows for better width-per-dimension usage ratio compared with a traditional tunnel using circular section.

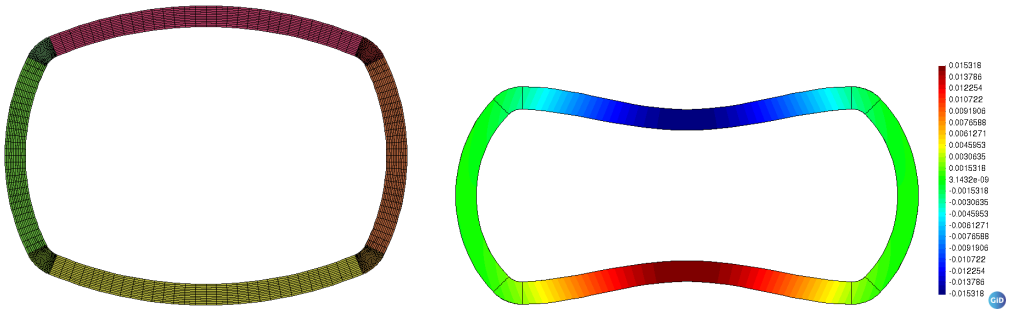

Figure 3: Displacement results of analysis with sub-rectangular tunnel. Left: undeformed structure; Right: deformed structure (scale = 100).

4 Conclusions

We propose an approach for analysis of non-circular tunnels. This approach combines the advantage of higher-order discretization method, i.e. IGA, with the simplicity and flexibility of VHRM to evaluate the deformation and internal forces of the sub-rectangular lining. In the first step, the statics analysis is performed to quantify the performance of the lining under a typical loading scenario. The extension to seismics analysis can be performed by using implicit dynamics or by using a simplified loading profile, as proposed in [4]. This is subject to further investigation. Future work includes segmental lining design and adding the interior columns.

Acknowledgments

Financial support by the German Science Foundation (DFG) (Project number 518862444) and Vietnam National Foundation for Science and Technology Development (NAFOSTED) (Project number DFG.105-2022.03) is gratefully acknowledged.

REFERENCES

[1] Bui et al, Integrated BIM-based Modelling and Simulation of Segmental Tunnel Lining by means of Isogeometric Analysis, *Finite Elements in Analysis and Design* (2023) **229**:104070.

[2] Ninic et al, BIM-to-IGA: A fully automatic design-through-analysis workflow for segmented tunnel linings, *Advanced Engineering Informatics* (2024) **46**:101137.

[3] Bui et al, A variationally consistent hyperstatic reaction method for tunnel lining design, *International Journal for Numerical and Analytical Methods in Geomechanics* **46**:205–217.

[4] Do et al, A new pseudo-static loading scheme for the hyperstatic reaction method - case of sub-rectangular tunnels under seismic conditions, *Sustainable and Resilient Infrastructure* **8**:340–356.

UKACM 2024 Conference, 10-12 April 2024, Durham University, Durham, UK
https://doi.org/10.62512/conf.ukacm2024.093

A Comparative Study of Electric and ICE Vehicle Suspension System for Vehicle-Bridge Interaction Dynamics

Kaustubh Deepak Kasle[1*], Shankar Krishnapillai[1], BN Rao[2]

[1] Machine Design Section, Department of Mechanical Engineering,
Indian Institute of Technology Madras, Chennai - 600036, India
kaustubhdkasle@gmail.com, skris@iitm.ac.in
[2] Structural Engineering Division, Department of Civil Engineering,
Indian Institute of Technology Madras, Chennai - 600036, India
bnrao@iitm.ac.in

Abstract

The suspension system plays a crucial role in vehicle dynamics, impacting ride comfort and safety. As electric vehicles (EVs) gain prominence as the future of transportation, understanding their unique dynamic behaviour becomes essential since they differ in mass and weight distribution from a similar conventional petrol-powered vehicle. The study is based on vehicle-bridge interaction dynamics where a vehicle while traversing on a bridge, induces structural vibrations that subsequently propagate feedback responses to the vehicle. A system of half car model (HCM) passing over a bridge is mathematically modelled and dynamics for both the vehicles is analysed, and the ride parameters are compared against each other. The HCM of the EV has 4 degrees of freedom (DOF), while the ICE vehicle has 5 DOF due to the consideration of on-board loads specific to internal combustion engine vehicles which induces high-frequency vibrations in the vehicle. The bridge is modelled as a simply supported Euler-Bernoulli beam and modal analysis is carried out to simplify the system. Additionally, road disturbances are taken into account which are caused by a standard speed breaker followed by class C road roughness adhering to international standards. The system of coupled equation is solved using MATLAB Simulink by applying the Runge Kutta numerical method.

Keywords: *Electric Vehicle; Half Car Model; Suspension System; Vehicle-Bridge Interaction.*

1 Introduction

The suspension system of a vehicle, consisting of springs, shock absorbers and linkages, isolates the vehicle body from the road disturbances and maintains a good contact between the tyre and road surface, thus playing a very crucial role when it comes to the comfort and safety of the passenger [1]. Electric vehicle (EV) being the future of transportation, it is important to study the unique dynamic behaviour of its suspension system. In conventional cars, the internal combustion engines (ICE) are mostly located in the front of vehicles and the centre of gravity (CG) of vehicles is biased forward, while in an EV due to the presence of batteries the CG is towards the centre and weight distribution is done effectively [2]. Moreover, the on-board loads due to the engine present in an ICE vehicle induces high frequency vibration in the overall system [3]. These forces are due to the reciprocating pistons present in the ICE, specifically in a 4-cylinder 4-stroke in-line engine which generate secondary unbalanced shaking/inertia force. In vehicle-bridge interaction dynamics, the passing vehicle excites bridge vibrations and these responses are simultaneously transmitted to the vehicle thus affecting the dynamic behaviour of the vehicle while traversing [4]. In this study, following are the novel contributions. A half car model (HCM) for an ICE vehicle, including secondary unbalanced forces is mathematically modelled and a relatively complex, vehicle-bridge interaction system is studied where the bridge includes road roughness and a sinusoidal bump. Additionally, a comparison of an equivalent EV model moving over this type of complex bridge is done.

2 Problem description

The HCM of the ICE (petrol-powered) vehicle has 5 degrees of freedom (DOF) because the ICE is considered as a separate lumped mass to include the secondary unbalanced forces and it is attached to the sprung mass of the vehicle using engine mounts while the HCM of the EV has only 4 DOF since the electric motor of the EV has comparatively negligible vibrations. Here, bridge is assumed as a simply supported Euler-Bernoulli beam having a sinusoidal bump of height 75 mm and chord length of 400 mm in the beginning and random road roughness of class C across the length of the bridge which is generated according the ISO 8608:2016 [5].

The equations of motion for this HCM are given below. Eqs. (1) and (2) represents the vertical displacement and pitching moment of the sprung mass respectively, while Eqs. (3) and (4) represents the vertical displacement of the front and rear unsprung masses respectively.

$$\ddot{Y} = \frac{1}{m_s}\left[\, k_1(y_1 - Y_1) + c_1(\dot{y}_1 - \dot{Y}_1) + k_2(y_2 - Y_2) + c_2(\dot{y}_2 - \dot{Y}_2) - k_m\left(Y_1 - y_{eng}\right) - c_m\left(\dot{Y}_1 - \dot{y_{eng}}\right)\right] \tag{1}$$

$$\ddot{\theta} = \frac{1}{J}\left[\, k_1(y_1 - Y_1).a_1 + c_1(\dot{y}_1 - \dot{Y}_1).a_1 - k_2(y_2 - Y_2).a_2 - c_2(\dot{y}_2 - \dot{Y}_2).a_2 - F_e.a_1\,\right] \tag{2}$$

$$\ddot{y_1} = \frac{1}{m_1}\left[\, k_{t1}\,(r_1 - y_1) - k_1(y_1 - Y_1) - c_1(\dot{y}_1 - \dot{Y}_1)\,\right] \tag{3}$$

$$\ddot{y_2} = \frac{1}{m_2}\left[\, k_{t2}(r_2 - y_2) - k_2(y_2 - Y_2) - c_2(\dot{y}_2 - \dot{Y}_2)\,\right] \tag{4}$$

Eq. (5) represents the vertical displacement of the engine mass.

$$\ddot{y_{eng}} = \frac{1}{m_{eng}}\left[\, k_m\left(Y_1 - y_{eng}\right) + c_m\left(\dot{Y}_1 - \dot{y_{eng}}\right) - F_{eng}\right] \tag{5}$$

Where,

$$Y_1 = Y + \theta.a_1\ ,\ Y_2 = Y - \theta.a_2 \quad and \quad F_e = k_m\,(\,Y_1 - y_{eng}\,) + c_m\left(\,\dot{Y}_1 - \dot{y_{eng}}\,\right)$$

Note that r_1 and r_2 are the road inputs given to the front and rear tyre of the ICE vehicle respectively. Similarly, equations of motion for the EV are formulated. Both the vehicles are chosen in such a way that they have similar power, same seating capacity and dimensions. Parameters for the vehicle are acquired from the car manufacturer website [6]. For bridge, Eq. (6) represents the equation of motion.

$$EI\,\frac{\partial^4 y}{\partial x^4} + m\,\frac{\partial^2 y}{\partial t^2} = f_{c1}(t)\,\delta(x - vt) + f_{c2}(t)\,\delta(x - (vt - a)) \tag{6}$$

Where, f_{c1} and f_{c2} are contact forces and $\delta(x - vt)$ is the dirac delta function. Modal Analysis of the beam is carried out and first 5 modes are considered for simulation. Parameters for the bridge are acquired from reference [4]. The road disturbance due to a sinusoidal bump followed by class C road roughness is generated using MATLAB Simulink. All the calculations are done assuming the vehicle to be moving with constant velocity of 20 kmph. Figs. 1 and 2 represent the HCM of an ICE vehicle moving over a bridge and generated road excitation which is given to the cars as input, respectively. The symbols used in the above equations are mentioned in Fig. 1. Note that a dot as an accent mark represents differentiation with respect to time.

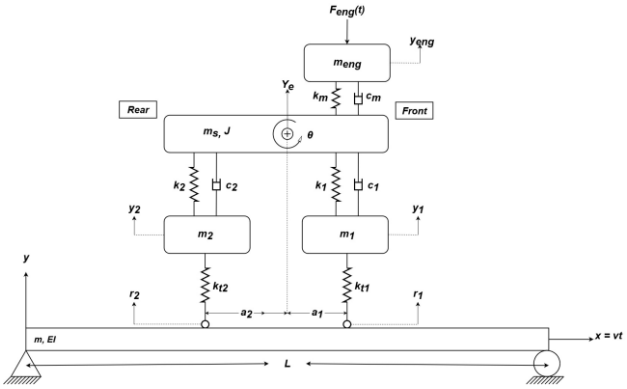

Figure 1: HCM of ICE vehicle moving over a bridge.

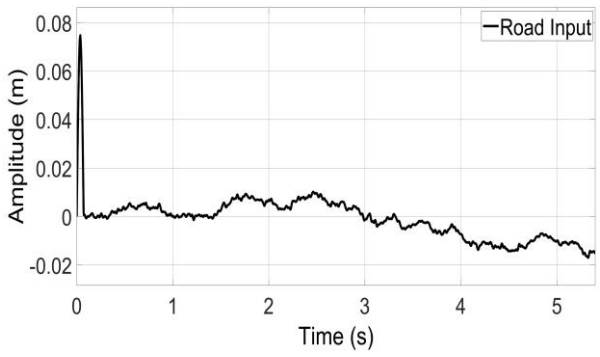

Figure 2: Road excitation due to sine bump and class C road roughness

The system of coupled equations is solved using the MATLAB Simulink package by applying the Runge-Kutta numerical method. Dynamic behaviour of both the car is studied is studied and compared in terms of the ride parameters like peak overshoot, pitching and vertical acceleration of the sprung mass and tyre displacement relative to the road excitation. Acceleration of the sprung mass indicates the ride comfort, where more the value less is the comfort [7]. Whereas road holding ability of the vehicle is given by road holding ratio which is a ratio of dynamic force generated on the tyre to the static force on that tyre, and the dynamic force depends upon the vertical displacement of the tyre. A ratio equal to or more that 1 indicates that the tyre has lost the contact with the ground [8], thus more the value less is the road holding ability.

3 Results and discussion

Figs. 3, 4 and 5 represent the vehicle responses for the vertical displacement, pitching and vertical acceleration of the sprung mass respectively and figs. 6 and 7 represent the displacement of front and rear tyre/unsprung mass respectively relative to the road excitation. Table. 1 shows the numerical values of these responses. It is observed that the suspension system of the EV outperforms that of the ICE vehicle when it comes to ride comfort and road holding and it is 5.4% and 7.55% better than that of the ICE vehicle respectively. Also, the maximum displacement of the EV is 11.76% less than the ICE vehicle and the pitching moment is seen 4.22% better in ICE vehicle.

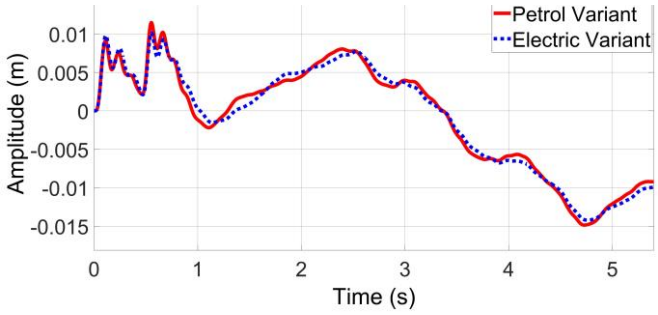

Figure 3: Vertical displacement of the sprung mass

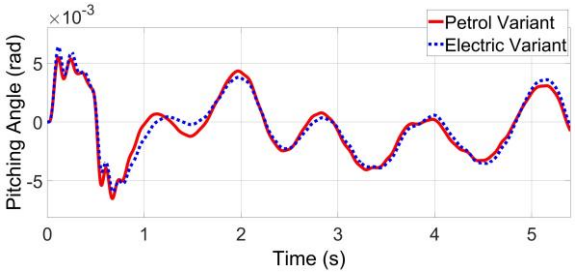

Figure 4: Pitching of the sprung mass

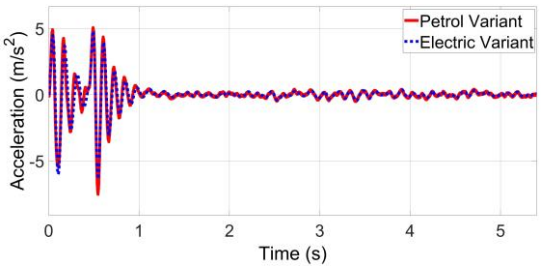

Figure 5: Vertical acceleration of the sprung mass

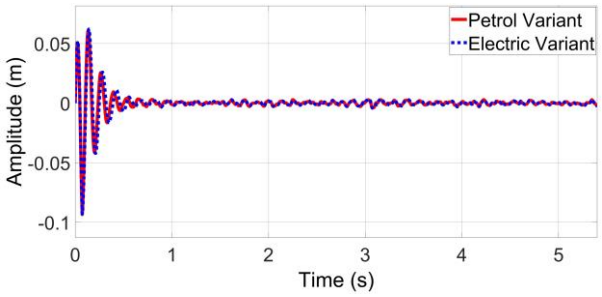

Figure 6: Vertical displacement of front unsprung mass

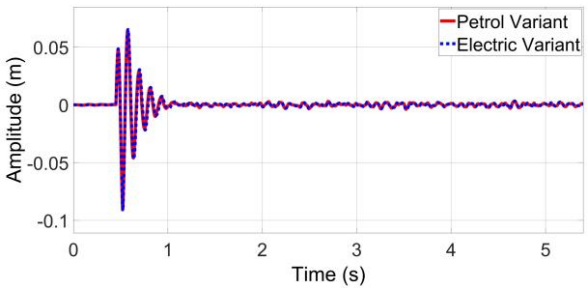

Figure 7: Vertical displacement of rear unsprung mass

Table 1. Numerical values of the responses.

Sr. No.	Variant	Maximum Displacement (m)	P2P Pitching Angle (deg)	RMS of Acceleration (m/s2)	RMS of Road Holding Ratio
1.	Petrol	0.01148	0.68 (4.22% Better)	1.091	0.4807
2.	Electric	0.01013 (11.76% Better)	0.71	1.032 (5.4% Better)	0.4444 (7.55% Better)

4 Conclusion

It can be concluded that the dynamic behaviour of the current EV model is more favourable when compared to the conventional ICE vehicle. The ride comfort and the road holding ability of the EV is observed 5.4% and 7.55% better as compared to the ICE vehicle, respectively. Also, the peak overshoot for the sprung mass is 11.76% better for the EV. However, for pitching moment the ICE vehicle proves to be better than the EV where the peak-to-peak angle of the ICE vehicle is 4.22% less than that of the EV. This is observed due to various factors, with the location of the centre of gravity being the most significant one. Weight distribution in EV is better than the ICE vehicle as it lies more towards the centre and bottom of the vehicle due to the placement of batteries in the floor making the vehicle more stable. Whereas in ICE vehicle, the engine is placed in the front which shifts the CG towards the front of the vehicle. Moreover, the onboard forces due to the engine in ICE vehicle marginally affects the overall dynamic behaviour of the car.

References

[1] A. Agharkakli, G. S. Sabet, and A. Barouz, “Simulation and Analysis of Passive and Active Suspension System Using Quarter Car Model for Different Road Profile,” *Int. J. Eng. Trends Technol.*, vol. 3, no. 5, pp. 636–644, 2012.

[2] P. Wang, “Effect of electric battery mass distribution on electric vehicle movement safety,” *Vibroengineering Procedia*, vol. 33, pp. 78–83, 2020, doi: 10.21595/vp.2020.21569.

[3] R. Jayachandran and S. Krishnapillai, “Modeling and optimization of passive and semi-active suspension systems for passenger cars to improve ride comfort and isolate engine vibration,” *JVC/Journal Vib. Control*, vol. 19, no. 10, pp. 1471–1479, 2013, doi: 10.1177/1077546312445199.

[4] J. P. Yang, “Theoretical Formulation of Three-Mass Vehicle Model for Vehicle-Bridge Interaction,” *Int. J. Struct. Stab. Dyn.*, vol. 21, no. 7, pp. 1–8, 2021, doi: 10.1142/S0219455421710048.

[5] V. Assets, J. Stevens, and I. S. O. S. Order, “INTERNATIONAL STANDARD ISO Mechanical vibration — Road surface profiles — Reporting of measured data,” vol. 2016, 2016.

[6] “Tata Motors,” 2023. https://cars.tatamotors.com/

[7] C. S. Dharankar, M. K. Hada, and S. Chandel, “Performance improvement of passive suspension of vehicles using position dependent damping,” *Int. J. Veh. Perform.*, vol. 4, no. 1, pp. 89–111, 2018, doi: 10.1504/ijvp.2018.088802.

[8] M. Ataei, E. Asadi, A. Goodarzi, A. Khajepour, and M. B. Khamesee, “Multi-objective optimization of a hybrid electromagnetic suspension system for ride comfort, road holding and regenerated power,” *JVC/Journal Vib. Control*, vol. 23, no. 5, pp. 782–793, 2017, doi: 10.1177/1077546315585219.

Finite Element and Meshless Methods in Deformation Analysis

UKACM 2024 Conference, 10-12 April 2024, Durham University, Durham, UK
https://doi.org/10.62512/conf.ukacm2024.055

Peridynamics: Past, Present and Future

Erkan Oterkus[1*], Selda Oterkus[2]

[1] Department of Naval Architecture, Ocean, and Marine Engineering, University of Strathclyde, Glasgow, G1 1QN, UK.
erkan.oterkus@strath.ac.uk

[2] Department of Naval Architecture, Ocean, and Marine Engineering, University of Strathclyde, Glasgow, G1 1QN, UK.
selda.oterkus@strath.ac.uk

Abstract

In order to determine the deformation response of materials and structures subjected to external loading conditions, classical continuum mechanics (CCM) was introduced by disregarding the atomistic structure. CCM has been successfully applied to numerous challenging problems. However, its governing equation faced a difficulty when there is any discontinuity in the structure such as a crack, since spatial partial derivatives in its governing equation are not defined for such a condition. To overcome this problem, a new continuum mechanics approach, Peridynamics (PD), was recently introduced with the intention that PD equations remain always valid whether there is any discontinuity in the structure or not. This character of PD makes this new approach a powerful tool for predicting crack initiation and propagation. Moreover, PD can be considered as the continuum version of molecular dynamics. Therefore, PD can be a suitable candidate for multi-scale analysis of materials. Furthermore, PD formulation can also be extended to other fields such as thermal diffusion, moisture diffusion, etc., so that it can be used as a single platform for multiphysics analysis of materials and structures with damage prediction capability. Hence, in this study, a brief information about peridynamics will be provided by covering past developments, presenting current progress, and highlighting potential future research directions.

Key words: *Peridynamics; fracture; non-local; continuum mechanics; multiscale; multiphysics*

1 Introduction

In order to determine the deformation response of materials and structures subjected to external loading conditions, classical continuum mechanics (CCM) was introduced by disregarding the atomistic structure. CCM has been successfully applied to numerous challenging problems. However, its governing equation faced a difficulty when there is any discontinuity in the structure such as a crack, since spatial partial derivatives in its governing equation are not defined for such a condition. To overcome this problem, a new continuum mechanics approach, Peridynamics (PD), was recently introduced with the intention that PD equations remain always valid whether there is any discontinuity in the structure or not. This character of PD makes this new approach a powerful tool for predicting crack initiation and propagation. In this study, a brief history of peridynamics and its formulation is given in the following sections.

2 Brief History of Peridynamics

The term “peridynamics” is a combination of two words “peri” and “dynamics” in Greek language. “peri” represents surrounding or horizon, i.e. influence domain in peridynamics, whereas “dynamics” represents force. There are some similarities between peridynamics and other existing continuum mechanics formulations. Amongst these Navier’s continuum mechanics formulation is based on interaction forces between molecules which are similar to peridynamic forces between material points. After establishing equations of motion in integro-differential equation form, Navier converted them to partial differential equation form using Taylor’s expansion. Kroner [1], who introduced the term “nonlocal”, proposed a new continuum mechanics formulation which contains both classical and nonlocal terms in its equations of motion. Rogula’s continuum mechanics formulation [2] is similar to original bond-based peridynamics formulation but without considering failure. dell’isola et al. [3] also mentioned that peridynamic formulation has similarities to the continuum mechanics formulation studied by Piola.

First peridynamic code, EMU, was developed at Sandia National Laboratories (USA). It has a capability of simulating wide range of problems. Although peridynamics is a continuum mechanics formulation, if its equations of motion are written in discrete form based on meshless approach, the form of these equations appears to be similar to the equations of motion used in molecular dynamics. Therefore, PD can be considered as the continuum version of molecular dynamics. There are already available various molecular dynamics codes. By using the analogy between molecular dynamics and peridynamics, peridynamic simulations can now be performed in one of the widely used molecular dynamics software, LAMMPS, developed at Sandia National Laboratories [4].

As mentioned earlier, there are fundamental differences between classical continuum mechanics and peridynamics. However, it is possible to implement peridynamics in a commercial finite element analysis framework [5]. To achieve this, first nodes are created to represent material points of peridynamics. Next, link elements or spring elements are introduced between nodes if they are within the horizon of each other. Note that the properties of link elements or spring elements are specified in a way that they correspond to a peridynamic bond. To represent failure, elements can be assumed to be broken if a particular failure criterion is satisfied.

Although peridynamics was introduced mainly for structural analysis, the formulation has been extended to other fields. It is now possible to perform thermal analysis [6], moisture analysis [7], computational fluid dynamics analysis [8], etc. by using peridynamics. It is also possible to determine the effect of different physical fields on each other. Therefore, multiphysics analysis can be done in a single peridynamic framework with damage prediction capability. This allows investigation of complex problems such as lightning strike on airplanes, popcorn cracking in electronic packages, cracking in nuclear pellets, etc.

It is also possible to perform multiscale analysis by using peridynamics. The length scale parameter of peridynamics, horizon, can be used to represent physical situations which cannot be properly represented by using classical approaches. These cases usually show themselves at very small scales due to molecular interactions. By properly calibrating the horizon parameter, peridynamics can be used to model materials at small scales. Moreover, peridynamic homogenisation can be utilised to determine homogenised properties of materials which contain defects at microstructure such as microvoids and microcracks.

The first journal paper on peridynamics appeared in 2000 by Silling [9]. Following this study, Silling and Askari [10] published a very important article describing the numerical implementation of peridynamics. The original peridynamic formulation, named as “bond based peridynamics”, has some limitations especially for the definition of material properties. To overcome this problem, Silling et al. [11] introduced “state” concept which led to state-based peridynamic formulation. First PhD thesis on peridynamics was completed at MIT in 2005 by Zimmerman [12]. He investigated a new continuum theory with long-range forces for solids. One year later, another PhD thesis was completed at Caltech by Dayal [13] and he studied nonlocal microstructural mechanics of active materials. The first book on peridynamics was written by Madenci and Oterkus [14]. A new journal, Journal of Peridynamics and Nonlocal Modeling, was also established in 2019 to present the latest developments in peridynamics research. During the same year, the world’s first research centre, PeriDynamics Research Centre (PDRC), was established at University of Strathclyde, Glasgow. There has been a significant increase in number of publications on peridynamics especially during the recent years. An extensive review of peridynamic publications can be found in Javili et al. [15].

3 Peridynamic Formulation

Peridynamics is a new continuum mechanics formulation. Therefore, the body is composed of infinitely small volumes called material points. Equation of motion in peridynamics can be expressed as

$$\rho(\mathbf{x})\ddot{\mathbf{u}}(\mathbf{x},t)=\int_{H}\left(\mathbf{t}\left(\mathbf{u}'-\mathbf{u},\mathbf{x}'-\mathbf{x},t\right)-\mathbf{t}'\left(\mathbf{u}-\mathbf{u}',\mathbf{x}-\mathbf{x}',t\right)\right)dH+\mathbf{b}(\mathbf{x},t) \tag{1}$$

which can also be written in discrete form as

$$\rho_{(k)}\ddot{\mathbf{u}}_{(k)}=\sum_{j=1}^{\infty}\left[\mathbf{t}_{(k)(j)}\left(\mathbf{u}_{(j)}-\mathbf{u}_{(k)},\mathbf{x}_{(j)}-\mathbf{x}_{(k)},t\right)-\mathbf{t}_{(j)(k)}\left(\mathbf{u}_{(k)}-\mathbf{u}_{(j)},\mathbf{x}_{(k)}-\mathbf{x}_{(j)},t\right)\right]V_{(j)}+\mathbf{b}_{(k)} \tag{2}$$

where ρ is the density of a material point, **x** is the original location of a material point, **u** represents the displacement of a material point, **b** is the body load of a material point, and *t* is time. ".." represents second derivative with respect to time. Force densities between two material points can be expressed as

$$\mathbf{t}_{(k)(j)}\left(\mathbf{u}_{(j)}-\mathbf{u}_{(k)},\mathbf{x}_{(j)}-\mathbf{x}_{(k)},t\right)=\frac{1}{2}A\frac{\mathbf{y}_{(j)}-\mathbf{y}_{(k)}}{\left|\mathbf{y}_{(j)}-\mathbf{y}_{(k)}\right|} \tag{3}$$

with the constant *A* defined as

$$A=4w_{(k)(j)}\left\{ad\left(\frac{\mathbf{y}_{(j)}-\mathbf{y}_{(k)}}{\left|\mathbf{y}_{(j)}-\mathbf{y}_{(k)}\right|}\cdot\frac{\mathbf{x}_{(j)}-\mathbf{x}_{(k)}}{\left|\mathbf{x}_{(j)}-\mathbf{x}_{(k)}\right|}\right)\theta_{(k)}+b\left(\left|\mathbf{y}_{(j)}-\mathbf{y}_{(k)}\right|-\left|\mathbf{x}_{(j)}-\mathbf{x}_{(k)}\right|\right)\right\} \tag{4}$$

and

$$\mathbf{t}_{(j)(k)}\left(\mathbf{u}_{(k)}-\mathbf{u}_{(j)},\mathbf{x}_{(k)}-\mathbf{x}_{(j)},t\right)=-\frac{1}{2}B\frac{\mathbf{y}_{(j)}-\mathbf{y}_{(k)}}{\left|\mathbf{y}_{(j)}-\mathbf{y}_{(k)}\right|} \tag{5}$$

with the constant *B* defined as

$$B=4w_{(j)(k)}\left\{ad\left(\frac{\mathbf{y}_{(k)}-\mathbf{y}_{(j)}}{\left|\mathbf{y}_{(k)}-\mathbf{y}_{(j)}\right|}\cdot\frac{\mathbf{x}_{(k)}-\mathbf{x}_{(j)}}{\left|\mathbf{x}_{(k)}-\mathbf{x}_{(j)}\right|}\right)\theta_{(j)}+b\left(\left|\mathbf{y}_{(k)}-\mathbf{y}_{(j)}\right|-\left|\mathbf{x}_{(k)}-\mathbf{x}_{(j)}\right|\right)\right\} \tag{6}$$

Note that **y** represents the current location of a material point. The peridynamic dilatation can be defined as

$$\theta_{(k)}=d\sum_{j=1}^{\infty}w_{(k)(j)}s_{(k)(j)}\frac{\mathbf{y}_{(j)}-\mathbf{y}_{(k)}}{\left|\mathbf{y}_{(j)}-\mathbf{y}_{(k)}\right|}\cdot\left(\mathbf{x}_{(j)}-\mathbf{x}_{(k)}\right)V_{(j)} \tag{7}$$

and the stretch term can be expressed as

$$s_{(k)(j)}=\frac{\left(\left|\mathbf{y}_{(j)}-\mathbf{y}_{(k)}\right|-\left|\mathbf{x}_{(j)}-\mathbf{x}_{(k)}\right|\right)}{\left|\mathbf{x}_{(j)}-\mathbf{x}_{(k)}\right|} \tag{8}$$

The influence function can be defined as

$$w_{(k)(j)}=\frac{\delta}{\left|\mathbf{x}_{(j)}-\mathbf{x}_{(k)}\right|} \tag{9}$$

where δ is the horizon size. The constants, *a*, *b*, and *d*, can be expressed as

$$a=\frac{1}{2}\left(\kappa-\frac{5\mu}{3}\right) \tag{10}$$

$$b=\frac{15\mu}{2\pi\delta^5} \tag{11}$$

$$d=\frac{9}{4\pi\delta^4} \tag{12}$$

where κ is the bulk modulus and μ is the shear modulus. For brittle materials, if the stretch between two material points exceeds critical stretch, then it is assumed that the bond (interaction) is broken. The critical stretch for isotropic materials can be defined as

$$s_c = \sqrt{\frac{G_c}{\left(3\mu + \left(\frac{3}{4}\right)^4 \left(\kappa - \frac{5\mu}{3}\right)\right)\delta}} \tag{13}$$

where G_c is the critical energy release rate.

4 Conclusions

Peridynamics is a new continuum mechanics formulation. It has several advantages with respect to classical continuum mechanics. It can be used as an alternative approach for both multiphysics and multiscale analysis of materials and structures with damage prediction capability. Potential future directions include additive manufacturing, artificial intelligence & machine learning, and peridynamic differential operator.

Acknowledgments

This material is based upon work supported by the Air Force Office of Scientific Research under award number FA8655-23-1-7037.

References

[1] E. Kröner, (1967). Elasticity theory of materials with long range cohesive forces, *International Journal of Solids and Structures*, 3(5), 731-742.
[2] D. Rogula, (1982). Nonlocal theory of material media, *Springer Vienna*, 123-222.
[3] F. Dell'Isola, U. Andreaus, U., L. Placidi, (2015). At the origins and in the vanguard of peridynamics, non-local and higher-gradient continuum mechanics: an underestimated and still topical contribution of Gabrio Piola, *Mathematics and Mechanics of Solids*, 20(8), 887-928.
[4] M. L. Parks, R. B. Lehoucq, S. J. Plimpton, S. A. Silling, (2008). Implementing peridynamics within a molecular dynamics code, *Computer Physics Communications*, 179(11), 777-783.
[5] R. W. Macek, S. A. Silling, (2007). Peridynamics via finite element analysis, *Finite elements in analysis and design*, 43(15), 1169-1178.
[6] Y. K. Galadima, E. Oterkus, S. Oterkus, (2022). Static condensation of peridynamic heat conduction model. *Mathematics and Mechanics of Solids*, 27(12), 2689-2714.
[7] C. Diyaroglu, S. Oterkus, E. Oterkus, E. Madenci, S. Han, Y. Hwang, (2017). Peridynamic wetness approach for moisture concentration analysis in electronic packages, *Microelectronics Reliability*, 70, 103-111.
[8] C. T. Nguyen, S. Oterkus, E. Oterkus, I. Amin, M. Ozdemir, A. H. El-Aassar, H. Shawky, (2021). Modelling of Eulerian incompressible fluid flows by using peridynamic differential operator. *Ocean Engineering*, 239, 109815.

[9] S. A. Silling, (2000). Reformulation of elasticity theory for discontinuities and long-range forces. *Journal of the Mechanics and Physics of Solids*, 48(1), 175-209.

[10] S. A. Silling, E. Askari, (2005). A meshfree method based on the peridynamic model of solid mechanics. *Computers & structures*, 83(17-18), 1526-1535.

[11] S. A. Silling, M. Epton, O. Weckner, J. Xu, E. Askari, (2007). Peridynamic states and constitutive modeling. *Journal of elasticity*, 88, 151-184.

[12] M. Zimmermann, (2005). A continuum theory with long-range forces for solids, *Massachusetts Institute of Technology*.

[13] K. Dayal, (2007). Nonlocal microstructural mechanics of active materials, *California Institute of Technology*.

[14] E. Madenci, E. Oterkus, (2013). Peridynamic theory and its applications, *Springer New York*.

[15] A. Javili, R. Morasata, E. Oterkus, S. Oterkus, (2019). Peridynamics review, *Mathematics and Mechanics of Solids*, 24(11), 3714-3739.

UKACM 2024 Conference, 10-12 April 2024, Durham University, Durham, UK
https://doi.org/10.62512/conf.ukacm2024.059

Estimate end bearing resistance of a circular foundation using small strain and large deformation finite element modelling

Shujin Zhou[1*], Wangcheng Zhang[1], Ashraf Osman[1]

[1] Department of Engineering, Durham University, Durham, DH1 3LE, UK.
shujin.zhou@durham.ac.uk
wangcheng.zhang@durham.ac.uk, ashraf.osman@durham.ac.uk

Abstract

Accurately predicting the end bearing resistance of the foundation is important for its design and application. This research compares the results of a circular foundation end bearing resistance in uniform clay from small strain finite-element (SSFE) analysis and large-deformation finite-element (LDFE) analysis, with focus on the effect of soil stiffness. Results show that the soil stiffness has little influence on the bearing capacity of a shallow foundation with a shallow failure mechanism; for a deeply buried foundation, however, a deep flow mechanism is developed, and the failure zone is influenced by the soil stiffness. It is found that, for a shallow foundation, artificially increasing the soil stiffness in SSFE analysis allows for obtaining the end bearing capacity at a smaller displacement without sacrificing accuracy; while employing increased soil stiffness for deeply buried foundations may lead to inaccurate results. For penetrating problems, e.g., pile installation and CPT (cone penetration test), SSFE analysis may underestimate the end bearing resistance factor without considering the installation effect.

Key words: *bearing resistance; soil stiffness; small strain finite-element analysis; large-deformation finite-element analysis*

1 Introduction

The bearing capacity problem was initially investigated for a strip (infinitely long) foundation using the plasticity approach [1] and further developed and employed for various shapes of foundation (e.g., circular, square, and rectangular foundations) considering shape factors [2, 3].

Soil stiffness is a crucial factor in many geotechnical applications, such as settlement analysis, cone penetration analysis and so on. Existing publications have indicated that the stiffness of clay soil has no influence on the undrained bearing capacity through small strain finite element (SSFE) analysis [4, 5]. However, some other research has shown that there are significant variations in the bearing capacity of foundations, such as strip footings [6], rectangular foundations [7], and bucket foundations [8], based on large deformation finite element (LDFE) analysis. In summary, significant uncertainty exists, with conflicting evidence regarding how soil stiffness impacts foundation bearing capacity.

This paper presents a numerical study of the end bearing resistance of a circular foundation in uniform clay with SSFE and LDFE analyses, where both shallow and deep foundations are considered. The soil flow mechanism is investigated in detail, and the influence of soil stiffness on the bearing capacity is numerically quantified.

2 Numerical modelling

Both SSFE and LDFE analyses are undertaken in this study to investigate the end bearing resistance of a circular foundation. For large deformation problem, the RITSS method (remeshing and interpolation technique with small strain [9]), falling in the category of Arbitrary Lagrangian and Eulerian (ALE) method, is developed and implemented in the commercial software ABAQUS. The flowchart of RITSS procedure is shown in Figure 1, where the whole analysis is divided into a series of incremental small strain analysis combined with frequent remeshing of the entire domain, followed by updating all field variables (i.e., stresses and material properties) from the old mesh to the new mesh. Small strain analysis is conducted with the foundation pre-embedded at a certain depth, and a displacement of $0.2D$ is set to reach its limit force.

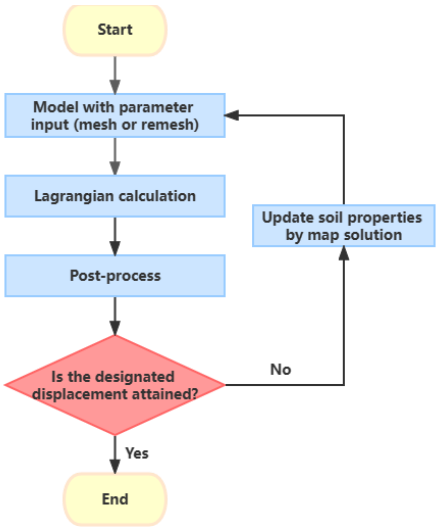

Figure 1: Overall numerical scheme of RITSS.

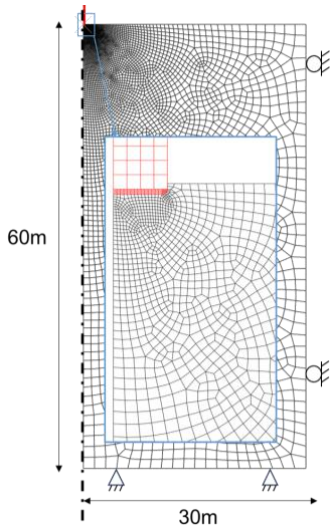

Figure 2: Typical mesh for numerical model.

Numerical model used in this study is shown in Figure 2. The circular foundation has a diameter of D = 1 m, and the largest penetration depth is 20D (to assess variations in end bearing capacity with burial depth). The foundation is simplified as a rigid body. The axisymmetric soil domain is chosen as 30 m in radius and 60 m in depth to minimize the influence of the boundary conditions. Hinge and roller conditions are applied along the base and two sides of the soil domain, respectively. Linear four-node quadrilateral elements (CAX4) with four internal Gauss points are used in the numerical model. A fine mesh is generated around the foundation to ensure the accuracy of end bearing resistance.

The soil is modelled as a linear elastic-perfectly plastic material obeying a Tresca yield criterion. Undrained soil condition is considered with a Poisson's ratio of ν = 0.495 and undrained shear strength s_u = 5 kPa. For simplification, the soil is taken as weightless, and only smooth (i.e., frictionless or α = 0, where α is the adhesion factor) soil-structure interface is simulated.

For clay soils, the rigidity index, I_r (= G/s_u, where G is the shear modulus), typically ranges between 50 and 500. To explore the impact of the rigidity index I_r on end bearing resistance, parametric analyses are conducted through SSFE and LDFE analyses, where I_r is varied across values of 50, 100, 300, and 500.

3 Numerical results

3.1 Shallow foundation

The effect of soil stiffness on the bearing capacity of a shallow circular foundation (pre-embedded 0.1D) is investigated through SSFE analysis. Figure 3a shows the failure mechanisms of the foundation for I_r = 50 and 500. The contour of maximum shear stress ($(\sigma_1 - \sigma_3)/2$, where σ_1 and σ_3 are the maximum and minimum principal stresses, respectively) displays that the plastic zone is developed beneath the tip extending to the soil surface, and the ranges of mobilized soil are comparable. SSFE analyses with various rigidity index I_r of 50, 100, 300 and 500 are conducted to explore the effect of soil stiffness. Figure 3b shows the bearing capacity factor, N_c, over normalized displacement, d/D. It can be seen that soil stiffness affects the initial load-displacement response but has little effect on the ultimate bearing capacity of a shallow circular foundation. The results from this study agree well with that from finite element limit analysis [2] and slightly larger than the empirical results [3]. This suggests that artificially increasing the value of I_r allows for obtaining the end bearing capacity at a smaller displacement without sacrificing accuracy.

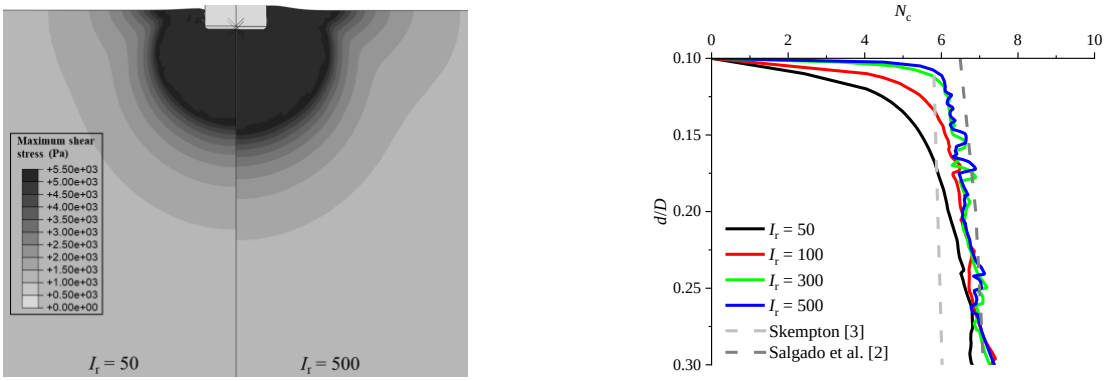

(a) (b)

Figure 3: Bearing capacity of a shallow foundation (SSFE): (a) failure mechanism; (b) bearing factors.

3.2 Deep foundation

The effect of soil stiffness on the bearing capacity of a deep circular foundation (or pile) (d/D > 5) is investigated through both SSFE and LDFE analysis. The soil flow mechanisms for the foundation pre-embedded at a depth of d/D = 5 from SSFE analysis for I_r = 50 and 500 are shown in Figure 4a. It is shown that the plastic area is localized around the foundation tip, and the yielding zone of I_r = 500 is significantly larger than that of I_r = 50. The bearing capacity factors for various I_r are depicted in Figure 4b. It is shown that the soil stiffness has a significant influence on the bearing capacity of a deeply buried circular foundation. This is because a foundation placed in soil with larger stiffness induces increased radial displacement, resulting in a higher pressure in the expansion of a cylindrical cavity. The findings from existing publications [2, 3] without considering the stiffness effect are incorporated for comparison, where discrepancy can be found.

This indicates that, for a deeply buried foundation, using increased value of I_r (for reaching the end bearing capacity at a small displacement) may lead to inaccurate results. Hence, LDFE analysis is necessary to determine the bearing capacity with certain realistic soil stiffness.

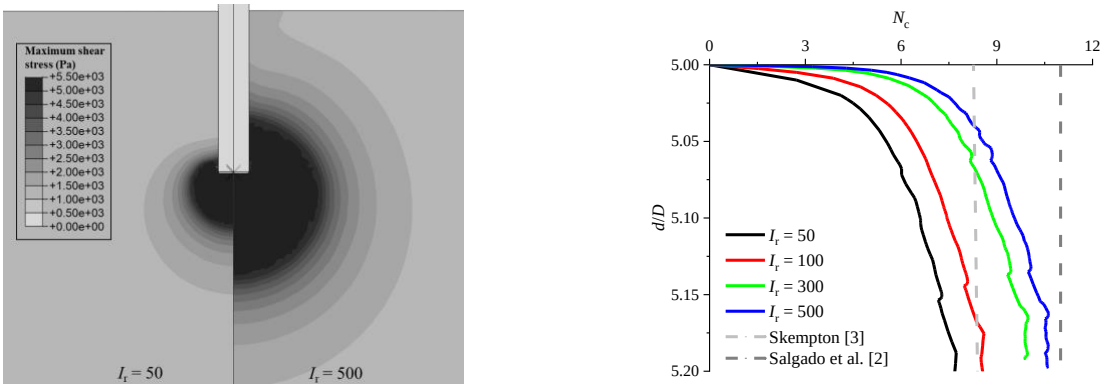

(a) (b)

Figure 4: Bearing capacity of a deep foundation (SSFE): (a) failure mechanism; (b) bearing factors.

Figure 5a shows the failure mechanisms at a penetration depth of d/D = 5 for I_r = 50 and 500, where the foundation is penetrated from soil surface through LDFE analysis. It is shown that the yielding zone of I_r = 500 is larger than that of I_r = 50, as is the extent of soil heaving. It can be seen that a deep failure mechanism occurs for I_r = 50, where the mobilized area is localized around the tip; while a shallow failure is observed for I_r = 500, where slip surfaces extend outwards and upwards to the ground surface.

Figure 5b shows the penetration resistance factor profiles over normalized penetration depths. The value of N_c gradually increases with the penetration depth and achieves a steady-state condition at a depth of d/D = 5 for I_r = 50, where a transition mechanism from shallow failure to deep failure occurs; while N_c continues to increase until d/D = 15 for I_r = 500. It can be seen that the critical depth for a deep failure mechanism increases as soil stiffness rises. As shown in Figure 5b, the end bearing resistance factor N_c increases by approximately 45% for a deep circular foundation, as soil rigidity I_r increases from 50 to 500. SSFE analyses for a pre-

embedded foundation (d/D = 5 and 10) with I_r = 50 are also included in Figure 5b for comparison, where N_c = 8 from SSFE analysis, while N_c = 10 from LDFE analysis.

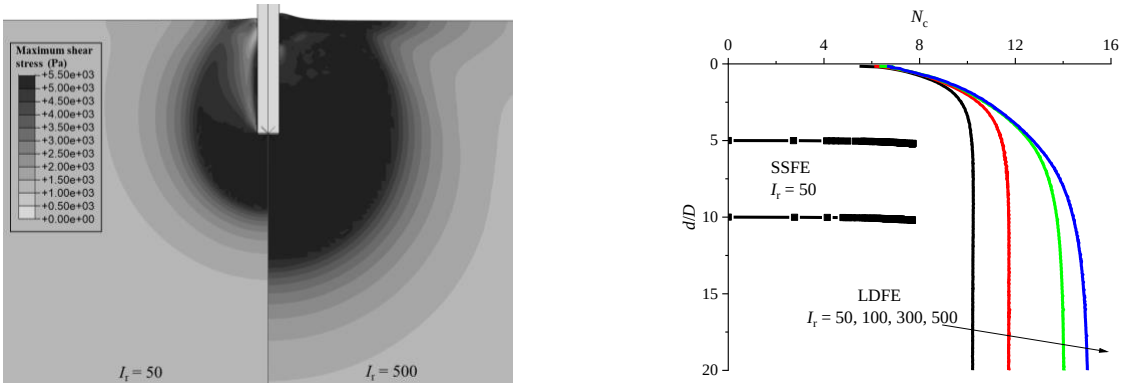

(a) (b)

Figure 5: Penetration behaviour (LDFE): (a) failure mechanism (d/D = 5); (b) bearing capacity factors.

4 Conclusions

Numerical simulations using Small Strain Finite Element (SSFE) and Large Deformation Finite Element (LDFE) methods are performed to investigate the effect of soil stiffness on the bearing capacity of a circular foundation. It is found that the soil stiffness has little influence on the bearing capacity of a shallow foundation with a shallow failure mechanism. However, for a deeply buried foundation, a deep flow mechanism is developed, and the failure zone is influenced by the soil stiffness. As the rigidity index increases from 50 to 500, the deep end bearing resistance is enhanced by up to 45%.

The observation regarding the impact of soil stiffness on end bearing resistance also holds practical significance for numerical modelling. For a shallow foundation, artificially increasing the soil stiffness in SSFE analysis allows for obtaining the end bearing capacity at a smaller displacement without sacrificing accuracy. However, employing increased soil stiffness for deeply buried foundations may lead to inaccurate results. For penetrating problems, e.g., pile installation and CPT (cone penetration test), SSFE analysis may underestimate the end bearing resistance without considering the installation effect. The findings presented here help practitioners in accurately determining soil stiffness parameters when conducting numerical modelling of foundation bearing capacity problems.

References

[1] Prandtl, L. (1920) Uber die harte plastischer korper. Nachr. Ges. Wiss. Gottingen, Math.Phys. Kl.:74-85.
[2] Salgado, R., Lyamin, A., Sloan, S. and Yu, H. (2004) Two-and three-dimensional bearing capacity of foundations in clay. Geotechnique 54(5):297-306.
[3] Skempton, A. (1951) The bearing capacity of clays. Selected papers on soil mechanics:50-59.
[4] Bransby, F. and Randolph, M. (1999) The effect of embedment depth on the undrained response of skirted foundations to combined loading. Soils and Foundations 39(4):19-33.
[5] Zhang, Y., Bienen, B., Cassidy, M. J. and Gourvenec, S. (2012) Undrained bearing capacity of deeply buried flat circular footings under general loading. Journal of Geotechnical and Geoenvironmental Engineering 138(3):385-397.
[6] Wang, C. and Carter, J. (2002) Deep penetration of strip and circular footings into layered clays. International Journal of Geomechanics 2(2):205-232.
[7] Ullah, S. N., Noor E. Khuda, S., Fook Hou, L., Suntharavadivel, T., & Albermani, F. (2020). Deep undrained bearing capacity of rectangular foundations in uniform strength clay. Journal of Geotechnical and Geoenvironmental Engineering, 146(10), 04020105.
[8] Xiao, Z., Fu, D., Zhou, Z., Lu, Y. and Yan, Y. (2019) Effects of strain softening on the penetration resistance of offshore bucket foundation in nonhomogeneous clay. Ocean Engineering 193:106594.
[9] Hu, Y. and Randolph, M. (1998) A practical numerical approach for large deformation problems in soil. International Journal for Numerical and Analytical Methods in Geomechanics 22(5):327-350.

Geotechnical Modelling 1: Pile Jacking to Rainfall-Induced Landslides

UKACM 2024 Conference, 10-12 April 2024, Durham University, Durham, UK
https://doi.org/10.62512/conf.ukacm2024.006

Energy-based bending solution for stiffened slabs-on-grade on expansive soils

Abubakr E. S. Musa[1*]

[1]Interdisciplinary Research Center for Construction and Building Materials, King Fahd University of Petroleum & Minerals, Dhahran 31261, Saudi Arabia

abubakr.musa@kfupm.edu.sa

Abstract

The stiffened slab-on-grade (SSOG) is known to be an efficient type of foundations for one to three-story buildings constructed on expansive soils. During its structural design, it is required to optimize the sizes and spacings of the stiffening beams to minimize the differential movement and this can best be achieved by developing an accurate continuous solution (in a functional form). In this study, Ritz method-based bending solution for SSOG is developed considering the tensionless behaviour of the subgrade reaction. The SSOG is treated as a beam on elastic foundation and the heave of the soil is introduced to the problem as an upward pressure. Ritz method formulation is developed with assumed deformed shape of the beam containing unknown constants to be determined from the minimization of the potential energy. Due to the central heave (mound shape) of the soil, there are zones near the edges of the beam with no contact between the beam and the supporting soil (i.e.: zero subgrade reaction). The exact locations of the zero-subgrade reaction zones are unknown initially and a systematic iterative approach is developed to determine their locations. The accuracy of the proposed solution is verified through comparison of the obtained deflection, bending moment and shear force of a selected numerical example with the results of a recently developed finite element-based design approach. In addition to its accuracy, the proposed solution has the advantage of being in a functional form which is useful for optimization purposes and facilitates further investigations of SSOG parameters.

Key words: *Stiffened slab-on-grade; Expansive soil; Energy methods; Ritz method, Beam on elastic foundation; Tensionless foundation.*

1 Introduction

Stiffened slab-on-grade (SSOG) is a slab-on-grade of a about 0.1 m thickness and stiffened by stiffening beams of considerable stiffnesses. It is an efficient type of foundations for light structures constructed on expansive soils as it has sufficient stiffness to prevent distortion of the superstructure as the soil heaves. Different design methods exist in literature for design of such type of foundations such as Building Research Advisory Board (BRAB) method [1], Post Tensioning Institute (PTI) method [2], Wire Reinforcement Institute (WRI) method [3], and the Australian Standards (AS2870) method [4], to mention a few. Some of these design approaches are conservative such as BRAB method as it considers uniform soil pressure along the contact zone between the SSOG and the soil.

Despite the progress being made in the analysis and design of SSOG, there is still alarming damage of buildings constructed on expansive soils [5]. As a comparison between some of the existing design methods, Abdelmalak (2007) [6] adopted 27 fictitious cases of SSOGs designed using WRI, PTI and AS2870 methods and he used the average beam depth obtained using the three methods as a reference for comparison. He concluded that the WRI method best correlated with the average beam depth and the AS2870 showed the poorest correlation among the three. Three years later, Abdelmalak co-authored a study by Briaud *et al.* [7] proposing a new design method based on a 2D finite element (FE) simulation of the soil and the SSOG is treated as a uniformly loaded flat plate of an equivalent thickness resting on the top of the mound. This work was refined and extended in 2016 to include SSOG under uniform pressure and line load [8]. The adopted 2D FE simulation in these studies [7,8] allows realistic interaction between the heaved soil and the SSOG as it considers the tensionless behaviour of the soil.

As the FE simulation yields a discrete solution, proposing a continuous bending solution to the problem of SSOG will be useful for optimization purposes and it will pave the way for investigating more parameters. Consequently, this study is oriented to develop Ritz method-based bending solution for SSOG resting on expansive soil considering the tensionless behaviour of the subgrade reaction. The SSOG is treated as beam on elastic foundation and the heave of the soil is introduced to the problem as an upward pressure. Due to the central heave (mound shape) of the soil, there are zones near the edges of the beam with no contact between

the beam and the supporting soil (i.e.: zero subgrade reaction) which are determined iteratively using a systematic approach. The accuracy of the proposed solution is verified through the comparison with the work of Briaud *et al.* [8] as they are both adopted tensionless behaviour of the supporting soil.

2 Problem description

The assumption of the equivalent uniform thickness of the SSOG adopted in the earlier studies [6-8] has also been adopted in this study. As shown in Fig.1, the problem is solved by superposition of the loaded SSOG and the free heave profile (the heave profile that can happen in the absence of the loaded SSOG). Superposition of the two yields a deformed shape of both the SSOG and the soil as shown in the figure. Due to the central heave, part of the slab will be hanged and not supported by the soil [7,8]. To accurately solve the problem using the concept of beam on elastic foundation, tensionless foundation needs to be adopted [9]. The subgrade reaction can thus be defined as follows:

$$k(x) = \begin{cases} 0.65\sqrt{\frac{E_s\, b}{EI}}\frac{E_s}{(1-\nu_s)^2}, & -(1-\alpha)L/2 < x < (1-\alpha)L/2 \\ 0\quad , & otherwise \end{cases} \tag{1}$$

where E_s and E are Young's modulus of the soil and concrete, respectively; ν_s is Poison's ratio of the soil; and b and I are the width and second moment of area of the SSOG model, respectively;

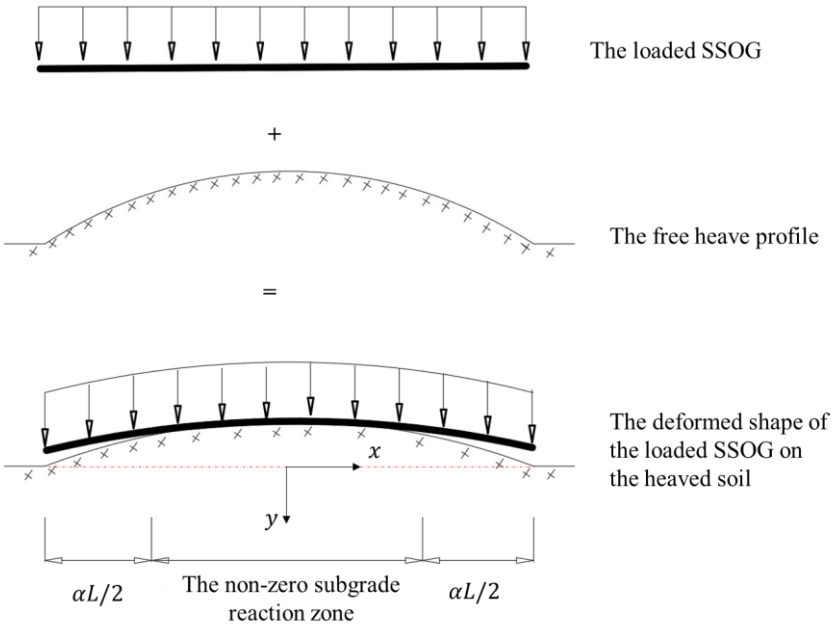

Fig. 1: SSOG model on a heaved soil

For a known swelling or heave profile, $y_s(x)$, the swell pressure can be introduced to the problem by [10]:

$$q_s(x) = y_s\, k \tag{2}$$

Thus, the total load is given by combining the initially applied load q_0 and the one resulting from the swelling of the soil as in Eq. (3). The problem can then be solved using Ritz method.

$$q(x) = q_0 + y_s\, k \tag{3}$$

3 Ritz method formulation

Due to deformation of the SSOG from the applied load and swelling of the soil, the potential energy stored in the SSOG can be defined as the difference between the strain energy stored in the SSOG U and the external work W. i.e.:

$$\Pi = \mathrm{U} - \mathrm{W} \tag{4}$$

where the strain energy and the work done by the external load are related to the deflected shape $y(x)$ by

$$\mathrm{U} = \frac{EI}{2} \int_{-L/2}^{L/2} \left(\frac{\partial^2 y}{\partial x^2}\right)^2 dx \tag{5}$$

and $$W = \int_{-L/2}^{L/2} (q\, y - k\, y^2/2)\, dx \tag{6}$$

To solve the problem using Ritz method, the solution is approximated by

$$\mathrm{y(x)} = \sum_{j=1}^{N} C_j \phi_j(x) \tag{7}$$

where C_j are constants to be obtained by minimizing the potential energy and $\phi_j(x)$ are expressions satisfying the geometric boundary conditions. Since the considered SSOG is treated as a free-free beam on elastic foundation with boundary conditions in the form of zero shear force and bending moment, there is no geometric boundary conditions to be satisfied and $\phi_j(x)$ can be taken as $x^{2(j-1)}$.

Substitution of Eqs. (5) to (7) into Eq. (4) leads to express the potential energy by:

$$\Pi = \frac{EI}{2} \int_{-L/2}^{L/2} \left(C_j \frac{\partial^2 \phi_j}{\partial x^2}\right)^2 dx - \int_{-L/2}^{L/2} \left(q\, C_j \phi_j - k\, (C_j \phi_j)^2/2\right) dx \qquad ,j, 1 \ldots N \tag{8}$$

where the repeated indices represent summation. This expression can then be minimized with respect to the unknown constants C_j which leads to the following system of equation:

$$[K]\{C\} = \{F\} \tag{9}$$

where $\{C\} = \{C_1, C_2, \ldots, C_N\}^T$ and the elements of the other two matrices are expressed as follows

$$K_{ij} = \int_{-\frac{L}{2}}^{\frac{L}{2}} \left(\frac{\partial^2 \phi_j}{\partial x^2} \frac{\partial^2 \phi_i}{\partial x^2}\right) + \frac{k}{EI}\left(\phi_j \phi_i\right) dx \quad i,j = 1, N \tag{10}$$

and $$F_i = \int_{-\frac{L}{2}}^{\frac{L}{2}} \left(\frac{q_0 + y_s\, k}{EI} \phi_i\right) dx \quad i = 1, N \tag{11}$$

The system of equations (Eq. (9)) can be solved to obtain the unknown constants. Then, the constants can be substituted in Eq. (7) to yield the deflected shape of the SSOG. The required bending moment and shear force can then be obtained by the following expressions:

$$M = -EI \frac{d^2 y}{dx^2} \tag{12}$$

$$V = -EI \frac{d^3 y}{dx^3} \tag{13}$$

The system of equations to be solved (Eq. (9)) contains unknown value α which defines the non-zero subgrade reaction zone (please see Fig. 1 and Eq. (1)). In this study, this coefficient is obtained using a systematic iterative approach. It is proposed to start the solution by assuming full contact between the SSOG and the heaved soil $\alpha = 0$, then α is increased by a very small amount $\Delta\alpha$ (say 0.01). At each iteration, the problem is solved to obtain the deflected shape and evaluate it at $(1 - \alpha)\frac{\mathrm{L}}{2}$. If it is found to be more than the heave at the same position, the solution stops and otherwise it will continue for the other iterations.

4 Numerical example and discussion

To verify the proposed method, a SSOG analysed earlier by Briaud *et al.* [7] has been solved in this study using the proposed method. Their solution was based on a 2D FE simulation of the flat loaded slab resting on a soil medium using Abaqus software. The numerical data are taken from Ref. [7] which are $L = 16.0\ m, h_{eq} = 0.38\ m, b = 1.0\ m, q_0 = 7.5\ kN/m, E = 20\ GPa, E_s = 60\ MPa$ and $\nu_s = 0.2$.

The obtained results using the proposed method are shown in Fig. 2 along with the results of Briaud *et al.* [7]

where excellent agreement can be seen. The deflected shape of the foundation (Fig. 2a) clarifies the separation between the foundation and the heaved soil leading to a hanging part of the SSOG. The bending moment results (Fig. 2b) indicate there is a considerable negative bending moment which necessitates top reinforcement of the stiffening beams. As the comparison verifies the accuracy of the proposed method, it can then be adopted to investigate the impact of more parameters on the behaviour of SSOG.

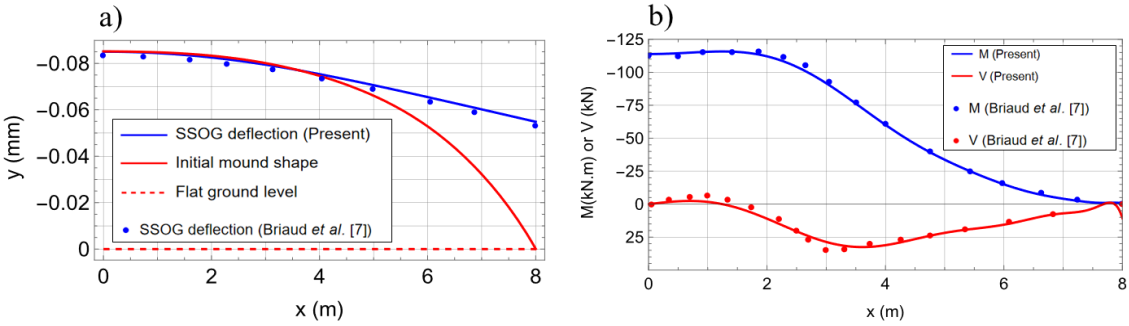

Fig. 2: The analysis results (a) the deformations and (b) bending moment and shear force diagrams.

5 Conclusions

Ritz method-based formulation has been developed for bending solution of SSOG on expansive soils considering the tensionless behaviour of the supporting soil. The heave profile is considered to be an input and the solution starts by assuming the deformed shape of the SSOG with unknown constants to be determined based on the minimization of the potential energy. As the central heave leads to separation between the SSOG and the heaved soil at the far ends of the SSOG, a systematic iterative approach is developed to determine the non-zero subgrade reaction zone. The proposed method is verified with a numerical example from the literature and excellent agreement is obtained. In addition to its accuracy, the proposed solution has the advantage of being in a functional form which is useful for optimization purposes and facilitates investigation of the impact of more parameters related to analysis and design of SSOG.

Acknowledgments

The author greatly acknowledges King Fahd University of Petroleum & Minerals (KFUPM) for the provided support to complete this work.

References

[1] BRAB (Building Research Advisory Board), (1968). "National research council criteria for selection and design of residential slabs." National Academy of Sciences, Washington, DC.

[2] Post-Tensioning Institute (PTI), (2004). "Design and Construction of Post-Tensioned Slabs-on-Ground", 3rd Ed., Phoenix, AZ, USA.

[3] Wire Reinforcement Institute (WRI), (1981). "Design of Slab-on- Ground Foundations", Findlay, Ohio, USA, August.

[4] Australian Standard (AS2870), (1996). "Residential Slabs and Footings", AS 2870 Standard House, Sydney NSW, Australia.

[5] M. A. Shams, (2019). "Analysis and Design of Stiffened Slab Foundations on Reactive Soils using 3D Numerical Modelling", Doctoral dissertation, Curtin University.

[6] R. I. Abdelmalak, (2007). "Soil structure interaction for shrink-swell soils "A new design procedure for foundation slabs on shrink-swell soils". Texas A&M University.

[7] J. Briaud, R. Abdelmalak & X. Zhang, (2010, September). "Design of stiffened slabs-on-grade on shrink-swell soils". In Proc. 5th Int. Conf. Unsaturated Soil, *International Center for Numerical Methods in Engineering, Barcelona, Spain.*

[8] J. Briaud, R. Abdelmalak, X. Zhang & C. Magbo, (2016). "Stiffened slab-on-grade on shrink-swell soil: New design method". *ASCE: J. of Geotech. and Geoenviron. Eng.*, 142(7), 04016017.

[9] A. E. S. Musa, M. A. Al-Shugaa & A. Al-Fakih, (2022). "Free–free beam resting on tensionless elastic foundation subjected to patch load". *Mathematics*, *10*(18), 3271.

[10] A. E. S. Musa, (2018). "An Analytical Bending Solution for Analysis and Design of Long Beams Constructed on the Expansive Soil". *Arabian Journal for Science and Engineering, 43*, 5203-5214.

UKACM 2024 Conference, 10-12 April 2024, Durham University, Durham, UK
https://doi.org/10.62512/conf.ukacm2024.016

SPATIAL VARIABILITY OF SOIL PROPERTIES IN SAUDI ARABIA: ESTIMATION OF CORRELATION LENGTH

Kun Zhang[1*], Marti Lloret-Cabot[1], Whangcheng Zhang[1], Alaa Kourdey[1]

[1] Department of Engineering, Durham University, Durham, DH1 3LE, UK.
kun.zhang@durham.ac.uk

Abstract. Spatial variability of soil properties plays an important role in geotechnical engineering, influencing the design and performance of geo-structures. This study investigates the characterisation of this spatial variability by examining in-situ soil data obtained from 74 Cone Penetration Tests (CPTs) conducted in a reasonably homogeneous granular fill of a large construction project in Saudi Arabia. The primary focus of this work is to assess, from the available in-situ CPT data, the spatial variability of this sand fills in terms of the vertical correlation length (θ_v). The autocorrelation function (ACF) method is used to estimate θ_v, and the geo-statistical patterns of all estimated θ_vs are analysed through the values of its mean (μ), standard deviation (σ), coefficient of variation (CoV), and fitted probability density function (pdf). An assessment of the accuracy in the estimated θ_vs is then carried out from the statistical analysis of $1,000$ one-dimensional ($1-D$) random fields with spatial statistical information similar to the in-situ fill. The study shows that as much as 25% error can be expected for the specific depth ($D = 10$m) and sampling interval ($dx = 0.01$m) of the 74 CPTs considered.

Key words: *Correlation length; Spatial variability; Random field; CPT; Saudi Arabia*

1 Introduction

Natural soils are heterogeneous and their characteristics exhibit spatial variability [1]. This inherent spatial variability is a significant source of uncertainty in stochastic geotechnical engineering, making its characterisation important for the design of geotechnical structures [2]. The correlation length serves as a key parameter in simulating soil spatial variability as it measures the distance between regions with similar geotechnical properties [2]. Even though the estimation of θ_v from in-situ CPT data has been extensively researched in the literature (e.g., [3]), studies quantifying the spatial variability of Arabian sandy soils are scarce.

The main objective of this research is therefore to statistically characterise the spatial variability of an Arabian granular fill in terms of the θ_v estimated from 74 CPTs available at a site of a very large construction project in Ras Al Khair, Saudi Arabia. An assessment of the accuracy of the estimated θ_vs is then carried out, including an investigation of how varying the number of CPTs (referred to as n in this paper) would affect the accuracy of estimated θ_v. The conventional ACF method (e.g., [3]) is the strategy applied to estimate θ_v from all the in-situ CPT profiles but it is unclear whether the obtained estimates are accurate or not with the limited set of CPT data used. To study this effect, a sufficiently large sample size of CPT data (e.g., $n = 1,000$) is desirable. For this purpose, $1,000$ artificial CPTs containing spatial statistical information similar to that of the in-situ sand fill are generated using the LAS method [4] and a statistical analysis is then carried out to quantify the influence that the number of CPTs (n) considered has in the accuracy of the estimated θ_vs.

2 Estimation of vertical correlation length from CPT data

2.1 In-situ geotechnical information available

A very large shipyard project is currently under construction in Ras Al-Kahir city, located in the Easter coastal part of Saudi Arabia. The huge dimensions of the project (covering an area of about $1,125$ha), the associated costs and the complex geotechnical conditions have allowed for an extensive soil investigation campaign. Seventy-four CPTs are available from an area of the project with a reasonably homoegenous granular soil and these 74 CPTs are used in this work to quantify the soil heterogeneity of the site in terms of vertical correlation length. Each of these CPTs included information on cone tipe resistance (q_c), sleeve fiction (f_s), friction angle (R_f) and pore water pressure (u) but only the tip resistance is considered here. For consistency, only the first $10m$ of measured tip resistances from the ground surface ($D = 10m$) are used in all CPTs. The sampling interval is also the same in all CPTs considered ($dx = 0.01m$).

2.2 Geo-statistical characterisation

The autocorrelation function (ACF) method is one of the most generally employed methods for estimating correlation length of soil properties from in-situ data (e.g. [3, 5, 6]), and is also applied in this study to determine θ_v from the CPT data. The application of the method requires that the data used is stationary, meaning that the mean and standard deviation of the data are constant in the space. As discussed, for instance in [3], it is common in geotechnical engineering to assume stationarity after removing a linear trend to the data and normalising the de-trended data by the standard deviation (calculated from the de-trended data). Applying this process to each individual CPT, leads to a set of de-trended and normalised tip resistances with an approximate zero mean and unit standard deviation (and hence satisfying the stationarity conditions). The stationary data is used to estimate the experimental correlation function $\hat{\rho}(\tau)$ approximated here as:

$$\hat{\rho}(\tau_j) = \frac{1}{k-j} \sum_{i=1}^{k-j+1} X_i X_{i+j}, \quad for \quad j = 0, \ldots k-1 \tag{1}$$

where τ is the lag distance between two points, X_i and $X_{(i+j)}$ are the CPT measurements, k is the total number of measured points and i is the total number of pairs of points.

This experimental correlation function $\hat{\rho}(\tau)$ is then best-fitted to a theoretical correlation model from where θ_v is found. From the different possible alternatives for $\rho(\tau)$, this research assumes a Markovian correlation structure defined by:

$$\rho(\tau) = \exp\left(-\frac{2|\tau|}{\theta}\right) \tag{2}$$

Fig. 1a shows the CPT tip resistance q_c for all in-situ CPTs investigated. In the plot, the thin lines indicate q_c values for each individual CPT profile and the thicker dashed line indicates the linear mean trend. Fig. 1b shows the de-trended and normalised q_c values. Fig. 1c shows the individual experimental correlation function for the vertical direction for each of the 74 CPTs used together with the best fitted theoretical correlation function (corresponding to the value of θ_v estimated from an average experimental correlation function which is indicated in the figure by a thicker dashed line). Fig. 1d illustrates the histogram based on all the estimated vertical correlation lengths as well as the fitted normal distribution showing that the estimated θ_vs are reasonably well-represented by a normal distribution with mean (μ=0.848m), standard deviation (σ=0.502m), coefficient of variation (CoV=0.592).

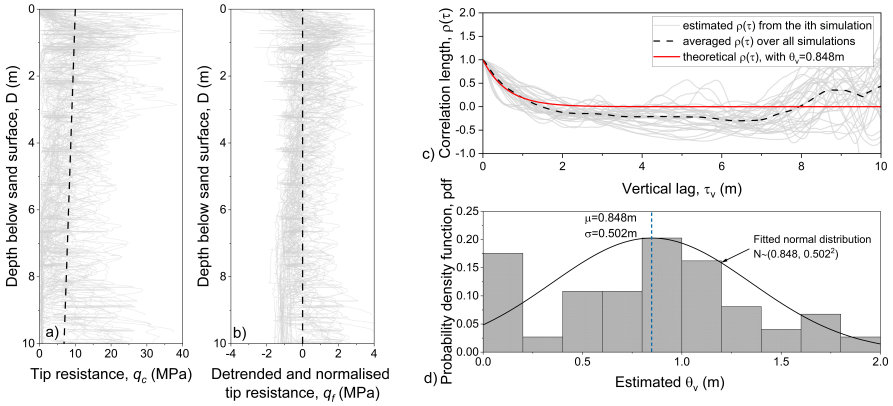

Figure 1: Geostatistical characterisation of in-situ CPT data: (a) tip resistance; (b) de-trended and normalised tip resistance; (c) Experimental and theoretical correlation functions and (d) histograms of estimated θ_vs.

3 Accuracy assessment based on fictitious CPT data

3.1 Artificial CPTs generated using 1-D LAS

The analysis of the above information raises the question of how accurate are our estimations for θ_v and, more interestingly, how an increased number of CPT would improve the accuracy of the obtained mean estimated θ_v. Quantitative evidence to answer this question can be obtained following the ideas discussed in [7] on generating $1-D$ random fields using the Local Average Subdvivision (LAS) method [4] and interpret them as artificial CPTs. In this context, LAS is utilised to generate $1,000$ $1-D$ random fields representing the fictitious CPT data with zero mean, unit standard deviation and a vertical correlation length θ_0=$0.848m$. The depth D and spacial sampling dx of the generated CPTs are as the ones used for the in-situ data (i.e., $D = 10m$ and $dx = 0.01m$).

3.2 Influence of number of CPTs

From the generated $1,000$ artificial CPTs it is possible to study the influence of n on the estimated θ_v, noting that D and dx are kept fixed in this analysis, so that the influence of these variables on the accuracy of the estimated θ_v (see e.g., [6]) does not affect the results. In order to analyse this influence, it is first necessary to estimate the θ_v in each artificially generated CPT following the same approach discussed for the in-situ data.

Fig. 2 shows the information from all estimated θ_v in a form that facilitates the discussion. The vertical axis corresponds to the ratio between the mean estimated θ_v over a specific number of CPTs (referred to $\bar{\theta}$ as in the figure), and the value of the θ_v used as input in LAS (indicated as θ_0). The horizontal axis corresponds to the number of CPTs n considered (using a logarithmic scale). The shadowed grey area in Fig. 2 shows the range of possible values of $\bar{\theta}/\theta_0$ for a given value of n. This area is bounded by two curves (indicated as dashed lines in the figure) that correspond to maximum and minimum values that the ratio $\bar{\theta}/\theta_0$ can take for a given value of n, amongst all $1,000$ CPTs. The continuous line within this shadow area shows how the ratio $\bar{\theta}/\theta_0$ varies with increasing n clearly illustrating the improvement on the averaged estimated θ_v with increasing n. For the particular case of n = 74, the analysis shows that the expected error in the averaged estimated θ_v can be as much as 25%.

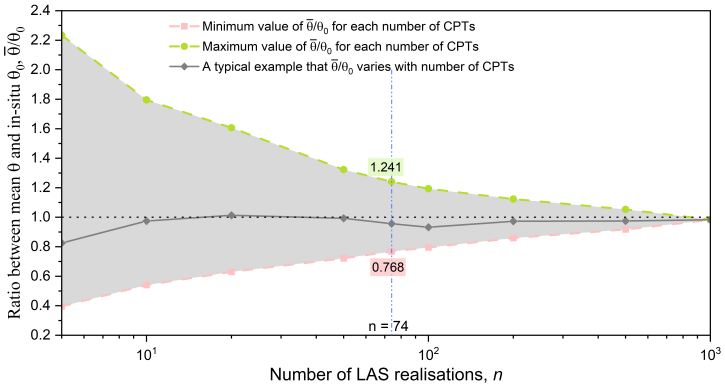

Figure 2: The upper and lower boundaries for the values of $\bar{\theta}/\theta_0$ varying with number of LAS realisations.

4 Conclusions

This work has presented an analysis of the spatial variability in the vertical direction of the tip resistances measured in a sandy deposit of a construction site in Saudi Arabia. Using 74 CPTs with a sampling distance of $dx = 0.01m$ and a total depth $D = 10m$, the estimated vertical correlation length obtained is $\theta_v = 0.848m$. Based on the results from a subsequent statistical analysis using $1,000$ $1-D$ random fields, the expected error in this estimation can be as much as 25%.

Acknowledgments

The first author of this research is sponsored by the China Scholarship Council-Durham scholarship.

REFERENCES

[1] K. K. Phoon and F. H. Kulhawy, "Characterization of geotechnical variability," *Canadian Geotechnical Journal*, vol. 36, no. 4, pp. 612–624, 1999.

[2] M. A. Hicks, J. D. Nuttall, and J. Chen, "Influence of heterogeneity on 3d slope reliability and failure consequence," *Computers and Geotechnics*, vol. 61, pp. 198–208, 2014.

[3] M. Lloret-Cabot, G. A. Fenton, and M. A. Hicks, "On the estimation of scale of fluctuation in geostatistics," *Georisk: Assessment and Management of Risk for Engineered Systems and Geohazards*, vol. 8, no. 2, pp. 129–140, 2014.

[4] G. A. Fenton and E. H. Vanmarcke, "Simulation of random-fields via local average subdivision," *Journal of Engineering Mechanics-Asce*, vol. 116, no. 8, pp. 1733–1749, 1990.

[5] J. Z. Zhang, K. K. Phoon, D. M. Zhang, H. W. Huang, and C. Tang, "Novel approach to estimate vertical scale of fluctuation based on cpt data using convolutional neural networks," *Engineering Geology*, vol. 294, p. 10, 2021.

[6] P. Christodoulou, L. Pantelidis, and E. Gravanis, "A comparative assessment of the methods-of-moments for estimating the correlation length of one-dimensional random fields," *Archives of Computational Methods in Engineering*, vol. 28, no. 3, pp. 1163–1181, MAY 2021.

[7] G. A. Fenton, "Random field modeling of cpt data," *Journal of geotechnical and geoenvironmental engineering*, vol. 125, no. 6, pp. 486–498, 1999.

UKACM 2024 Conference, 10-12 April 2024, Durham University, Durham, UK
https://doi.org/10.62512/conf.ukacm2024.019

CONSEQUENCES OF TERZAGHI'S EFFECTIVE STRESS DECOMPOSITION IN THE CONTEXT OF FINITE STRAIN PORO-MECHANICS

Giuliano Pretti[1]*, William M. Coombs[1], Charles E. Augarde[1]

[1] Department of Engineering, Durham University, Durham, DH1 3LE, UK.
giuliano.pretti@durham.ac.uk, w.m.coombs@durham.ac.uk, charles.augarde@durham.ac.uk

Abstract. Poro-mechanics is a branch of mechanics considering the hydro-mechanical behaviour of a porous solid medium whose pores are saturated by a fluid. The presence of both these constituents significantly influences the overall macro-response of the material.

Regardless of the application, Terzaghi's effective stress decomposition is a well-established hypothesis regarding how the total stress tensor is decomposed into a part directly related to strain (effective stress) and a part borne by the fluid phase (interstitial pressure). The assumption of an incompressible solid medium physically justifies Terzaghi's effective decomposition. However, under the further assumption of finite strain mechanics, a more restrictive constraint on the volume change arises, which the vast majority of formulations neglect.

This work details how disregarding this constraint on the volume change can lead to the violation of solid mass balance, which can be counted among the fundamental principles of continuum mechanics. Furthermore, to address this issue practically, an ad hoc stress-strain relationship is designed to respect Terzaghi stress decomposition and solid mass balance in the context of finite-strain hyper-elasticity.

Key words: *Poro-mechanics; Finite strain-mechanics; Mass conservation; Hyper-elasticity*

1 Introduction

A plethora of materials with a wide range of applications see their mechanical behaviour as severely influenced by the presence of an interstitial fluid. The subject that aims to study this type of material is poromechanics, which Biot first described in [1], and it has been later expanded to finite strain.

If focusing on the hydro-mechanical behaviour of porous media, three mechanisms govern the volume change: the compressibility of the two constituents (i.e., the solid and the fluid phases) and the allowed drainage. In particular, this last phenomenon deals with the conditions applied on the boundary of the sample, which, in turn, are a function of the considered problem. On the other hand, modelling the constituents as compressible (or not) depends on the specific material. In geomechanics, it is often assumed that both these constituents, i.e., the soil grains and the water, are incompressible since the drainage conditions drive the main volume change. In particular, this work investigates how the assumption of incompressible solid phase and the definition of the Eulerian porosity n constraint the values of the Jacobian J[1]. When violated, the solid mass is not conserved, and the considered equations lose physical meaning. The following developments heavily draw on Pretti *et al.* [2].

[1] A rigorous definition of the Eulerian porosity n and the Jacobian J are given below in Section 2.

2 Main assumptions and framework

When considering a material composed of two phases, there exist multiple assumptions regarding each constituent and the way they interact. This work adopts the following assumptions:

- **A.1** thermal effects are not considered;
- **A.2** one fluid fully saturates the solid porous skeleton. These are juxtaposed continua;
- **A.3** the phases do not exchange mass;
- **A.4** the solid phase is incompressible;
- **A.5** the fluid is non-viscous;
- **A.6** the material undergoes finite strain deformations and rotations;
- **A.7** the considered continuum is isotropic;

Owing to hypothesis **A.6**, the considered material's configuration varies with time. Hence, $\boldsymbol{x}$ denotes the position shared by the two constituents in the current configuration (assumption **A.2**). $\boldsymbol{X}$ indicates the original position of the solid phase, while the original position of the fluid is unnecessary for this work. A mixed particle[2] occupies an initial volume $d\Omega = d\Omega^{sk} \cup d\Omega^{f}$ and a current one $d\omega = d\omega^{sk} \cup d\omega^{f}$. Since the solid phase is described in a Lagrangian way, the same particle is considered for the volumes $d\Omega^{sk}$, $d\omega^{sk}$, while fluid phase volumes $d\Omega^{f}$ and $d\omega^{f}$ are not occupied by the same fluid. The motion of the mixed particle is therefore tracked by following its solid constituent, i.e., $\boldsymbol{x} = \boldsymbol{\varphi}\left(\boldsymbol{X}^{sk}, t\right)$, with $\boldsymbol{\varphi}$ being the mapping between the original and current configurations. This mapping allows to define the deformation gradient $\boldsymbol{F} := \frac{\partial \boldsymbol{\varphi}(\boldsymbol{X}^{sk},t)}{\partial \boldsymbol{X}^{sk}}$, whose determinant, named Jacobian, describes the volume change of the mixed particle, i.e., $d\Omega = J\, d\omega$. For mathematical (invertibility of the mapping) and physical reasons (volumes cannot be negative), the Jacobian must satisfy the condition $J > 0$. To describe which portion of the current volume is occupied by the fluid phase, the Eulerian porosity is defined as $n := \frac{d\omega}{d\omega^{f}}$, with n_0 being its initial value. The definition of the Eulerian porosity entails that its values are always bounded between zero and one, i.e.,

$$0 < n < 1. \tag{1}$$

As demonstrated by Borja and Alarcón [3] for assumption **A.6**, the simultaneous adoption of the above assumptions **A.1**-**A.5** leads to the Terzaghi effective decompositions, i.e., the total stress tensor can be additively decomposed into an effective part (related to a strain measure) and a fluid interstitial pressure.

3 Constraint on the Jacobian

Owing to hypothesis **A.3**, the equations of mass conservation can be written separately for the two constituents. If the solid mass conservation is considered, this is expressed by

$$\frac{d}{dt}\Big|_{X^{sk}} \left(\int_{\omega} \rho^{sk} (1-n)\, dv \right) = 0, \tag{2}$$

where $\frac{d}{dt}\Big|_{X^{sk}} (\bullet) = (\dot{\bullet})$ indicates the material derivative tracking the solid phase, and ρ^{sk} the current solid density. After a few manipulations and owing to assumption **A.4**, the above equation can be rewritten as

$$n = 1 - \frac{1}{J}(1 - n_0). \tag{3}$$

[2] A mixed particle is a particle in which, according to hypothesis **A.2**, both consistents coexist.

If the inequalities presented in (1) are substituted in the above equation, it follows that

$$\begin{cases} J > (1-n_0); & \text{(4a)} \\ \dfrac{1}{J}(1-n_0) > 0. & \text{(4b)} \end{cases}$$

While (4b) is trivially satisfy by $J > 0$ and $0 < n_0 < 1$, it can be seen that (4a) places a more restrictive constraint on the Jacobian. Inequality (4a) suggests that the progressive expulsion of the fluid makes the material gradually evolve only into its solid constituent, incompressible as assumed by **A.4**.

4 Hyper-elastic constitutive relationship

There are different ways to include the constraint provided by Eq. (4a) into the equations. Well-established practices to (weakly) include a constraint are the Lagrange multiplier or the penalty method (see to Pretti *et al.* [2] for a list of advantages and disavantages of these).

Regardless, this work adopts another technique to enforce the constraint (4a), which consists of modifying the stress-strain relationship. This adaptation is remarkably straightforward for those materials exhibiting an decomposition into a volumetric and the deviatoric part. If an isotropic (assumption **A.7**) Hencky material is considered, its effective free energy function can be adapted to include (4a) as follows

$$\hat{\Psi}^{sk}_{inc}(\boldsymbol{\varepsilon},\boldsymbol{\alpha}) = \frac{K}{2n}(\varepsilon^e_v)^2 + \frac{3}{2}G\left(\varepsilon^e_q\right)^2, \quad \text{with } \varepsilon_v := \ln J, \quad \text{and } \varepsilon_q := \sqrt{\frac{2}{3}\left(\boldsymbol{\varepsilon} - \frac{\varepsilon_v}{3}\boldsymbol{I}^{(2)}\right) : \left(\boldsymbol{\varepsilon} - \frac{\varepsilon_v}{3}\boldsymbol{I}^{(2)}\right)} \quad (5)$$

where the invariants of $\boldsymbol{\varepsilon} := \frac{1}{2}\ln(\boldsymbol{F}\boldsymbol{F}^T)$ have been adopted, $\boldsymbol{I}^{(2)}$ denotes the second-order identity tensor, and **:** the double contraction. $K > 0$ and $G > 0$ indicate the bulk parameter and the shear modulus.

5 Numerical example & Conclusions

Further assumptions: the above constitutive relationship has been implemented into a Material Point Method (MPM) $\boldsymbol{u} - p^f$ formulation. Further assumption necessary to run the example are as follows:

- **A.8** the fluid barotropic and obeys to this constitutive law $\dot{\rho^f} = \frac{\rho^f}{K^f}\dot{p^f}$, with ρ^f being the current fluid density, K^f the fluid bulk modulus and p^f Cauchy fluid pressure;
- **A.9** the flow exhibits low *Reynolds numbers*, which permits to consider the *Darcy* equation for the fluid flow, i.e., $\boldsymbol{q}^f = -\frac{\kappa}{g}\left(\frac{\partial p^f}{\partial \boldsymbol{x}} - \rho^f \boldsymbol{f}\right)$, with $\boldsymbol{q}^f$ being the relative fluid flux, κ the hydraulic conductivity, $\frac{\partial \bullet}{\partial \boldsymbol{x}}$ the gradient with respect to the current position, and $\boldsymbol{f}$ the self-weight acceleration;
- **A.10** hydraulic conductivity obeys to the *Kozeny-Carman* formula, $\kappa = c\frac{n^3}{(1-n)^2}$, with c constant.

Example scope: the aim of this example is to demonstrate the difference between a standard Hencky material and one described by Eq. (5). **Setup:** the column illustrated in Figure 1 is subjected to a gravitational acceleration $b = 1{,}000$ m s^{-2}, which ramps linearly from the start of the simulation until the $1{,}000$ steps and kept constant for the remaining $2{,}000$ steps of the simulation[3]. The bulk modulus for the original Hencky material $\bar{K}$ is set up to match the initial tangent elastic modulus given by Eq. (5),

[3]The reason for such a substantial acceleration lies in the opportunity to cut the costs of the simulation. Since the difference between the two materials lies in the effective stresses, the column must consolidate, and this load accelerate this process.

Table 1: Parameters considered in the analyses in Section 5.

Solid phase		Fluid phase	
G	$3 \cdot 10^5$ Pa	K^f	$2.2 \cdot 10^9$ Pa
ρ^s	2650 kg m^{-3}	ρ_0^f	1000 kg m^{-3}
Porous material			
κ_0		$1 \cdot 10^{-5}$ m s^{-1}	
n_0		0.3	
Simulation Parameters			
H, n_z^{els}		1 m, 20	
mmp		4	

† mmp is the number of material points per direction per element.

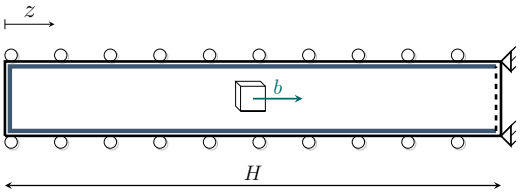

Figure 1: Illustration of the elastic column under self-weight. Rollers are applied on the top and bottom sides, while atmospheric pressure is applied at the right-hand side of the problem. Figure reproduced from Pretti *et al.* [2].

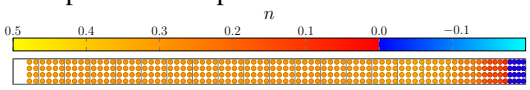

(a) Eulerian porosity for the original Hencky material, $\tilde{t} = 157^{th}$ time-step.

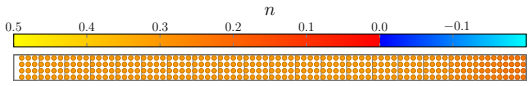

(b) Eulerian porosity for the improved Hencky material, $\tilde{t} = 157^{th}$ time-step.

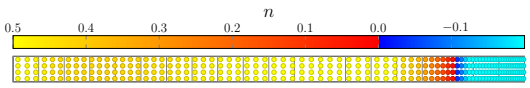

(c) Eulerian porosity for the original Hencky material, final time-step.

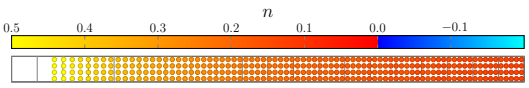

(d) Eulerian porosity for the improved Hencky material, final time-step.

Figure 2: Columns at $\tilde{t} = 157^{th}$ step and the end of each simulation. Figure from Pretti *et al.* [2].

i.e., $K = \bar{K}\, n_0 = 5 \cdot 10^5$ Pa. **Results discussion:** as it can appreciated from Figure 2a, the original Hencky material results in negative porosities quite early in the analysis. From this point, this simulation loses physical meaning, and the column surprisingly swells before failing (Figure 2c). On the other hand, the new material does not fail for the quite sustantial time of the simulation (Figures 2d). **Conclusions:** Overall, when considering an incompressible solid phase of a porous material, the Jacobian is subjected to a more severe constraint, inherited from the Eulerian porosity. Disregarding this restriction leads to the solid mass violation. A material respectful of this law was introduced and its effectiveness tested.

REFERENCES

[1] Biot, M. A. General theory of three-dimensional consolidation. *J. Appl. Phys.* (1941) **12.2**:155–164.

[2] Pretti, G. and Coombs, W.M, and Augarde, C.E., and Puigvert, M.M. and Gutiérrez, J.A.R. Preserving non-negative porosity values in a bi-phase elasto-plastic material under Terzaghi's effective stress principle. *Mech. Mater.* (2024).

[3] Borja, R. I. and Alarcón, E. A mathematical framework for finite strain elastoplastic consolidation Part 1: Balance laws, variational formulation, and linearization. *Comput. Methods Appl. Mech. Eng.* (1995) **122.1-2**:145–171.

UKACM 2024 Conference, 10-12 April 2024, Durham University, Durham, UK
https://doi.org/10.62512/conf.ukacm2024.060

A non-hysteretic simplification to the Glasgow Coupled Model (GCM)

Takudzwa Mutsvairo[1*], Marti Lloret-Cabot[1], Paul Hughes[1], Sravan Muguda-Viswanath[1], Ana Sofia Dias[1]

[1] Department of Engineering, Durham University, Durham, DH1 3LE, UK
takudzwa.m.mutsvairo@durham.ac.uk; marti.lloret-cabot@durham.ac.uk;
paul.hughes2@durham.ac.uk

Abstract

The Glasgow Coupled Model (GCM) is an established elasto-plastic constitutive model developed to capture the coupled hydro-mechanical response of unsaturated soils. This study highlights the unique capabilities of the GCM in modelling the water retention and mechanical behaviour of unsaturated soils. Namely, its ability to capture the scanning, main wetting and main drying water retention responses, the mechanical response (including volume change and shear strength), and the coupling between the water retention and mechanical behaviour. However, due to the multiple yielding scenarios that a given stress path can trigger, numerical integration of the model is challenging and adjustments towards a more simplified approach are desirable if the model is to be used in geotechnical practice. For this purpose, the capabilities of a simplified non-hysteretic version of the GCM, designed to streamline its formulation, are investigated in this paper. The non-hysteretic model requires less parameters and simplifies the identification of the elasto-plastic mechanism activated by a stress path, at the expense of limiting some of the original modelling abilities.

Key words: *Constitutive modelling, Unsaturated soils, Water retention behaviour, Mechanical behaviour, Hysteresis, Hydromechanical-Coupling.*

1 Introduction

Soils used in the construction of civil engineering infrastructure such as road and railway embankments are compacted, thus under unsaturated conditions, where voids between solid particles are filled with both liquid (water) and gas (air). The mechanical behaviour of unsaturated soils is greatly influenced by the amount of water present within the voids, and this is described by the Soil-Water Retention (SWR) response that relates water content (w) or degree of saturation (S_r) to matric suction (s) defined as the difference between pore air pressure (u_a) and pore water pressure (u_w). An important feature of unsaturated soils is that their soil-water retention curve exhibits hysteresis, where the evolution of S_r against s measured during drying differs from that measured during wetting. In order to capture this behaviour, the Glasgow Coupled Model (GCM) assumes that the hysteresis can be represented as an elasto-plastic process (as illustrated in Figure 1) [1].

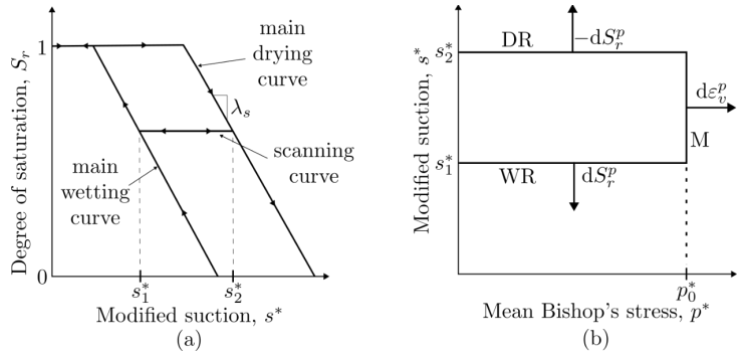

Figure 1: The GCM model under isotropic stress conditions: (a) Hysteretic water retention behaviour; (b) Mechanical (M), Drying Retention (DR), and Wetting Retention (WR) yield curves (after [1])

The GCM is able to represent water retention hysteresis through the use of two yield curves: one to represent plastic (or irreversible) decrements of degree of saturation ($-dS_r^p$) during drainage of pore water (Drying Retention, DR yield curve); and one to represent plastic increments of degree of saturation (dS_r^p) during filling of voids with water (Wetting Retention, WR yield curve) (Figure 1). One additional mechanical yield curve (M) is used to represent irreversible increases of plastic strain ($d\varepsilon_v^p$). The GCM is also able to represent the couplings between water retention and mechanical behaviour through a number of coupled movements between the three yield curves [1].

2 The GCM

The original formulation of the GCM was developed for isotropic stress states [1], then later extended to general stress states [2]. The GCM constitutive stress variables for isotropic stress states include the mean Bishop's stress (p^*) and modified suction (s^*) defined as follows:

$$p^* = p - S_r u_w - (1 - S_r)u_a = \bar{p} + S_r s \tag{1}$$

$$s^* = n(u_a - u_w) = ns \tag{2}$$

Where p is the mean total stress, $\bar{p}$ is the mean net stress, and n is the porosity. Note that when the soil becomes saturated ($S_r = 1$), Equation 1 for p^* becomes $p' = p - u_w$, where p' is the saturated mean effective stress for saturated soils. A detailed description of the elasto-plastic framework, including the governing equations, can be seen in previous works [2] and only a very brief description of the most relevant features for this work is included next. Elastic increments of volumetric strains ($d\varepsilon_v^e$) are related to the gradient of the elastic swelling line (κ) in v: lnp^* plane, where v is the specific volume. As discussed in [3], elastic variations of degree of saturation (dS_r^e) are assumed to be zero in the GCM (Figure 1a) to avoid inconsistent representations of the transitions between saturated and unsaturated conditions. The hardening parameters of the M, DR and WR yielding curves are p_0^*, s_1^*, and s_2^*, respectively (Figure 2).Yielding only on the M curve under isotropic stress conditions, produces plastic increments of volumetric strain ($d\varepsilon_v^p$) which are related to the gradient of the normal compression line (λ) in v: lnp^*plane. Yielding on the DR or WR yielding curve alone would produce plastic decrements or increments of S_r and these are related to the gradient of main drying and wetting retention curves (λ_s) in the S_r: lns^* plane (Figure 1a).

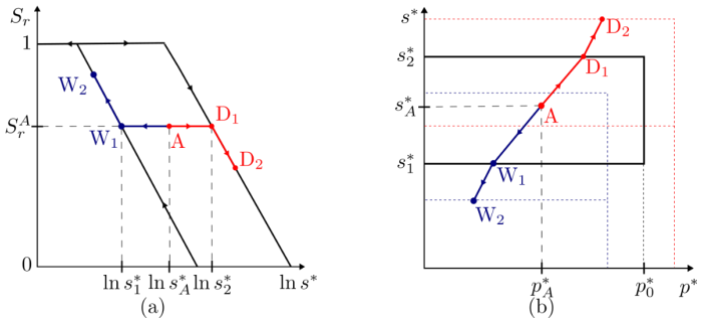

Figure *2*: The GCM model for isotropic stress conditions: (a) Typical wetting and drying water retention behaviour; (b) Typical wetting and drying paths involving water retention yielding.

To demonstrate how hysteresis is represented within the GCM, a soil under unsaturated conditions ($S_r < 1$) is considered, which state is on a scanning curve in the water retention plane S_r: lns^*, and located within the elastic domain in the s^*: p^* plane as shown by point A in Figure 2. During drying (without any mechanical yielding), plastic decrements of degree of saturation ($-dS_r^p$) start to occur after reaching the main drying curve at point D_1 (indicated by the drying retention hardening parameter s_2^*). Yielding on DR causes a coupled upward and outward movement of the WR and M respectively. This coupling mechanism represents the stabilising effect that the increasing number of meniscus water bridges during drying has on the soil skeleton (as $-dS_r^p$ hinders slippage at the interparticle contacts causing an increase in the mechanical hardening parameter p_0^*). An equivalent behaviour is observed for the typical wetting

path A-W_1 represented in Figure 2. Upon reaching the main wetting curve at point W_1, plastic increments of degree of saturation (dS_r^p) occur causing a downward and inward movement of the DR and M respectively. Due to the yielding on WR during wetting, the additional stabilising force offered by the number of meniscus water bridges at the interparticle contacts decreases, resulting in a lower value of the mechanical hardening parameter. During mechanical yielding, slippage occurs at the interparticle and interpacket contacts, causing a reduction in the size of the voids within the soil. This leads to a shift of the SWR response to higher values of modified suction [1]. These couplings between the water retention and mechanical behaviour are intrinsic within the GCM formulation and are controlled by the model parameters k_1 and k_2. Coupled movements of M during yielding on the DR and WR yield curves are given by coupling parameter k_1, whereas coupled movements of DR and WR during yielding on M are controlled by the second coupling parameter k_2. The number of parameters, yield curves and coupled movements result in a challenging mathematical framework for calibration and computational purposes [3,4]. The main computational challenge is associated with the determination of which is the correct model response activated by the stress path and adjustments towards a more simplified approach are desirable if the model is to be used more broadly, including in geotechnical practice. The study of such simplification by means of a non-hysteretic version of the GCM is the main goal of this paper.

3 A non-hysteretic form of the GCM

To adapt this non-hysteretic simplification, the two yield curves of the GCM associated with the water retention response (DR and WR) are merged to a single yield curve (Figure 3), streamlining the representation of yielding occurrences while simplifying the characterisation of the initial stress state. Any stress path in the water retention plane (S_r: lns^*), whether wetting or drying, would involve water retention yielding and the corresponding evolution of $S_r$would follow a single main water retention curve as illustrated in Figure 3a. For instance, the equivalent of the generic initial stress state A included in Figure 2, would correspond to A=D_1=W_1 when hysteresis is not considered (Figure 3), meaning that the initial value of s^* at A defines the initial position of WR and DR yield curves (as $s_A^* = s_1^* = s_2^*$).

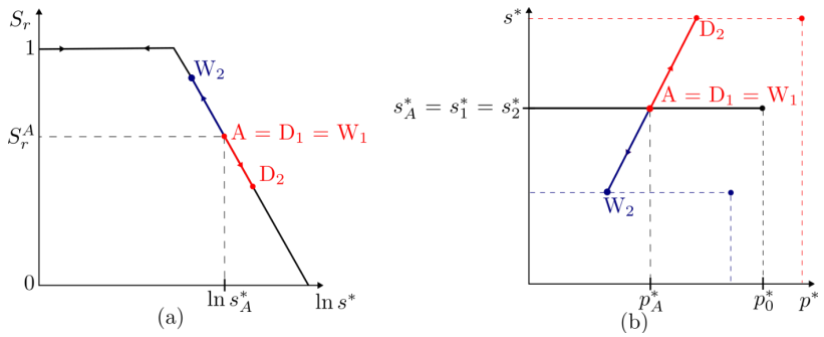

Figure *3*: The non-hysteretic GCM version for isotropic stress conditions: (a) Typical wetting/drying retention behaviour in the S_r: lns^*plane; (b) Typical DR and WR yielding stress paths in the s^*:p^*plane.

Six different material responses are possible within the GCM, including elastic behaviour, water retention yielding (DR and WR only), mechanical yielding (M only), and simultaneous yielding (M and WR) and (M and DR) as illustrated in Figure 4a. The coupling parameter k_1 marks the trajectory of the top and bottom corners in the lns^*: lnp^* plane (i.e., intersection between M and DR or between M and WR, respectively) during water retention yielding. Similarly, k_2 marks the trace of top and bottom corner movements during mechanical yielding (Figure 4a).

If hysteresis is not considered, the possible model responses simplify because of the highly unlikely occurrence of the elastic response and of yielding on only the M (Figure 4b). Elasto-plastic variations of degree of saturation and plastic volumetric strains are still represented. For instance, any increases of modified suction during drying would cause yielding on DR, producing irreversible decreases of S_r. Irreversible shrinkage during drying (i.e., simultaneous yielding between M and DR yield curves) is also still possible with the non-hysteretic version of the GCM. However, this model response would be highly dependent on the stress path and how it compares with the gradient of k_1 in lns^*: lnp^* plane (see Figure 4b).

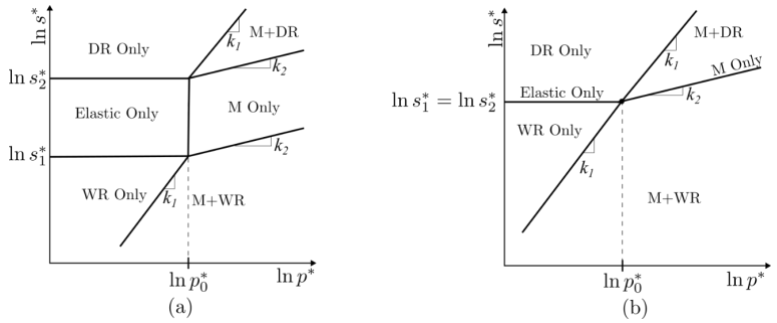

Figure *4*: Elastic and Elasto-plastic mechanisms in $\ln s^*:\ln p^*$plane: (a) GCM; and (b) non-hysteretic version of the GCM.

3.1 Discussion

Within the framework of the GCM, the separation of the DR and WR yield curves in the $s^*:p^*$plane to account for hysteresis allows for a wide range of modified suction values, at which scanning behaviour can be represented. This is particularly useful when modelling soils with a marked hysteretic behaviour and which are not possible to represent with the simplified version of the GCM presented here. More interesting, is the range of possible values of modified suction that a drying stress path (i.e., increases of suction) can experience when mechanical yielding begins to occur (see Figure 2b). A consequence of the range of modified suction values is that many different drying paths can activate yielding on M and cause plastic compression on drying (note that during a drying path, $p^*$and s^* would both increase as a consequence of the suction increase during drying as seen in Equations 1 and 2). Yielding on only the M during drying is highly unlikely to be predicted by the non-hysteretic version presented here, as the M yield curve is reduced to a single point and it will only be predicted when the direction of the drying stress path coincides exactly with the gradient of k_2 in the $\ln s^*:\ln p^*$plane as indicated in Figure 2b. However, it is still possible to represent plastic shrinkage on drying by the non-hysteretic GCM if the stress path activates simultaneous yielding between M and DR curve (see Figure 2b). Future research is needed in this direction to further investigate the likelihood of representing irreversible shrinkage on drying and to investigate how well the non-hysteretic GCM responses compare against experimental results.

4 Conclusions

This study introduces a non-hysteretic simplification to the GCM, where the two water retention yield curves (DR and WR) are merged into a single yield curve. This simplification reduces the number of parameters required and removes the occurrence of elastic changes in degree of saturation. It also makes the determination of the model mechanism active a much simpler process as less intersections of the stress path with a particular yield curve are needed (given that the initial stress state is already on the WR and DR yield curves). However, this simplification leads to some modelling limitations especially in the representation of plastic volumetric strains during drying paths which are only possible for simultaneous yielding on M and DR.

References

[1] S. J. Wheeler., R.S. Sharma., M.S.R., Buisson (2003). Coupling of hydraulic hysteresis and stress–strain behaviour in unsaturated soils, Géotechnique, 53(1)., 41-54.
[2] M. Lloret-Cabot., M. Sánchez., S.J. Wheeler., (2013). Formulation of a three-dimensional constitutive model for unsaturated soils incorporating mechanical–water retention couplings. International Journal for Numerical and Analytical Methods in Geomechanics, 37(17), pp.3008-3035.
[3] M. Lloret-Cabot., S.J. Wheeler., M. Sánchez (2017). A unified mechanical and retention model for saturated and unsaturated soil behaviour, Acta Geotechnica 12: 1
[4] M. Lloret-Cabot., S.J. Wheeler., A. Gens., S.W. Sloan (2021). Numerical integration of an elasto-plastic critical state model for soils under unsaturated conditions, Computers and Geotechnics, 137., 104299.-21.

UKACM 2024 Conference, 10-12 April 2024, Durham University, Durham, UK
https://doi.org/10.62512/conf.ukacm2024.071

Comprehensive Post-Failure Analysis of Rainfall-Induced Landslides Under Various Rainfall Patterns

Xian Liu[1,2], Guotao Ma[1], Mohammad Rezania[1], Xueyou Li[2], Shuihua Jiang[3], Mohaddeseh Mousavi Nezhad[4]

[1] School of Engineering, University of Warwick, Coventry, CV4 7AL, UK
[2] School of Civil Engineering, Sun Yat-Sen University, Zhuhai 519082, P. R. China
[3] School of Infrastructure Engineering, Nanchang University, Nanchang 330031, P. R. China
[4] School of Engineering, University of Liverpool, Liverpool, L69 3BX, UK
Liux597@mail2.sysu.edu.cn
Derek.ma.1@warwick.ac.uk
M.rezania@warwick.ac.uk
Lixueyou@mail.sysu.edu.cn
Sjiangaa@ncu.edu.cn
M.Mousavi-Nezhad@liverpool.ac.uk

Abstract

Rainfall infiltration presents a significant hazard to slope stability in various global regions. While most previous researches focus on the variations in the factor of slope safety under rainfall infiltration, there is a notable lack of attention to post-failure behaviors of slopes, e.g., the large deformation of slopes triggered by rainfall is often ignored. This is due to the traditional slope stability analysis methods, such as the limit equilibrium method (LEM) and finite element method (FEM), struggle with modeling large deformation of soils. Moreover, the impact of rainfall patterns on the post-failure behaviors of rainfall slopes remains unexplored. To address these issues, this study proposes a new effective coupled method to quantify the post-failure behaviors of landslides affected by different rainfall patterns, employing a combination of FEM and the Generalized Interpolation Material Point (GIMP) method. The results show that the slope failure times for different rainfall patterns are 14 h (uniform), 14 h (advanced), 4 h (delayed), 9 h (intermediate), and 11 h (intermittent), with corresponding runout distances of 2.76 m, 2.95 m, 2.06 m, 2.31 m, and 2.55 m, respectively. Analyzing the large deformation analysis of rainfall-induced landslides can offer new insights to quantitatively identify post-failure features of such disasters.

Key words: *Landslides; Rainfall infiltration; GIMP; Rain patterns*

1 Introduction

Rainfall is widely acknowledged as the principal trigger for landslides [1-3]. As it infiltrates the soil, it not only increases the water content and unit weight but also affects the shear strength and matric suction, ultimately leading to a decrease or loss of these properties. Up to now, the majority of current research concentrates on the stability analysis of rain-induced slopes by assessing the minimum factor of safety (FS_{min}), the post-failure behaviors of slopes, such as the runout distance, frequently receives less attention [4-5]. Additionally, numerical studies have shown that rainfall patterns significantly influence the stability of unsaturated slopes, directly impacting the distribution of pore water pressure within the slope. If the effects of rainfall patterns on slope stability are overlooked, the accuracy of reliability estimations and the predicted post-failure behaviors of slopes at risk of rainfall-induced failure may not align with geotechnical practices.

To address these, this paper aims to explore the impact of rainfall patterns on slope stability and quantify the post-failure behaviors of slopes. A hybrid approach combining the FEM and GIMP is proposed, using a slope example as a case study for validation. The findings of this study offer significant contributions to the risk assessments of rain-induced landslides under actual rainfall event, providing new insights and methodologies to enhance their accuracy and reliability.

2 Problem description

Unsaturated seepage analysis of slope under rainfall is a complicated process due to the dynamic variations of pore water pressure, matrix suction and water content distribution over time. The Richards' equation is adopted here for the simulation the rainfall infiltration process on the slope [6]:

$$\frac{\partial}{\partial x}\left(k_x \frac{\partial h}{\partial x}\right)+\frac{\partial}{\partial y}\left(k_y \frac{\partial h}{\partial y}\right)+Q=\frac{\partial \theta}{\partial t} \tag{1}$$

where h is the total head; k_x and k_y are the hydraulic conductivities in x and y directions, respectively; θ denotes the volumetric water content; t is the time; Q represents the applied boundary flux. The GIMP-based MPM3D, an open-source code, to evaluate the large deformation of slopes in our simulations. More details about GIMP algorithm can be found in [7-8].

3 Illustrative Example

In this Section, a slope example experiencing rainfall infiltration, as shown in Fig. 1, is utilized to depict the comprehensive process of landslides triggered by rainfall under rainfall patterns. The slope has a height of 10 m, a foundation of 4 m and a slope angle of 35.5°. Table 1 summarizes the soil properties that used in the analysis [4]. The key soil parameters include the saturated hydraulic conductivity (k_s) of 1×10^{-5} m/s and the effective friction angle (ϕ) of 30°. Following [4], the soil layer is initially unsaturated with a uniform matric suction of 20 kPa. In Fig. 3, the rainfall boundary is represented by blue lines and applied to the surface of slope, the lateral boundaries of the slope are defined as free-roller and impermeable in the normal direction, indicated by green lines. Furthermore, the slope's bottom boundary is established as a free-roller and impermeable in both directions. Additionally, groundwater is not considered in this study and is assumed to be deep [9].

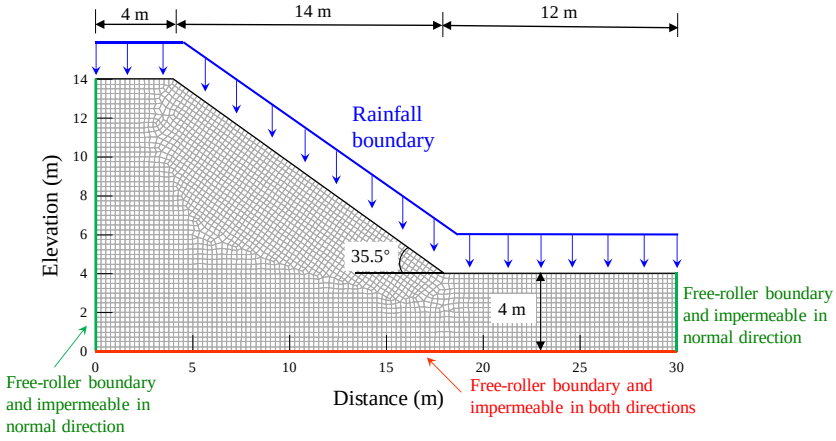

Figure 1. The geometry of slope

Initially, the seepage and stability analyses of the slope are conducted under a uniform rainfall pattern, maintaining a constant rainfall intensity, e.g., $R = 5\times10^{-6}$ m/s. For the seepage analysis, the van Genuchten model is applied, characterized by parameters a = 4.905 kPa and n = 1.4. The slope is discretized into 3847 finite elements with the size of 0.25 m, as shown in Fig. 1. The time of rainfall infiltration takes 20 h.

Table 1 Values of soil parameters

Soil Parameters	Definition	Value
k_s	Saturated hydraulic conductivity, m/s	1×10^{-5}
c	Effective cohesion, kPa	0
ϕ	effective friction angle, °	30
E	Young's modulus, MPa	100
a	Curve-fitting parameters, kPa	4.905
n	Curve-fitting parameters	1.4
n	Initial porosity	0.3
η	Hydraulic conductivity parameter, m^{-1}	1.962
γ	Unit weight of soil, kN/m^3	26.5
γ_w	Unit weight of water, kN/m^3	9.8

Fig. 2 displays the contours of pore-water pressure, along with the corresponding critical slip surface of

pressure increases in the shallow parts of the slope, lead to the soil in these areas will be becomes almost saturated. However, the soil at greater depths remains in its natural condition. The FS_{min} decreases as the rain event continues. Fig. 2(c) demonstrates that the slope remains stable after 13 h rainfall infiltrate (i.e., FS_{min} >1.0), indicating that rainfall lasting less than 13 hours will not trigger a landslide. However, as depicted in Fig. 2(d), when the duration of rainfall extends to 14 h, the FS_{min} falls below 1.0, signifying means that the slope becomes unstable at this point.

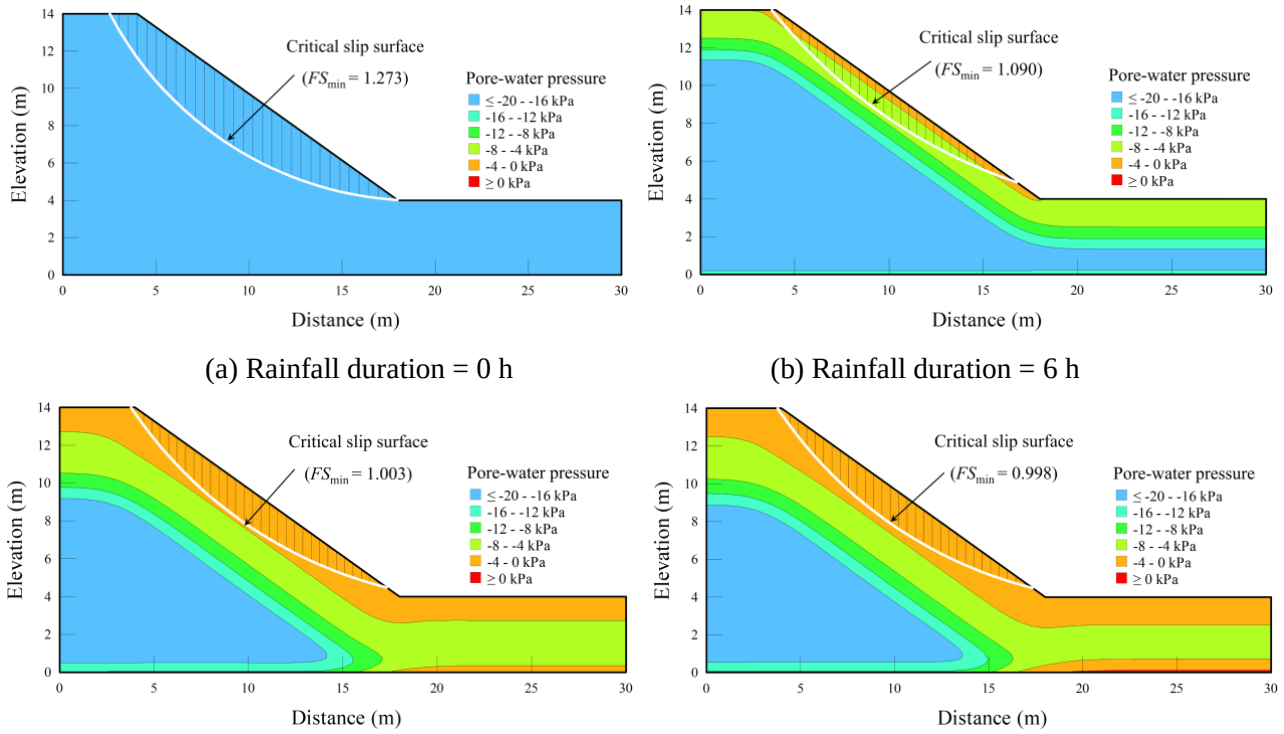

(a) Rainfall duration = 0 h

(b) Rainfall duration = 6 h

(c) Rainfall duration = 13 h

(d) Rainfall duration = 14 h

Figure 2. Contours of pore-water pressure and the corresponding critical slip surface of slopes at different rainfall durations

Figure 2(d) reveals that the slope fails, initiating a landslide with significant deformation occurring after 14 h. Therefore, the seepage analysis results at the time of 14 hours were extracted and employed to set the initial conditions for particles in the MPM simulation. These conditions include degree of saturation, pore water pressure, and stresses. In MPM simulation, the slope will be discretized into a total of 5755 particles with a background grid size of 0.4 m × 0.4 m, and the MPM simulation time is set as 11 s. The kernel interpolation facilitates the mapping of pore-water pressure from the FEM model to the MPM model, with the results of this process illustrated in Fig. 3. Notably, the distribution of pore-water pressure in the MPM model closely matches the FEM results following the mapping. Figure 4 presents the MPM simulation result of the landslide after 14 hours rainfall, and the runout distance is 2.76 m.

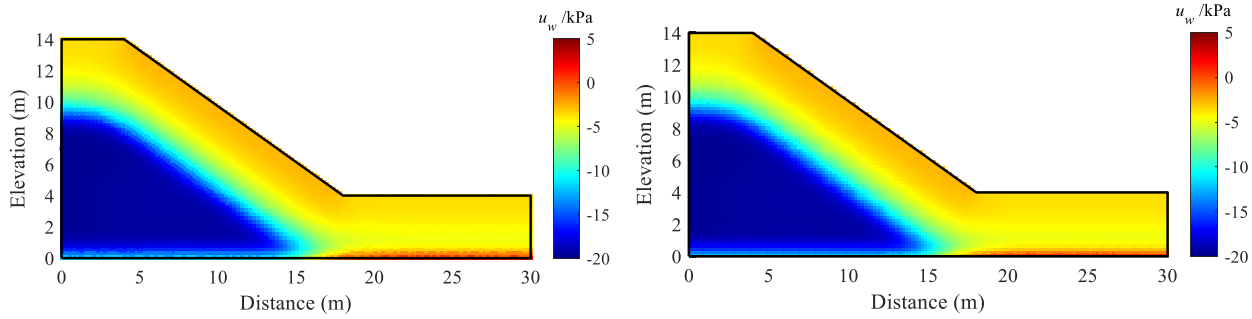

(a) FEM model

(b) MPM model

Figure 3. Comparison of pore-water pressure between the FEM models and MPM models

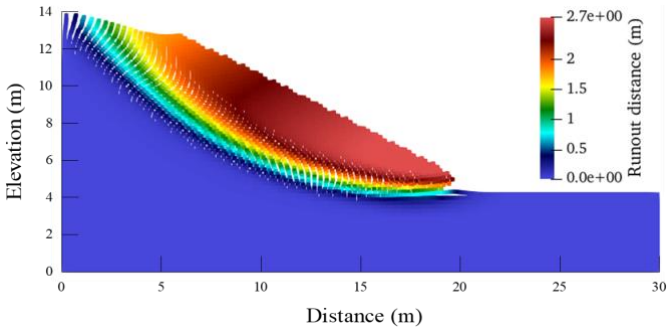

Figure 4. Results of MPM simulation after 14 h rainfall

As reported by [10], this paper highlighted the significant role of rainfall patterns on slope stability, and four different rainfall patterns, e.g., Uniform, Advanced, Delayed and Intermediate. Additionally, in daily life, the rain events may not always be continuous, and [11] categorizes such sporadic rainfall as intermittent. Therefore, to assess the impact of rainfall patterns on the stability and runout distance of rainfall-induced slopes, these five rainfall patterns, are analysed here. Keep the amount of rainfall as the same in all five cases, the detailed information about these five rainfall patterns can be seen in Fig. 5. Fig. 6 displays the contours of pore-water pressure and the corresponding failure times under various rainfall patterns. It is evident that the slope's failure occurs at different times for different rainfall patterns. Notably, the slope fails earlier in the case of delayed rainfall pattern (e.g., after 4 hours), this is possibly due to the high rainfall intensity at the start of rainfall event, resulting in larger amount of rainwater infiltration into the soil. Consequently, the shallow parts of the slope become saturated more quickly, leading to an earlier slope fail.

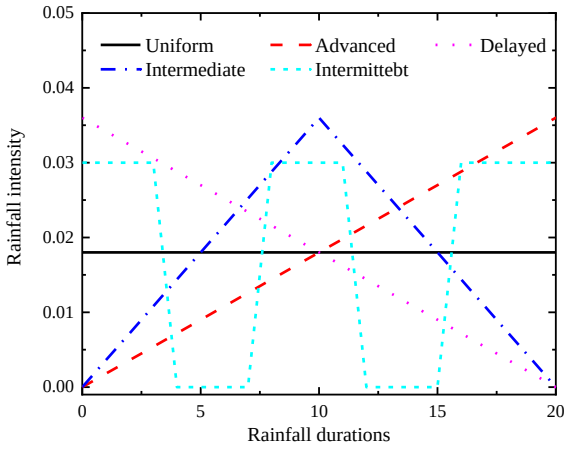

Figure 5. Comparison of rainfall intensity versus rainfall duration for five rainfall patterns

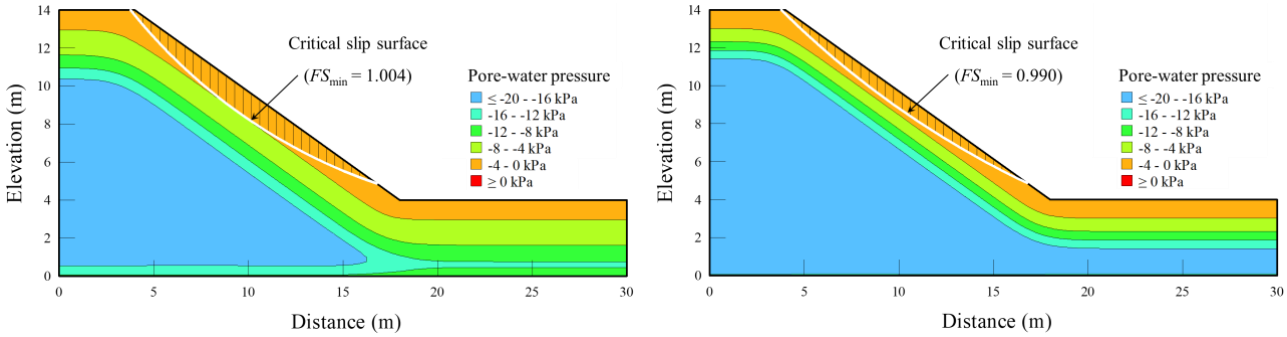

(a) Advanced (t = 14 h) (b) Delayed (t = 4 h)

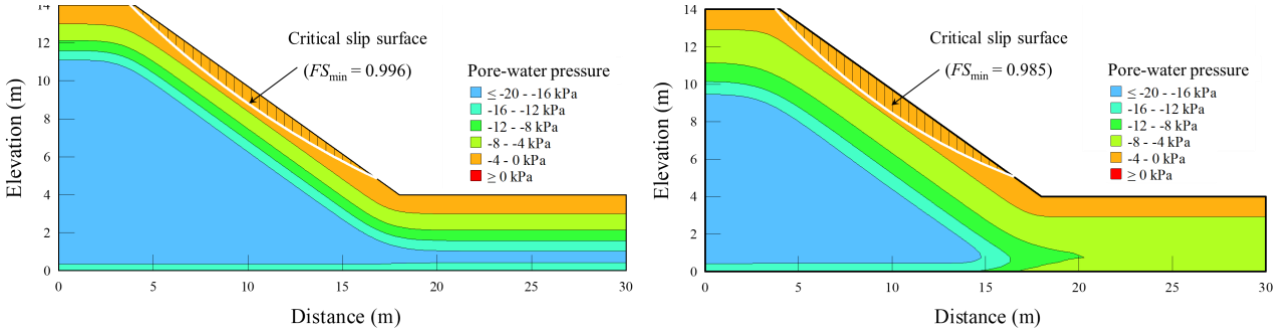

(c) Intermediate (t = 9 h) (d) Intermittent (t = 11 h)

Figure 6. Contours of pore-water pressure and the corresponding failure time under four rainfall patterns

The results presented in Fig. 6 are then applied to the MPM model for analyzing large deformations, with the calculated runout distances under various rainfall patterns illustrated in Fig. 7 for comparison. It is observed that delayed rainfall patterns lead to shorter runout distances. This phenomenon can be attributed to the earlier failure of the slope, which in turn results in a smaller wetted zone. Consequently, the mass of the landslide is reduced, leading to shorter runout distances. The advanced rainfall pattern results in the longest runout distance, likely due to the extended duration of rainfall, allowing more rainwater to impact slope stability. Overall, rainfall patterns significantly influence slope stability, not only affecting the FS_{min} and the timing of slope failure, but also impacting the risk assessment of the slope post-landslide events.

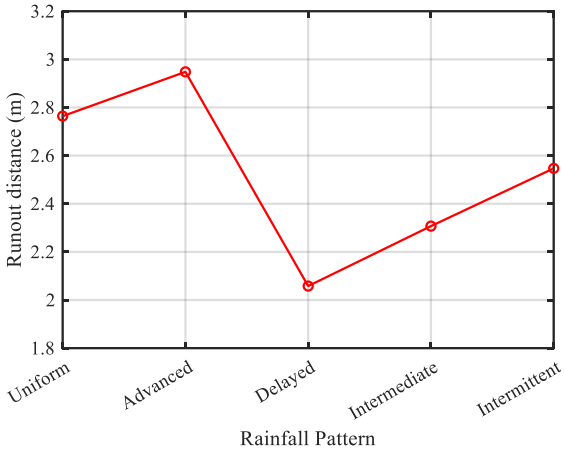

Figure 7. Relationship between the runout distances and rainfall patterns

4 Conclusions

This paper proposes a hybrid methodology that integrates the FEM and GIMP for simulating rain-induced landslides, and quantitatively assesses the post-failure behaviors of slopes through runout distance. Moreover, the study examines the impact of five prevalent rainfall patterns (i.e., uniform, advanced, delayed, intermediate and intermittent) on slope stability. The respective failure times for these patterns are 14 h, 14 h, 4 h, 9 h, and 11 h, with corresponding runout distances of 2.76 m, 2.95 m, 2.06 m, 2.31 m, and 2.55 m. The study reveals that relying solely on the uniform rainfall pattern may lead to biased results of both the failure timing and runout distance of slopes. Incorporating a widely range of rainfall patterns provides a more thorough insight into slope stability and enhances risk assessment accuracy.

Acknowledgments

The financial support by supported by the European Commission's RFCS project MINRESCUE (Contract RFCS-RPJ-899518) and the National Natural Science Foundation of China Project (Contract: 51909288, 52150610492, 52350610265) are gratefully acknowledged.

References

[1] Bandara, S., Ferrari, A., Laloui, L. (2016). Modelling landslides in unsaturated slopes subjected to rainfall

infiltration using material point method. International Journal for Numerical and Analytical Methods in Geomechanics, 40(9), 1358-1380.

[2] Chang, Z. L., Huang, F. M., Huang, J. S., Jiang, S. H., Zhou, C. B., Zhu, L., (2021). Experimental study of the failure mode and mechanism of loess fill slopes induced by rainfall. Engineering Geology, 280, 105941.

[3] Jiang, S. H., Liu, X., Ma, G., Rezania, M. (2024). Stability analysis of heterogeneous infinite slopes under rainfall-infiltration by means of an improved Green-Ampt model. Canadian Geotechnical Journal, https://doi.org/10.1139/cgj-2023-0203.

[4] Liu, X., Wang, Y. (2021). Probabilistic simulation of entire process of rainfall-induced landslides using random finite element and material point methods with hydro-mechanical coupling. Computers and Geotechnics, 132, 103989.

[5] Yerro, A., Soga, K., & Bray, J. (2019). Runout evaluation of Oso landslide with the material point method. Canadian Geotechnical Journal, 56(9), 1304-1317.

[6] GEO-SLOPE International, L., (2008). Seepage modeling with SEEP/W 2007 Version: an engineering methodology [computer program], GEO-SLOPE International Ltd., Calgary.

[7] Ma, G., Rezania, M., Nezhad, M. M. (2022a). Stochastic assessment of landslide influence zone by material point method and generalized geotechnical random field theory. International Journal of Geomechanics, 22(4), 04022002.

[8] Ma, G., Rezania, M., Mousavi Nezhad, M., Hu, X. (2022b). Uncertainty quantification of landslide runout motion considering soil interdependent anisotropy and fabric orientation. Landslides, 19(5), 1231-1247.

[9] Li, X., Liu, X., Liu, Y., Yang, Z., Zhang, L. (2023). Probabilistic slope stability analysis considering the non-stationary and spatially variable permeability under rainfall infiltration-redistribution. Bulletin of Engineering Geology and the Environment, 82(9), 350.

[10] Wu, L. Z., Xu, Q., & Zhu, J. D. (2017). Incorporating hydro-mechanical coupling in an analysis of the effects of rainfall patterns on unsaturated soil slope stability. Arabian Journal of Geosciences, 10, 1-11.

[11] Lanza, L. G. (2000). A conditional simulation model of intermittent rain fields. Hydrology and Earth System Sciences, 4(1), 173-183.

Geotechnical Modelling 2: Rock Failure and Structural Interaction

UKACM 2024 Conference, 10-12 April 2024, Durham University, Durham, UK
https://doi.org10.62512/conf.ukacm2024.001

Continuum (PFEM) and discrete (DEM) modelling of pile installation in rocks

Matteo O. Ciantia[1,2*]
[1]School of Science and Engineering
University of Dundee
Small's Lane, DD1 4HR, Dundee, UK
e-mail: m.o.ciantia@dundee.ac.uk
[2]Department of Earth and Environmental Sciences
University of Milano-Bicocca
Piazza della Scienza 4, 20126 Milan, IT
e-mail: matteo.ciantia@unimib.it

Abstract

Recent advancements in computational efficiency have enabled the application of advanced numerical models to solve challenging large-displacement soil structure interaction problems such as pile installation in non-linear irreversible materials prone to softening type of behaviour. Such challenging problems however require specialized approaches due to material and geometrical non linearities combined to the large deformation soil-structure interaction. This paper presents a comparison of two approaches for modelling open ended (OE) pile installation in soft, crushable and collapsible rocks. The first approach employs the Discrete Element Method (DEM), which represents the rock as separate particles bonded together, and introduces a new contact model for highly porous rocks. The second approach uses the Geotechnical Particle Finite Element Method (GPFEM) and investigates the coupled hydromechanical effects during pile installation using a robust and mesh-independent implementation of an elastic-plastic constitutive model at large strains. The DEM approach explores the micromechanical features of pile plugging and unveils the mechanisms behind radial stress distributions inside and outside the plug. The study highlights the strengths and limitations of each modelling technique, providing insights into the behaviour of OE piles installed in soft rocks.

Key words: *Displacement piles, Large deformations, DEM, GPFEM, Installation, Chalk*

1 Introduction

Designing foundations in soft, porous rocks presents a significant challenge due to the material's complex mechanical behaviour. Upon loading soft rocks may crush and collapse and, if saturated, consequent pore water pressure build up would further reduce the effective stress. Material behaviour would then change from stiff elastic to a non-linear irreversible soil-like one, characterised by completely different hydraulic properties. Whilst for low levels of loading, an elastic response may facilitate design, the insertion of a rigid body like a steel pile will definitively remould the rock [1] and therefore suffer from the above-mentioned consequences. Small scale physical modelling in soft rocks has revealed that the damage process is completely different when comparing a closed-ended cone shaped pile with an open-ended (OE) tubular one [2]. For this reason, the post-installation stress field will change depending on the geometry of the penetrating object. Current practice for pile design in soft rocks is moving towards cone penetration test (CPT) methods [3] where radial stress profiles around open-ended piles pushed into soft rocks are inferred from the CPT response. This is a promising step forward although it is not yet clear if such stress profiles are representative for large diameter OE piles.

In recent years, several numerical methods able to overcome difficulties related to large deformations and various types of non-linearities have been developed. On one side, the Discrete Element Method (DEM), often used to investigate elemental soil behaviour, has been shown to be an appropriate tool that with reasonable computational power can be used to simulate boundary value problems (BVPs). Several boundary value problems including pile penetration [4,5] and screw piles [6] have been investigated using the DEM.

On the other hand, amongst various continuum approaches, the Geo-Particle Finite Element Method (GPFEM) has been shown to be able to manage large deformations and address the complexities of nonlinear soil behaviour [7]. GPFEM has been shown to be suitable to investigate CPT installation and interpretation in structured ground [8]. Thanks to its robust large deformation hydro-mechanically-coupled formulation it was used to study installation problems in chalk in partially drained conditions [9].

Both DEM and GPFEM have advantages and disadvantages. For example, whilst DEM only requires calibration of simple physical parameters to capture soil behaviour quite realistically at the macroscale, it is computationally demanding, particularly if hydro-mechanical problems need to be modelled. In contrast, continuum approaches were developed from the outset to solve BVPs, but strongly depend on the ability of the constitutive relationship used to accurately simulate soil behaviour. In this work DEM and GPFEM are used to investigate the installation process of an OE pile in a soft rock. Reference experimental data by [2] that used X-ray tomography will be used as a validation dataset.

1 Numerical frameworks

1.1 DEM for porous rocks

The behaviour of rocks has been historically modelled in DEM by introducing cohesive bonds through the Bonded Particle Method (BPM) [10]. [11] recently developed a bond-softening damage model able to capture the complex pressure dependent behaviour of weakly cemented porous rocks. Such a contact model, which is used in this study, is defined within the macro-element framework characterized by a generalized force-displacement failure envelop. The behaviour in the (i) normal (N), (ii) tangential (V) and (iii) bending direction ($\breve{M}$) is linear elastic within the yield surface, according to Euler beam theory. The overbar symbols $\widetilde{M}, \bar{N}$ and $\bar{V}$ represent the size of the yield surface on a given axis and are function of the bond tensile (σ_0) and shear (τ_0) strength. Once the combined load reaches the yield surface the bond starts accumulating damage. This damage variable (D_d) then affects the size of the yield surface modifying σ_0 and τ_0 through plastic softening. D_d depends on the irreversible displacements in the normal u_n^p and tangential u_s^p direction and the irreversible rotation θ_b^p. Refer to [11] for details on calibration and model parameters.

1.2 GPFEM of structured soils

The GPFEM is based on a standard FEM framework that, through continuous remeshing, mitigates mesh distortion issues. The efficiency of the numerical approach lies in the use of low-order triangular elements which simplify the remeshing process. To avoid interlocking issue, a mixed formulation is used. The constitutive model used in this work is an extension of Modified Cam Clay to incorporate bonding [12]. In addition to the standard preconsolidation pressure of the unbonded material p_s, an extra internal variable related to the tensile strength of the rock (p_t) is used to account for bonding. The shape of yield surface is controlled by M_f while $M_g$controlles the plastic flow. The hardening internal variables evolve with deviatoric and volumetric plastic strains. $\rho_{s,t}$ and $\xi_{s,t}$ are constitutive model parameters controlling the rate of hardening and softening. The material parameters reported in [9] were calibrated against a combination of literature data and element tests on Saint Nicholas at Wade (SNW) chalk [13]. Refer to [9] for further details.

2 Model pile simulations

Figure 1 shows the numerical model reproducing the experimental set up for the model pile installation tests in SNW chalk by [2]. In the experiment a tubular pile with external diameter of 8 mm and wall thickness of 1 mm was jacked to a depth of 2 cm in a cylinder of diameter 100 mm and length of 120 mm. The axisymmetric simplification of the geometry along with some geometrical quantities are represented in Figure 1. The figure also shows the DEM and GPFEM numerical model initial conditions. Axisymmetric conditions for DEM models are extremely challenging due to the particles on the symmetry axis and therefore a 3D model is used. The rock domain is generated using the periodic cell replication method PCRM [14]. It consists of a combination of different techniques aimed at speeding up large DEM models generation. To reduce the computational burden, the PSD of destructured chalk was upscaled by a factor of 2.1 near the pile (<0.6D) increasing to a factor of 4.8 at 2.5D. Considering that the damage model is framed to be scale independent the scaling used does not affect the calibrated parameters [11]. The maximum and minimum particle size was 0.18 mm and 0.066 mm, respectively, with a d50 of 0.116 mm. To limit scale effects on potential plugging behaviour [4], this scaling value was chosen to provide a sufficient number of particles in contact with the pile whilst keeping the computational burden manageable. Pile wall thickness (t_w) to d50 ratio is 4.0. To mitigate computational load and prevent boundary effects, the edges of the DEM domain are coupled with a Finite Difference Model (FDM). Additional details on DEM-FDM model coupling are available in [11]. Given the significant stiffness contrast between the pile and the rock, the pile representation is simplified by using a rigid,

non-deformable wall and the installation force is obtained as the sum of the vertical contact forces. The GPFEM model generation is much simpler as initial conditions can be directly assigned as for classic FE models. Moreover, axisymmetric conditions are easily modelled with continuum methods and are hence here used. Although the experiments were performed pushing the pile slow enough to attain drained conditions, the simulations were carried out using a coupled hydro-mechanically formulation. As with the DEM model, the pile is simplified as a perfectly rigid wall and the installation force is measured as the sum of the contact forces. Boundary conditions are represented in Figure 1.

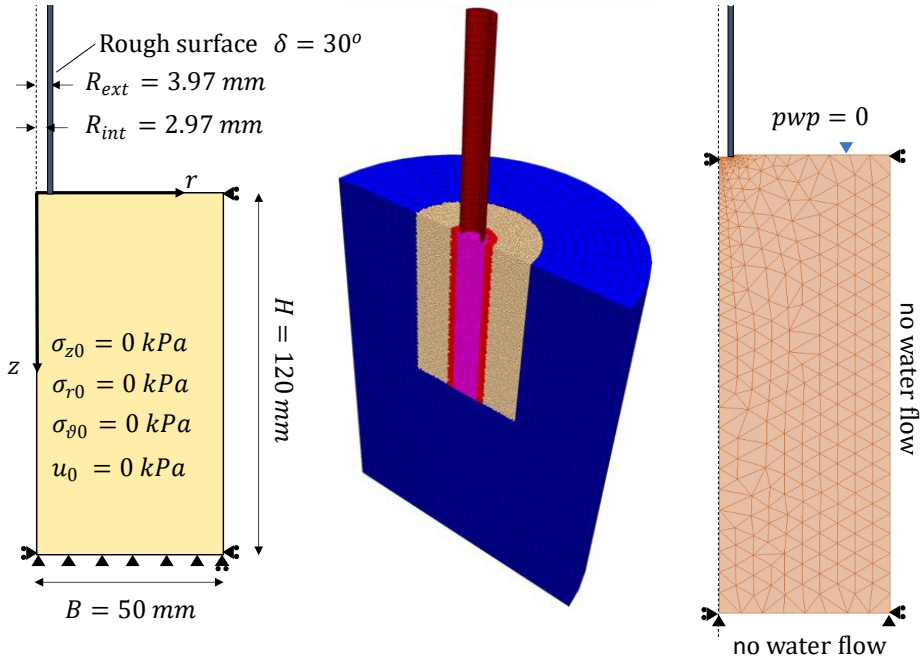

Figure 1: Model pile tests experimental setup by [2] along with geometrical quantities and snapshots of the discrete and continuum numerical model initial states.

2.1 Results

Figure 2 compares the experimental against the load displacement curve predicted by the two numerical models. The general trend is very similar although the GPFEM simulation seems to underpredict the penetration force. There are several reasons for such discrepancy. These include for example, the constitutive model softening parameters or the approximation of the flat tip with a curved geometry to avoid the sharp corners. Figure 2 also shows contours of the radial stresses close to the pile tip. Whilst the continuum and discrete model results appear very similar a more quantitative comparison would be required for a proper comparison.

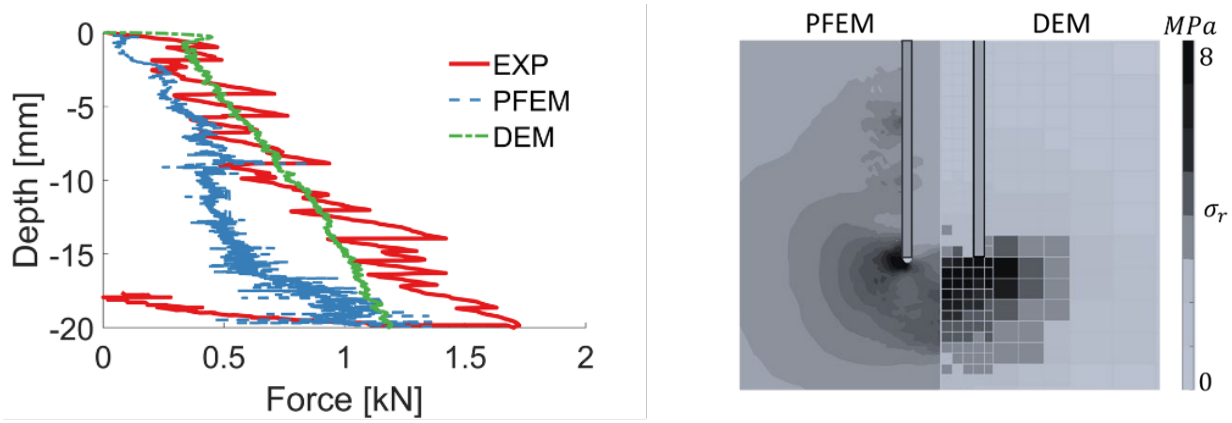

Figure 2: Force displacement curves (left) and radial stress contours (right) at the end of installation.

3 Conclusions

Two different numerical approaches, namely the DEM and GPFEM have been used to simulate open- ended pile installation in a soft chalk. Both procedures were able to overcome the difficulties associated with large displacements, large strains as well as geometrical, material and contact nonlinearities. The good agreement between the two methods and the experimental data indicates that both approaches are adequate for the investigation of open-ended pile installation in chalk

Acknowledgments

This work is funded by the ICE-PICK EPSRC EP/W00013X/1 project.

References

[1] Buckley, R. M., Jardine, R. J., Kontoe, S., et al. (2017). Ageing and cyclic behaviour of axially loaded piles driven in chalk. *Géotechnique*, 68(2):146–161.
[2] Alvarez-Borges, F. J., Richards, D. J., Clayton, C. R. I., et al. (2018). Application of X-ray computed tomography to investigate pile penetration mechanisms in chalk. *Proceedings of the Chalk 2018 Conference*, pp. 565–570.
[3] Jardine, R. J., Buckley, R. M., Liu, T., et al. (2023). The axial behaviour of piles driven in chalk. *Geotechnique*, pp. 1–45.
[4] Cerfontaine, B., Ciantia, M. O., Brown, M. J., et al. (2023). DEM study of particle scale effect on plain and rotary jacked pile behaviour in granular materials. *Computers and Geotechnics*, 161, pp. 105559.
[5] Ciantia, M. O., O'Sullivan, C., & Jardine, R. J. (2019). Pile penetration in crushable soils: Insights from micromechanical modelling. Proceedings of the 17th European Conference on Soil Mechanics and Geotechnical Engineering, pp. 298–317.
[6] Sharif, Y. U., Brown, M. J., Ciantia, M. O., et al. (2021). Using discrete element method (DEM) to create a cone penetration test (cpt)-based method to estimate the installation requirements of rotary-installed piles in sand. *Canadian Geotechnical Journal*, 58(7): 919–935.
[7] Carbonell, J. M., Monforte, L., Ciantia, M. O., et al. (2022). Geotechnical particle finite element method for modeling of soil-structure interaction under large deformation conditions. *Journal of Rock Mechanics and Geotechnical Engineering*, 14(3): 967-983
[8] Oliynyk, K., Ciantia, M. O., & Tamagnini, C. (2021). A finite deformation multiplicative plasticity model with non–local hardening for bonded geomaterials. *Computers and Geotechnics*, 137, pp. 104209.
[9] Previtali, M., Ciantia, M. O., & Riccio, T. (2023). Numerical installation of OE piles in soft rocks within the GPFEM framework. *Proceedings of the 10th European Conference on Numerical Methods in Geotechnical Engineering.*
[10] Potyondy, D. O., & Cundall, P. A. (2004). A bonded-particle model for rock. *International Journal of Rock Mechanics and Mining Sciences*, 41(8): 1329–1364.
[11] Zheng, J., Previtali, M., Ciantia, M.O., et al. (2023). Micromechanical numerical modelling of foundation punching in highly porous cemented geomaterials in a virtual Centrifuge environment. *CNRIG 2023*, pp. 390–397.
[12] Monforte, L., Ciantia, M. O., Carbonell, J. M., et al. (2019). A stable mesh-independent approach for numerical modelling of structured soils at large strains. *Computers and Geotechnics*, 116, pp. 103215.
[13] Riccio, T., Previtali, M., Ciantia, M.O., et al. (2023). The soft-oedometer: a simple test to calibrate advanced constitutive models for CPT simulations in soft socks. *CNRIG 2023*, 477–484.
[14] Ciantia, M. O., Boschi, K., Shire, T., et al. (2018). Numerical techniques for fast generation of large discrete-element models. *Proceedings of the Institution of Civil Engineers: Engineering and Computational Mechanics*, 171(4), 147–161.

UKACM 2024 Conference, 10-12 April 2024, Durham University, Durham, UK
https://doi.org/10.62512/conf.ukacm2024.015

G-PFEM Numerical Study of the Downward Trapdoor Problem

Ying Cui[1, 2*], Matteo O. Ciantia[2,3], Mamoru Kikumoto[1], Marco Previtali[2]

[1] Department of Engineering, Yokohama National University, Yokohama, JP.
sai-ei-mx@ynu.ac.jp, kikumoto-mamoru-fc@ynu.ac.jp
[2] School of Science and Engineering, University of Dundee, Dundee, Scotland, UK
m.o.ciantia@dundee.ac.uk, m.z.previtali@dundee.ac.uk
[3] Department of Earth and Environmental Sciences, University of Milano Bicocca, Milan, IT
matteo.ciantia@unimib.it

Abstract

The downward trapdoor provides a valuable framework for investigating stress distribution and ground movement during tunnel excavation. Numerous efforts have been made to devise analytical methods based on experimental observations. The area above the trapdoor experiences gravitational flow, and it becomes an active soil pressure condition with the lowering of the trapdoor. Due to the substantial discontinuous movement between the trapdoor and the adjacent stationary support, significantly discontinuous deformations arise at the boundary between the active zone above the trapdoor and the stationary zone. This complexity renders the trapdoor problem challenging by traditional continuum analysis methods. To confront this challenge, the present study employs the Particle Finite Element Method for geotechnical applications (G-PFEM) to simulate the downward trapdoor problem. The effectiveness of this approach is demonstrated by replicating a model experiment included in the literature. The simulation captures the gravitational flow of the surrounding ground as the trapdoor descends, and the numerical results, encompassing stress distributions, ground displacements, and surface settlements, closely correspond to experimental data. Moreover, to underscore the advantages of employing G-PFEM, a larger displacement is applied to the trapdoor. The results indicate significant changes in ground displacement and corresponding earth pressure as the trapdoor displacement increases, ultimately leading to substantial slope failure like large deformation.

Key words: *Trapdoor; aluminium-rod; numerical modelling; particle finite element method*

1 Introduction

The downward trapdoor is an experimental apparatus device used to investigate stress distribution changes and ground movement potentially occurring during tunnel excavation [1]. Various efforts have been made to develop analytical methods based on experimental observations. As the trapdoor descends, the area above it experiences gravitational flow, leading to an active soil pressure condition. Due to the large displacements involved and the significant discontinuous movement between the trapdoor and the adjacent stationary support, leading to discontinuous deformations at the edge of the trapdoor, [2] the trapdoor problem is challenging for traditional continuum analysis methods.

To address this, researchers have implemented a smooth deformation gradient at the node around the trapdoor edge, which differs from real experimental conditions [3]. Furthermore, large displacements forming the sinkholes resulting from tunnel excavation cannot be adequately simulated by traditional continuum analysis methods. To overcome these limitations, this study utilizes the Particle Finite Element Method for geotechnical applications (G-PFEM) [4] to simulate the downward trapdoor problem. The effectiveness of this approach is demonstrated by replicating a model experiment introduced in the literature [5]. Additionally, larger displacements were applied to the trapdoor to investigate the mechanical behaviour of the surrounding ground.

2 Model description

2.1 The G-PFEM

In this study, the Particle Finite Element Method for geotechnical applications (G-PFEM) [5] is used. G-PFEM is a continuum-based Updated Lagrangian method specifically designed for simulating large strain soil structure interaction problems, as demonstrated by Monforte et al. (2017) [6]. The approach uses continuous remeshing to mitigate element distortion. The computational burden associated with continuous remeshing is

mitigated by adopting low-order, constant strain mixed formulation triangular elements, while h-refinement allows for increased accuracy. Additional details can be found in Carbonell et al. (2022) [4].

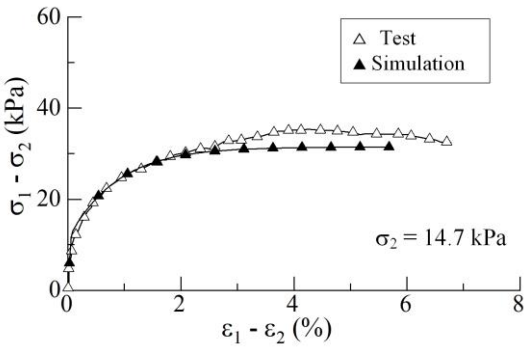

Figure 1: Biaxial compression test simulatoin

Table 1. Parameters for the MCC model

E (MPa)	20
ν	0.2
M_f	1.6
M_g	1.5
ρ_s	125
p_{s0} (kPa)	22.1
χ_s	0.3
l_c (mm)	1.5

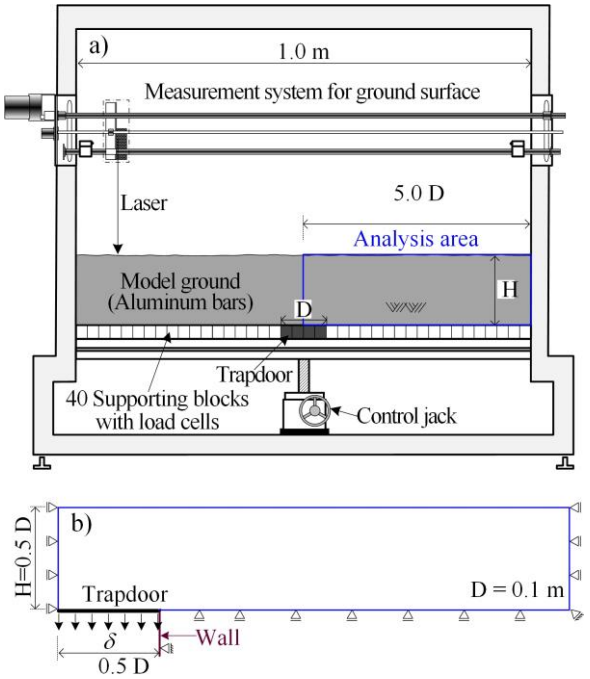

Figure 2: Modelling of the downward Trapdoor a) Two-dimensional trapdoor experiment apparatus (after [2]) b) Corresponding analysis area and boundary conditions

2.2 Constitutive model (modelling of the ground)

The mechanical behaviour of the aluminium rods is characterized using an isotropic hardening plasticity model based on the multiplicative decomposition of the deformation gradient. The yield surface and non-associated plastic potential are implemented through the Modified Cam Clay (MCC) model. The size of the yield surface in stress invariant space ($p' - q$) is given by the pre-consolidation stress $p_s := \dot{\gamma}\rho_s p_s(-\hat{V} + \chi_s \hat{D})$, where$\rho_s, \chi_s$ are hardening parameters and $\hat{V}, \hat{D}$ are the volumetric and deviatoric plastic strains, respectively. These plastic strain variables are substituted by their non-local counterparts to alleviate mesh dependency during strain localization. The model parameters are determined by fitting the results of biaxial compression tests, as depicted in Figure 1, listed in Table 1. The same parameter set is utilized for the trapdoor simulation except for p_s which is adjusted based on the stress conditions of the ground.

2.3 Modelling of the downward Trapdoor

Figure 2a) shows the two-dimensional trapdoor experimental setup [2]. As the trapdoor descends, the upper ground displaces accordingly, causing the surrounding ground to loosen. Thus, the trapdoor can model the loosening of the surrounding ground during activities such as tunnelling or mining.

Only a half-section was set as the analysis area, considering the plane-symmetry of the experimental setup. The analysis area and the boundary conditions are shown in Figure 2b). The trapdoor is modelled by a rigid wall, and a downward displacement is applied on the wall to simulate the lowering of the trapdoor in the experiment. With the lowering of the trapdoor, the upper ground is moving with gravity. The contact forces on this rigid wall were compared with the earth pressure on the trapdoor. It's important to note that in our approach, as for the experiments, we uniformly apply the same displacement across the entire plate. This is different from some other studies, where a smooth deformation gradient is used around the edge of the trapdoor to prevent mesh-interlocking issues caused by the highly discontinuous deformation at that edge.

In the trapdoor experiment, the aluminium rods flow into the space created with a lowered Trapdoor and adjacent plates. Therefore, a rigid vertical wall plate is set on the edge of the trapdoor to create the same space as the experiment that can control the horizontal movement of the ground. In the simulation the trapdoor is lowered to 10 mm.

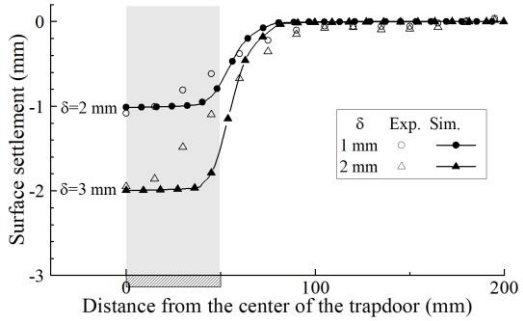

Figure 3: Surface settlement profile

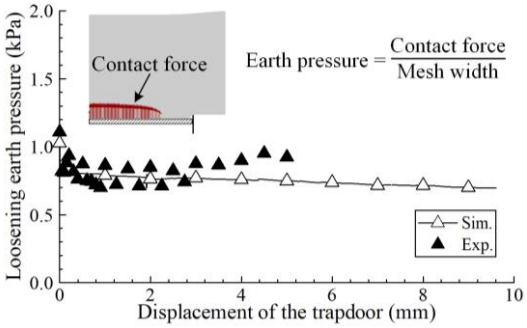

Figure 4: Variation of loosening earth pressure

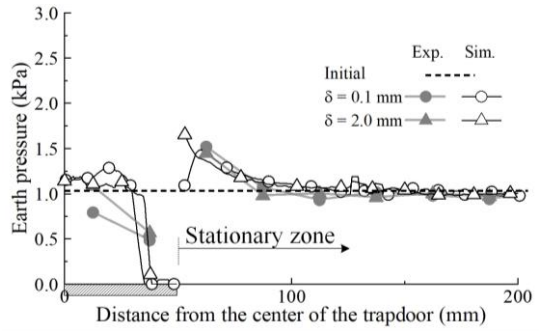

Figure 5: Earth pressure distribution

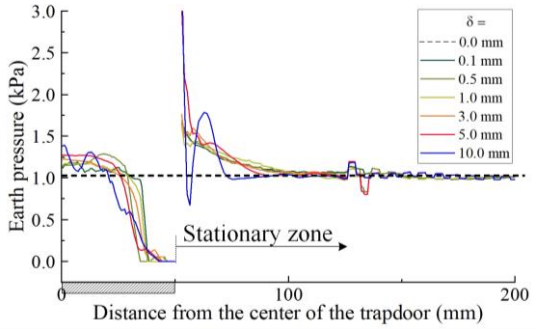

Figure 6: Variation of the earth pressure distribution

3 Results and discussion

3.1 Comparison with the experimental result

The surface settlement and earth pressure observed in the trapdoor experiment and G-PFEM are compared to validate the numerical simulation performance. Figure 3 illustrates the surface settlement profile, indicating that the maximum settlement occurs at the centre of the trapdoor with nearly identical values in both experiment and analysis. However, the settlement on the trapdoor is larger in the analysis compared to the experiment. Figure 4 presents the variation of the loosening earth pressure acting on the trapdoor. The earth pressure is calculated by dividing the contact force by the corresponding acting area size (mesh size). The loosening pressure is then obtained by averaging the earth's pressure. The experimental and simulation results show an initial rapid decrease in loosening earth pressure, followed by a stabilization phase. This observation suggests that the simulation effectively captures the experimental findings. Figure 5 compares the earth pressure distribution when the trapdoor is lowered to 0.1 mm and 2 mm. Both the earth pressure acting on the trapdoor and the surrounding stationary zone closely align with the experimental results. Additionally, the variation of the earth pressure distribution curve with trapdoor descent is accurately captured by the simulation.

3.2 Variation of the earth pressure distribution and ground movement

Figure 6 depicts the temporal evolution of the variation in earth pressure distribution. Up to a 3mm descent of the trapdoor, minimal changes in distribution are observed. However, upon reaching a 5mm descent, there is an increase in earth pressure at the stationary zone, accompanied by a slight decrease in the relaxed earth pressure acting on the trapdoor. Notably, descent up to 10mm reveals significant deformations resembling landslides occurring in the surrounding ground. These changes in the earth pressure distribution can be attributed to subsequent alterations in ground movements, as will be explained later.

3.3 Ground movement with lowering trapdoor

Figure 7a) illustrates the displacement of the surrounding ground caused by the lowering of the trapdoor, represented as a percentage relative to the lowering displacement of the trapdoor at each step. It is evident from the figure that the ground above the trapdoor moves downward concurrently with the descent of the trapdoor. This observation aligns with findings from previous studies, indicating that in cases of shallow overburden, the ground surface directly mirrors the displacement of the trapdoor. When the descent of the

trapdoor is less than 3mm, the subsidence pattern of the surrounding ground remains relatively consistent. However, when it exceeds 5.0mm, deformation of the surrounding ground occurs over a wider area.

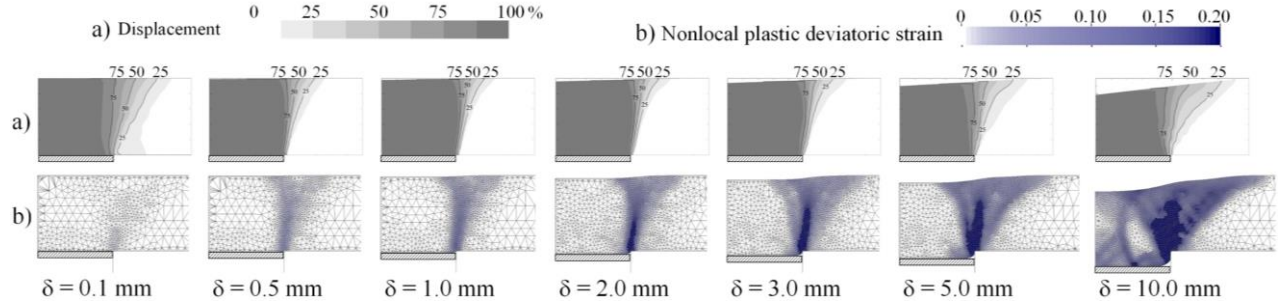

Figure 7: Development of a) ground displacement; b) shear band

Figure 7b) shows the shear zones generated by the movements of the surrounding ground formations. In the initial stage of displacement (0.5 mm in Fig. 7b)), inclined shear bands emerge slightly from the edge of the trapdoor and vertically extend towards the ground surface. As the displacement progresses, these shear bands gradually expand to the stationary zone, developing a large inverted triangular shape.

This observation suggests that for trapdoor displacements larger than 5 mm, the ground on the stationary zone becomes an active earth pressure zone, causing the upper ground soil to flow towards the trapdoor side. It is believed that these changes, including the gradual enlargement of the influence area of the surrounding ground due to the lowering of the trapdoor, ultimately lead to the collapse of the surrounding ground. This large deformation results in the redistribution of earth pressure (load redistribution), as depicted in Figure 6.

4 Conclusions

In this short paper, the applicability of the G-PFEM to model the trapdoor problem is validated through comparison with experimental results from the literature. The potential for further studies using G-PFEM are also discussed. We show that:

a) G-PFEM offers the advantage of simplifying and clarifying trapdoor displacement modelling, as it can directly apply large localized displacements. The simulation results demonstrate good agreement with the experimental results for surface settlement, load distribution, and temporal changes in loosening pressure.

b) for large trapdoor displacements, the surrounding ground tends towards a slope failure-like mode, accompanied by corresponding changes in load distribution. This suggests the potential for simulating surrounding ground failure due to large trapdoor displacements, enabling discussions of tunnel excavation stability in scenarios involving significant failures such as sinkholes.

References

[1] Terzaghi, K. (1936), Stress distribution in dry and saturated sand above a yielding trapdoor, Proc. of the 1st International Conference on Soil Mechanics and Foundation Engineering, Cambridge, Mass., 35-39.

[2] Mahdi, A., Han, J., Jawad, S. and Abdulrasool, G. (2017), Investigation of stability of soil arching under surface loading using trapdoor model tests, Proceedings of the 19th International Conference on Soil Mechanics and Geotechnical Engineering, Seoul: 889-892.

[3] George, T. I., Dasaka, S. M. (2023). Mechanics of arch action in soil arching, Acta Geotechnica, Volume 18, pages 1991–2009.

[4] Carbonell, J. M., Monforte, L., Ciantia, M. O., Arroyo, M., & Gens, A. (2022). Geotechnical particle finite element method for modeling of soil-structure interaction under large deformation conditions. Journal of Rock Mechanics and Geotechnical Engineering, 14(3), 967-983.

[5] Kikumoto, M. (2004), study on earth pressure mechanics around a tunnel, Ph.D. thesis, Kyoto University.

[6] Monforte, L., Carbonell, J.M., Arroyo, M., and Gens, A. (2017). Performance of mixed formulations for the particle finite element method in soil mechanics problems. Computational Particle Mechanics, 4(3): 269–284. Springer International Publishing.

[7] Monforte, L., Ciantia, M. O., Carbonell, J. M., Arroyo, M., & Gens, A. (2019). A stable mesh-independent approach for numerical modelling of structured soils at large strains. *Computers and Geotechnics*, 116, 103215.

UKACM 2024 Conference, 10-12 April 2024, Durham University, Durham, UK
https://doi.org/10.62512/conf.ukacm2024.017

A coupled damage-plasticity DEM bond contact model for highly porous rocks

Jinhui Zheng*, Matteo Ciantia, Marco Previtali, Jonathan Knappett

School of Science and Engineering, University of Dundee, Dundee, DD1 4HN, UK.
2431370@dundee.ac.uk

Abstract

In view of the significant stress loss induced by stuructural collapse when simulating high-porous soft rocks using traditional damage bond models in DEM (discrete element methd) modelling, a novel damage bond contact model is proposed to capture the ductile failure of high-porous cemented soft rocks. To address the unrealistic physical contact distribution resulting from the use of spherical particles in DEM modelling and consider the physical presence of broken bonds, far-field interaction is introduced between grains when two untouched particles reach a specific activation gap, enabling the genration of stable, highly porous open structure samples while using spherical DEM particles. The final results demonstrate that this newly developed model facilitates the transition from the purely elastic rock-like behaviour stage to the transitional ductile failure stage of porous soft rocks, as well as reproduces the softening/hardening response of soft rocks under different confinements.

Key words: *DEM contact model; High-porous bonded soft rock; Far-field interaction; Micro mechanics.*

1 Introduction

In general, rocks with an unconfined compressive strength (UCS) within the range of 0.5 to 25 MPa are collectively referred as soft rocks [1]. Typical examples include chalk, calcarenites and porous tuffs. Typical microstructure of soft rocks is usually characterised by angular grains connected by a chemical bond formed during their sedimentation and diagenesis process. This configuration often leads to a high-porous structures characterized by inter and intra-granular voids. Due to this, soft rocks exhibit unique mechanical responses, showing elastic rock-like behaviour transitioning to soil-like behaviour induced by the damaged microstructure during loading [2]. Under triaxial loading conditions, the behaviour depends on the confinement, as two competing effects develop in the sample: i) softening induced by bond degradation and ii) hardening attributed to the granular structure resulting from the rearrangement of particles. These two microscale effects are at the base of the complex behaviour oof soft rocks.

In recent years, there has been a growing trend in constructing engineering projects on porous rocks. For example, monopiles supporting offshore wind turbines built on the chalk in the North Sea [3] require a more economic foundation design while the intricate mechanical characteristics of high-the material poses challenges in assessing foundation bearing capacity, often leading to conservative designs. From a numerical perspective, the key to developing an improved foundation design lies in using advanced models enabling a comprehensive reproduction the complicated mechanical behaviour. Over the past few decades, several constitutive models based on plasticity theory and considering damage to cemented bonds, as well as models considering bond degradation based on macro-element method, have been proposed [4] [5]. However, these models regard soft rocks as continuous mediums and would require continuum modelling frameworks able to manage discontinuities and large deformations. These include PFEM [6], MPM [7], XFEM [8].

As an effective approach to address discontinuity issues, there are currently numerous models developed based on the DEM to describe the behaviour of cemented soft rocks. These models primarily focus on replicating the damage induced softening of cemented bonds to capture the ductile failure of soft rocks. For example, Nguyen et al. [9] proposed a damage bonded model by considering the bond damage caused by tension and shearing, where the evolution of bond damage follows an exponential damage law attributed to the plastic deformation of the bond. Subsequently, a new model incorporating compressive damage was developed by Senanayake et al. [10] based on Nguyen et al. [9]'s work. Zheng et al. [11] provided a damage DEM model for bonded rocks that can reflect bond damage caused by compression, tension, shearing and rotation. Nonetheless the above-mentioned models are still limited in comprehensively capturing the behaviour of high-porous soft rock because unbonded contacts are only created after bonds breakage, resulting in significant stress loss in numerical samples during loading. In reality, bond degradation is a progressive process, and the initial intact bond can be degraded into several segments [12], some fragments

can still transfer the load even though the bond structure is completely broken. To improve the computational efficiency, most DEM models do not incorporate bond fragments in the model, leading to the inability of numerical broken bonds to transfer the load. In addition, most DEM models use spherical particles to decrease computational burden, hence posing significant challenges in capturing realist porosities of the remoulded rock.

To comprehensively consider the physical presence of broken bonds and contact distribution of irregular particles, a far-field interaction is introduced based on Zheng et al. [11]'s damage model. The performance of this newly developed model is then evaluated through simulating isotropic and triaxial tests, showcasing its promising ability to capture the typical behaviour of high-porous bonded soft rocks.

2 Limit of current damage bond model

Although current damage model has been proven to reproduce the response of soft rocks in both lab and BVP (boundary value problem) tests, its ability to reproduce the behaviour of high-porous soft rocks (porosity >0.5) still needs to be investigated. Triaxial ($\sigma_3 = 1$MPa) and isotropic tests are simulated to demonstrate the incapability of current damage models to simulate high-porous rocks (porosity=0.52). The PSD of the numerical sample can be found in Zheng et al. [11]. A cylinder-shaped numerical sample is created, comprising approximately 18k particles, with dimensions of 240mm in height and 120mm in diameter with an upscaling ratio is 50. Where interparticle bonded contact forces are calculated based on Zheng et al. [11]'s work and related model parameters are summarized in Table 1. As indicated in the table model parameters listed can be categorized into three families. *Elastic parameters*, which includes the particle effective modulus (bond effective modulus) E_{mod} ($\bar{E}_{mod}$) and the particle normal-to-shear stiffness (bond normal-to-shear stiffness) κ^*($\bar{\kappa}^*$). *Strength parameters*, including tensile strength σ_t, compressive strength σ_t and cohesion C. *Softening parameters* u_c^n, u_c^s and θ_c^b, controlling the bond damage rate in the normal, shear and rotation directions.

Simulated results are shown in Fig. 1. Unlike the ductile failure observed in most experiments (see Fig. 1 left from Lagioia & Nova [2]), a completely stress loss happens after initial elastic stage in both two elements tests (Fig. 1 middle and right). In isotropic tests, samples need to undergo significant compression deformation to restore the previous stress level. From a microscopic perspective, this is because, during the fracture of most bonds, the physical contacts between particles are not sufficient, and numerical samples cannot establish a stable microscopic structure to withstand external loads. Slowing down the softening rate of bonds slightly decreases the effect, but not sufficiently to properly reproduce the post-peak observed. Moreover decreasing the softening rates lead to non-realistic shearing responses.

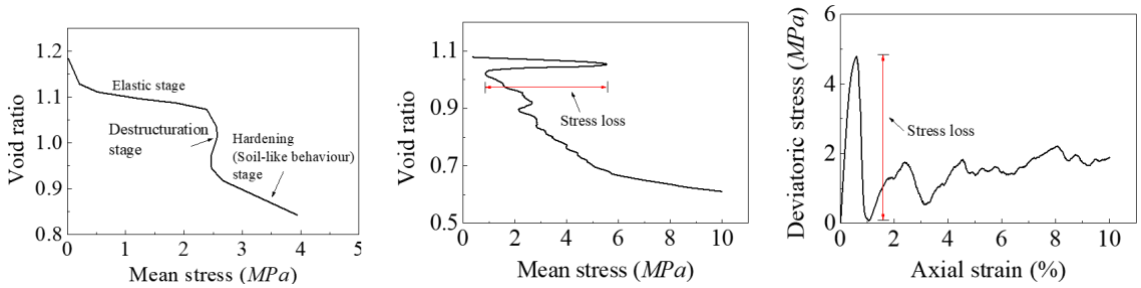

Fig. 1: Experimental (left) and simulated (middle and right) isotropic and triaxial tests without far-field interaction.

3 Far-field interaction

To replicate the behaviour of high-porous soft rocks in DEM modelling is important to capture the rock response during the destructuration stage. Capturing the collapse caused by bond breakage and accurately account for the introduction of unbonded contacts is key. To overcome the limitations shown in the previous section the concept of far-field interaction is introduced.

An irregular intact bond fractures into several fragments, with some active fragments capable of transferring load between grains even after bond breakage. However, in DEM modelling, broken bonds are deleted. To replicate this process, far-field interaction is here introduced to consider the physical existence of broken

active fragments, as shown in Fig. 2. The introduction of far-field interaction replaces the function of transiting interparticle loads by active segments of the fractured bond, without affecting the computational efficiency of the model. Furthermore, Fig. 2 also presents another scenario to account for the far-field interaction—physical contact due to irregular particles in real rock samples. The use of spherical particles cannot accurately replicate a genuine physical contact distribution, as there should be more physical contacts surrounding a specific grain compared to when using spherical particles. A similar concept has been reported in Hentz et al. [13]. The unboned contact force introduced by the far-field interaction is updated incrementally according to the linear contact model, while the bonded contact is calculated following Zheng et al. [11]'s model, the total contact force of the contact is the sum of these two types of contact forces.

Table 1. Model related parameters.

Parameter	Family	Value
$\boldsymbol{E_{mod}}$	Elastic	$0.83GPa$
$\boldsymbol{\bar{E}_{mod}}$		$4.5GPa$
$\boldsymbol{\kappa^*}$ ($\boldsymbol{\bar{\kappa}^*}$)		4.5
$\boldsymbol{\sigma_c}$	Strength	$30MPa$
$\boldsymbol{\sigma_t}$		$10\ MPa$
$\boldsymbol{C}$		$10\ MPa$
$\boldsymbol{u_c^n}$ ($\boldsymbol{u_c^s}$)	Softening	$0.0305d_{00}\ m$
$\boldsymbol{\theta_c^b}$		$0.01rad$

Far-field interaction in DEM modelling entails generating unbonded contacts between untouched spherical particles. The activation timing of the far-field interaction depends on the gap between two particles, denoted as g_a. To investigate the effect of far-field interaction, setting $g_a = 0.17d_{00}$ based on the numerical bonded sample created in section 2, where d_{00} is the minimum particle diameter of the rock grains. The results, with and without the far-field interaction, are compared in Fig. 3. In contrast to the results in Fig. 1, introducing the far-field interaction leads smaller stress loss allowing to achieve a transition from brittle to ductile failure of the sample. Furthermore, the numerical sample replicates similar responses to high-porous soft rocks under different confinements. As for typical experiments in the literature (data in Fig.3 right from Lagioia & Nova [2]), the sample subjected to 4 MPa confinement exhibits a typical three-stage response (elastic-destructuration-hardening), while the sample under 1 MPa confinement shows a continuous softening.

Fig. 2: Schematic diagram of the far-field interaction: (left) Far-field interaction considering the physical contact of irregular particle and (right) considering the physical presence of broken bond.

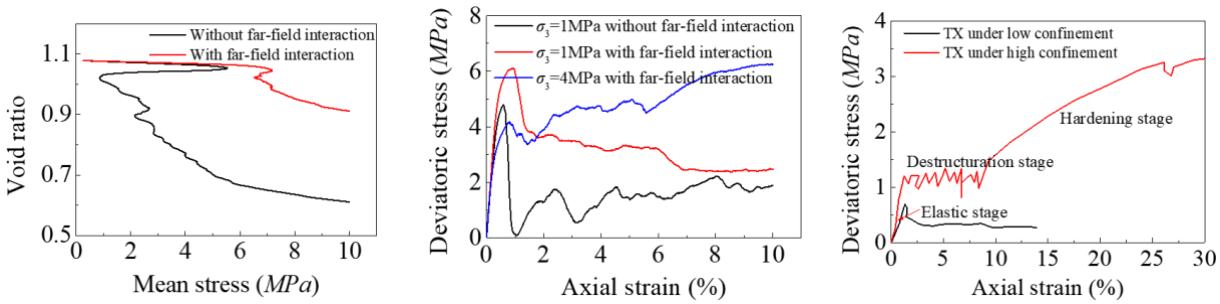

Fig. 3: Simulated isotropic (left) and triaxial (middle) tests without far-field interaction; typical experimental TX response (right).

4 Conclusions

To address the brittle failure when simulation high-porous soft rocks using DEM, the concept of far-field interaction is introduced to account for the physical presence of bonds fragments. Such far-field interaction enables the rock's response to transition from rock-like to soil-like without stress loss whilst still using spherical particles. The model is shown to be able to capture diverse shearing responses of soft rocks under varying confinements. This highlights the potential of the newly developed damage bond model to accurately replicate the behaviour of high-porous soft rocks for large scale simulations.

Acknowledgments

This work is an output from the ICE-PICK project, funded by the New Investigator Award EPSRC grant EP/W00013X/1. Also thanks to the CSC scholarship (202008330363) to support the first author's study.

References

[1] Johnston, I. W. (1991). Geomechanics and the emergence of soft rock technology. *Australian Geomechanics*, 21, 3–26.
[2] Lagioia, R., & Nova, R. (1995). An experimental and theoretical study of the behaviour of a calcarenite in triaxial compression . *Geotechnique*, 45(4), 633–648.
[3] Buckley, R. M., Jardine, R. J., Kontoe, S., et al. (2018). Effective stress regime around a Jacked steel pile during installation ageing and load testing in chalk. *Canadian Geotechnical Journal*, 55(11), 1577–1591.
[4] Ciantia, M. O., & Di Prisco, C. (2016). Extension of plasticity theory to debonding, grain dissolution, and chemical damage of calcarenites. *International Journal for Numerical and Analytical Methods in Geomechanics*, 40(3), 315–343.
[5] Nova, R., & Parma, M. (2011). Effects of bond crushing on the settlements of shallow foundations on soft rocks. *Geotechnique*, 61(3), 247–261.
[6] Carbonell, J. M., Monforte, L., Ciantia, M. O., et al. (2022). Geotechnical particle finite element method for modeling of soil-structure interaction under large deformation conditions. *Journal of Rock Mechanics and Geotechnical Engineering*, 14(3), 967–983.
[7] Coombs, W. M., Augarde, C. E., Brennan, A. J., et al. (2020). On Lagrangian mechanics and the implicit material point method for large deformation elasto-plasticity. *Computer Methods in Applied Mechanics and Engineering*, 358, 112622.
[8] Belytschko, T., & Gracie, R. (2007). On XFEM applications to dislocations and interfaces. *International Journal of Plasticity*, 23(10–11), 1721–1738.
[9] Nguyen, N. H. T., Bui, H. H., Nguyen, G. D., et al.. (2017). A cohesive damage-plasticity model for DEM and its application for numerical investigation of soft rock fracture properties. *International Journal of Plasticity*, 98, 175–196.
[10] Senanayake, S. M. C. U., Haque, A., & Bui, H. H. (2022). An experiment-based cohesive-frictional constitutive model for cemented materials. *Computers and Geotechnics*, 149, 104862.
[11] Zheng, J., Previtali, M., Ciantia, M.O., et al. (2023). Micromechanical Numerical Modelling of Foundation Punching in Highly Porous Cemented Geomaterials in a Virtual Centrifuge Environment. In Palermo (Ed.), *CNRIG 2023* (pp. 390–397).
[12] Ciantia, M. O., Castellanza, R., Crosta, G. B., et al. (2015). Effects of mineral suspension and dissolution on strength and compressibility of soft carbonate rocks. *Engineering Geology*, 184, 1–18.
[13] Hentz, S., Donzé, F. V., & Daudeville, L. (2004). Discrete element modelling of concrete submitted to dynamic loading at high strain rates. *Computers & Structures*, 82(29), 2509–2524.

UKACM 2024 Conference, 10-12 April 2024, Durham University, Durham, UK
https://doi.org/10.62512/conf.ukacm2024.048

MODELLING POST-FAILURE BEHAVIOUR OF CHALK CLIFFS WITH THE MATERIAL POINT METHOD

Sam J. V. Sutcliffe[1]*, William M. Coombs[1], Wangcheng Zhang[1], Ravindra Duddu[2]

[1] Department of Engineering, Durham University, Durham, DH1 3LE, UK.
sam.sutcliffe@durham.ac.uk
w.m.coombs@durham.ac.uk, wangcheng.zhang@durham.ac.uk
[2] Department of Civil and Environmental Engineering, Vanderbilt University, Nashville, TN 37212
ravindra.duddu@vanderbilt.edu

Abstract. This work evaluates the use of the Material Point Method (MPM) with continuum damage-plasticity to model fracture for the use of a combined pre- and post-failure simulation. MPM is used to allow for large deformations and geometry changes without mesh distortion and damage diffusion. An integral non-local continuum damage model is used to model brittle fracture, which avoids the mesh-dependency issues exhibited by local models. The modelling approach is demonstrated on chalk cliff collapse problems, where the final state of the rock formation after the failure is of importance and critically linked to further failure processes.

Key words: *chalk cliff collapse; post failure, large deformation, brittle fracture, damage-plastic*

1 Introduction

Cliff collapse represents a significant danger to communities that are situated or operate near cliff fronts [1], causing damage when the debris falls down onto the beach-front below, but also posing a hazard to structures and people situated at the top of the cliff. Coastal chalk cliffs ranging from 10 m to 100 m tall are a prominent feature around South-Eastern United Kingdom, Northern France, and Germany [2]. These cliffs experience very high rates of erosion, making them a geo-hazard that must be evaluated carefully. The chalk cliffs tends to undergo brittle failure when under moderate shear and tensile loads of ≈ 1 MPa [3]. Collapse causes large piles of debris to form around the base of the cliffs, which provides stability and helps protect the cliff from further collapse [2]. It is therefore important to not only understand the initiation of failure, but also the mass transport and post-failure behaviour of the collapse to accurately model recurrent failures. Modelling both the fracture and mass transport of the collapse is not trivial with the Finite Element Method (FEM), due to the large deformation run-out causing highly distorted meshes that introduce numerical issues. Pre-failure FEM-based models of chalk cliffs have been presented in [3] and [4], evaluating the effects of geometry and shear strength in a linear elastic or elasto-plastic setting. This paper uses the Material Point Method (MPM) [5] to allow for large deformation and geometry changes, while using damage and plasticity to model failure and collapse.

2 Material Point Method

The MPM [5] combines an Eulerian computational mesh with Lagrangian material points (MPs) that are allowed to move through the mesh. Multiple discrete bodies in a system are approximated as groups of MPs, and as such geometry changes are represented by the motion of MPs. As the mesh is reset at the beginning of every step, it may never become degenerate. A key advantage of the MPM is that history dependant variables are stored and used on the MPs, so fields like damage cannot suffer any numerical

diffusion.

The MPM uses finite element machinery, with interpolation (or shape) functions, S_{vp}, linking the vertices of the mesh, v, with the MPs, p. The momentum balance equation is solved at the nodes of the background mesh, with the strong form:

$$\rho \frac{Dv}{Dt} = \nabla \cdot \sigma + f_b, \tag{1}$$

where ρ is the density of the body with a velocity, v, which is subject to body forces, f_b that generate a Cauchy stress field, σ. Applying Galerkin's method, discretising and approximating the volume integrals over the body Ω as summations over MPs, each representing a volume, V_p, and associated mass, m_p, we arrive at an equation that may be solved explicitly at the nodes

$$M_v a_v = \sum_p^{N_{mp}} \nabla S_{vp} \sigma_p V_p + \sum_p^{N_{mp}} S_{vp} m_p g, \tag{2}$$

where M_v is the nodal mass matrix (in this case lumped and diagonal). Once accelerations a_v, and subsequently velocities are found at the nodes, the velocity of the MPs are found by interpolating from nodes to MPs. The MPs are then advected in space, and the original computational mesh discarded and reset (or redefined).

3 Continuum damage

The use of continuum damage combined with plasticity allows for modelling progressive failure of material under combined tension and shear loading [6]. In linear elastic damage, based on the strain equivalence hypothesis that the undamaged strain is equal to the damaged strain $\bar{\varepsilon} = \varepsilon$, the undamaged stress $\bar{\sigma}$ can be related to the actual damaged stress state σ via

$$\sigma = (1-d)\bar{\sigma} = (1-d)[D^e]\varepsilon = (1-d)[D^e]\bar{\varepsilon}. \tag{3}$$

Here a uniform single scalar isotropic degradation function is shown, where $0 \leq d \leq 1$ is the scalar damage (0 represents an undamaged material), and $[D^e]$ is the elastic constitutive matrix. As in [6], this is weakly coupled with a plasticity model based on a Mohr-Coloumb yield surface where plasticity acts in the undamaged stress space, and damage effectively acts as a softening law. By separately degrading the volumetric and deviatoric components it is possible for a tensile-compressive split in degradation, such as

$$\sigma = (1 - g_v(d, tr(\bar{\sigma})))tr(\bar{\sigma}) + (1 - g_d(d))(\bar{\sigma} - \frac{1}{3}tr(\bar{\sigma})) \tag{4}$$

The aim of the model is to have some residual shear and compressive strength, governed by the limits of the functions g_v and g_d as $d \to 1$. Stress is updated with a local elastic-predictor plastic-corrector, and Eq. (4) is then used as a non-local damage-corrector to map the undamaged plastic stress into damaged space. The current damage level is set by a viscous-regularised maximum stress history κ and a softening parameter η, via an exponential softening function. A characteristic time τ enforces a maximum damage increment rate. A damage criteria is required to define the driving stress Y which updates κ, here a form of Drucker-Prager criterion is used

$$Y = \frac{3}{3 + \tan\theta} \left(\sqrt{3J_2} + \frac{I_1}{3} \tan\theta \right) \tag{5}$$

where I_1 and J_2 are the first and second invariant of the undamaged Cauchy stress and its deviator, and θ is the damage frictional angle. The driving stress is regularised with a non-local integral scheme [6], to avoid mesh dependency in the strain softening.

4 Numerical results: Joss Bay case study

An example of chalk cliff collapse measured in [7] and analysed in [4] with FEM and a Mohr-Coloumb model is analysed using the proposed MPM framework. The cliff is modelled as a homogeneous chalk material, of density $1700\,\mathrm{kg\,m^{-3}}$, with initial Young's modulus $E = 1\,\mathrm{GPa}$ and Poisson's ratio of $\nu = 0.24$ [4]. A 2D plane strain section of height $H = 15.5\,\mathrm{m}$, with a length of $2H$ is considered. The front of the cliff has three main features: a sloped lower section with an angle of around 78 degrees, a wave cut notch $L_n = 0.5\,\mathrm{m}$ at the foot with an angle of 45 degrees, and an initial tension crack $2.2\,\mathrm{m}$ back from the cliff front [7].

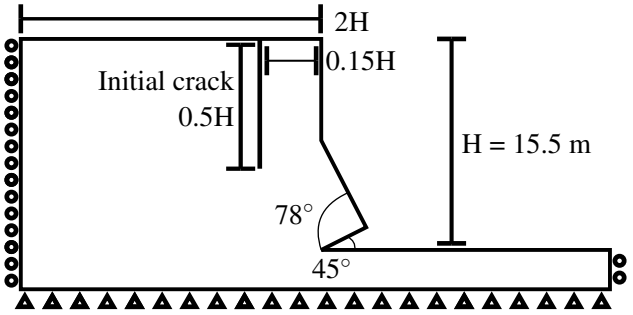

Figure 1: Numerical problem setup

Strength parameters of the plastic model are taken as the highest possible bound of cohesion $c = 1000\,\mathrm{MPa}$, and friction angle $\phi = 50^\circ$, with zero dilatancy. It is assumed that under compression the residual bulk modulus of the material is reduced to 1 %, the tensile bulk modulus vanishes to 1×10^{-7}%, and the shear modulus of the material is varied from $1 - 0.5$ %.

The damage criteria parameters are: a frictional angle $\theta = 60^\circ$ and tensile initiation stress $\sigma_f = 20\,\mathrm{kPa}$ inferred from [4], a ductility of $\eta = 5$, giving a very low fracture energy $\simeq 10\,\mathrm{J\,m^{-2}}$, and the viscous characteristic time is taken as $\tau = 1$ s. Experimentally finding a length scale is possible, however here it is numerically taken as $l_c = 0.18$ m - a patch size roughly 4 times the mesh resolution.

As seen in Fig. 2, the shape of the debris pile is highly sensitive to the residual strength of the chalk. In Fig. 2a the very small residual strength causes a highly mobilised flow of chalk forming a debris pile similar in angle $\theta \simeq 15^\circ$ to larger collapses in [2]. In Fig. 2b the larger residual shear strength causes a steeper pile - more closely matching the measured 44° debris angle in [7], with a qualitatively more intact debris texture.

5 Observations

The MPM shows promise for modelling cliff collapse in pre and post failure behaviour, and that it may be used for forward modelling of other brittle cliff collapse such as in marine ice cliffs. It was found the use of plasticity and isotropic damage allows for the modelling of shear failure under gravity driven

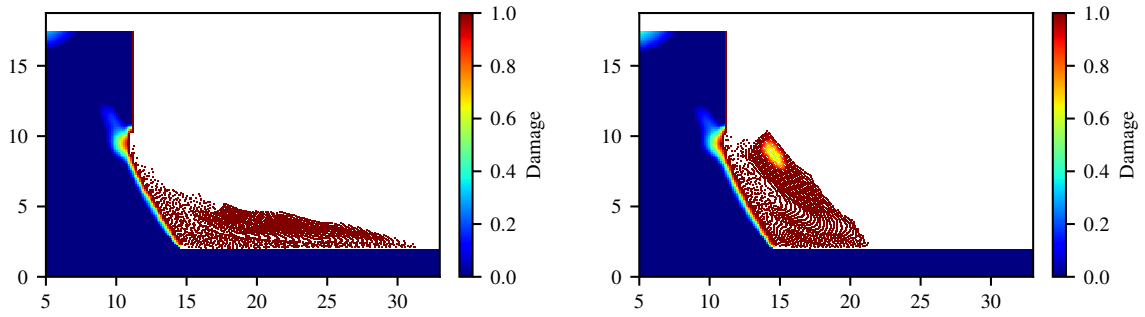

(a) Residual shear strength 0.5 %
$\phi_{residual} = 30°$

(b) Residual shear strength 1 %
$\phi_{initial} = \phi_{residual} = 50°$

Figure 2: Numerical results

loads, with the damage model allowing for non-local softening behaviour and plasticity de-activating the damage at large inelastic strains. Numerically the shape of the chalk debris post failure is highly sensitive to the residual shear strength, further work should find a meaningful way of calibrating this parameter.

Acknowledgements

The authors would like to thank the non-linear solid mechanics group at Durham University for providing fruitful discussion and insight on related topics. This research has been funded by the Durham Department of Engineering through an Engineering Doctoral Studentship. The second and fourth authors acknowledge the support of the Royal Society (IES\R1\211032).

REFERENCES

[1] Eric C.F. Bird. “Cliff Hazards and Coastal Management”. In: *Journal of Coastal Research* (1994), pp. 299–309.

[2] Elisabeth T. Bowman and W. Andrew Take. “The runout of chalk cliff collapses in England and France—case studies and physical model experiments”. en. In: *Landslides* 12.2 (Apr. 2015), pp. 225–239.

[3] Guido Wolters and Gerald Müller. “Effect of Cliff Shape on Internal Stresses and Rock Slope Stability”. In: *Journal of Coastal Research* 24.1 (2008), pp. 43–50.

[4] T. D. Styles, J. S. Coggan, and R. J. Pine. “Back analysis of the Joss Bay Chalk Cliff Failure using numerical modelling”. In: *Engineering Geology* 120.1 (June 2011), pp. 81–90.

[5] D. Sulsky, Z. Chen, and H. L. Schreyer. “A particle method for history-dependent materials”. en. In: *Computer Methods in Applied Mechanics and Engineering* 118.1 (Sept. 1994), pp. 179–196.

[6] Peter Grassl and Milan Jirásek. “Plastic model with non-local damage applied to concrete”. en. In: *International Journal for Numerical and Analytical Methods in Geomechanics* 30.1 (2006), pp. 71–90.

[7] J. N. Hutchinson. “Field meeting on the coastal landslides of Kent: 1–3 July 1966”. In: *Proceedings of the Geologists’ Association* 79.2 (Jan. 1968), pp. 227–237.

Geotechnical Modelling 3: MPM, PFEM and Soil-Structural Interaction

UKACM 2024 Conference, 10-12 April 2024, Durham University, Durham, UK
https@//doi.org/10.62512/conf.ukacm2024.009

SIMULATION OF STRAIN LOCALISATION WITH AN ELASTOPLASTIC MICROPOLAR MATERIAL POINT METHOD

Ted J. O'Hare[1*], Panos A. Gourgiotis[2], William M. Coombs[1] and Charles E. Augarde[1]

[1] Department of Engineering, Durham University, Durham, DH1 3LE, UK.
[*]ted.o'hare@durham.ac.uk, w.m.coombs@durham.ac.uk, charles.augarde@durham.ac.uk
[2] Mechanics Division, National Technical University of Athens, Zographou, GR-15773, Greece.
pgourgiotis@mail.ntua.gr

Abstract. The thickness of shear bands, which form along slip surfaces during certain modes of geotechnical failure, depends directly on the size of the soil particles. Classical continuum models, however, are invariant to length scale, so the strain localisation zone cannot converge to a finite size when employing numerical techniques such as the finite element method. Instead, the present approach adopts the micropolar (Cosserat) continuum, a weakly non-local higher-order theory which incorporates a characteristic length and allows independent rotations of the material micro-structure as well as transmission of couple stresses. As a result, strain can localise naturally in micropolar continua to form realistic finite-sized shear bands. By extending an elastic finite-strain micropolar implementation of the material point method (a numerical method well-suited to modelling large deformation problems) with an elasto-plastic constitutive model suitable for geomaterials, this novel combined approach will provide a powerful tool to analyse numerically challenging localisation problems in geotechnics.

Key words: *micropolar; Cosserat; material point method; strain localisation*

1 Introduction

When modelling geotechnical failure events with conventional mesh-based techniques underpinned by a classical continuum theory, two key problems arise. The first concerns the magnitude of deformation generally brought about by such events. Attempts to use numerical techniques like the finite element method (FEM) here can lead to severe distortion of the mesh – and, in extreme cases, element inversion – such that the method begins to falter and accuracy is not guaranteed, if a solution can even be produced at all. Moreover the remedial task of subsequently re-meshing the deformed domain only brings further problems, particularly surrounding projection of history variables and the increase in computational cost and algorithmic complexity. Far better suited to modelling such large-deformation problems are the various *particle*-based methods which are not, conversely, hindered by any deviation from an initial geometry. Here we introduce the material point method (MPM) [1], a particle method which utilises a mesh only for the purpose of computations – not for tracking the material – which is reset for each time- or load-step and does not therefore experience significant distortion. Although the material body is discretised into particles, the MPM has a commonality with much of the FE idiom through the way it operates on the mesh, readily allowing for implementation of FE formulations. This is the method adopted for this work.

The second problem is less insidious but far more fundamental and more complicated to remedy. Shear failure in geomaterials usually occurs in concentrated regions called *shear bands* in a process known as *strain localisation*. But because shear bands represent a sharp discontinuity in the displacement field, if the underlying partial differential equation (PDE) used to describe the event has the local displacement as

its sole primary field variable – and does not impose an artificial smoothing technique – then it loses one of its conditions for ellipticity (or hyperbolicity in the case of dynamic analysis). The governing system is now ill-posed for the problem at hand and will not produce reliable results; numerical simulations do not converge to a particular failure load or shear band thickness with mesh refinement, and are instead fully mesh-dependent.

Our chosen solution is to supplant the classical approach with micropolar (or Cosserat) theory [2], which supposes that the rotation of each element of the micro-structure is independent of the rotation of the surrounding continuum. The independent *micro-rotations* and their spatial gradient (*curvature*) regularise the ill-posedness of the PDE, smoothing the solution field around the shear band with respect to a length scale which is generally taken to be indicative of the size of the micro-structure (e.g. the diameter of a soil particle). Numerical simulations based on the micropolar continuum can therefore reliably predict shear bands with a thickness depending on the scale of the constituent micro-structure, as observed in real localisation events.

This paper details an approach building on [3–6], whereby the geometrically-exact micropolar theory is extended for elasto-plasticity with a pressure-dependent yield surface, and implemented within the MPM. A cursory overview of the adopted continuum theory and numerical method is given, and further details including numerical examples will be provided during the oral presentation.

2 The micropolar continuum

2.1 Kinematics

With reference to Figure 1a, a micropolar continuum occupies a volume Ω in its current (deformed) configuration. The translation vector u_i emanates from the Cartesian reference position X_i of each point in the undeformed volume Ω_0 to its current position x_i in Ω, and the deformation gradient tensor $F_{i\theta} = \frac{\partial x_i}{\partial X_\theta}$ provides the fundamental link between reference and current coordinates. At every point in the micro-continuum there exists a rigid body, attached to which is a set of axes that are free to rotate independently of deformation occurring at the continuum scale. Each rotated axis w_i in the current configuration is related to its counterpart W_ψ in the reference configuration via $w_i = Q_{i\psi} W_\psi$, where $Q_{i\psi} \in \mathrm{SO}(3)$ is a proper orthogonal tensor termed the *micro-rotation* tensor. The rotation may also be parameterised as a vector φ_k, identified as the axis of rotation with the angle its magnitude. A skew-symmetric tensor $\Phi_{ij} = -e_{ijk}\varphi_k$ (where e_{ijk} is the third-order Levi-Civita, or *permutation*, tensor) is then used to compute the micro-rotation tensor using the (Euler-)Rodrigues formula

$$Q_{i\psi} = \delta_{i\psi} + \frac{\sin|\varphi|}{|\varphi|}\Phi_{i\psi} + \frac{1-\cos|\varphi|}{|\varphi|^2}\Phi_{ij}\Phi_{j\psi}, \tag{1}$$

where $\delta_{i\psi}$ denotes the Kronecker delta and $|\varphi|$ is the magnitude of φ_k. For our purposes, two spatial measures are used to quantify micropolar deformation: a stretch tensor, and a measure of the rotation gradient named the *left curvature tensor* which endows the theory with its non-local property

$$V_{ij} = F_{i\theta}Q_{j\theta} \qquad \text{and} \qquad k_{ij} = -\frac{1}{2}Q_{i\gamma}e_{\gamma\tau\eta}Q_{p\tau}\frac{\partial Q_{p\eta}}{\partial X_\pi}Q_{j\pi}. \tag{2}$$

A multiplicative elasto-plastic split is assumed for both the deformation gradient $F_{i\theta} = F^e_{iA}F^p_{A\theta}$ and the micro-rotation tensor $Q_{i\theta} = Q^e_{iA}Q^p_{A\theta}$, where the superscripts denote the elastic and plastic parts. Hence

the elastic stretch is defined $V^e_{ij} = F^e_{iA} Q^e_{jA}$ and the curvature simply decomposes additively:

$$k_{ij} = k^e_{ij} + k^p_{ij}. \tag{3}$$

2.2 Elastic constitutive laws and balance equations

The Cauchy stress σ_{ij} and couple-stress m_{ij} (moment per unit area) are obtained from the elastic deformation measures using a neo-Hookean hyperelastic model [3]

$$J\sigma_{ij} = \frac{\lambda}{2}(J^2-1)\delta_{ij} + \mu(V^e_{ik}V^e_{jk} - \delta_{ij}) + \frac{\kappa}{2}(V^e_{ik}V^e_{jk} - V^e_{ik}V^e_{kj}) \tag{4}$$

$$Jm_{ij} = V_{ik}(\alpha k^e_{ll}\delta_{kj} + \beta k^e_{kj} + \gamma k^e_{jk}) \tag{5}$$

where $J = \det(F)$ is the volume ratio between the original and deformed states, and λ (first Lamé constant), μ (second Lamé constant), κ, α, β and γ are constitutive parameters. An internal length scale L is then given by $L = \sqrt{(\beta+\gamma)/2\mu}$. The spatial forms of linear and angular momentum balance in the quasi-static case read

$$\frac{\partial \sigma_{ij}}{\partial x_j} + p_i = 0 \qquad \text{and} \qquad \frac{\partial m_{ij}}{\partial x_j} - e_{ijk}\sigma_{jk} + q_i = 0, \tag{6}$$

where p_i and q_i are the body force and body couple respectively.

2.3 Elasto-plastic constitutive model

This formulation uses a conventional elastic predictor-plastic corrector algorithm to map the stress state at a material point onto the yield surface f, which has the Drucker-Prager form [5]

$$f = \sqrt{3J_2} + \frac{A}{3}\sigma_{kk} - c \tag{7}$$

using the modified second invariant J_2 of deviatoric stress $s_{ij} = \sigma_{ij} - \frac{1}{3}\sigma_{kk}$,

$$J_2 = a_1 s_{ij}s_{ji} + a_2 s_{ij}s_{ij} + \frac{a_3}{L^2} m_{ij}m_{ji} \tag{8}$$

where a_1, a_2 and a_3 are heuristics, and constants A and c which are related to the material's internal friction, dilatancy and cohesion. The yield function is satisfied through the use of plastic flow rules which chart the evolution of the elastic stretch and plastic curvature – see [3] for an implicit implementation.

3 Numerical formulation

To initialise an MPM analysis, the material is discretised into a number of Lagrangian material points which occupy a grid of elements joined together at nodes. All history variables including volume, stress, strain, force and translation are tracked using the MPs. In each step, the requisite quantities are mapped from the MPs to the nodes using grid shape functions in order to perform a standard FE-type computation. Once the nodal solution is obtained, it is then mapped to the MPs and their positions and state variables are updated. At this point, the grid is reset to its initial position ready for the next step. This process

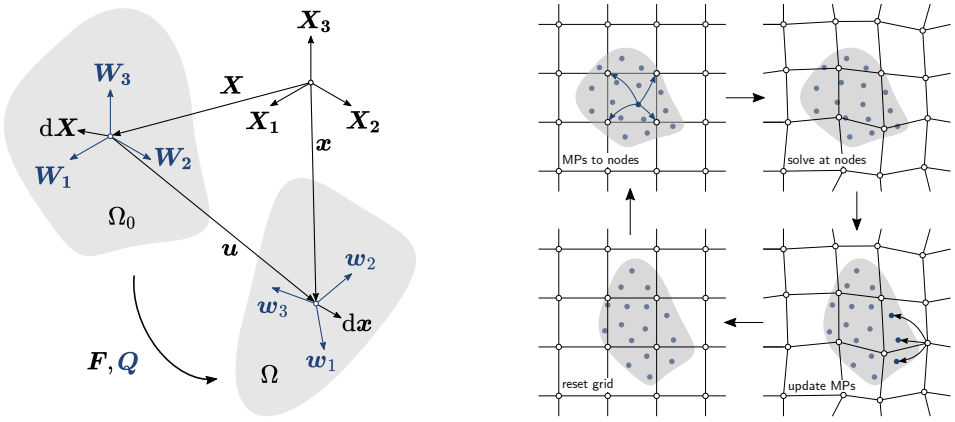

(a) (b)

Figure 1: (a) the total kinematics of a micropolar continuum, with the rotational elements shown in blue; (b) the main steps of an MPM algorithm, reproduced from [6].

is then repeated for as many time- or load-steps the analysis requires. See Figure 1b for a graphical overview of a general MPM algorithm.

Although our general approach to modelling strain localisation in geomaterials has been set out, the format of this contribution limits any further elaboration of the formulation or presentation of examples. Specific details of the implementation of elasto-plastic geometrically-exact micropolar theory within the MPM will instead follow in the oral presentation. It is hoped that this novel numerical tool will offer a more robust and reliable way to analyse challenging localisation problems involving large deformations such as landslides.

Acknowledgment. This work was supported by the EPSRC [grant number EP/T518001/1].

REFERENCES

[1] Sulsky, D., Chen, Z. and Schreyer, H.L. A particle method for history-dependent materials. *Computer Methods in Applied Mechanics and Engineering* (1994) **118**(1-2):179-196.

[2] Cosserat, E. and Cosserat, F. *Théorie des corps déformables*. A. Hermann et fils, Paris (1909).

[3] Bauer, S., Dettmer, W.G., Perić, D. and Schäfer, M. Micropolar hyperelasto-plasticity: constitutive model, consistent linearization, and simulation of 3D scale effects. *International Journal for Numerical Methods in Engineering* (2012) **91**:39-66.

[4] Neuner, M., Rigueiro, R.A. and Linder, C. A unified finite strain gradient-enhanced micropolar continuum approach for modeling quasi-brittle failure of cohesive-frictional materials. *International Journal of Solids and Structures* (2022) **254-255**:111841.

[5] de Borst, R., Sabet, S.A. and Hageman, T. Non-associated Cosserat plasticity. *International Journal of Mechanical Sciences* (2022) **230**:107535.

[6] O'Hare, T.J., Gourgiotis, P.A., Coombs, W.M. and Augarde, C.E. An implicit Material Point Method for micropolar solids undergoing large deformation. *Computer Methods in Applied Mechanics and Engineering* (2024) **419**:1166688.

UKACM 2024 Conference, 10-12 April 2024, Durham University, Durham, UK
https://doi.org/10.62512/conf.ukacm2024.014

EFFECTS OF STRUCTURE AND STRAIN LOCALIZATION IN PFEM SIMULATIONS OF CPTU TESTS IN A NATURAL CLAY

Kateryna Oliynyk[1,2*], **Matteo O. Ciantia**[1,3], **Claudio Tamagnini**[2]

[1] School of Science and Engineering, University of Dundee, Dundee, DD1 4HN, UK.
2439697@dundee.ac.uk, m.o.ciantia@dundee.ac.uk
[2] Department of Civil and Environmental Engineering, University of Perugia, Perugia, Italy.
kateryna.oliynyk@unipg.it, claudio.tamagnini@unipg.it
[3] Department of Earth and Environmental Sciences, University of Milano Bicocca, Milan, Italy.
matteo.ciantia@unimib.it

Abstract. The mechanics of cone penetration in CPTu tests in a silty clay was investigated with the PFEM, using a recently proposed finite deformation plasticity model for natural geomaterials – the FD_MILAN model – which incorporates the *bond strength* P_t as an internal variable quantifying the effects of structure, and is equipped with a *characteristic length* ℓ_c to regularize the numerical solutions in presence of strain localization. The results of the PFEM simulations show that the deformations around the piezocone are strongly affected by the characteristic length. In particular, when ℓ_c/R is sufficiently small, the deformation field may be affected by clearly visible shear bands. The soil around the piezocone is subjected to a very strong destructuration process, which leads to the complete loss of bond strength in a large region around the cone tip and shaft. As a consequence, the use of literature empirical correlations in the interpretation of the CPTu test data in heavily structured soils could result in a significant underestimation of both the undrained strength and the overconsolidation ratio of the soil deposit.

Key words: *CPTu tests; Natural clay soils; Strain localization; Nonlocal plasticity; PFEM*

1 Introduction

In recent times, the analysis of CPTu tests performed with piezocones, *i.e.*, standard electric penetrometers equipped with pore pressure transducers, has attracted significant interest in the research community. Conventional interpretation methods of CPTu tests are typically based on empirical or semi–empirical approaches adopting quite simplified assumptions about the deformation field around the cone tip. In reality, the deformation field induced by the cone penetration may be much more complex. The aim of this work is to use the Particle Finite Element Method (PFEM, [1]) to investigate in more detail this particular aspect of the problem and its impact on CPTu measurements.

2 Piezocone test in a saturated structured soil

In a typical CPTu test, a standard piezocone with radius R = 1.78 cm and a cone tip angle of 60° is inserted in the soil body at a constant penetration speed of 2.0 cm/s. At any penetration depth, the cone resistance q_c is computed as the ratio F_c/A_c between the resultant force acting at the base of the cone, F_c, and the cone base area, $A_c = \pi R^2$. The piezocone is equipped with two pore pressure probes, located at the cone mid–height and at its base, where the pore pressure u is calculated as the cone advances.

In the present study, the penetration process has been modeled as an axisymmetric problem, considering a limited penetration depth of $20R$, in a soil mass characterized by a constant initial effective stress state

with σ_{z0} = 100 kPa, $\sigma_{r0} = K_0\sigma_{z0}$ and K_0 = 0.6, and a constant zero initial pore water pressure (*i.e.*, both soil unit weight and the specific weight of water were set to zero). The isotropic hardening elastoplastic constitutive model for finite deformations – the FD_MILAN model – recently proposed by the Authors [2] has been adopted for the soil. The model, based on the multiplicative decomposition of the deformation gradient, incorporates two scalar internal variables: the preconsolidation pressure P_s, which accounts for the hardening/softening effects due to volumetric and deviatoric plastic strains, and the bond strength P_t, which quantifies, from a macroscopic point of view, the effects of material fabric and interparticle bonding. The FD_MILAN model was calibrated on experimental data from a soft natural silty clay, the Osaka clay, provided in ref. [3], which has been chosen as a representative natural structured soil deposit. The material constants adopted in the simulations are provided in Fig. 1. The preconsolidation pressure P_{s0} of the soil was set equal to 120 kPa, while two different structure levels were considered, namely a weakly structured soil (P_{t0} = 5 kPa) and a strongly structured soil (P_{t0} = 60 kPa). In this last case, the brittle behavior resulting from the softening process associated to destructuration makes the soil susceptible to strain localization. In order to deal with this phenomenon, the model is equipped with a non–local version of the hardening laws, incorporating a characteristic length ℓ_c which controls the thickness of the shear bands [4].

3 PFEM simulation of cone penetration

A series of PFEM simulations of CPTu tests in saturated Osaka clay was performed to investigate the effects of the characteristic length, ℓ_c, adopted for the soil and of its initial bond strength, P_{t0}. As the effects of soil permeability on the computed CPTu results were discussed in refs. [5, 6], k_h was kept constant and equal to 1.0e-8 m^2/s/kPa. A fully coupled hydromechanical setting was adopted, using the mixed u–Θ–p_w formulation of ref. [1].

The contour maps of the accumulated plastic deviatoric deformation, E_s^p, and of the bond strength, P_t, obtained in simulations r01 and r02 at two different penetration depths are shown in Fig. 1. The results in the top row refer to a characteristic length ℓ_c/R = 0.14, while those in the bottom row to ℓ_c/R = 0.42. When the characteristic length is small, the plastic deviatoric strain field displays clearly visible shear bands, which originate in correspondence of the piezocone sleeve and then propagate downwards until they reach the cone axis well below the cone tip (Fig. 1a, top row). As the cone advances, the zone of soil between the tip and the shear band is deformed until the shear band disappears. At the same time, a new shear band is initiated at the cone flank and the localized deformation mechanisms is replicated again over and over. During the penetration process, the destructuration process going on around the advancing piezocone is indeed quite strong (Fig. 1b, top row). Almost complete degradation of the bond strength is occurring in a zone of soil which extends below the cone tip by 2–3 times the cone radius R, and laterally by about one cone radius from the piezocone shaft. The geometry of the destructured soil regions closely follow the pattern of shear bands observed in Fig. 1a.

As the characteristic length scale increases to ℓ_c/R = 0.42 the pattern of the deviatoric plastic strain is significantly different (Fig. 1a, bottom row). At the same penetration depths, the contours of E_s^p evolve in a much more regular fashion, following the shape of the cone (Fig. 1b, bottom row). This depends on the fact that the shear band width increases with ℓ_c, and for the large value of ℓ_c/R adopted in simulation r02, the thickness of the eventual shear bands become of the same order of the cone radius, making the bands almost undetectable.

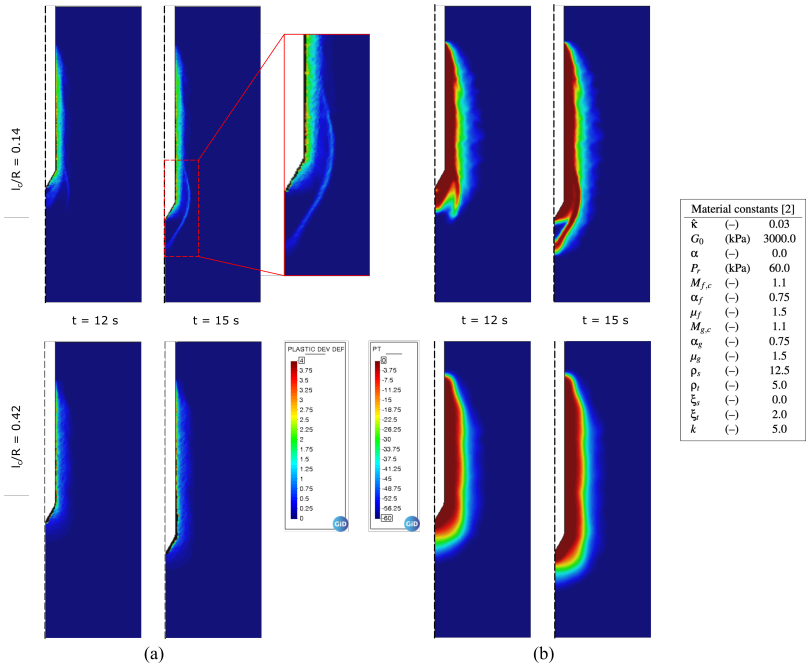

Figure 1: Contour maps of: a) accumulated plastic deviatoric strain E_s^p at two different time stations, with ℓ_c/R = 0.14 (top row) and ℓ_c/R = 0.42 (bottom row); b) bond strength P_t at two different time stations, with ℓ_c/R = 0.14 (top row) and ℓ_c/R = 0.42 (bottom row).

The computed average values of the net cone resistance $\overline{q}_n = \overline{q}_c - \sigma_{z0}$ in the four simulations are reported in Tab. 1. The adopted value of the characteristic length has only a minor impact on the test results for both values of P_{t0} considered, with differences smaller than 4%. On the contrary, the initial bond strength has a much larger impact on the simulation results, with $\overline{q}_n$ increasing by about 100 kPa as P_{t0} increases from 5 kPa to 60 kPa. Further insight on the computed results can be obtained by interpreting them in terms of existing correlations with conventional indicators of the soil behavior such as: a) the peak and ultimate undrained shear strength (s_u^p and s_u^u), and b) the yield stress in oedometric compression (σ_y). These quantities, calculated with the FD_MILAN model for the two different initial states considered, are reported in Tab. 1. By normalizing the net cone resistance with the two values of the undrained shear strength, the two cone factors – $N_c^p = \overline{q}_n/s_u^p$ and $N_c^u = \overline{q}_n/s_u^u$ – are obtained, see Tab. 1. The peak cone factor N_c^p decreases significantly with increasing initial bond strength, and for the strongly structured soil is much lower than the values typically reported in the literature for clays (in the range between 9 and 15). This depends on the fact that s_u^p is conventionally determined at first yield, in a fully structured state, while $\overline{q}_n$ is significantly affected by the destructuration occurring in the soil around the cone tip.

A correlation between the net cone resistance and the oedometric yield stress has been proposed by Mayne and coworkers for non–structured, inorganic clays [7]. The corresponding values of σ_y, denoted with the symbol σ_y^M, are reported in Tab. 1, together with the real and estimated overconsolidation ratios, OCR = σ_y/σ_{z0} and OCR^M = σ_y^M/σ_{z0}. For the weakly structured soil, OCR and OCR^M are quite close to each other. For the strongly structured soil the values of OCR^M are about 180% smaller than the actual values of OCR. This result is consistent with the previous observations made on cone factor values, and

Table 1: Program of PFEM simulations and selected results: average values of net cone resistance ($\overline{q}_n$); apparent undrained peak and ultimate strengths (s_u^p, s_u^u) and corresponding peak and ultimate cone factors (N_c^p, N_c^u); yield stress in oedometric compression (σ_y) and overconsolidation ratio (OCR = σ_y/σ_{z0}); yield stress in oedometric compression (σ_y^M) and overconsolidation ratio (OCR^M = σ_y^M/σ_{z0}) provided by the correlation of ref. [7].

run #	P_{t0} (kPa)	ℓ_c/R (–)	$\overline{q}_n$ (kPa)	s_u^p (kPa)	s_u^u (kPa)	N_c^p (–)	N_c^u (–)	σ_y (kPa)	OCR (–)	σ_y^M (kPa)	OCR^M (–)
r01	60	0.14	558.49	120.84	42.42	4.62	13.17	525.49	5.25	184.30	1.84
r02	60	0.42	570.53	120.84	42.42	4.72	13.45	525.49	5.25	188.27	1.88
r03	5	0.14	456.03	50.66	42.42	9.00	10.75	169.92	1.70	150.49	1.50
r04	5	0.42	466.32	50.66	42.42	9.20	10.99	169.92	1.70	153.89	1.54

is to be attributed to the intense destructuration suffered by the soil during the penetration process.

4 Conclusions

The deformation field around the cone tip can be characterized by strain localization. When this occurs, its evolution with time is not stationary, as it is assumed in some CPTu modeling approaches based on the theory of cavity expansion or on the Strain Path Method. Surprisingly, the significant differences observed in soil deformations around the cone tip for different values of ℓ_c/R are not reflected in the calculated net cone resistance q_n, which is practically independent of ℓ_c. Due to the strong destructuration occurring around the cone tip, the use of literature N_c values in the interpretation of the CPTu test results would provide an undrained strength value closer to the ultimate value rather than the peak one. For the same reason, the use of literature correlations to estimate the oedometric yield stress would lead to a significant underestimation of the overconsolidation ratio OCR of a strongly structured soil.

Acknowledgments

The ICE-PICK project, funded by the EPSRC NIA grant EP/W00013X/1, is gratefully acknowledged.

REFERENCES

[1] L. Monforte et al. “Performance of mixed formulations for the particle finite element method in soil mechanics problems”. In: *Comp. Part. Mech.* 4.3 (2017), pp. 269–284.

[2] K. Oliynyk, M. O. Ciantia, and C. Tamagnini. “A finite deformation multiplicative plasticity model with non–local hardening for bonded geomaterials”. In: *Comp. & Geotechnics* 137 (2021).

[3] T. Adachi et al. “Stress–strain behavior and yielding characteristics of Eastern Osaka clay”. In: *Soils and Found.* 35 (1995), pp. 1–13.

[4] K. Oliynyk, M. O. Ciantia, and C. Tamagnini. “PFEM Modeling of Strain Localization Processes in Non–local Multiplicative Plasticity”. In: *Proc. IACMAG 2022*. Springer. 2023, pp. 118–125.

[5] M. O. Ciantia, K. Oliynyk, and C. Tamagnini. “Finite Deformation Modelling of Cone Penetration Tests in Saturated Structured Clays”. In: *Proc. IACMAG 2022*. Springer. 2023, pp. 195–202.

[6] K. Oliynyk, M. O. Ciantia, and C. Tamagnini. “Effect of Soil Permeability on CPTu Test Results in Structured Clay Soils”. In: *8th CNRIG, Palermo*. Springer. 2023, pp. 460–467.

[7] P. W. Mayne et al. “Geomaterial behavior and testing”. In: *Proc. 17th ICSMGE*. IOS Press, 2009, pp. 2777–2872.

UKACM 2024 Conference, 10-12 April 2024, Durham University, Durham, UK
https://doi.org/10.62512/conf.ukacm2024.018

STUDY OF LANDSLIDES THROUGH A STABILISED SEMI-IMPLICIT MATERIAL POINT METHOD

M. Xie[1]*, P. Navas[2], S. López-Querol[1]

[1] Dept. of Civil, Environmental & Geomatic Engineering, University College London, UK.
mian.xie.18@ucl.ac.uk, s.lopez-querol@ucl.ac.uk
[2] Dept. Continuum Mechanics and Theory of Structures, UPM, Madrid, Spain. pedro.navas@upm.es

Abstract. In this research, a new semi-implicit two-phase double-point material point method is proposed, in which the soil and water phases are modelled using two distinct sets of material points, both being stabilised with a novel approach. The Nor-Sand constitutive model is implemented to simulate more realistic soil behaviour. Some landslide numerical examples are presented to investigate the performance of the proposed method and highlight the importance of using the double-point approach. The formulation with two sets of material points shows significantly different but more reliable results in the cases of landslides, compared with the conventional single-point approach. Furthermore, this research shows that the additional computational cost given by the additional water material points is acceptable. Therefore, it is recommended to use two sets of material points for some large deformation geotechnical problems.

Key words: *Material Point Method; Fractional-step method; Large deformation; Stabilisation*

1 Introduction

The Material Point Method (MPM) has become a popular continuum method for modelling large deformation geotechnical problems such as landslides. The MPM formulation is very similar to that of the Finite Element Method (FEM), except that the iteration points (i.e., material points) can move independently from the mesh, which is set to its original position at every step. Special treatment of iteration points and mesh allows MPM to model large deformation problems without mesh distortion; however, instabilities, such as quadrature error, cell-crossing noise and volumetric locking, arise. Although many researchers have attempted to solve these instabilities, fully stabilising the MPM is still a challenging task. Due to its unstable nature, MPM studies usually adopt explicit approaches and basic constitutive models.

To ensure convergence in an explicit approach, the time step must be smaller than the critical time step controlled by the Courant–Friedrichs–Lewy (CFL) condition. The critical time step defined by this condition is related to the bulk modulus of the material. Pore water is usually an important factor in geotechnical problems. However, the bulk modulus of water is about 100 times larger than that of the soil, resulting in an extremely small critical time step in a traditional explicit soil-water coupled MPM formulation. The time step of an implicit approach is not limited by the CFL condition, but the convergence issue can easily be raised when using an advanced constitutive model. Recently, the semi-implicit two-phase MPM has been derived based on the incremental fractional step method [1, 2]. In this approach, the water phase is solved implicitly, resulting in a significantly larger time step compared to the fully explicit approach. However, the available methods [1, 2] use a single set of material points to model both the soil and water phases (so-called single-point approach) with a very basic constitutive model. We have derived a new semi-implicit two-phase double-point MPM, in which the soil and water phases are modelled using two distinct sets of material points. The proposed method is stabilised by a newly derived modified F-bar method aiming to stabilise advanced constitutive models, in which both

deformation gradient increment and last converged elastic left Cauchy-Green tensors are stabilised. The Nor-Sand constitutive model is implemented to simulate the soil behaviour in a more realistic way. The derivation and formulation are presented in our extended paper [3].

In this research, some landslide examples are presented, to investigate the performance of the modified F-bar method and highlight the importance of using the double-point approach. More numerical examples, validations and the method of B-spline MPM can be found in the extended paper [3].

2 Numerical examples

2.1 Landslides - dry condition

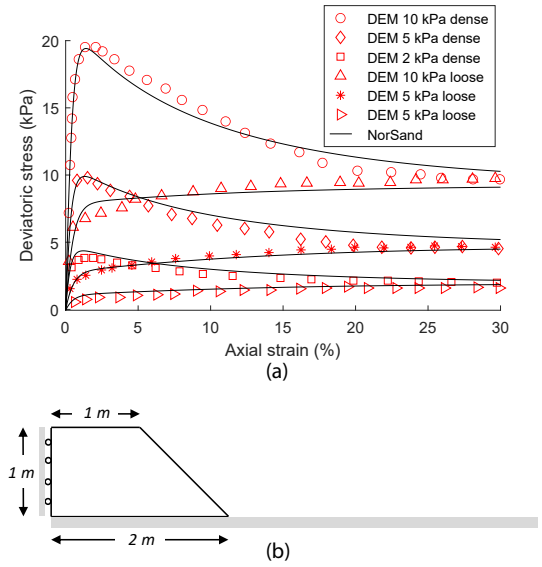

Figure 1: (**a**) Calibration of Nor-Sand with DEM drained triaxial; (**b**) Illustration of numerical model [3].

Parameter	Value
Soil density $\rho_s[kg/m^3]$	2,500
Shear modulus $G[kPa]$	4,000
Swelling index κ	0.002
Reference specific volume v_{c0}	1.88
Compression index λ	0.012
Slope of the critical state line M	0.7097
Yield function constant N	0.3
Plastic potential constant $\bar{N}$	0.3
Hardening coefficient h	300
Maximum dilatancy multiplier α	-4.5
Initial specific volume v_0 (dense)	1.629
Initial specific volume v_0 (loose)	1.736
Gravitational acceleration $g[m/s^2]$	-9.81
Initial porosity n_0	0.4
Initial hydraulic conductivity $k_0[m/s]$	5×10^{-3}

Table 1: Parameters for Landslides with Nor-Sand model.

Lu et al. [4] studied the problems of landslides using the discrete element method (DEM). DEM simulations [4] were conducted using dry granular materials with different particle shapes. Also, drained triaxial tests were conducted for these particles using DEM. In this research, we focus on spherical particles without rolling resistance [4]. The parameters of the Nor-Sand constitutive model are calibrated with the DEM drained triaxial tests using the single-element finite strain driver derived by Xie et al. [3]. Both Nor-Sand and the DEM stress-strain curves are presented in Fig. 1(a). The calibrated Nor-Sand parameters for the landslides simulations are summarised in Tab. 1.

Fig. 1(b) shows the geometry and boundary condition of the numerical model. The roller boundary condition is applied on the sides of the background mesh, and the fixed boundary condition is applied on the bottom of the background mesh to represent a rough surface. A 0.05 m wide square mesh with 4^2 material point per cell is used. The mesh is further refined to 0.025 m for the sensitive analysis purpose. The single-phase B-spline MPM is used with the Nor-Sand constitutive model. The total simulation time is 6 s for both dense and loose conditions, and the landslides are almost static at this time.

Fig. 2 presents the simulation results of the proposed method with different stabilisation methods. As

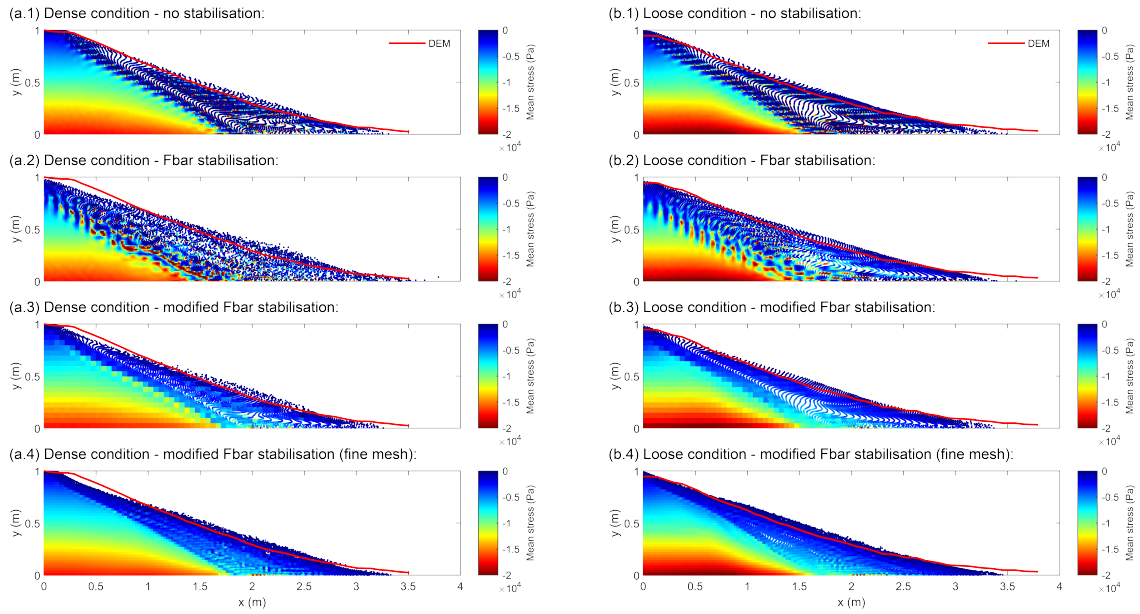

Figure 2: Comparison of different stabilisation methods under the (**a**) dense condition (**b**) loose condition

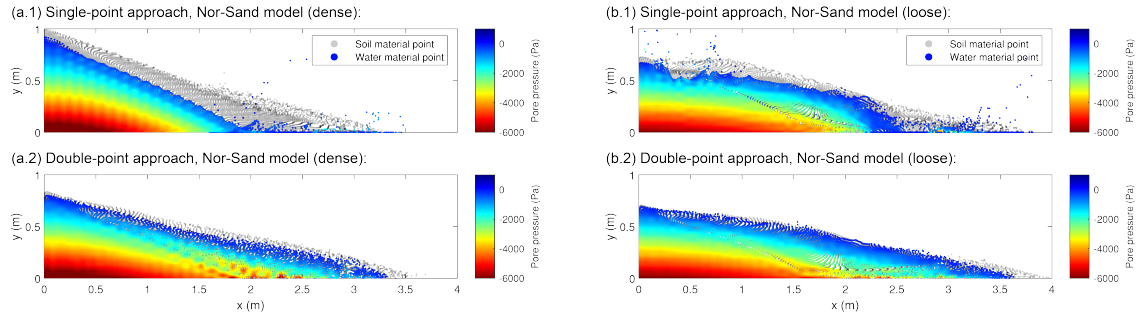

Figure 3: Comparison of the single- and double-point methods under the (**a**) dense condition (**b**) loose condition.

we can see, the standard F-bar method is not able to fully stabilise the stress oscillations under very large deformation. The performance of the standard F-bar method is even worse in the case of dilative granular material (i.e., dense condition), as shown in Figs. 2(a.2) and (b.2). On the contrary, the modified F-bar approach proposed by Xie et al. [3] can sufficiently eliminate stress oscillations. A higher resolution stress contour can be obtained by refining the mesh as shown in Figs. 2(a.4) and (b.4). However, a 0.05 m mesh is sufficient to ensure the accuracy of this numerical example. In addition, Fig. 2 shows an excellent agreement between DEM and B-spline MPM with the calibrated Nor-Sand constitutive model.

2.2 Landslides - fully saturated condition

For landslides with fully saturated condition, the same geometry and boundary conditions are applied as in the previous dry condition. A 0.05 m wide square mesh with 4^2 material point per cell is used. In addition, the same Nor-Sand parameters are used. The additional parameters for two-phase MPM are

documented in Tab. 1. The model initialisation process follows Xie et al. [3]. The total time, excluding the initialisation, is 12 s, when the propagation of the landslide becomes static in all cases.

The simulations are conducted using both semi-implicit single- and double-point approaches stabilised by the modified F-bar method. The soil's effective stress contour is omitted for these fully saturated landslides because it follows a similar pattern as that in the previous dry cases. An interested reader may refer to Xie et al. [3] where the soil stress contour is plotted. The pore water pressure contours are presented along with the soil material points. As shown in Fig. 3, the soil material points are represented as grey dots underneath the water material points. Although water material points are attached to soil material points in a single-point approach, we can still graphically present the water and soil material points separately. This is because in the water material points have their own velocities, and their position can be updated based on the velocities and initial coordinates.

As we can see in Fig. 3, the water phases of the single-point approach experience extensive instability in the case of the Nor-Sand model under both dense and loose conditions. On the contrary, the double-point approach is very stable. This phenomenon has not been reported in previous single-point MPM studies and may be due to two reasons: (a) a basic constitutive model (e.g. Mohr-Coulomb and Drucker-Prager) is used that cannot capture a realistic soil behaviour and (b) the pore pressure contour is plotted on the soil material points. Despite instabilities, the single-phase approach shows significantly stiffer behaviour compared to the double-point approach for the landslide problem, as shown in Fig. 3. The landslides are not fully generated in a single-phase approach with the Nor-Sand model, resulting in an underestimated runout distance and an overestimated angle of repose. In addition to accuracy, the computational efficiency of the double-point approach has also been assessed. Single- and double-point simulations have been repeated in the same computational environment. The additional computational cost of the double-point approach fluctuates from 14% to 16%, which is acceptable.

3 Conclusions

The modified F-bar method shows promising performance on MPM with a Nor-Sand model under very large deformation, whereas the F-bar method fails to stabilise the problem in this scenario. The MPM with Nor-Sand model can reproduce the DEM simulations for landslide problems as long as the material parameters are carefully calibrated. The two-phase double-point MPM is more stable and accurate than the single-point approach. In addition, the double-point approach only increases the computational cost by about 15%.

REFERENCES

[1] Kularathna, S., Liang, W., Zhao, T. et al. A semi-implicit material point method based on fractional-step method for saturated soil. *Int. J. Numer. Anal. Methods Geomech.* (2021) **45**:1405–1436.

[2] Yuan, W., Zheng, H., Zheng, X. et al. An improved semi-implicit material point method for simulating large deformation problems in saturated geomaterials. *Comput. Geotech.* (2023) **161**:10561.

[3] Xie, M., Navas, P. and López-Querol, S. A stabilised semi-implicit double-point material point method for soil-water coupled problems. *arXiv* (2024) arXiv:2401.11951.

[4] Lu, Z., Jin, Z. and Kotronis, P. Numerical analysis of slope collapse using SPH and the SIMSAND critical state model. *J. Rock Mech.* (2022) **14**:169–179.

UKACM 2024 Conference, 10-12 April 2024, Durham University, Durham, UK
https://doi.org/10.62512/conf.ukacm2024.092

DYNAMIC THREE-DIMENSIONAL RIGID BODY INTERACTION WITH HIGHLY DEFORMABLE SOLIDS, A MATERIAL POINT APPROACH

Robert Bird[1]*, Giuliano Pretti[1], William M. Coombs[1], Charles E. Augarde[1], Yaseen U. Sharif[2], Michael J. Brown[2], Gareth Carter[3], Catriona Macdonald[3], Kirstin Johnson[3]

[1]Department of Engineering, Durham University, Durham, England, UK.
robert.e.bird@durham.ac.uk
[2]School of Science and Engineering, University of Dundee, Dundee, Scotland, UK.
[3]British Geological Survey, Edinburgh, Scotland, UK.

Abstract. The ability to model rigid body interaction with highly deformable solids is a very useful tool in geoengineering, including the modelling of drag anchors on seabeds and seabed ploughing [7, 1]. However, these simulations entail several numerical challenges, such as modelling frictional contact, and incorporating inertia forces for analyses whose simulated time is considerable. Here the implicit Generalised Interpolation Material Point Method (GIMPM) is adopted to model the highly deformable solid, whilst a rigid body is used to model the significantly stiffer engineering object, such as an anchor. The whole system is integrated in time with the Newmark method with interaction between the two bodies occurring through a normal penalty contact and a penalty enforced Coulomb stick-slip friction law.

Key words: *Material Point Method; 3-dimensional; contact; rigid body*

1 Introduction

Understanding the penetration potential of an anchor is important for buried offshore infrastructure, such as power transmission cables for offshore renewable energy installations. However, modelling the penetration of an anchor into the seabed is challenging due to non-linear processes (large deformation, plasticity, contact) that must be taken into account. In this work an implicit GIMPM [4] is used to model the soil, whilst the anchor is represented by a discretised rigid body. The interaction between the bodies is achieved using a penalty contact [3]. An implicit analysis is used since it facilitates larger time increments compared to explicit approaches, particularly important with a refined discretisation. This paper outlines the key ingredients required to model anchor penetration using the material point method.

2 GIMP formulation with rigid body contact

For this approach an updated Lagrangian framework is adopted to model a system undergoing large deformations, [5, 4]. The weak statement for a material with domain, Ω and boundary $\partial\Omega$, interacting with a rigid body, Ω_R, with boundary, $\partial\Omega_R$,via the contact surface $\partial\Omega_C \subset \partial\Omega_R$ is

$$\underbrace{\int_{\varphi_t(\Omega)} (\nabla_x \eta)_{ij}\sigma_{ij}dV + \int_{\varphi_t(\Omega)} \rho\eta_i\ddot{u}_i dV - \int_{\varphi_t(\Omega)} \eta_i b_i dV}_{\text{deformable body}} + \underbrace{\int_{\varphi_t^R(\Omega_R)} \rho_R\zeta_i\ddot{w}_i dV - \int_{\varphi_t^R(\Omega_R)} \eta_i g_i dV}_{\text{rigid body}} + \int_{\varphi_t^R(\partial\Omega_C)} (\zeta_i - \eta_i) f_i dS = 0 \tag{1}$$

where the component in the last row is the contact between the two bodies. For the deformable body, φ_t is its motion, η the test function, σ_{ij} is Cauchy stress, u_i are the displacements with acceleration $\ddot{u}_i$, ∇_x is the gradient operator in the updated coordinate system (denoted by the lower case x), b_i is the body force. φ_t^R is the motion of the rigid body, w_i and $\ddot{w}_i$ are its displacement and acceleration, ζ is the test function, and g_i is the body force. Here the rigid body is considered to be the *main* contact surface whilst the deformable body is the *secondary*, the interaction between the two therefore is integrated over the contact surface of the rigid body $\varphi_t^R(\partial\Omega_C)$ with f_i being the normal and frictional forces imparted from the deformable body onto the rigid body modelled using the penalty method [2].

The domain corresponding to the deformable body, Ω, is discretised by a number of GIMP material points on a regular hexahedral background grid, with the GIMP basis used to link the material points p to the vertices of the background grid v, [4]. The GIMP basis functions and associated derivatives take the matrix forms $[S_{vp}]$ and $[\nabla S_{vp}]$. The rigid body domain is discritised by tetrahedral elements K to form the mesh $\mathcal{T}$, with flat triangular elements ∂K discretising the contact boundary $\partial\mathcal{T}_c$. Linear basis functions are used for the tetrahedral and triangular elements of the rigid body and have the respective matrix forms $[M]$ and $[\hat{M}]$. With these definitions, the discretised from of (1) is

$$\begin{aligned}\{R\} = &\underset{\forall p}{\mathbf{A}} \left([\nabla_x S_{vp}]^T \{\sigma_p\} V_p + \rho [S_{vp}]^T \{\ddot{u}_p\} - [S_{vp}]^T \{b\} \right) V_p \\ &+ \sum_{K\in\mathcal{T}} \int_K \rho [C]^T [M]^T \{\ddot{w}_h\} dV - \sum_{K\in\mathcal{T}} \int_K \rho [C]^T [M]^T \{g\} dV + \{R_c\},\end{aligned} \tag{2}$$

where $\{R_c\}$ is the contact residual, described in the next section, $[C]^T$ is a condensation matrix that ensures no relative movement between rigid body nodes, condensing all nodal degrees of freedom to only six; three for displacement and three for rotation. To form a linear set of equations to be solved, (2) is integrated in time with the Newmark method and is linearised about its primary variables (displacement of the background grid and motion of the rigid body).

3 Rigid Body interaction with Material Points

To model contact, the node-to-surface type formulation is applied here to the GIMPM [2, 3]. It is important to track any of the corners of the GIMP domains that interact with the rigid body, Figure 1, with contact determined using the closest point projection (CPP) method with the gap and gap vector functions, g^n and g_i^n,

$$g_i^n(\xi^\alpha(\tau),\tau) = g^n(\xi^\alpha(\tau),\tau) n_i(\xi^\alpha(\tau),\tau) = x_i(\tau) - x_i'(\xi^\alpha(\tau),\tau) \qquad \text{and} \qquad g^n = g_i^n n_i. \tag{3}$$

Above, τ is time, x_i is the GIMP domain's corner position, x_i' is the projected position onto the rigid body and ξ^α, with $\alpha \in [1,2]$, is the local coordinate of the triangular element ∂K that the GIMP corner is in contact with, shown in red in Figure 1. The derivative of g_i^n with respect to time gives the normal $\mathring{g}_i^n$ and a relative tangential velocity, $\mathring{g}_i^t$, which enables a description of the movement of a particle along the rigid body,

$$g_i^t = \int_T \mathring{g}_i^t \, \mathrm{d}t = \int_T \mathring{g}_i^{slip} \, \mathrm{d}t + \int_T \mathring{g}_i^{stick} \, \mathrm{d}t = g_i^{slip} + g_i^{stick}. \tag{4}$$

Using the above definitions, and following the work of [3], the contact residual can now be written as

$$\{R_c\} = \int_{\partial K\in\partial\mathcal{T}_c} \left(\delta g^n n_i p_i^n + \delta\xi^\alpha p_\alpha^t \right) \, \mathrm{d}x = 0 \tag{5}$$

where δg^n and $\delta\xi^\alpha$ are first variations provided in [3], p_i^n and p_α^t are respectively the normal and tangential point forces, with $(\cdot)^\alpha$ and $(\cdot)_\alpha$ respectively defining the contravariant and covariant variables. The covariant form of the tangential force is $p_\alpha^t = p_i^t(\partial x_i'/\partial\xi^\alpha)$ where p_i^t is a Cartesian vector of the frictional force and ε_n is the normal penalty, and $p_i^n = \varepsilon_n g_i^n$ is the Cartesian form of the normal force. p_i^t is modelled using Coulomb stick-slip friction, it has two states, an elastic stick state and a dissipative slip state, respectively given as,

$$p_i^{stick} = \varepsilon_t g_i^{stick} \quad \text{and} \quad p_i^{slip} = \mu|p_n|\frac{\mathring{g}_i^{slip}}{||\mathring{g}_i^{slip}||} \quad \text{if} \quad ||p^{stick}|| > \mu|p_n| \tag{6}$$

where $\mu|p^n|$ is the sticking force, μ is a constant coefficient of friction and ε_t is the tangential penalty. The law is subject to the Karush-Kuhn-Tucker (KKT) conditions: $f = ||p_i^{stick}|| - \mu p_n \leq 0$, $\lambda \geq 0$ and $f\lambda = 0$, where f is a yield surface and λ is the rate of tangential slip. The state of contact is found using the trial elastic state provided in [2], if the elastic trial state is within the yield surface there is a stick condition, otherwise the contact points is slipping.

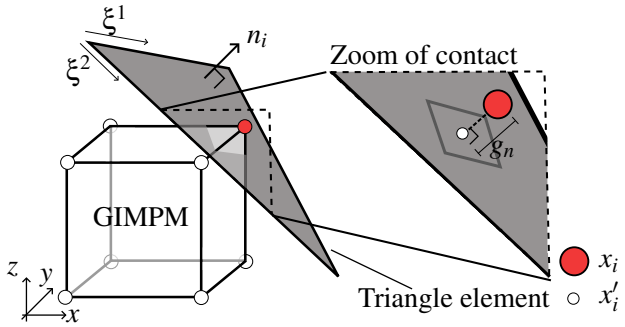

Figure 1: Diagram of the contact between a GIMP domain and a rigid body triangle.

4 Numerical investigation

To validate the method, two problems are considered: a sphere rolling down an inclined slope to test the stick/slip contact [6], and an anchor is dragged through soil to demonstrate that the method is robust.

3D Rolling sphere: The results for this problem are provided in Figure 2a. The slope has dimensions $W = L = 5$m and the sphere a diameter $d = 0.5$m. The background element size, $h = 0.25$ m, with 8 GIMPs within each element. A time step of 0.01s is used and to make the slope rigid all degrees of freedom are constrained. Three coefficients of friction are considered, at $\mu = 0.0$ and 0.2 slip behaviour should occur, whilst at 0.4 it is a stick condition. The results in Figure 2a show very good agreement with the analytical result [6].

Anchor: The second problem is an anchor being dragged through a soil with a relative density of 38%, the material is modelled as linear elastic-plastic, the latter modelled with the Drucker-Prager model; both the anchor and soil are subject to gravity. This example demonstrates the method to be robust to a complex engineering scenario, and demonstrates the potential to model complicated geotechnical engineering problems. The anchor is being pulled at a velocity of 0.5 m/s, the grid size is $h = 0.2$ m with 8 GIMPs per element and the time step is 0.04 s. Figure 2b shows the anchor at load step 5 and Figure 2c at load step 100. Blue and red are respectively negative and positive vertical displacements.

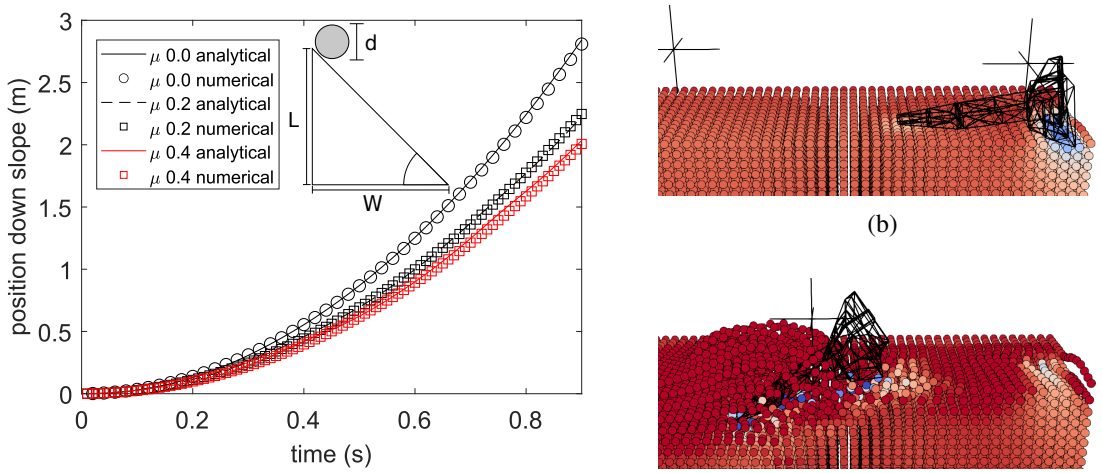

Figure 2: (a) shows a comparison of numerical and analytical results of a ball rolling down a hill, inset is the problem geometry. (b) and (c) show half an anchor being pulled through soil at load steps 5 and 100.

5 Conclusion

A GIMPM for modelling contact with rigid bodies has been presented, it shows good agreement with analytical solutions and is able to model complicated geoengineering problems. The next step is to use the method to quantify the penetration of different anchor geometries in realistic soil conditions.

Acknowledgements

This work was supported by the Engineering and Physical Sciences Research Council [grant numbers EP/W000970/1, EP/W000997/1 and EP/W000954/1].

REFERENCES

[1] Robinson, S., Brown, M.J., Matsui, H., Brennan, A., Augarde, C., Coombs, W. and Cortis, M. *A cone penetration test (CPT) approach to cable plough performance prediction based upon centrifuge model testing*, *Can. Geotech. J.*, (2021) **58**(10):1466-77.

[2] Wriggers, P. *Computational contact mechanics*. Springer, Vol. 2., (2006).

[3] Pietrzak, G., and Curnier, A. *Large deformation frictional contact mechanics: continuum formulation and augmented Lagrangian treatment*, *Comput. Methods Appl. Mech. Eng.*, (1999) **177**(3-4):351-381.

[4] Charlton, T.J., Coombs, W.M., and Augarde, C.E. *iGIMP: An implicit generalised interpolation material point method for large deformations*, *Comput. Struct.*, (2017) **190**:108-125,

[5] Coombs, W.M., and Augarde, C.E. *AMPLE: a material point learning environment*, *Adv. Eng. Softw.*, (2020) **139**:102748

[6] Bardenhagen, S.G., Brackbill, J.U., and Sulsky, D., *The material-point method for granular materials*, *Comput. Methods Appl. Mech. Eng.*, (2000) **187**(3-4):529-541

[7] Sharif, Y.U., Brown, M.J., Coombs, W.M., Augarde, C.E., Bird, R., Carter, G., MacDonald, C., & Johnson, K. (2023). *Characterization of Anchor Penetration Behaviour for Cable Burial Risk Assessment*. In *9th Int. SUT OSIG Conference "Innovative Geotechnologies for Energy Transition"*, London, September 12-14:555–562.

UKACM 2024 Conference, 10-12 April 2024, Durham University, Durham, UK
https://doi.org10.62512/conf.ukacm2024.101/

Numerical simulation of in-situ free fall cone penetrometer tests using the material point method

Debasis Mohapatra [1*], Saeideh Mohammadi[1], Maarit Saaresma[2], Joonas Virtasalo[2], Wojciech Sołowski[1]

Department of Civil Engineering, Aalto University, Espoo, Finland.
debasis.mohapatra@aalto.fi, wojciech.solowski@aalto.fi
[2]Geological Survey of Finland, Espoo, Finland
maarit.saresma@gtk.fi, joonas.virtasalo@gtk.fi

Abstract

This paper proposes a numerical framework to simulate in-situ free fall cone penetration tests conducted on soft and sensitive marine clay. First, the free fall cone penetration tests are carried out at an offshore site in the northern part of the Gulf of Finland, Baltic Sea. The numerical simulation employs the Generalized Interpolation Material Point Method to replicate the process of indentation of the cone penetrometer into the clay. The clay is modelled using an advanced constitutive model that considers the effect of strain rate and strain softening associated with the dynamic penetration process. The simulation uses a friction contact model to represent the interface between the cone penetrometer and the clay. The numerical simulation accurately replicates the penetration process associated with the tests.

Keywords: *Free fall cone penetrometer test, Generalized Interpolation Material Point Method, Contact Problems, Strain rate, Destructuration.*

1 Introduction

The free fall cone penetrometer tests (FF-CPT) are simple, rapid, and cost-effective tests often used in seabed characterization [1]. However, there are still uncertainties in the interpretation of the test data and its correlation with the soil properties. Currently, the correlations used are largely empirical and analytical [2–4], primarily due to the complexities associated with numerically simulating the dynamic penetration process. Therefore, the development of reliable numerical models capable of replicating the dynamic penetration process may lead to more accurate correlations and data interpretation, thereby enhancing the precision of soil properties obtained with FF-CPT.

The experimental [3,5] and numerical studies [6,7] point out that the uncertainties in FF-CPT data interpretation could be due to the wide range of strain rates associated with the test. However, the determination of the strain rate effect on the shear strength of soil is quite complicated due to its possible dependency on soil properties, cone penetrometer parameters (e.g., geometry, density), and impact velocity. Further, the marine clays are also sensitive, and their undrained shear strength reduces during the cone penetration process due to the destructuration of clay. Not considering the effects of strain rate and destructuration on clay will significantly influence the accuracy of the numerical simulation.

In the present study, we replicate an in-situ free fall cone penetrometer test results with the Generalized Interpolation Material Point Method simulation. The numerical simulation results that consider the effect of strain rate and destructuration of clay well replicate the dynamic penetration process.

2 Problem description

The study area is situated to the south of Kytö Island in the Gulf of Finland, north of the Baltic Sea. Three FF-CPT tests were conducted at this location using the Graviprobe 2.0 (@dotOcean). The Graviprobe free fall penetrometer (FFP) has a length of 1.97 meters, weighs 20.2 kilograms, and has a diameter of 0.05 meters. The Graviprobe is dropped from the sea surface, and it accelerate in free fall and penetrates into the seabed with an impact velocity of approximately 7.6 m/s. The variation of acceleration with depth associated with the three different FF-CPT experiments is shown in Figure 2. Triaxial tests carried out on soil samples collected from the location suggest that the undrained shear strength of the soil sample varies between 6-7 kPa.

This paper uses Generalized Interpolation Material Point Method (GIMP) as encoded in Uintah software (http://uintah.utah.edu/) for numerical simulation of the FF-CPT. The numerical geometry of the model is defined by taking advantage of the axisymmetric condition of the test (Figure 1). The lateral and vertical spread

of the soil domain is decided based on a few trial analyses, so that the boundaries will not influence the outcome of the numerical simulation. The dimensions of free fall penetrometer are consistent with the Graviprobe dimensions used in the experiment. For numerical modelling, the domain is discretized by using a structured mesh of square size (5mm× 5mm) with 4 material points in the cell. These corresponds to 10364 number of material points in the simulation. The simulations assume frictional contact with friction coefficient (μ), implemented in Uintah by [8]. The simulation uses a more recent friction contact algorithm , which uses logistic regression to identify the interface between two materials in contact.

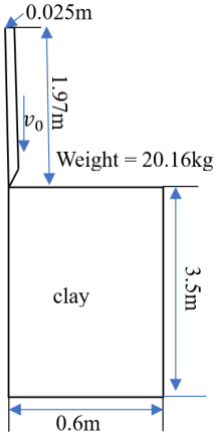

Figure 1. Numerical model of FF-CPT. Unit: m

The simulation uses the Tresca material model extended to consider the effect of strain rate and destructuration on undrained shear strength as mentioned in [9,10]. The undrained shear strength of clay is expressed as a function of strain rate ($\delta\gamma$), accumulated shear strain (ξ), and sensitivity (S_t) as:

$$s_u(\delta\gamma, \xi, S_t) = s_{u,ref}\left[\left(\frac{\delta\gamma}{\delta\gamma_{ref}}\right)^{\beta}\right]\left[\frac{1}{S_t} + \left(1 - \frac{1}{S_t}\right)e^{\frac{-3\xi}{\xi_{95}}}\right] \quad (1)$$

where $s_{u,ref}$ is reference shear strain at reference strain rate ($\delta\gamma_{ref}$), β is the strain rate parameter associated with the power law, and ξ_{95} is the accumulated shear strains required to obtain 95% reduction of the shear strength. For small deformations, the dynamic undrained shear modulus also depends on the shear strain rate and can be estimated as:

$$G_u(\delta\gamma) = G_{u,ref}\left(\frac{\delta\gamma}{\delta\gamma_{ref}}\right)^{\beta} \quad (2)$$

Table 1 summarizes the various model parameters considered in the study. The reference undrained shear strength ($s_{u,ref}$) of clay is set to be 6.5 kPa based on the results from Triaxial experiments. The value of reference shear strength ($\delta\gamma_{ref}$) is calculated to be 0.56 s^{-1} based on cone penetration test (CPT) [3]. The simulation uses all the other material parameters same as those used for the numerical replication of the fall cone test and model FF-CPT simulation in [11,12].

Table 1: Material parameters for numerical simulation

$s_{u,ref}$ (kPa)	$\delta\gamma_{ref}$ (s^{-1})	β	$G_{u,ref}$ (kPa)	v_u	S_t	ξ_{95} (s^{-1})	ρ (kN/m^3)	μ
6.5	0.56	0.08	$167s_{u,ref}$	0.495	10	10	15	0.65

3. Numerical results

Figure 2 illustrates that the variation of FFP acceleration with depth obtained from numerical simulation closely matches that obtained from FF-CPTs. The final penetration depth obtained from the numerical simulation is 1.78 meters, which aligns well with the experimental range of 1.8 to 1.95 meters. In Figure 3a, the final displacement contour of the FFP is depicted. Figure 3b shows the variation of shear strain rate in the soil at time t = 0.12 seconds from the start of penetration. The shear strain rate is predominant at the tip of the FFP and in the soil layer surrounding it. As indicated in Equations (1) and (2), the undrained shear strength in these regions is expected to increase with an increase in shear strain rate. Figure 3c displays the variation of normalized undrained shear strength ($s_u/s_{u,ref}$) in the domain at time t = 0.12 seconds from the start of penetration. It demonstrates that the undrained shear strength of the soil surrounding the FFP (approximately 0.01 meters) reduces drastically due to a very high accumulation of shear strain in that region. Destructuration has a more predominant influence in this region. Beyond that region, the effect of strain rate on the strength of the soil is predominant.

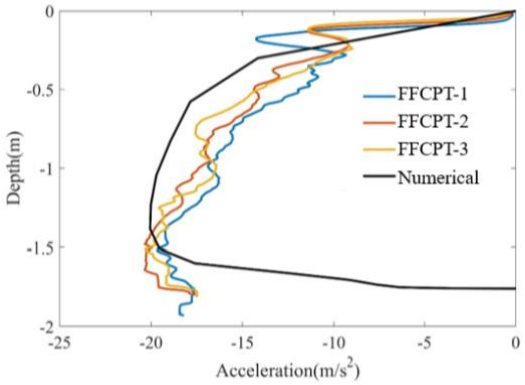

Figure 2: Variation of cone acceleration with depth.

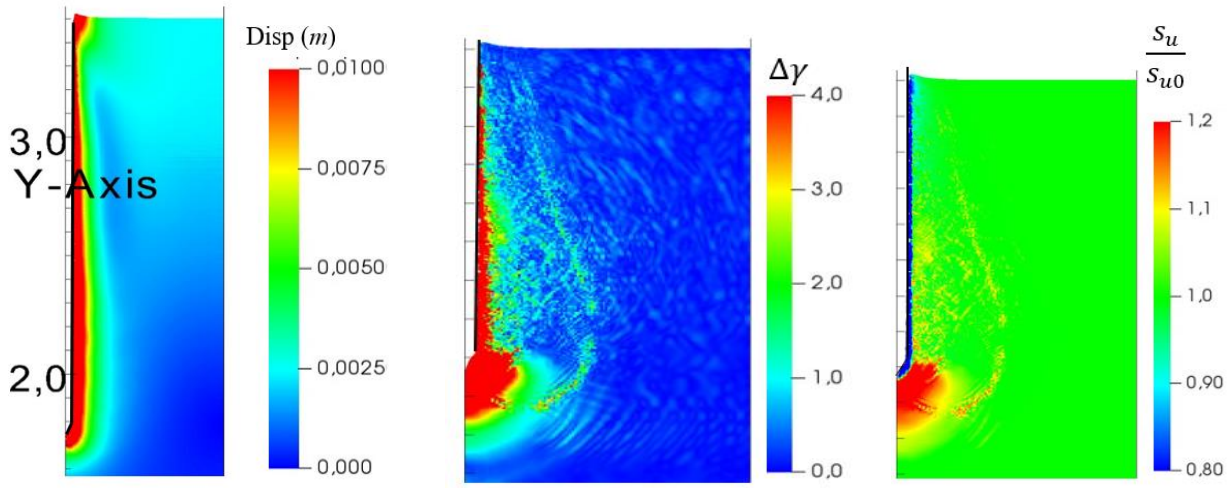

(a) t=1 sec. (b) t=0.12 sec. (c) t =0.12sec

Figure 3: (a) The displacement contour at the end of FF-CPT, (b) Contour of shear strain rate at t= 0.12 sec., and (c) Contour of normalized undrained shear strength at t = 0.12sec.

3 Conclusions

This paper presents a comprehensive numerical simulation of a free fall cone penetrometer test conducted at an offshore site using the Generalized Interpolation Material Point Method (GIMP). The undrained shear strength of the clay obtained from laboratory triaxial tests is utilized for the numerical simulation. An extended Tresca material model is employed to account for the effects of strain rate and strain softening caused by the

destructuration of clay during the dynamic cone penetration process. The simulation utilizes the same material parameters as those employed in previous numerical replications of fall cone tests and laboratory-scale FF-CPTs [9,10]. The experimental results are accurately reproduced by the numerical simulation, demonstrating that the numerical framework employed in this study can effectively capture the dynamic penetration mechanism associated with soft and sensitive clays.

Acknowledgments

This research is part of the Geomeasure project, funded by the Academy of Finland (grant number 347602).

References

[1] Stark N, Hay AE, Trowse G. Cost-effective geotechnical and sedimentological early site assessment for ocean renewable energies. 2014 Oceans - St John's, OCEANS.

[2] Chow SH, Airey DW. Soil strength characterisation using free-falling penetrometers. *Geotechnique* 2013;63:1131–1143.

[3] Chow SH, O'Loughlin CD, White DJ, Randolph MF. An extended interpretation of the free-fall piezocone test in clay. *Geotechnique* 2017;67:1090–1103.

[4] Bezuijen A, Den Hamer DA, Vincke L, Geirnaert K. Free fall cone tests in kaolin clay. *Physical Modelling in Geotechnics* 2018;1:285–91.

[5] Chow SH, Asce AM, Airey DW. Free-Falling Penetrometers: A Laboratory Investigation in Clay. *Journal of Geotechnical and Geoenvironmental Engineering* 2014;140:201–214.

[6] Moavenian MH, Nazem M, Carter JP, Randolph MF. Numerical analysis of penetrometers free-falling into soil with shear strength increasing linearly with depth. *Computers and Geotechnics* 2016;72:57–66.

[7] Zambrano-Cruzatty L, Yerro A. Numerical simulation of a free fall penetrometer deployment using the material point method. *Soils and Foundations* 2020;60:668–682.

[8] Bardenhagen SG, Guilkey JE, Roessig KM, Brackbill JU, Witzel WM, Foster JC. An Improved Contact Algorithm for the Material Point Method and Application to Stress Propagation in Granular Material. CMES 2001;2:509–22.

[9] Tran QA, Sołowski W. Generalized Interpolation Material Point Method modelling of large deformation problems including strain-rate effects – Application to penetration and progressive failure problems. *Computers and Geotechnics* 2019;106:249–65.

[10] Einav I, Randolph M. Effect of strain rate on mobilised strength and thickness of curved shear bands. *Geotechnique* 2006;56:501–504.

[11] Mohapatra D, Li Z, Saresma M, Virtasalo J, Solowski W. Replication of fall cone test on marine clay with a Generalized Interpolation Material Point Method simulation. In: Zdravkovic L KSTDTA, editor. *10th European Conference on Numerical Methods in Geotechnical Engineering*, 2023, p. 1–7.

[12] Mohapatra D, Saresma M, Virtalaso J, Solowski W. Numerical Simulation of a Laboratory-Scale Free Fall Cone Penetrometer Test in Marine Clay with the Material Point Method. *VIII International Conference on Particle-Based Methods*, CIMNE; 2023.

Innovative Computational Approaches in Composite Material Analysis

UKACM 2024 Conference, 10-12 April 2024, Durham University, Durham, UK
https://doi.org/10.62512/conf.ukacm2024.002

MODELLING FRACTURE BEHAVIOUR IN FIBRE-HYBRID 3D WOVEN COMPOSITES

Anna Weatherburn[1]*, Anne Reinarz[1], Stefano Giani[1], Stefan Szyniszewski[1]

[1] Department of Engineering, Durham University, Durham, DH1 3LE, UK.
anna.t.weatherburn@durham.ac.uk

Abstract. Modelling fracture within 3D woven composites is a significant challenge and the subject of ongoing research due to their complex hierarchical structures. This challenge is heightened when modelling 3D woven composites with multiple fibre types, referred to as fibre-hybrid 3D woven composites. This work addresses this challenge through the development of a novel methodology for modelling fracture in fibre-hybrid 3D woven composites. The bulk of preceding research into fracture modelling of 3D woven composites has focused on single-fibre-type woven composites with limited research into fibre-hybrid 3D woven composites. Research has focused on highly simplified models, often relying on experimental results [1], [2], [3]. In contrast, this work will apply fracture modelling techniques to high-fidelity finite element models of 3D woven composites resulting in simulations of fracture behaviour comparable to the behaviour observed in experimental tests. 3D woven composites possess exceptional properties such as improved out-of-plane strength, stiffness, fracture toughness, fatigue resistance and damage tolerance compared to more traditional 2D woven composites [4], [5], [6], [7]. However, currently the use of 3D woven composites in industry is limited by a lack of knowledge about their behaviour. Manufacturing and testing the required number of samples is prohibitively expensive and time-consuming resulting in the need for accurate models of 3D woven composite behaviour. The novel fracture model for fibre-hybrid 3D woven composites developed in this work will serve as a foundational tool for developing new material designs, paving the way for innovation and the widespread adoption of 3D woven composites in a diverse range of industries.

Key words: *fracture modelling; finite element; 3D woven composites*

1 Introduction

The utilization of 3D woven composites in engineering applications has garnered significant attention due to their exceptional mechanical properties compared to traditional 2D woven composites [4], [5], [6], [7]. However, accurately modeling fracture behavior within these materials, particularly in cases involving multiple fibre types, remains a considerable challenge. This work presents a novel methodology for modeling fracture in fibre-hybrid 3D woven composites, aiming to address this challenge and advance the understanding and utilization of these innovative materials.

3D woven composites (3DWCs) were first manufactured in the 1970s. 3D woven composites are fibre-reinforced composites similar to the carbon fibre found in bike frames or the glass-fibre used in wind turbine blades where fibres are woven together and then infused with a resin. However, 3D woven composites differ from these traditional 2D woven composites in that they also have reinforcements in the through-the-thickness or z-direction, as in Figure 1. These through-the-thickness binder yarns, or Z-tows, inhibit delamination between the layers of woven composite resulting in improved mechanical properties.

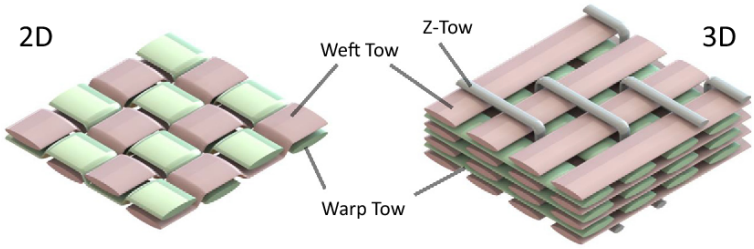

Figure 1: 2D and 3D woven composites with warp, weft and through-the-thickness yarns or Z-tows labelled. [8]

Currently, the reported benefits of 3DWCs include improved through-the-thickness mechanical properties, improved manufacturing processes and better design flexibility compared to 2D woven composites [9]. These benefits make 3D woven composites an attractive prospect in many engineering applications. However, uptake of the technology has been slow due to a poor understanding of the material's behaviour, namely due its intricate hierarchical structure and the complex interactions between the components within the composite. To enable the widespread use of 3D woven composites in industry detailed high-fidelity models of the behaviour of 3D woven composites under loading are required.

2 Problem description

Accurate fracture behaviour models of 3D woven composites are limited to a small number of models. The hierarchical structure of 3D woven composites and the interaction between the fibre and resin within the composite presents inherent complexities in modelling fracture behaviour. This challenge is further compounded in fibre-hybrid 3D woven composites, where multiple fibre types interact within the composite structure.

Fibre-hybrid 3D woven composites can provide greater benefits over 'pure' 3D woven composites with each fibre type contributing towards the overall material properties. For example, in this work, brittle but strong carbon fibre are combined with weaker but tough polypropylene fibres creating a material which is stronger than a purely polypropylene weave but tougher than a purely carbon fibre weave.

Despite their benefits, due to the complexity of their behaviour and challenges in manufacturing, fibre-hybrid 3D woven composites are currently rarely used in industry and modelling techniques of their behaviour are not well-established. No high-fidelity fibre-hybrid 3D woven composite fracture models accounting for the level of detail presented in this work have been previously reported. Previous research efforts have primarily focused on single-fibre-type woven composites or have relied on extremely simplified models and experimental data [3], [10], [11], [12]. Consequently, there exists a gap in the understanding the fracture behaviour of fibre-hybrid 3D woven composites, hindering their widespread adoption in various industries.

The basis of the fibre-hybrid 3D woven composite fracture model developed in this work is a high-fidelity finite element model of the weave produced by a code currently under development at the University of Bristol. This finite-element model is then adapted in this work to model fibre-hybrid 3D woven composites and to model fracture within the material. Before a fracture model can be developed, an elastic model of the fibre-hybrid weave must first be established. This extended abstract will present these initial results. The proposed methodology will integrate advanced fracture mechanics principles with

high-fidelity finite element analysis to model fracture behaviour in fibre-hybrid 3D woven composites.

3 Numerical results

The numerical results presented in this section will include a validation of the elastic model based on experimental results conducted on an initial material design and numerical results for different fibre volume fractions and stiffness ratios between fibre types.

3.1 Validating the Elastic Model against Experimental Results

Table 1: Table of numerical and experimental results of warp and weft Young's Moduli for a baseline and fibre-hybrid composite.

		Young's Modulus (Warp) [GPa]	Young's Modulus (Weft) [GPa]
Numerical	Baseline	20	11
	Fibre-Hybrid	16	9
Experimental	Baseline	66 $\pm$5	76 $\pm$5
	Fibre-Hybrid	13 $\pm$1	12 $\pm$1

Tensile tests were conducted for both a baseline 3D woven composite, woven from purely carbon fibre, and a fibre-hybrid 3D woven composite, woven from polypropylene fibres and carbon fibre. Table 1 compares the numerical and experimental results for Young's Modulus for the baseline and fibre-hybrid composites. The warp and weft Young's Moduli are the values of Young's Modulus measured when testing the material unit cell or samples in the warp or weft direction, see Figure 1. In the initial stages of the research, the values for Young's Modulus are within the correct order of magnitude, however the model fails to capture the true behaviour of the material. The baseline model in particular massively underestimates the values for Young's Modulus.

3.2 Fibre-Type Volume Fraction within 3D Woven Composite

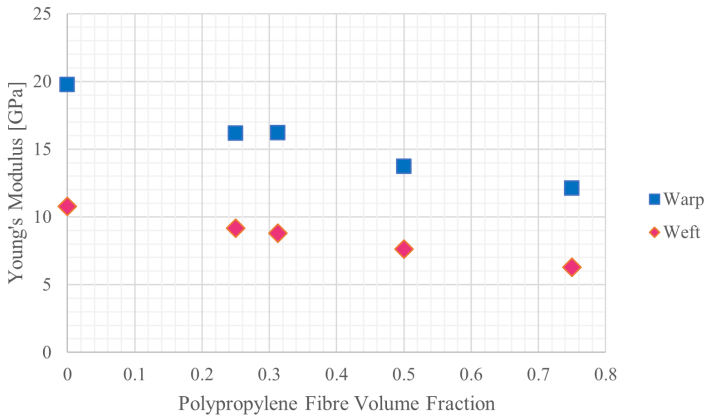

Figure 2: Young's Modulus for both warp and weft directions for polypropylene fibre volume fractions (e.g. compared to carbon fibre) of 0, 0.25, 0.3, 0.5 and 0.75.

The fibre-type volume fraction is the number of one type of fibre compared to the other fibre type within a fibre-hybrid 3D woven composite, e.g. if half of the yarns are one fibre type the fibre-type volume fraction will be 0.5. Figure 2 presents the Young's Moduli in the warp and weft direction for five different fibre-type volume fractions.

3.3 Stiffness Ratio within 3D Woven Composite

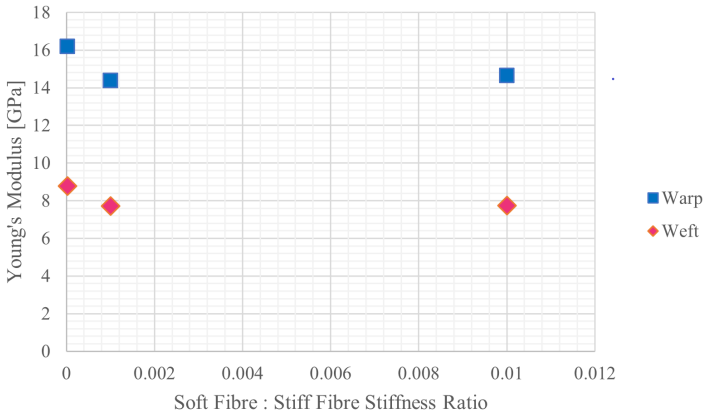

Figure 3: Young's Modulus for both warp and weft directions for three different stiffness ratios between one soft fibre type and one stiff fibre type.

The stiffness ratio within a fibre-hybrid 3D woven composite is the ratio between the stiffness for each fibre-type, if one fibre type has a stiffness that is ten times smaller than the other fibre type the stiffness ratio would be 0.1. Figure 3 presents the Young's Moduli in the warp and weft direction for three different stiffness ratios.

4 Conclusions

In conclusion, the development of a novel methodology for a high-fidelity finite element model of fibre-hybrid 3D woven composites represents a significant advancement in composite materials research and design. By addressing the challenges associated with accurately predicting fracture behavior, this work will further lay the foundation for enhanced understanding and utilization of these innovative materials across various industries. Preliminary results show that an initial elastic model of fibre-hybrid 3D woven composites using the proposed methodology required some further assessment and adaptations to fully capture the true behaviour of the material. Moving forward, continued improvements and the application of an optimisation process to the proposed methodology hold promise for advancing the adoption of fibre-hybrid 3D woven composites within industry.

Acknowledgments

This work was conducted under the the Aura Centre for Doctoral Training in Offshore Wind Energy and the Environment. The authors would like to thank EPSRC and NERC[Grant number: EP/S023763/1, Project Reference: 2744497] for providing financial support for this project.

References

[1]Wu Xu et al. "Highly tough 3D woven composite materials: Fracture characterization and toughening mechanisms". In: *Theoretical and Applied Fracture Mechanics* 124 (2023), p. 103734. ISSN: 0167-8442. DOI: https://doi.org/10.1016/j.tafmec.2022.103734.

[2]Sohail Ahmed et al. "Impact Response of Carbon/Kevlar Hybrid 3D Woven Composite Under High Velocity Impact: Experimental and Numerical Study". en. In: *Applied Composite Materials* 27.3 (June 2020), pp. 285–305. ISSN: 1573-4897. DOI: 10.1007/s10443-020-09809-3.

[3]Raúl Muñoz et al. "Influence of hybridisation on energy absorption of 3D woven composites under low-velocity impact loading. Modelling and experimental validation". en. In: *International Journal of Impact Engineering* 165 (July 2022), p. 104229. ISSN: 0734-743X. DOI: 10.1016/j.ijimpeng.2022.104229.

[4]Fredrik Stig and Stefan Hallström. "Assessment of the mechanical properties of a new 3D woven fibre composite material". In: *Composites Science and Technology* 69.11-12 (2009), pp. 1686–1692.

[5]Alexander E Bogdanovich. "Advancements in manufacturing and applications of 3D woven preforms and composites". In: *Proceeding of the 16th international conference on composites materials (ICCM-16)*. 2007, pp. 8–13.

[6]Licheng Guo et al. "Damage evolution of 3D woven carbon/epoxy composites under tension-tension fatigue loading based on synchrotron radiation computed tomography (SRCT)". In: *International Journal of Fatigue* 142 (2021), p. 105913.

[7]Yanqi Hu, Zekan He, and Haijun Xuan. "Impact Resistance Study of Three-Dimensional Orthogonal Carbon Fibers/BMI Resin Woven Composites". en. In: *Materials* 13.1919 (Jan. 2020), p. 4376. ISSN: 1996-1944. DOI: 10.3390/ma13194376.

[8]Kevin R. Hart et al. "Mechanisms and characterization of impact damage in 2D and 3D woven fiber-reinforced composites". In: *Composites Part A-applied Science and Manufacturing* 101 (2017), pp. 432–443. URL: https://api.semanticscholar.org/CorpusID:49425944.

[9]In: *3D Fibre Reinforced Polymer Composites*. Ed. by Liyong Tong, Adrian P. Mouritz, and Michael K. Bannister. Oxford: Elsevier Science, 2002, pp. 219–236. ISBN: 978-0-08-043938-9. DOI: https://doi.org/10.1016/B978-008043938-9/50022-3. URL: https://www.sciencedirect.com/science/article/pii/B9780080439389500223.

[10]Yanneck Wielhorski et al. "Numerical modeling of 3D woven composite reinforcements: A review". In: *Composites Part A: Applied Science and Manufacturing* 154 (Mar. 2022), p. 106729. ISSN: 1359-835X. DOI: 10.1016/j.compositesa.2021.106729.

[11]Deepak K. Patel, Anthony M. Waas, and Chian-Fong Yen. "Compressive response of hybrid 3D woven textile composites (H3DWTCs): An experimentally validated computational model". In: *Journal of the Mechanics and Physics of Solids* 122 (Jan. 2019), pp. 381–405. ISSN: 0022-5096. DOI: 10.1016/j.jmps.2018.08.018.

[12]Huaiyu Lu et al. "A progressive damage model for 3D woven composites under compression". en. In: *International Journal of Damage Mechanics* 28.6 (June 2019), pp. 857–876. ISSN: 1056-7895. DOI: 10.1177/1056789518793994.

UKACM 2024 Conference, 10-12 April 2024, Durham University, Durham, UK
https://doi.org/10.62512/conf.ukacm2024.035

A HIGHER-ORDER FINITE ELEMENT FRAMEWORK FOR HYPER-VISCO-ELASTODYNAMICS OF SOFT MULTIFUNCTIONAL COMPOSITES

Chennakesava Kadapa[1], **Mokarram Hossain**[2]

[1] School of Computing, Engineering and Bult Environment, Edinburgh Napier University, Edinburgh.
c.kadapa@napier.ac.uk
[2] Zienkiewicz Institute for Modelling, Data and AI, Swansea University, Swansea.
mokarram.hossain@swansea.ac.uk

Abstract. Smart multifunctional polymeric composites such as electroactive polymers, magnetoactive polymers and active hydrogels find numerous applications in soft robotics, energy harvesting, flexible electronic devices, tactile sensors, precision drug delivery devices etc.. Accurate simulation of large-deformation and large-strain response of these composites under different stimuli requires sophisticated formulations to capture multiphysical interactions at the interface between solid mechanics, electromagnetism and chemical transport. Moreover, the viscoelastic characteristics of the underlying polymer and the high-frequency (dynamic) response require different time integration schemes for solving ordinary differential equations of two different orders, resulting in inconsistencies and discretisation errors [4]. This contribution presents a novel unified computational framework for simulating the response of electroactive polymers [1, 4] and magnetoactive polymers [2], including the effects of growth [1, 3], viscoelasticity [2] and elastodynamics [4]. Several benchmark examples and problems of practical interest are presented to demonstrate the performance of the proposed framework.

Key words: *Smart materials; Mixed formulation; Finite Element Method; Hyperelasticity; Viscoelasticity.*

1 Formulation

Following the Hamilton's principle, the action functional, $\mathcal{A}$, for the displacement-pressure-magnetic potential ($\boldsymbol{u}/p/\phi$) formulation can be written as

$$\mathcal{A} = \int_0^{t_f} \mathcal{L}(\boldsymbol{u}, \boldsymbol{v}, p, \phi, t)\, dt \tag{1}$$

where $\boldsymbol{u}$ is displacement, $\boldsymbol{v}$ is velocity, p is pressure, ϕ is magnetic potential, t is time, t_f is final time and $\mathcal{L}$ is the Lagrangian which, in terms of total kinetic energy ($\mathcal{T}$) and total potential energy ($\mathcal{V}$) is given as

$$\mathcal{L} = \int_{\mathcal{B}_0} \frac{1}{2}\rho_0 \boldsymbol{v}^2 \, \mathrm{d}V \quad - \quad \left[\int_{\mathcal{B}_0} \Psi(\overline{\boldsymbol{C}}, p, \phi)\, \mathrm{d}V + \int_{\mathcal{B}_0} \Psi_p \, \mathrm{d}V - \mathcal{V}_{\text{ext}}\right] \tag{2}$$

where $\mathrm{d}V$ is the elemental volume in the reference configuration and Ψ_p is the energy function for imposing the incompressibility constraint, see Kadapa and Hossain [5] for the details.

The total energy function is given by

$$\Psi = \Psi_\infty^{\text{mech}}(\bar{I}_1, \bar{I}_2, J) + \Psi^{\text{vol}}(J) + \Psi_v^{\text{mech}}(\bar{\boldsymbol{C}}, \boldsymbol{A}) + \Psi_{\text{hm}}^{\text{magn}}, \tag{3}$$

where $\Psi_{\infty}^{\text{mech}}(\bar{I}_1, \bar{I}_2, J)$ is the deviatoric hyperelastic energy function, $\Psi^{\text{vol}}(J)$ is the volumetric energy function, $\Psi_{v}^{\text{mech}}(\bar{\boldsymbol{C}}, \boldsymbol{A})$ is the energy function contribution from viscoelastic behaviour, and $\Psi_{\text{hm}}^{\text{magn}}$ is the energy function contribution due to the magnetic field. $\bar{I}_1$ and $\bar{I}_2$ are the first and second invariants of $\bar{\boldsymbol{C}}$. $\boldsymbol{A}$ is the internal state variable, and it is a second-order strain-like tensor. The viscous part is given as

$$\Psi_{v}^{\text{mech}}(\bar{\boldsymbol{C}}, \boldsymbol{A}) = \sum_{k=1}^{s} \frac{G_v^{(k)}}{2} \left[\boldsymbol{A}^{(k)} : \bar{\boldsymbol{C}} - 3 - \ln(\det(\boldsymbol{A}^{(k)})) \right], \tag{4}$$

with the evolution equation for the internal variable $\boldsymbol{A}$ as

$$\dot{\boldsymbol{A}}^{(k)} = \frac{1}{\tau^{(k)}} \left[\bar{\boldsymbol{C}}^{-1} - \boldsymbol{A}^{(k)} \right], \tag{5}$$

where k is the summation counter, s is the number of Maxwell elements, and $G_v^{(k)}$, $\boldsymbol{A}^{(k)}$ and $\tau^{(k)}$, respectively, are the shear modulus, internal variable and relaxation time for the kth member of the Maxwell model.

The finite element formulation is derived using the calculus of variations. The discrete matrix system for the increments in displacements ($\Delta\mathbf{u}$), pressure ($\Delta\mathbf{p}$) and magnetic potential ($\Delta\boldsymbol{\phi}$) can be written as

$$\begin{bmatrix} \mathbf{K}_{\boldsymbol{uu}} & \mathbf{K}_{\boldsymbol{u}p} & \mathbf{K}_{\boldsymbol{u}\phi} \\ \mathbf{K}_{p\boldsymbol{u}} & \mathbf{K}_{pp} & \mathbf{0} \\ \mathbf{K}_{\phi\boldsymbol{u}} & \mathbf{0} & \mathbf{K}_{\phi\phi} \end{bmatrix} \begin{Bmatrix} \Delta\mathbf{u} \\ \Delta\mathbf{p} \\ \Delta\boldsymbol{\phi} \end{Bmatrix} = - \begin{Bmatrix} \mathbf{R}_{\boldsymbol{u}} \\ \mathbf{R}_{p} \\ \mathbf{R}_{\phi} \end{Bmatrix}. \tag{6}$$

For the soft-magnetic case, displacement, pressure and potential are the unknowns, but for the hard-magnetic case, the magnetic field is specified as the user input; thus, the only displacement and pressure fields are the unknowns for the hard-magnetic case. Quadratic Bézier elements are used for displacement and potential fields, and linear elements are used for the pressure field. The generalised-alpha time integration scheme is used for the time integration of elastodynamics as well as for solving the evolution equations of internal variables in the viscoelastic part of the constitutive models, thus resulting in a unified framework.

1.1 Viscoelastic part

Using the generalised-alpha scheme [2], the evolution equation for the internal variable becomes

$$\dot{\boldsymbol{A}}_{n+\alpha_m}^{(k)} = \frac{1}{\tau^{(k)}} \left[\bar{C}_{n+\alpha_f}^{-1} - \boldsymbol{A}_{n+\alpha_f}^{(k)} \right] \tag{7}$$

with

$$\dot{\boldsymbol{A}}_{n+\alpha_m}^{(k)} = \alpha_m \dot{\boldsymbol{A}}_{n+1}^{(k)} + (1-\alpha_m) \dot{\boldsymbol{A}}_{n}^{(k)}, \tag{8a}$$

$$\boldsymbol{A}_{n+\alpha_f}^{(k)} = \alpha_f \boldsymbol{A}_{n+1}^{(k)} + (1-\alpha_f) \boldsymbol{A}_{n}^{(k)}, \tag{8b}$$

$$\dot{\boldsymbol{A}}_{n+1}^{(k)} = \frac{1}{\gamma \Delta t} \left[\boldsymbol{A}_{n+1}^{(k)} - \boldsymbol{A}_{n}^{(k)} \right] + \frac{\gamma - 1}{\gamma} \dot{\boldsymbol{A}}_{n}^{(k)}. \tag{8c}$$

where n and $n+1$ are the previous and current load/time steps, respectively, and α_f, α_m and γ are the time integration parameters, see [2] for the details.

2 Numerical examples

2.1 A soft magnetoactive gripper

A gripper with four hands [2] as shown in Fig. 1a comprises an active layer and a passive layer. The loading is such that the specified value of magnetic potential is zero on the diagonal faces and a time-dependent value of $\bar{\phi}$ is applied on end faces. A quarter portion of the model is modelled with a mesh of 640 BQ2/BQ1 elements. Simulations are carried out for different combinations of the viscous shear modulus (G_v) and the relaxation time (τ), and the response is presented as displacement of a point at the free end in Fig. 1b. Typical deformed shapes of the gripper are shown in Fig. 1c. For a constant value of G_v, the time needed for the gripper to achieve the desired deformed shape increases with the relaxation time. Moreover, for a constant relaxation time (τ), the gripper takes longer to reach the desired deformed shape for higher values of the viscous shear modulus.

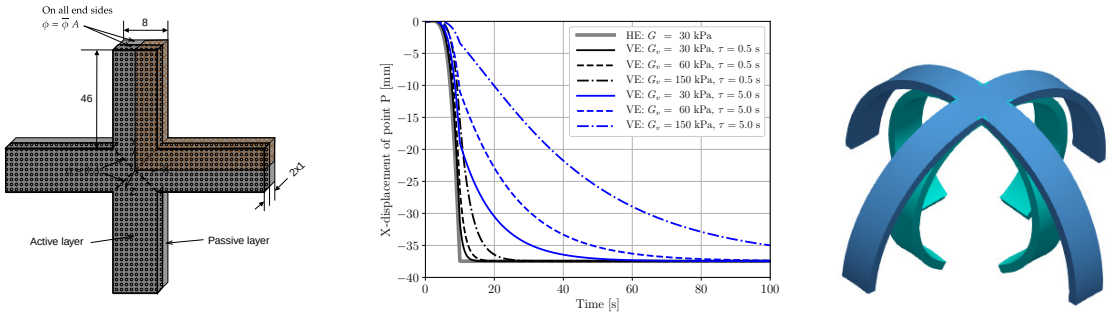

(a) (b) (c) $G_v = 150$ kPa and $\tau = 0.5$ s

Figure 1: Soft-magnetic gripper: (a) problem setup, (b) displacement response, and (c) deformed shapes at $t = 10$ s obtained with hyperelastic model (cyan) and viscoelastic model (blue).

2.2 Magnetoactive cantilever for sensing

We consider a hard magnetoactive cantilever beam shown in Fig. 2 with applications in sensing or vibration control. The Young's modulus is 300 kPa, the Poisson's ratio 0.5 and the density is 1060 kg/m^3. The residual and applied magnetic fields are in the same direction. As shown in Fig. 2, the frequency response obtained with the numerical simulations matches well with the analytical solution.

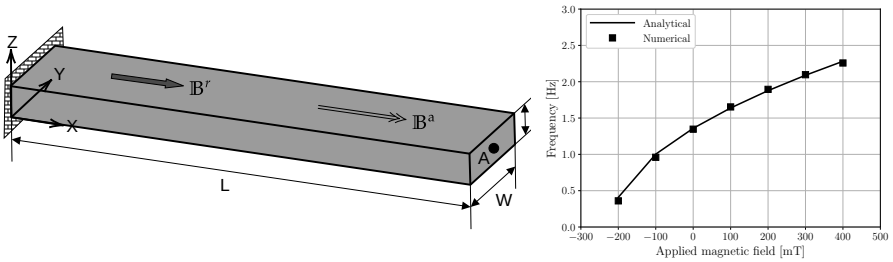

Figure 2: Cantilever beam: (Left) problem setup and (Right) variation of the frequency of vibration against the applied magnetic field.

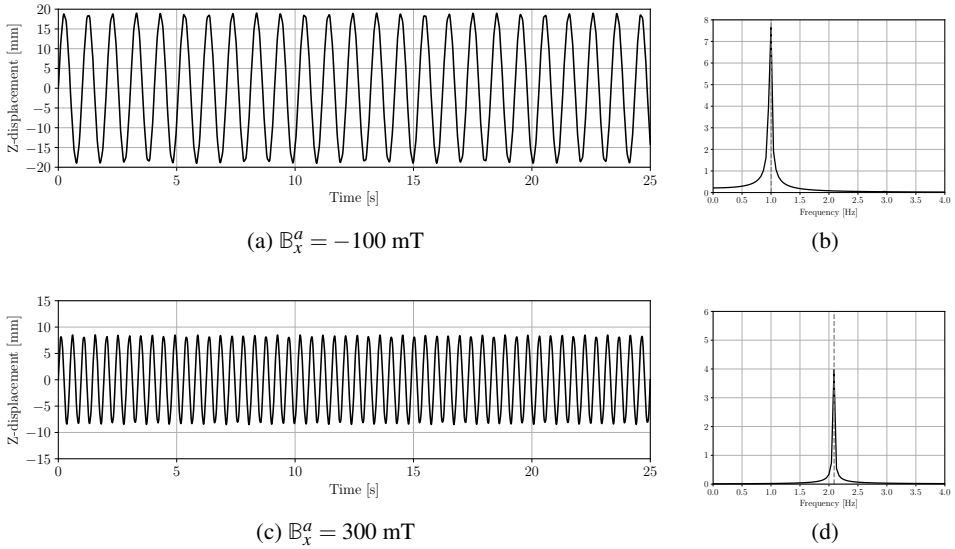

(a) $\mathbb{B}_x^a = -100$ mT (b)

(c) $\mathbb{B}_x^a = 300$ mT (d)

Figure 3: Cantilever beam: displacement response of point A, along with the discrete Fourier transform plots, for different values of applied magnetic field.

3 Conclusions

This contribution presents a higher-order finite element analysis framework for simulating the nonlinear response of multifunctional composites by taking their hyperelastic constitutive models and viscoelastic behaviour into account. The response of a MAP gripper is studied for different values of viscoelastic shear modulus and relaxation time to understand their effect on the gripper's performance. The adapted mixed displacement-displacement formulation not only helps in modelling the perfectly incompressible behaviour but also yields computationally efficient simulations using fewer load/time steps.

REFERENCES

[1] Z. Li, C. Kadapa, M. Hossain, J. Wang (2023): A numerical framework for the simulation of coupled electromechanical growth. *Computer Methods in Applied Mechanics and Engineering*, 414:116128.

[2] C. Kadapa and M. Hossain (2022). A unified numerical approach for soft to hard magneto-viscoelastically coupled polymers, *Mechanics of Materials*, 166:104207.

[3] C. Kadapa, Z. Li, M. Hossain, J. Wang (2021). On the advantages of mixed formulation and higher-order elements for computational morphoelasticity. *Journal of the Mechanics and Physics of Soldis*, 148:104289.

[4] C. Kadapa and M. Hossain (2020). A robust and computationally efficient finite element framework for coupled electromechanical. *Computer Methods in Applied Mechanics and Engineering*, 372:113443.

[5] C. Kadapa and M. Hossain. A linearized consistent mixed displacement-pressure formulation for hyperelasticity. *Mechanics of Advanced Materials and Structures*, 29:267-284, 2022.

UKACM 2024 Conference, 10-12 April 2024, Durham University, Durham, UK
https://doi.org/10.62512/conf.ukacm2024.036

BIO-INSPIRED CELLULAR NANOCOMPOSITE SHELLS: STABILITY ANALYSIS

Behnam Sobhani Aragh[1*], Wei Tan[2], David Hughes[1]

[1] School of Computing, Engineering and Digital Technologies, Teesside University, Tees Valley, Middlesbrough, TS1 3BX, UK.
B.Sobhaniaragh@tees.ac.uk, D.J.Hughes@tees.ac.uk
[2] School of Engineering and Materials Science, Queen Mary University of London, London E1 4NS, UK.
Wei.Tan@qmul.ac.uk

Abstract. The pressing global issues of climate change, sustainability, and energy efficiency spark an urgent demand for resilient lightweight structures. Consequently, porous cellular materials have emerged as a promising category of lightweight materials, capable of concurrently meeting various requirements, ranging from structural stiffness to thermal insulation. While the majority of metal foam studies focus on random porosity, recent research actively pursues economic multi-functionality through precise control of pore size and density. This approach draws inspiration from bio-inspired functionally graded materials, which prioritises gradual transitions, observed in the intriguing instances of squid beaks and varying bone porosity. Consequently, this paradigm has given rise to novel continuously graded porous (CGP) metal foam structures. Building upon these concepts, this paper introduces an innovative numerical model to analyse the buckling behaviour of bio-inspired CGP nanocomposite cylindrical shells. An effective constitutive law for an elastic isotropic metal matrix containing distributed elastic carbon-nanotubes (CNTs) is estimated, considering CNTs agglomeration through an Eshelby-Mori-Tanaka (EMT) approach. Unlike conventional methods, Euler-Bernoulli beams model stiffeners within CGP shells for a more realistic representation of stiffener effects. Equilibrium equations based on Reddy's higher-order shell theory are derived using the Euler equation, and stability equations are obtained through the variational method. The stability equations were solved employing the generalised differential quadrature and Levy techniques. The intricate interplay between CNTs and porosity distributions significantly affects the stability behaviour of CGP shells. These findings offer valuable insights for designing closed-cell cellular stiffened shells with optimal porosity to improve buckling stability.

Key words: *Closed-cell cellular; Buckling Stability; Porous nanocomposites*

1 Introduction

The climate change and the looming scarcity of resources have catalyzed a pressing need for the development of resilient, efficient, and lightweight structures. These structures, which also possess multifunctional properties, are crucial for advancing high-tech industries through innovative engineering designs. Among various solutions, porous cellular materials, particularly metal foams, stand out due to their capacity to fulfill a spectrum of requirements ranging from structural stiffness to thermal insulation. Recent research has pivoted towards the creation of metal foams with controlled internal pore size and density, inspired by the concept of bio-inspired functionally graded materials (FGMs). These materials emulate biological strategies to mitigate stress concentrations, exemplified by the gradual material transitions in squid beaks and the variation of porosity in bones, leading to the innovation of continuously graded

porous (CGP) structures.

Advancements in nanotechnology, particularly the integration of carbon nanotubes (CNTs) into metallic matrices through advanced fabrication techniques such as spark plasma sintering and laser powder bed fusion, have opened new avenues for enhancing the mechanical properties of nanocomposites. Analysis of the scanning electron microscopy (SEM) images [1] revealed that the resulting nanocomposites exhibited CNT aggregation, which resulted in localized areas of higher CNT concentration than the average volume fraction throughout the material. In recent years, a substantial body of literature has been focused on investigating the effects of nanomaterials, specifically CNTs, on the structural behaviour of engineered systems. Sobhani Aragh et al. [2] conducted a study where they used the Eshelby-Mori-Tanaka (EMT) approach, an effective homogenization technique, to examine how the degree of CNT aggregation within the ceramic matrix phase affects the mechanical response of nanocomposite shells.

This paper aims to address the research gap in the mechanical buckling of CGP stiffened cylindrical shells enhanced by agglomerated CNTs, presenting an effective numerical model to investigate their buckling behavior. It focuses on the effects of porosities and CNT distributions through the shell's thickness on stability, considering the positioning of stiffeners and employing the Eshelby-Mori-Tanaka (EMT) technique for a comprehensive continuum model. This study contributes to the understanding of the complex interplay between material composition, structural reinforcements, and loading conditions in determining the buckling performance of advanced composite shells.

2 Problem description

Illustrated in Fig. 1 is the configuration of a CGP open cylindrical shell characterized by its mean radius R, wall thickness h, and overall length L. Fabricated from a closed-cell porous nanocomposite material, the shell maintains a consistent porosity coefficient and CNT volume fraction throughout its structure, albeit with a gradual variation in thickness.

2.1 Micro-mechanical modelling of accumulated CNTs

The prediction of the nanocomposite shells' effective mechanical properties is facilitated through a dual-parameter EMT model, which builds upon Eshelby's original theory by incorporating the Mori-Tanaka method for addressing multiple inhomogeneities within a defined space [3]. This approach synergizes Eshelby's equivalent elastic inclusions concept with Mori-Tanaka's average stress theory across the matrix, identifying distinct material properties of inclusions in high CNT concentration areas. The degradation of elastic properties due to CNT agglomeration is quantified using accumulation parameters δ and γ, which delineate the volume fractions of CNTs within inclusions and their distribution in the matrix, respectively. Benveniste's revisitation provides the expression for the effective elastic tensor, which is as follows [3]

$$\mathbb{C} = \mathbb{C}_m + f_c < (\mathbb{C}_m - \mathbb{C}_m) : \mathbb{A}^{MT} > : \left[f_m \mathbb{I} + f_c < \mathbb{A}^{MT} > \right]^{-1} \tag{1}$$

where

$$\mathbb{A}^{MT} = \left[\mathbb{I} + \mathbb{S} : {\mathbb{C}_m}^{-1} : (\mathbb{C}_c - \mathbb{C}_m) \right]^{-1} \tag{2}$$

where $\mathbb{I}$ denotes the fourth-order unit tensor, $\mathbb{S}$ represents the fourth-order Eshelby tensor, which is specialised to the inhomogeneities with cylindrical geometry, representative of the straight and long CNTs, $\mathbb{A}^{MT}$ is a fourth-order tensor referred to as concentration factor, and the brackets denote an average.

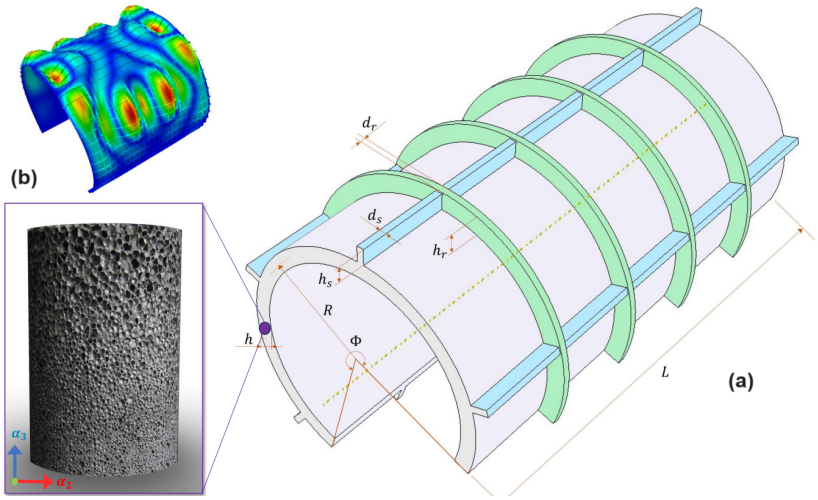

Figure 1: **a)** A schematic depiction of a CGP shell, reinforced with rings and stringers. **b)** A cross-sectional view of the shell illustrating the variation in pore size across its thickness.

2.2 Modelling of porosity dispersion

In this work, the shell's elastic moduli and density are thus estimated, highlighting parameters like the porosity and mass density coefficients, which facilitate a through-thickness gradation of properties using a power-law distribution. This approach enables creating both symmetric and asymmetric porosity profiles, with adjustments to certain parameters affecting the material's Young's modulus and density distribution radially.

2.3 Fundamental formulations and Numerical solution

A detailed kinematic framework is established based on the Reddy higher order shell theory (RHST), meticulously capturing displacements and rotations through nonlinear relationships. This framework delves into both membrane and shear strains, underlining the pivotal role of elastic coefficients in constitutive relations. The equilibrium and stability investigation is profoundly expanded by incorporating detailed equations that reflect geometric and material nonlinearities. These equations, rooted in the principles of potential energy, lay down a sophisticated equilibrium and stability criterion. Our methodology leverages a unique combination of the Lev́y method and generalized differential quadrature, providing a robust numerical tool for the accurate determination of critical buckling loads.

3 Numerical results and discussion

After evaluating the effectiveness of our methodology, which is not detailed here due to space constraints, we selectively showcase a few test cases. The (10,10) SWCNTs as the reinforcement phase and copper as the metal matrix are selected. The material properties of metal matrix (copper) are E_m = 130 GPa and v_m = 0.34. The material properties of the (10,10) SWCNTs are ${E_c}^{11}$ = 5.6466 TPa, ${E_c}^{22}$ = 7.06 TPa, ${G_c}^{12}$ = 1.9445 TPa, and ${v_c}^{22}$ = 0.175 at room temperature (300 K).

The effect of the parameter ξ_p, known as porosity coefficient, on the buckling behaviour of the CGP

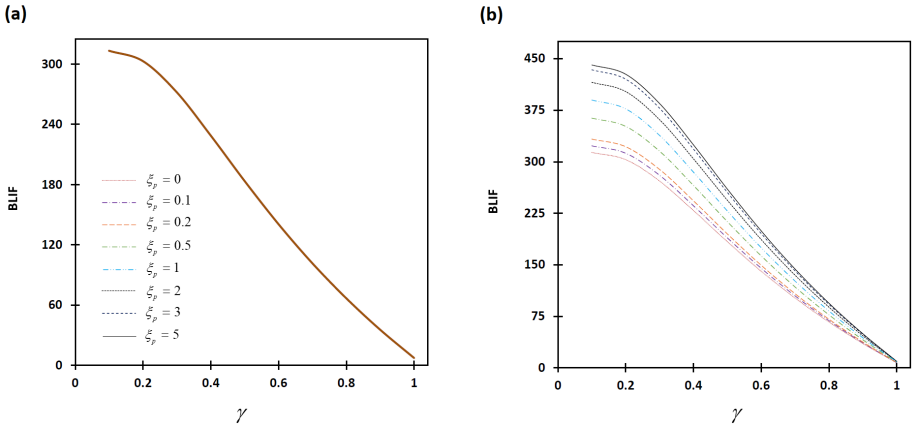

Figure 2: Influence of the parameter ξ_p on the buckling behaviour of the CGP stiffened shell for different agglomeration degrees of CNTs. ($R/h = 20$, $L/R = 2$, $\Phi = \pi/2$, $N_r = N_s = 15$, $\delta = 0.1$, $\zeta = 2$). **a)** Classic profile ($a = 1$, $b = 0$). **b)** Symmetric profile ($a = 1$, $b = 1$).

stiffened shell is compared in Figs. 2a and 2b for different porosity distribution profiles. The tendency of CNTs to aggregate more in the inclusions has a detrimental impact on the mechanical buckling behaviour of cylindrical shells [2]. This trend has been also observed in this figure. Comparing Figs. 2a and 2b reveals that for different agglomeration degrees of CNTs within the metal matrix, the porosity distributions symmetrically with respect to the mid-surface of the shell has a remarkable impact on the buckling behaviour of the CGP shell. However, when it comes to Classic porosity distribution, the parameter ξ_p has a negligible effect on the buckling load intensity factor (BLIF) of the CGP shell.

4 Conclusions

This study has developed and applied a numerical model to explore the buckling behavior of bio-inspired CGP nanocomposite cylindrical shells, incorporating metal foams and CNT reinforcements. The investigation focused on the impact of geometrical parameters, porosity variability, and CNT distribution on the shells' stability. Key findings reveal that CNT distribution and porosity symmetry significantly affect buckling performance, suggesting that optimized porosity and CNT layouts enhance structural stability. The research has provided valuable insights for designing composite shells with improved stability and resilience, indicating a path forward for creating lightweight, robust structures leveraging CNTs and porosity distributions.

REFERENCES

[1] Talò, M., Krause, B., Pionteck, J., Lanzara, G. and Lacarbonara, W. An updated micromechanical model based on morphological characterization of carbon nanotube nanocomposites. *Composites Part B: Engineering* (2017) **115**:70–78.

[2] Sobhaniaragh, B and Nejati, M and Mansur, WJ. Buckling modelling of ring and stringer stiffened cylindrical shells aggregated by graded CNTs. *Composites Part B: Engineering* (2017) **124**:120–133.

[3] Gross, D. and Seelig, T. *Micromechanics and homogenization*. Springer,(2018).

UKACM 2024 Conference, 10-12 April 2024, Durham University, Durham, UK
https://doi.org/10.62512/conf.ukacm2024.040

Effects of ply hybridisation on delamination in hybrid laminates at CorTen steel/M79LT-UD600 composite interfaces

M. Burhan[1*], C. Sands[1], T. McCreight[1], Z. Ullah[1]

[1]Advanced Composites Research Group, School of Mechanical and Aerospace Engineering, Queen's University Belfast, Belfast, BT97FG, United Kingdom,
* M. Burhan[1] (mburhan01@qub.ac.uk)

Abstract

The present study conducts a comprehensive examination of fracture behaviour in hybrid composites subjected to static loading, combining both numerical and experimental approaches. Specifically, the investigation focuses on hybrid laminates to elucidate the effect of ply hybridisation on delamination within dissimilar metal-composite interfaces. Variation in ply orientation and stacking sequence is also explored to investigate their effects on fracture behaviour. Additionally, monolithic angle-ply laminates are also considered to assess free edge delamination at dissimilar interfaces. Numerical analysis is employed to evaluate interlaminar stresses at dissimilar interfaces in both monolithic and hybrid laminates. This analysis utilises a developed semi-analytical framework, integrating dimensional analysis to derive expression for interlaminar stresses. Through the utilisation of a numerical model, non-dimensional functions are calculated, further refining the understanding of interlaminar stress distributions at the dissimilar interfaces. The findings highlight the influence of ply orientation and stacking sequence on the mechanical performance and delamination behaviour of dissimilar interfaces. By offering insights into fracture mechanisms, this research provides valuable guidance for optimising the design and enhancing the performance of both monolithic and hybrid laminates in structural applications. The combination of numerical and experimental investigations yields a comprehensive understanding of fracture behaviour, contributing to advancements in composite materials design and applications.

Key words: *free edge effect, hybrid laminates, Interlaminar stresses, semi-analytical framework*

1 Introduction

Carbon Fiber Reinforced Polymer (CFRP) materials possess exceptional properties including high strength, stiffness, corrosion resistance, and damping behaviour. However, their complex manufacturing processes, higher costs, poor impact, and residual strength properties have prompted the exploration of alternative solutions for lightweight structural applications. Hybrid laminates based on steel and composites, have emerged as a promising alternative to address these challenges [1,2]. The mismatch in thermal and structural properties in hybrid laminates often result in a weakened interface. Due to this reason, various strategies, such as adhesive bonding, chemical treatments, and mechanical surface treatment of metals, have been employed to enhance interfacial adhesion. Moreover, one of the advantages of hybrid materials is a significant control over composite material properties through the selection of fibre, matrix, and ply orientation [3]. This study aims to investigate the effects of different hybridisation techniques on the interface delamination between CorTen steel and carbon-epoxy M79LT-UD600 under remote tensile loading. Five distinct stacking sequences, including steel plate overlayed with 90°composites [St/90], [CFRP/St/CFRP], [St/CFRP/St/CFRP/St]), and steel overlaid with symmetric laminates $[\mathrm{St}/\pm 45]_{\mathrm{s}}$, $[\mathrm{St}/0/90]_{\mathrm{s}}$ are assessed for fracture behaviour. To ensure robust adhesion, a modified epoxy film, HexBond 679, an adhesive compatible with M79 resin and specifically designed for composite-to-steel bonding is utilised. In addition, angle-ply laminates$[\pm\theta_{\mathrm{n}}]_{\mathrm{s}}$, where θ=10º, 20º, 30º, and n=1, 3, of M79/UD600 are also considered.

2 Semi-analytical framework

In Fig. 1, a general laminate is presented, where H and h are the thickness of the bottom and top substrate respectively, $L \gg H$ and $2W = 15H$ is the length and width of the laminate respectively. The two substrates here are referred to as bottom layer and top layer. This investigation encompasses a class of carbon-based reinforced composites for bottom layer and a class of metals for top layer. The laminate is subjected to loading using displacement control δ and the reaction forces can be used to calculate remote stresses σ_{∞}. Global coordinates of the laminate are represented with xyz-axes, where xy is in-plane and z is out-of-plane directions, respectively, and is situated at the bottom surface of bottom layer. Each ply is modelled as a linear

elastic, homogenous, and transversely isotropic material. The resin rich layer is modelled as a transition layer at the interface between the bottom and top layers and the elastic properties used are similar to matrix.

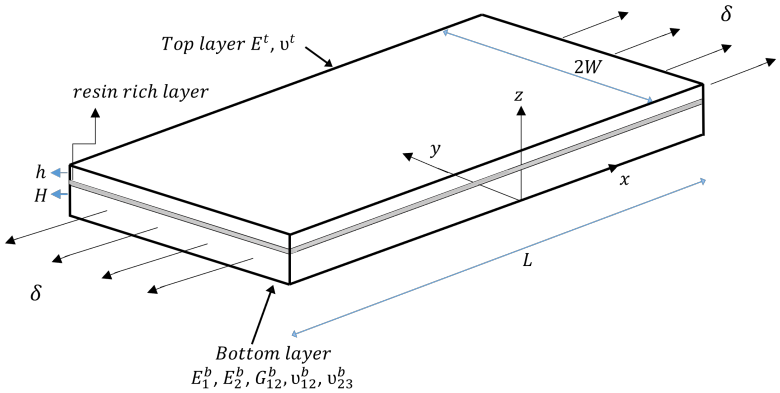

Fig. 1. Three-dimensional bi-material laminate with dimensions and material properties.

2.1 Dimensional analysis

The out-of-plane interlaminar stresses for a general laminate as in Fig. 1 depend on the set of parameters such as remote stresses σ_∞, elastic properties of bottom layer $\left(E_1^b, E_2^b, G_{12}^b, \upsilon_{12}^b, \upsilon_{23}^b\right)$ and top layer (E^t, ν^t), the laminate thickness of bottom layer (H) and top layer (h), and distance from free edge of the laminate (y). Therefore, the out-of-plane interlaminar stresses σ_{iz} for any arbitrary material and geometry is written as

$$\sigma_{iz} = \pi \begin{Bmatrix} (\sigma_\infty), (y), (H, h), \\ \left(E_1^b, E_2^b, G_{12}^b, \upsilon_{12}^b, \upsilon_{23}^b\right), (E^t, \upsilon^t) \end{Bmatrix}, \quad i \in \{x, y, z\}. \tag{1}$$

The elastic properties of carbon composites (bottom layer) is represented by their *trace* $\Im_b$ [4]. It is noted here that $\Im_b$ for carbon-based composites are evaluated from 3D stiffness material. The reference values used here for $\Im_b$ is $\Im_b^* = 200\ GPa$, which is close to the mean value of a range of carbon-based composites considered. The elastic constants for CorTen steel is shown in Table 1. Therefore, following sequential elimination for a given top layer material system, the non-dimensionalised groups can be written as

$$\pi = \pi \left\{ \frac{\sigma_{iz}}{\sigma_\infty}, \frac{\Im_b}{\Im_b^*}, \frac{h}{H}, \frac{y}{H} \right\}. \tag{2}$$

The out-of-plane interlaminar stresses in a bi-material system for a given stacking sequence reads:

$$\sigma_{iz}(\omega, \eta, y') = \sigma_\infty\, \chi_{iz}(\omega, \eta, y'), \tag{3}$$

where χ_{iz} are non-dimensional stress functions of non-dimensional parameters $\omega = \Im_b/\Im_b^*$ (normalised material parameter), $\eta = H/h$ (relative thickness), and $y' = y/H$ (distance from free edge normalised by bottom ply thickness).

Material	$\boldsymbol{E(GPa)}$	υ
CorTen Steel	207	0.29

Table 1: Elastic properties of CorTen Steel.

For a general laminate with a given material system, the interlaminar stresses at the dissimilar interface for a given stacking sequence can be written as

$$\sigma_{iz}(y') = \sigma_\infty\, \chi_{iz}(y'). \tag{4}$$

3 Experimental results

3.1 Specimen and material characteristics

Mechanical characteristics	E_{11}(GPa)	$E_{22} = E_{33}$ (GPa)	$G_{12} = G_{13}$ (GPa)	G_{23} (GPa)	$\nu_{12} = \nu_{13}$	ν_{23}
Value	136.5	10.1	4.1	3.4	0.37	0.5
Standard deviation	19.4	0.8	0.9	-	-	-

Table 2. Mechanical characteristics of M79/UD600.

The materials considered in this study are carbon/epoxy M79/UD600 and CorTen steel. Following the hand layup of hybrid and angle-ply laminates, mechanical characterisation are performed for the material M79/UD600. The mechanical characteristics of the material system are experimentally assessed using $[0_8]$,

$[90_8]$, and $[\pm 45_2]_s$ laminates and are summarised in Table 2 with ν_{23}=0.5 as an assumption. Strains are evaluated using extensometer, strain gauge, or a combination of both on each specimen. Nominal ply thickness measured after curing is h^o= 0.617 mm and the thickness for a steel shim is H=1.5 mm.

3.2 Testing, observation, and results

All the laminates plates are cured at 80°C for eight hours in an autoclave following the temperature and pressure cycles recommended by the CFRP material manufacturer. After curing, the laminates are cut into length ≥ 200 mm, and 20 mm width specimens. The tests are performed on Zwick 100 testing machine in displacement control with 2 mm/min as the crosshead speed. The specimen gauge length is taken as ≥ 130 mm. Tests are run until the first indication of fracture, involving a combination of visual detection, audible detection, and measured stiffness load indicated by a discontinuous jump in the load deflection curve during static tests. The stress-strain curves of the laminates under investigation are shown in Fig. 2.

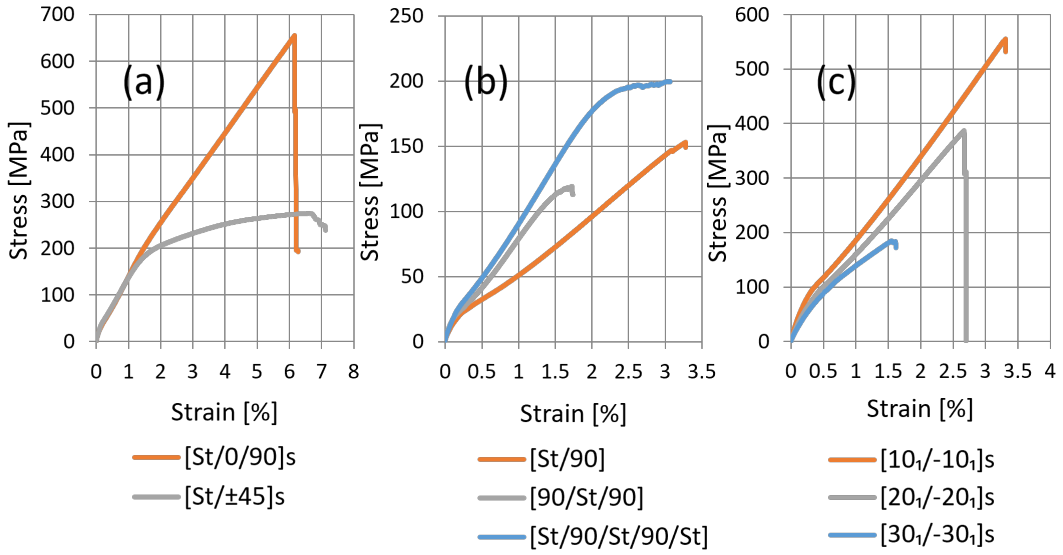

Fig. 2. Stress-strain curves of both monolithic and hybrid laminates.

Stacking sequence	Tested specimens		Average fracture stress (MPa)		Standard deviation (MPa)	
	$n=1$	$n=3$	$n=1$	$n=3$	$n=1$	$n=3$
$[\pm 10_n]_s$	3	4	565	449	15	30
$[\pm 20_n]_s$	3	3	409	220	21	34
$[\pm 30_n]_s$	6	4	199	121	31	5

Table 3 Test configurations and its corresponding tensile test results.

In case of hybrid laminates, linear behaviour of stress-strain graph is observed in $[\mathrm{St}/0/90]_s$ until an unstable delamination occurs at the St/0 and 0/90 interface. While, in $[\mathrm{St}/\pm 45]_s$ laminate, the behaviour of stress-strain is non-linear until the delamination first occurs at the interface of St/45 interface. Moreover, [St/90] show transverse crack in composite followed by an immediate delamination in the St/90 interface. Another laminate is considered with a semi-elliptical pre-crack introduced at the interface of [St/90] laminate. Prominent delamination is observed at the St/90 interface. Laminate configurations [90/St/90], and [St/90/St/90/St] exhibits similar behaviour except that the [90/St/90] shows less load carrying capacity than the rest. In case of angle-ply laminate, it is observed that the delamination growth is very unstable, and failure occurs instantaneously after initiation in $[\pm 10_n]_s$ and $[\pm 20_n]_s$ laminates. The behaviour of $[\pm 30_n]_s$ laminates is observed exhibiting less unstable delamination. The average tensile fracture stress for delamination onset for each laminate configuration is illustrated in Table 3.

4 Computation of interlaminar stresses

The computation of normalised interlaminar stresses are performed semi-analytically using finite element analysis and Equation (4) for a small displacement in $[\mathrm{St}/\pm 45]_s$ laminate at the St/45 and 45/-45 interfaces.

The composite plies are assumed as linearly elastic, homogenous, and orthotopic material. The interlaminar stresses for an arbitrary remote strain 10^{-2} at different interfaces are provided in Fig. 3. Since σ_{zz} is compressive and σ_{yz} is insignificant at 45/-45 interface, only σ_{xz} shows singular behaviour that contributes to mode III delamination. At the hybrid St/45 interface, interestingly all three stresses exist. However, σ_{yz} is tending towards zero at free edge. Both σ_{zz} and σ_{xz} show singular behaviour and hence contribute to mixed-mode delamination at hybrid St/45 interface. Therefore, for a given interlaminar strengths, hybrid St/45 interface can initiate fracture before 45/-45 interface. The same observation is reflected in the experiments. A similar numerical investigation can be performed for other hybrid and monolithic laminates considered to know what interlaminar stresses exist which contribute to delamination. Furthermore, an average quadratic-based criterion can be used to estimate the delamination.

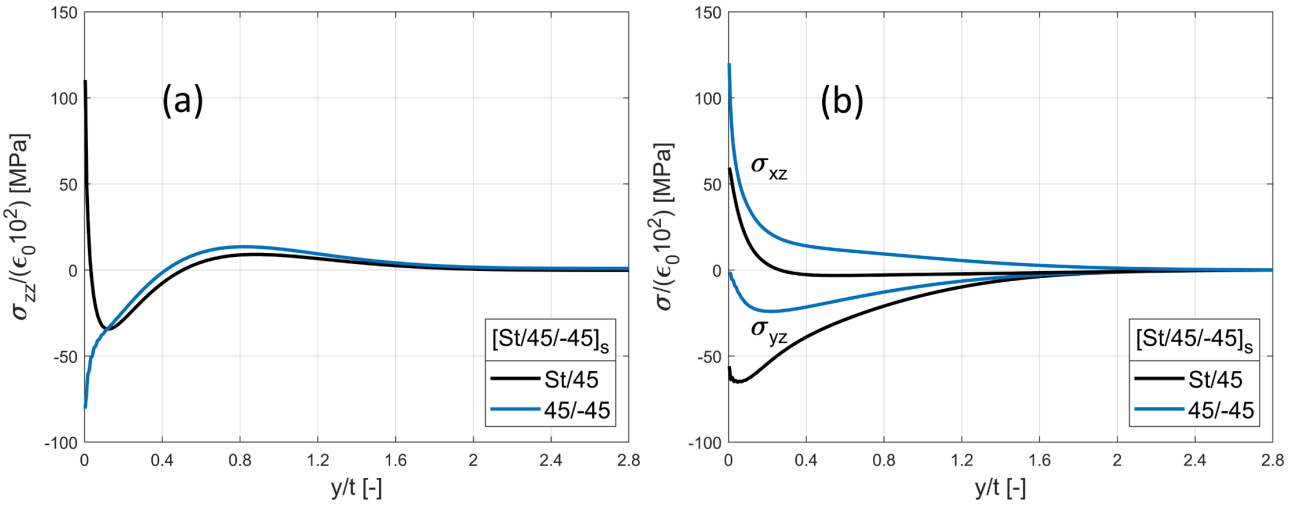

Fig. 3. Effects of (a) material parameters and (b) geometric parameter, on non-dimensional stress function in metal/90 bi-material system.

5 Conclusions

The mechanical and fracture behaviour is investigated at the dissimilar interfaces in monolithic as well as hybrid laminates. A semi-analytical framework is developed to calculate the interlaminar stresses at the dissimilar interface. It is observed that interlaminar normal and shear stress is responsible for the delamination in $[\mathrm{St}/\pm 45]_s$ at the St/45 interface. The numerical approach can be extended to investigate stresses in other laminates considered. Moreover, an extensive experimental campaign is performed to investigate the behaviour of hybrid laminate. It is seen that $[\mathrm{St}/0/90]_s$ laminate undergoes matrix cracking in 90 plies along with the delamination at the St/0 and 0/90 interfaces. This may be because of the existence of singular interlaminar stresses interacting with transverse cracks. Meanwhile, $[\pm 10_n]_s$ and $[\pm 20_n]_s$ laminates show unstable delamination at the dissimilar interface.

Acknowledgments

This study was conducted as part of the Belfast Maritime Consortium UKRI Strength in Places project, 'Decarbonisation of Maritime Transportation: A return to Commercial Sailing' led by Artemis Technologies, Project no. 107138.

References

[1] Vermeeren CAJR. An Historic Overview of the Development of Fibre Metal Laminates. Appl Compos Mater 2003 104 2003;10:189–205. https://doi.org/10.1023/A:1025533701806.

[2] Sinmazçelik T, Avcu E, Bora MÖ, Çoban O. A review: Fibre metal laminates, background, bonding types and applied test methods. Mater Des 2011;32:3671–85..

[3] GuruRaja MN, HariRao AN. Influence of Angle Ply Orientation on Tensile Properties of Carbon/Glass Hybrid Composite. J Miner Mater Charact Eng 2013;01:231–5..

[4] Tsai SW, Melo JDD. An invariant-based theory of composites. Compos Sci Technol 2014;100:237–43. https://doi.org/10.1016/j.compscitech.2014.06.017.

UKACM 2024 Conference, 10-12 April 2024, Durham University, Durham, UK
https://doi.org/10.62512/conf.ukacm2024.041

Computational Micromechanics of Composites: Debonding Failure and Matrix Cracking Under Transverse Type Load

Faiz Hamzah.1*, Jose L. Curiel-Sosa1
1 Department of Mechanical Engineering, The University of Sheffield, Sir Frederick Mappin Building, Mappin Street, S1 3JD Sheffield, United Kingdom.
mfbhamzah1@sheffield.ac.uk

Abstract

Composites are widely utilized across various industries due to their exceptional properties, allowing design flexibility and complexity. There are different scales of composites numerical study, and this study aims to understand the damage mechanisms observed in microscale composites undergoing transverse compressive load. This understanding is achieved through prediction via simulation and micromechanical computational analyses. Based on previously conducted experimental studies, Zumaquero et. al. studied different stages of damage progression through microscopical inspection of the tested coupons[1]. The compressive failure behaviour of composites in the transverse direction was observed, revealing the preferential debonding angle is between 70 to 80°. Subsequently, the growth of the interface debonding failure becomes stable, and the kinking angle towards the matrix was found to be between 50 to 60°, consistent with the numerical predictions by Correa et al. using the Boundary Element Method (BEM) [2]. These findings motivate the current study, where a UD RVE model with a periodic boundary condition (PBC) is developed using the random sequential algorithm (RSA) and the angles of debonding and kinking failure are observed. To predict the onset of matrix cracking and the crack propagation, the extended FEM modelling approach [3] is used and the LaRC05 failure criterion is implemented through a compiled UMAT. The Drucker-Prager model served as the constitutive law for matrix yielding behaviour, while cohesive elements were assigned to predict the debonding failure of the fibre-matrix interface. In addition, the Phase-Field Fracture (PF) method is also used to predict matrix cracking behaviour and the results from both LaRC05 and PF are compared to investigate the efficiencies of both methods. The study concludes that the initial direction of failure predicted agrees with that microscopically observed in experiments. This research aims to contribute to the development of computational tools leading eventually to more resilient and precisely engineered composites for diverse applications.

Keywords: *Micromechanical modelling; Debonding; Matrix cracking; LaRC05; Drucker-Prager model; cohesive elements, Phase-field.*

1 Introduction

The computational modelling of failure in composite materials is a challenging task as it involves various complex failure mechanisms, regardless of the model scale. In this paper, the study aims to investigate the formation of debonding at the interface and the initiation and propagation of matrix cracks in microscale composites under transverse type load. The investigation implements two different failure criteria to compare the differences in the failure behaviour in the composites. The cohesive zone model (CZM) is used to capture the interface debonding phenomena in an RVE model. As the debonding failure tends to grow along the interface and propagate towards the matrix region, the LaRC05 and Phase-field (PF) model is then used to investigate the crack behaviour in the matrix. This viewpoint of computational micromechanics allows prediction of material performance, optimization of material properties, insights into complex failure mechanisms as well as provide validation to experimental findings.

2 Interface debonding and matrix cracking phenomena

Fibre-matrix interface debonding

The debonding failure of the interface is implemented using the CZM method. CZM is a modelling method widely used to predict the onset and propagation of fibre-matrix interface debonding failure. This approach is defined by a bi-linear traction separation law, as can be seen in Figure 1. In a bilinear traction separation law, K represents the initial elastic stiffness, N_{max} is the maximum traction or, in this case, represents the interface

strength while δ_n^{fail} is the critical interface separation, and δ_n^{init} indicates the displacement or small debonding at damage initiation.

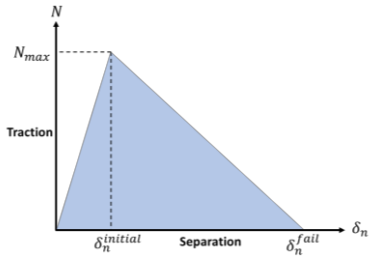

Figure 1. A bi-linear cohesive law to describe the behaviour of CZM in the interface.

Predicting Matrix Crack Initiation and Propagation

LaRC05 failure criterion

LaRC05 is reliable and accurate in predicting the strength value of a matrix dominated failure with its ability to provide the plane of the fracture angle which is crucial in XFEM modelling method. This failure criterion enables the assumption that the matrix failure may appear on an arbitrary plane parallel to the fibre direction. The failure is controlled by the combination of both transverse and longitudinal shear (τ_{nT} , τ_{nL}), as well as normal tractions (σ_n) on the corresponding plane. Two failure modes are considered in which these modes rely on the value of normal traction and the failure index as per equation (1) below.

$$f_{mat} = \begin{cases} \left(\frac{\tau_{nT}(\theta)}{S_T - \mu_T \sigma_n(\theta)}\right)^2 + \left(\frac{\tau_{nL}(\theta)}{S_L - \mu_L \sigma_n(\theta)}\right)^2 + \left(\frac{\sigma_n(\theta)}{Y_T}\right)^2, & \sigma_n(\theta) \geq 0 \\ \left(\frac{\tau_{nT}(\theta)}{S_T - \mu_T \sigma_n(\theta)}\right)^2 + \quad \left(\frac{\tau_{nT}(\theta)}{S_L - \mu_L \sigma_n(\theta)}\right)^2, & \sigma_n(\theta) < 0 \end{cases} \tag{1}$$

The failure index value indicates the failure state where; the matrix is predicted to be undamaged when $f_{mat} < 1$ and failed when $f_{mat} = 1$.

$$\mu_T = -\frac{1}{tan(2\emptyset_0)}, S_T = \frac{Y_C}{2tan(\emptyset_0)}, \mu_L = S_L \frac{\mu_T}{S_T} \tag{2}$$

Y_T, Y_C, S_L and S_T represent the failure strength of UD composites under transverse tensile, transverse compressive, longitudinal shear and transverse shear loads, respectively. LaRC05 criterion also enable the implementation of the friction effect into the model, represented by μ_L and μ_T for friction coefficients under longitudinal shear stress and transverse shear stress [4]. Lastly, $\emptyset$ is the through-the-thickness direction and the general value for composites is $53 \pm 2°$ obtained via experimental study in [5]. The matrix crack initiation and the direction of the crack propagation are defined by this failure criterion, which was implemented through the UDMGINI user subroutine.

Phase-field fracture method

The Phase-field fracture (PF) allows the capture of complex fracture phenomena such as the merging of cracks, nucleation, and crack branching in composites. This method was first mentioned by Griffith in [6] based on the thermodynamical analysis, where, according to the first law of thermodynamics, growth of a crack can only occur if a process implies that the total energy of a system decreases or remains constant with an increase in the crack area. The thermodynamic balance was used in the PF formulations (i.e. AT1, AT2, and PF-CZM) where normalization parameter, C_w, degradation function, $g(\boldsymbol{\phi})$ and geometric functions, $\alpha(\boldsymbol{\phi})$ define the specific PF (Table 1). This formulation represents the total potential energy, Π, in a domain of an elastic body, Ω, and evolving internal discontinuities, Γ (see Figure 2).

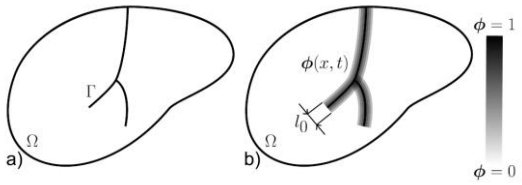

Figure 2. (a) Schematic representation of a body with an internal discrete continuity, (b) Schematic representation of a Phase-field approximation of a similar discontinuity pattern.

The AT1 model, uses a quadratic degradation function and a linear geometric function, while the AT2 model uses quadratic functions for both geometric and degradation functions. The Phase-Field Cohesive zone model (PF-CZM) uses a quadratic geometric function and a rational degradation function [7]. The use of PF to investigate the decohesion of the interface will be considered as part of the future scope. The length scale parameter is used to control the material strength in AT1 and AT2 formulations, while in the PF-CZM model, the strength is explicitly defined and is not affected by the length scale parameter.

Model	$\boldsymbol{\alpha(\phi)}$	$\boldsymbol{g(\phi)}$	$\boldsymbol{Cw}$	$\boldsymbol{l^0}$
AT1	$\boldsymbol{\phi}$	$(1-\boldsymbol{\phi})2$	$\frac{2}{3}$	$\frac{8GcE}{3\sigma_c^2}$
AT2	$\boldsymbol{\phi}2$	$(1-\boldsymbol{\phi})2$	$\frac{1}{2}$	$\frac{27GcE}{256\sigma_c^2}$
PF-CZM	$2\boldsymbol{\phi}-\boldsymbol{\phi}2$	$(\frac{(1-\phi)^p}{(1-\phi)^p+Q(\phi.)})$	$\frac{\pi}{4}$	[-]

Table 1. Geometric and degradation functions for AT1, AT2 and PF-CZM models

3 Numerical example: 3D RVE under transverse compressive load with cohesive zone model, phase-field and LaRC05 criteria[1]

In this study, a periodic 3D RVE subjected to remote transverse load is developed. The fibre and matrix region were meshed using a 6-node linear triangular prism (C3D6) and 8-node linear brick (C3D8R) respectively. A periodic boundary condition is applied to the model to ensure the continuity of displacements across the RVE boundaries. The angle of initial debonding and the matrix cracking is observed.

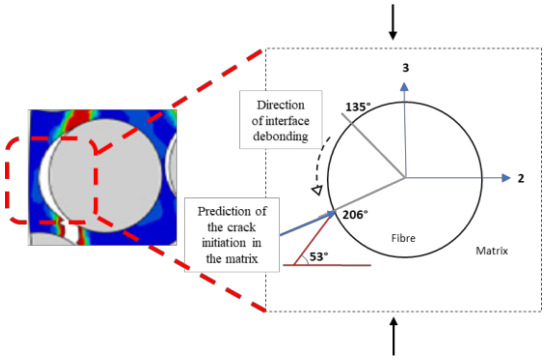

Figure 3. The debonding failure of the interface and predicted crack initiation angle in the matrix

A detailed investigation of the progress of failure and cracks within the micromechanical models reveals the different phases of failure processes. The initiation of the fibre-matrix interface debonding due to the high shear stress was first observed, at around 45° (or 130°- 140°) in the transverse direction to the fibre (see Figure 3**)**. Due to the matrix undergoing shear plastic deformation and maximum stiffness degradation, the debonding of the interface grows until it reaches an angle of ~206° [1], [8]. It is expected that one will observe similarities between the LaRC05 and the phase-field model by examining the crack development under compression, Figure 4 (a) and (b). An example of a stress-strain graph comparison between LaRC05 and PF is shown in Figure 4 (c).

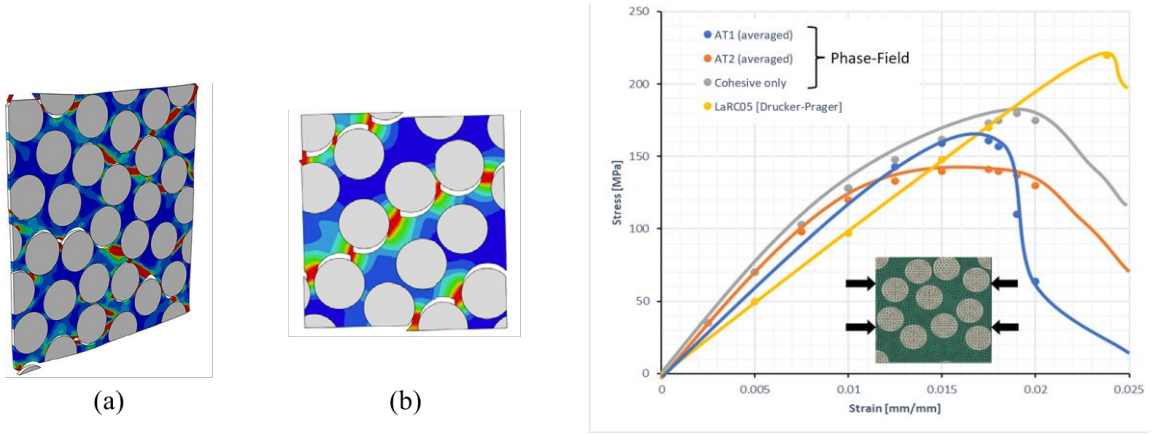

Figure 4. (a) RVE-LaRC05 [4] *and (b) RVE-PF*[7] *shows the similarities of the debonding failure and crack pattern in the matrix. (c) shows the example of stress-strain graph comparison between Phase-field (PF) methods and LaRC05 with Drucker-Prager criterion extracted from* [7], [9].

4 Conclusions

Computational micromechanics was employed to simulate the mechanical response of a fibre-reinforced composite subjected to transverse compression at the microscale level by implementing different failure criteria. In general, it was observed that microscale failure within the composites initiated at the interface due to the concentration of stress around the fibre and weak properties of both the matrix and the interface. The predicted debonding expanded to the cracking of the matrix. The observed debonding failure demonstrates good agreement with experimental results. The comparison between LaRC05 and the Phase-field fracture (PF) method is investigated. The accuracy of PF is found to be highly affected by the loading scenario. According to [7] Further investigation on both methods shows great potential and significance of both LaRC05 and PF methods could become highly profound in expanding areas of computational micromechanics of composites.

References

[1] P. L. Zumaquero, E. Correa, J. Justo, and F. París, "Microscopical observations of interface cracks from inter-fibre failure under compression in composite laminates," *Compos Part A Appl Sci Manuf*, vol. 110, no. April, pp. 76–83, 2018, doi: 10.1016/j.compositesa.2018.04.004.

[2] E. Correa, F. París, and V. Mantič, "BEM analysis of inter-fibre failure under compression in composites: Comparison between carbon and glass fibre systems," *Plastics, Rubber and Composites*, vol. 40, no. 6–7, pp. 333–341, 2011, doi: 10.1179/1743289810Y.0000000014.

[3] J. L. Curiel-Sosa, B. Tafazzolimoghaddam, and C. Zhang, "Modelling fracture and delamination in composite laminates: Energy release rate and interfacial stress," *Compos Struct*, vol. 189, no. January, pp. 641–647, 2018, doi: 10.1016/j.compstruct.2018.02.006.

[4] X. Wang *et al.*, "Prediction of the inter-fiber mechanical properties of composites: Part II Failure criterion based on micromechanics and cross-scale stress calculation," *Compos Struct*, vol. 271, no. February, p. 114126, 2021, doi: 10.1016/j.compstruct.2021.114126.

[5] S. T. Pinho, L. Iannucci, and P. Robinson, "Physically-based failure models and criteria for laminated fibre-reinforced composites with emphasis on fibre kinking : Part I : Development," vol. 37, pp. 63–73, 2006, doi: 10.1016/j.compositesa.2005.04.016.

[6] A. A. Griffith and M. Eng, "VI. The Phenomena of Rupture and Flow in Solids."

[7] J. Macías, A. Arteiro, F. Otero, P. P. Camanho, and J. Reinoso, "Micro-mechanical analysis of composite materials using Phase-Field models of brittle fracture," *European Journal of Mechanics, A/Solids*, vol. 102, Nov. 2023, doi: 10.1016/j.euromechsol.2023.105069.

[8] E. Correa, V. Mantič, and F. París, "Numerical characterisation of the fibre-matrix interface crack growth in composites under transverse compression," *Eng Fract Mech*, vol. 75, no. 14, pp. 4085–4103, 2008, doi: 10.1016/j.engfracmech.2008.03.005.

[9] X. Wang *et al.*, "Prediction of the inter-fiber mechanical properties of composites: Part I standardization micro-scale modelling method and damage analysis," *Compos Struct*, vol. 271, no. February, p. 114127, 2021, doi: 10.1016/j.compstruct.2021.114127.

Machine Learning Applications in Engineering

Efficient Stochastic Analysis of Landslide Post-Failure Characteristics Using Dimension Reduction Method and Machine Learning

Jianping Li[2], Guotao Ma[1*], Shuihua Jiang[2], Mohammad Rezania[1], Mohaddeseh Mousavi Nezhad[3]

[1] School of Engineering, University of Warwick, Coventry CV4 7AL, UK.
[2] School of Infrastructure Engineering, Nanchang University, 999 Xuefu Road, Nanchang 330031, China.
[3] School of Engineering, University of Liverpool, Liverpool, L69 3BX, UK.
Jianping_lee@email.ncu.edu.cn
Derek.ma.1@warwick.ac.uk
Sjiangaa@ncu.edu.cn
M.rezania@warwick.ac.uk
M.Mousavi-Nezhad@liverpool.ac.uk

Abstract

Landslides pose a significant global threat due to their sudden occurrence and their widespread influence. The inherent spatial variability of soil properties brings great uncertainty to the post-failure behavior of landslides. Generally, the assessment of the uncertainties of slope post-failure characteristics through probabilistic large deformation analysis is determined for assessing and mitigating landslide risks. However, probabilistic landslide simulation based on brute-force Monte Carlo is complex and time-consuming. Therefore, this study proposes a two-stage dimension reduction method and machine learning model-based stochastic approach for improving the efficiency of quantifying the uncertainties of slope post-failure characteristics, which considers the spatial variability of shear strength. In the proposed method, the random field is firstly generated using the Karhunen-Loève expansion (KLE) method. Then, the slope post-failure characteristics parameters of pre-analysis samples are obtained using the generalized interpolation material point method (GIMP). Finally, based on the extreme gradient boosting (XGBoost) with sliced inverse regression (SIR) technique, a binary classification surrogate model is constructed to relate random field variables to the maximum relative displacement (R_d) in the characteristic parameters. Results show that the reduced input dimension from 1080 to 100 through KLE is still too high for constructing the surrogate model, while SIR is used for the second-dimensional reduction from 100 to 20 of input variables to improve the accuracy of the surrogate model up to 0.98. The proposed model is used to identify hazardous samples, and we simply utilize large deformation analysis on hazardous samples. It suggests that the proposed method in this study is capable of quantifying the uncertainties of slope post-failure characteristics with accuracy and high efficiency dropping time-consuming GIMP.

Key words: *Landslides; Stochastic analysis; Material point method; Post-failure characteristics; Surrogate model.*

1. Introduction

Landslides are one of the most frequent disasters worldwide [1]. Predicting post-landslide behavior is crucial for risk assessment and disaster mitigation. The study of post-landslide behavior has always been an interesting topic for researchers. With the development of the Material Point Method (MPM), it has been widely used to investigate large deformation problems in simulating landslides [2]. In recent years, more and more scholars have realized that the heterogeneity of soil properties can have a significant impact on the response of post-landslide behavior, and traditional deterministic methods are no longer able to meet the requirements for assessing and mitigating disaster risks [3]. As a result, many studies proposed probabilistic simulation methods for quantifying the heterogeneity of rock and soil materials in landslides. However, the use of random field (RF) theory and large deformation numerical methods in landslide probability simulation often faces the challenge of low computational efficiency. Consequently, most current studies lack sufficient sample sizes for computing the statistical characteristic values of post-failure characteristic parameters, leading to inaccurate results. This study presents a novel method for probabilistic estimation of post-landslide characteristic parameters in heterogeneous rock and soil parameters. The effectiveness of the proposed method is

demonstrated through a clay slope example. This research approach is of great significance for practical landslide risk assessment and provides new insights and methods to improve its accuracy and reliability.

2. Methodology

The two-stage dimension reduction method and machine learning model-based stochastic approach is proposed to enhance the efficiency of quantifying uncertainties in slope post-failure characteristics. The proposed method begins by generating a RF using the KLE method. Subsequently, the slope post-failure characteristic parameters are determined for pre-analysis samples using the generalized interpolation material point method (GIMP). Finally, a binary classification surrogate model is constructed using the extreme gradient boosting (XGBoost) algorithm and the sliced inverse regression (SIR) technique to establish the relationship between the RF variables and the maximum relative displacement (R_d) of the characteristic parameters. Hence, it is feasible to identify samples experiencing significant deformation failure using a surrogate model. Only samples undergoing substantial slope failure are directly pertinent to calculating the statistical of the characteristic parameters. The flowchart for the proposed approach is shown in Fig. 1.

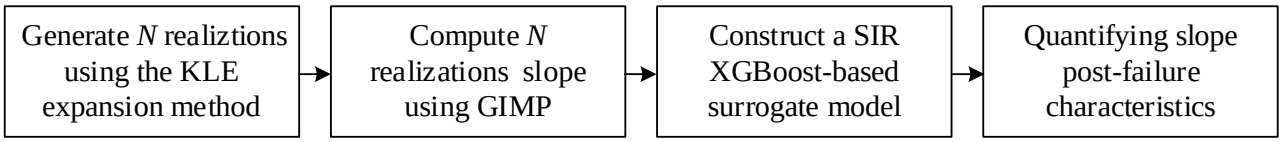

Fig. 1. Flowchart for the proposed approach

2.1. Stochastic MPM

In geostatistics, the spatial variability of soil properties is frequently represented through the utilization of a numerically generated random field (RF) that is based on autocorrelation functions (ACF). In this study, single exponential autocorrelation function is employed to characterize the spatial autocorrelation of the soil parameters, which is expressed as [4]

$$\rho\left(\tau_x,\tau_y\right)=\exp\left[-\left(\frac{\tau_x}{\delta_h}+\frac{\tau_y}{\delta_v}\right)\right] \tag{1}$$

where, ρ is the autocorrelation coefficient of quantities between two spatial locations, the lags $\tau_x = | x_i - x_j |$ and $\tau_y = | y_i - y_j |$ are the absolute distances between two spatial locations in horizontal and vertical directions, respectively; δ_h and δ_v are the scale of fluctuation in horizontal and vertical directions, respectively. Then, the Karhunen-Loève expansion (KLE) method, which is a generation method for RFs, is widely employed to simulate the spatial variability of soil parameters due to its ability to obtain accurate results with fewer truncation terms [4]. Next, the KLE method is adopted to discretize the Gaussian RFs of soil parameters [4], and the matrix operation process for generating the Gaussian RFs of soil parameters can be expressed as

$$\boldsymbol{H}=\mu+\left[\sigma\mathrm{diag}\left(\sqrt{\boldsymbol{\lambda}}\right)\times\boldsymbol{F}^{\mathrm{T}}\right]^{\mathrm{T}}\times\boldsymbol{W} \tag{2}$$

where μ and σ represent the mean and standard deviation of a soil parameter, respectively; $\boldsymbol{H}$ is the matrix for implementing the soil parameter with dimensions of $m\times1$, where m is the number of RF grids; $\mathrm{diag}(\sqrt{\lambda})$ is an $N\times N$ diagonal matrix composed of N eigenvalues; $\boldsymbol{W}$ is a standard random vector with dimensions $N\times1$, $\boldsymbol{W}=\left(\xi_1,\xi_2,\cdots,\xi_N\right)^{\mathrm{T}}$; $\boldsymbol{F}$ is the matrix of eigenfunctions with dimensions of $m\times N$.

In terms of MPM, we have employed the GIMP-based MPM3D, an open-source code, to mitigate the grid-crossing instability in our simulations. The stochastic MPM captures spatial variability by generating RFs of parameters through the KLE method, and models large deformation processes using the GIMP. Multiple calculations are performed within the Monte Carlo framework.

2.2. Binary Classification Surrogate Model

To improve the computational efficiency of the probabilistic simulation of landslides to obtain enough landslide samples to accurately estimate the statistics of the landslide characteristic parameters, a binary

classification surrogate model is used in this study to find out the failure samples in advance, which is very effective for the computation of the statistics of the characteristic parameters in small probability events of landslides.

The Extreme Gradient Boosting (XGBoost) model, an ensemble model based on gradient boosting decision trees consisting of a series of regression trees, was proposed by Chen and Guestrin [5]. It possesses high accuracy and sufficient flexibility, making it commonly used in constructing surrogate models in geotechnical engineering [5]. However, the dimensionality of the RF vector (input variables) is often high when considering the spatial variability of parameters, leading to a curse of dimensionality problem for the model. To tackle this issue, dimensionality reduction technique was proposed for the input random variable matrix by Li et al. [6]. Since the Sliced Inverse Regression (SIR) method proposed by Li [7] is highly reliable, easy to implement, and widely applied, we adopt it to project the high-dimensional input variables into a lower-dimensional space while preserving the information contained in the data as much as possible, effectively addressing the curse of dimensionality problem in this study.

3. Numerical model setup

The numerical model is a plane strain problem with a clay slope as shown in Fig. 2. The geometry of slope with a height of 28 m, a slope angle of 36.87° (3:4). The material point grid model has a background grid size of 1 m × 1 m, with 14,336 material points placed in the X and Y directions spacing of 0.25 m. The RF grid size is consistent with the background grid size. The bottom of the slope (Y = 0 m) is completely fixed, while the left (X = 0 m) and right (X = 112 m) sides are constrained by vertical rollers.

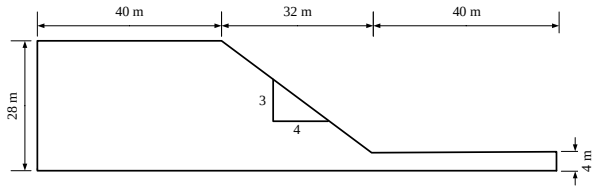

Fig. 2. Diagram of a clay slope model

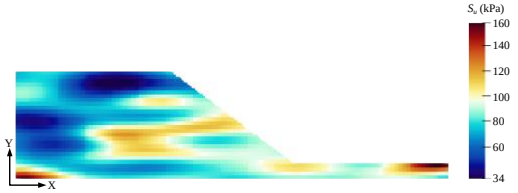

Fig. 3. A typical sample of random fields for S_u

Assuming that the undrained shear strength follows a lognormal distribution with a mean of 80 kPa and a *COV* of 0.3. The single exponential autocorrelation function shown in Eq. (1) is used to simulate the spatial autocorrelation of undrained shear strength (S_u), with autocorrelation distances of 24 m and 6 m in the X and Y directions, respectively. The unit weight, Young's modulus, and Poisson's ratio of the soil are taken as 20 kN/m^3, 100 MPa, and 0.3, respectively. These parameters are treated as deterministic, as their contributions on slope large deformation characteristics are not remarkable as reported in Cheuk et al. [8]. The residual undrained shear strength is set as 50% of the original strength. The softening modulus is set as 50 kPa. The initial in situ stresses are generated using gravitational loading. The gravity acceleration is 9.81 m/s^2. The total duration of simulation for the calculation is 20 s, with each time step taking 7.5×10^{-4} s. when soil deposits become stable according to kinematic energy and unbalanced force of the system [2].

4. Results

When the number of eigenmodes n = 100, it can meet the accuracy requirement of the ratio factor $\varepsilon \geqslant 95\%$ [4]. Therefore, a total of 100 random variables needs to be discretized for the RFs of S_u. A typical sample of RFs of S_u as shown in Fig. 3. The red regions denote larger S_u values representing the mechanically strong zones, while the blue regions represent relatively smaller S_u values specifying the mechanically weaker zones in the slope soil.

After obtaining the RF implementations of S_u, it is necessary to calculate the statistics of the landslide characteristic parameters. To save computation time, a binary classification surrogate model is constructed for finding landslide samples. Initially, 100 sets of implementations of RFs considering the spatial variability of S_u are generated using KLE method. Subsequently, large deformation analyses of landslides are performed based on 100 sets of random field implementations using GIMP. The maximum relative displacement value is extracted for all samples. The threshold for the maximum relative displacement is set to 1 m. XGBoost is used to construct a direct relationship between random field variables and maximum relative displacement.

Although the KLE method has significantly reduced the dimensionality of the input variables, a 100-dimensional input variable can still significantly affect the accuracy of the surrogate model. Therefore, in this study, the SIR method is used in advance to reduce the input variables from 100 dimensions to 20 dimensions, which improves the accuracy of the surrogate model from 0.72 to 0.98. Based on the binary classification surrogate model constructed by the SIR-XGBoost model, the maximum relative displacement of a landslide is calculated whether it is greater than a threshold value using the 1000 times Latin hypercube sampling technique. These 685 landslide samples are identified. The direct calculation of these 685 samples leads directly to the statistical of the landslide characteristic parameters. The values of the calculated runout distances are shown in Fig. 4. Its mean value is 24.30 and standard deviation is 8.63.

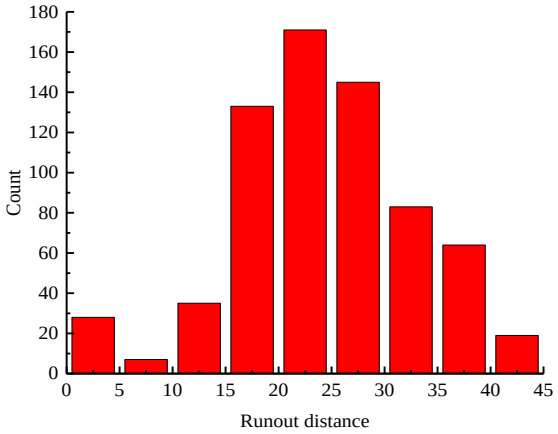

Fig. 4. Distribution of predicted runout distances

5. Conclusions

This study quantitatively evaluates the uncertainties and variabilities of runout distances in heterogeneous clay slope. The SIR method is used in advance to reduce the input variables, which improves the accuracy of the surrogate model. The proposed method in this study is capable of quantifying the uncertainties of slope post-failure characteristics with accuracy and high efficiency dropping time-consuming GIMP. It provides a practical process for improving the landslide characteristic parameters.

Acknowledgments

The financial support by the National Natural Science Foundation of China Project (Contract 52150610492 and 52350610265) are gratefully acknowledged.

References

[1] Jiang. S. H, Huang. J, Griffiths. D. V, Deng. Z. P, (2022). Advances in reliability and risk analyses of slopes in spatially variable soils: A state-of-the-art review. *Computers and Geotechnics*, 141, 104498.

[2] G. Ma, M. Rezania, M. Mousavi Nezhad, (2022). Stochastic assessment of landslide influence zone by material point method and generalized geotechnical random field theory. *International Journal of Geomechanics*, 22(4), 04022002.

[3] G. Ma, M. Rezania, M. Mousavi Nezhad, B. Shi, (2023). Post-failure analysis of landslides in spatially varying soil deposits using stochastic material point method. *Rock and Soil Mechanics*, 43(7), 2003-2014.

[4] Jiang. S. H, Li. D. Q, Zhang. L. M, Zhou. C. B, (2014). Slope reliability analysis considering spatially variable shear strength parameters using a non-intrusive stochastic finite element method. *Engineering geology*, 168, 120-128.

[5] Chen. T, Guestrin. C, (2016). Xgboost: A scalable tree boosting system. *In Proceedings of the 22nd acm sigkdd international conference on knowledge discovery and data mining* (pp. 785-794).

[6] Li. D. Q, Zheng. D, Cao. Z. J, Tang. X. S, Qi. X. H, (2019). Two-stage dimension reduction method for meta-model based slope reliability analysis in spatially variable soils. *Structural Safety*, 81, 101872.

[7] Li. K. C, (1991). Sliced inverse regression for dimension reduction. *Journal of the American Statistical Association*, 86(414), 316-327.

[8] Cheuk. C. Y, Ho. K. K. S, Lam. A. Y. T, (2013). Influence of soil nail orientations on stabilizing mechanisms of loose fill slopes. *Canadian Geotechnical Journal*, 50(12), 1236-1249.

Phase-Field Modelling for Predicting Fracture and Degradation in Materials

UKACM 2024 Conference, 10-12 April 2024, Durham University, Durham, UK
https://doi.org/10.62512/conf.ukacm2024.026

PHASE-FIELD-BASED CHEMO-MECHANICAL MODELLING OF CORROSION-INDUCED CRACKING IN REINFORCED CONCRETE

Evžen Korec[1,3*], Milan Jirásek[2], Hong S. Wong[1] and Emilio Martínez-Pañeda[3]

[1]Department of Civil and Environmental Engineering, Imperial College London, Exhibition Road, London SW7 2AZ, United Kingdom, e.korec20@imperial.ac.uk, hong.wong@imperial.ac.uk

[2]Department of Mechanics, Faculty of Civil Engineering, Czech Technical University in Prague, Thákurova 7, Prague 166 29, Czech Republic, milan.jirasek@cvut.cz

[3]Department of Engineering Science, University of Oxford, Oxford OX1 3PJ, UK.
emilio.martinez-paneda@eng.ox.ac.uk

Abstract. A new model for corrosion-induced cracking in reinforced concrete is presented [3,4]. Corrosion-induced damage leads to the delamination/spalling of concrete cover (responsible for 70-90% of prematurely deteriorated reinforced concrete structures) or even structural failure as infamously documented by recent collapses of RAAC panels in British schools [2]. The state-of-the-art knowledge of the involved chemo-mechanical processes was captured in several coupled parts of the model. Firstly, the diffusion-driven reactive transport of iron ions from the corroding steel rebar and their precipitation into rust (both in concrete pore space and into dense rust layer in the vicinity of rebar) were simulated. The transport of aggressive species such as chlorides to the steel rebar and the enhanced transport of all considered species through cracks were considered. Rust has a significantly lower density than original steel. Thus, the constrained accumulation of rust in dense rust layer and concrete pores exerts pressure on concrete which was predicted and a new precipitation eigenstrain concept was introduced. The mechanical properties of rust were taken into consideration. The quasi-brittle fracture of concrete was then simulated with the phase-field model. The proposed model was implemented in COMSOL Multiphysics software and solved numerically with the finite element method. Both uniform and non-uniform corrosion case studies were investigated and validated with experimental data. Importantly, the model allows to simulate the impact of the magnitude of the current density on the propagation rate of cracks, which has been puzzling researchers for over 25 years.

Key words: *Reinforced concrete, Impressed current tests, Corrosion-induced cracking, Reactive transport in porous media, Phase-field fracture*

1 Introduction

This contribution is concerned with the modelling of corrosion-induced cracking in reinforced concrete. Corrosion of steel reinforcement is responsible for the premature deterioration of 70-90% of all concrete structures [1]. This results in considerable damage or even structural collapse as witnessed by recent aerated concrete panels failures in the UK forcing at least partial closures in more than 100 schools in England [2]. The investigated corrosion-induced cracking is a dominant degradation mechanism that causes the fracture of concrete cover and its subsequent delamination or spalling, eventually exposing embedded steel members to the elements. The proposed model [3, 4] captures key chemo-mechanical

processes leading to corrosion-induced cracking and allows the prediction of the service life of reinforced concrete structures exposed to various aggressive species (typically chlorides or carbon dioxide).

2 Model

The proposed model [3, 4] specifically resolves (i) the transport of chlorides through concrete matrix considering chloride binding, (ii) the gradual corrosion initiation of steel surface assuming constant corrosion current density, (iii) the reactive transport of iron released from the steel surface to the pore space of concrete, (iv) the subsequent precipitation of iron species into rust that blocks the pore space, (v) the precipitation-induced pressure caused by the accumulation of compressible rust under confined conditions, (vi) the fracture of concrete employing a numerically robust phase-field fracture model and (vii) the enhanced transport of chlorides and iron species through cracks described by a damage-dependent diffusivity tensor. The resulting model consists of seven differential equations for seven associated unknown field variables, which are solved by the finite element method employing the software package COMSOL Multiphysics.

By taking into consideration processes (iii)-(v), the presented model differs from other models available in the literature. It has been argued [5] that modelling these processes is necessary to simulate the corrosion-induced cracking process accurately because it allows: (I) to capture the delaying effects of concrete pore space surrounding rebar and of cracks on corrosion-induced cracking while also considering the pressure of gradually forming rust in concrete pores. Also, (II) it takes into consideration the compressibility and elastic properties of the rust, which were found to importantly affect the corrosion-induced crack width [3].

3 Numerical results and discussion

A gradual corrosion initiation of the steel surface leads to the non-uniform distribution of precipitated rust, as demonstrated in Fig. 1a depicting the numerically predicted distribution of rust in 3 years for the experimental setup considered by Chen et al. [6]. The distribution of rust is characterized by precipitate (rust) saturation ratio $S_p = \theta_p / p_0$, where θ_p is a precipitate (rust) volume fraction and p_0 is the porosity of concrete. The local value of S_p in the vicinity of the corroding rebar was found to be strongly affected by cracks that facilitate the enhanced transport of iron ions away from the steel surface. For this reason, the maximum of the rust saturation ratio shifts to the vicinity of less-developed upper lateral cracks, which cannot facilitate the transport of as many iron ions as the other better-developed cracks. Interestingly, the predicted maximum of the precipitate saturation ratio reaches only 30 % of the pore space. This indicates that under natural conditions, the accumulation of rust in pore space can last for years before the pore space is eventually filled. Cracks were also found to significantly affect the transport of aggressive species (such as chlorides) to the steel surface and neglecting crack-facilitated chloride transport was not found to be a conservative assumption as it leads to the underestimation of sustained damage.

The capability of the model to predict a crack width in time was validated with the experimental results of Ye et al. [7]. The tested concrete specimens with a minimal cover of 10 mm were for 32 days subjected to cyclic drying and wetting with 60 g/l sodium chloride solution. The employed values of chloride threshold ($T = 0.56$ wt. % of cem.) and corrosion current density ($i_a = 2.3$ $\mu A/cm^2$) were not reported by [7], so they were estimated by fitting the reported steel mass loss in time. The resulting prediction

of the surface crack width of the vertical crack perpendicular to the upper concrete surface (Fig. 1b) reveals a very good agreement with experimental data, providing a safe upper bound them. In addition, the predicted crack width was found to be very sensitive to the geometric size of the anodic (corroding) region and porosity of concrete.

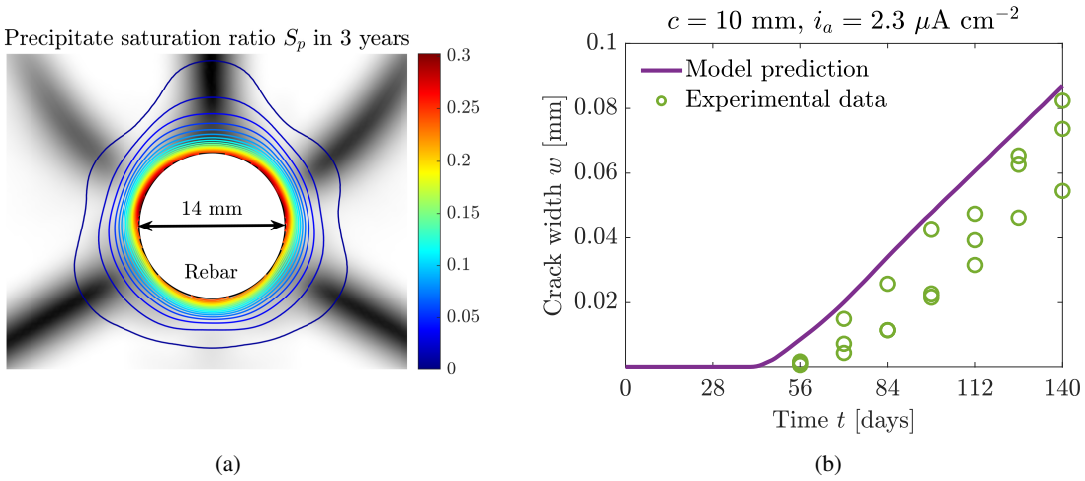

(a) (b)

Fig. 1: (a) Contours of the precipitate saturation ratio S_p in the vicinity of a rebar for the test of Chen et al. [6] in 3 years. The phase-field variable ϕ characterizing cracks is shown in the back in a grey scale bar (0 (uncracked) – white, 1 (fully cracked) – black). (b) The predicted evolution of surface crack width is compared to the experimental measurements of Ye et al. [7].

4 Conclusions

The proposed model (i) allows for the capture of the delaying effects of concrete pore space surrounding rebar and of cracks on corrosion-induced cracking while also considering the pressure of gradually forming rust in concrete pores, and (ii) takes into consideration the compressibility and elastic properties of the rust, which were found to importantly affect the corrosion-induced crack width [3]. The ability of the model to simulate both chloride transport and corrosion-induced cracking accurately was validated against the experimental results of Chen et al. [6] and Ye et al. [7], revealing very good agreement with the experimentally measured chloride content and crack width in time.

The numerical results from analysed case studies suggest that (iii) under the conditions of natural chloride-induced corrosion, where the current density is typically below 10 μA/cm^2, the accumulation of rust in pore space can last for years before pore space is eventually filled. (iv) Varying length of the corroding (anodic) region on the rebar surface significantly affects the crack width. Because chloride-induced corrosion is well-known to have a pitting character, the obtained results indicate that it is not possible to draw a direct link between the mass loss of steel rebars and the surface crack width, unless the distribution and size of anodic regions are known. (v) The strong dependency of the crack width on the size of the anodic region suggests that three-dimensional simulations are necessary to model localised chloride corrosion (i.e. non-uniform along the length of a rebar) and results of two-dimensional studies cannot be

straightforwardly extended to real structures without risking seriously erroneous assessment. The proposed model can analyse sections of complex reinforced concrete components and thus be employed to analyse various academically and industrially relevant scenarios of highly localised chloride corrosion.

Acknowledgments

The authors gratefully acknowledge stimulating discussions with Prof Nick Buenfeld (Imperial College London), Prof Carmen Andrade (CIMNE International Center for Numerical Methods in Engineering, Barcelona) and Prof Milan Kouril (University of Chemistry and Technology, Prague). We would like to express our special thanks to former master's student Jiahang Yu (Imperial College London) whose diligent work on his master's thesis project paved the way for this study. E. Korec acknowledges financial support from the Imperial College President's PhD Scholarships. M. Jirásek acknowledges the support of the European Regional Development Fund (Center of Advanced Applied Sciences, project CZ.02.1.01/0.0/0.0/16_19/0000778). E. Martínez-Pañeda was supported by an UKRI Future Leaders Fellowship [grant MR/V024124/1]. We additionally acknowledge computational resources and support provided by the Imperial College Research Computing Service (http://doi.org/10.14469/hpc/2232).

REFERENCES

[1] Gehlen, C., Andrade, C., Bartholomew, M., Cairns, J., Gulikers, J., Javier Leon, F., Matthews, S., McKenna, P., Osterminski, K., Paeglitis, A., Straub, D., 2011. *Fib Bulletin 59 - Condition control and assessment of reinforced concrete structures exposed to corrosive environments (carbonation/chlorides)*, fib - The International Federation for Structural Concrete.

[2] *RAAC: Public buildings at risk from concrete failure, experts warn*, BBC News, https://www.bbc.co.uk/news/uk-66690256

[3] E. Korec, M. Jirásek, H.S. Wong, E. Martínez-Pañeda, *Phase-field chemo-mechanical modelling of corrosion-induced cracking in reinforced concrete subjected to non-uniform chloride-induced corrosion*, Theoretical and Applied Fracture Mechanics. (2023) 104233.

[4] E. Korec, M. Jirásek, H.S. Wong, E. Martínez-Pañeda, *A phase-field chemo-mechanical model for corrosion-induced cracking in reinforced concrete*, Construction and Building Materials. 393 (2023) 131964.

[5] Angst, U.M., 2018. *Challenges and opportunities in corrosion of steel in concrete*. Materials and Structures 51, 1-20.

[6] Chen, J., Zhang, W., Tang, Z., Huang, Q., 2020. *Experimental and numerical investigation of chloride-induced reinforcement corrosion and mortar cover cracking*. Cement and Concrete Composites 111, 103620.

[7] Ye, H., Jin, N., Fu, C., Jin, X., 2017. *Rust distribution and corrosion-induced cracking patterns of corner-located rebar in concrete cover*. Construction and Building Materials 156, 684-691.

UKACM 2024 Conference, 10-12 April 2024, Durham University, Durham, UK
https://doi.org/10.62512/conf.ukacm2024.030

A PHASE-FIELD MODEL OF MECHANICALLY-ASSISTED CORROSION OF BIOABSORBABLE METALS

Sasa Kovacevic[1]*, Wahaaj Ali[2,3], Emilio Martínez-Pañeda[1], Javier Llorca[2,4]

[1]Department of Engineering Science, University of Oxford, Oxford OX1 3PJ, UK
sasa.kovacevic@eng.ox.ac.uk, emilio.martinez-paneda@eng.ox.ac.uk
[2]IMDEA Material Institute, C/Eric Kandel 2, 28906 Getafe, Madrid, Spain
wahaajaly@gmail.com, javier.llorca@imdea.org
[3]Department of Materials Science and Engineering, Universidad Carlos III de Madrid, 28911, Spain
[4]Department of Materials Science, Polytechnic University of Madrid, 28040 Madrid, Spain

Abstract. Magnesium alloys exhibit great potential for use as implants that gradually and entirely dissolve in the human body after healing. Rapid corrosion in body fluids and the susceptibility to pitting corrosion and stress corrosion cracking are the main reasons limiting the widespread use of Mg alloys as a biodegradable material. The concurrence of mechanical loading and a corrosive environment dramatically accelerates the corrosion rate and promotes crack propagation, leading to the sudden failure of implants. A phase-field model is developed to simulate the corrosion of bioabsorbable metals in biological fluids. The model incorporates both Mg dissolution and the transport of Mg ions in solution. The framework captures pitting corrosion and incorporates the role of mechanical fields in enhancing the corrosion of biodegradable metals. The model is validated against *in vitro* corrosion data on Mg alloys immersed in simulated body fluid. The potential of the model to capture mechano-chemical effects is demonstrated by considering bioabsorbable coronary stents subjected to mechanical loading. The results show that pitting severely compromises the structural integrity of the stent and the application of mechanical loading initiates a pit-to-crack transition and crack propagations, leading to premature fracture after a short time in solution. This work extends phase-field modeling to biomaterial degradation and provides a novel mechanistic tool for assessing the service life of bioabsorbable medical devices.

Key words: *Diffuse interface; Bioabsorbable implants; Stress-assisted corrosion; Pitting corrosion*

1 Introduction

Magnesium (Mg) based alloys have great potential for implants that gradually dissolve *in vivo* at a synchronized rate with bone/tissue growth and safely absorb into the human body after healing with no implant residues. Complete dissolution eliminates the need for a second surgical intervention for implant removal, thereby reducing additional trauma and recovery time for the patient. However, rapid corrosion rates of Mg alloys in body fluids and their susceptibility to mechanical loading in the case of load-bearing implants impede their potential. Fast dissolution undermines implants to fulfill designed requirements during the healing process. The concurrence of mechanical loading and an aggressive environment (body fluid) dramatically accelerates the dissolution rate and promotes crack initiation and crack propagation, leading to premature implant failures with life-threatening consequences. Simulation tools that can assess the evolution of corrosion over time and the corresponding degradation in mechanical properties can help prevent such scenarios.

Existing methods to assess the corrosion performance of bioabsorbable implants rely on experimentation or phenomenological models. While experimental tests are time-consuming and costly, phenomenologi-

cal models fail to incorporate the underlying mechanisms of corrosion in body fluids. As they lack actual corrosion mechanisms and do not provide any insight into the interplay between mechanics and environment, they have limited applicability for implant design. This work presents the first physics-based model for assessing the corrosion of bioabsorbable Mg alloys in biological fluids. The model is based on the diffuse interface (phase-field) formulation. It incorporates the underlying mechanisms of biocorrosion and the synergistic effect of mechanical loading and a corrosive environment. In the diffuse interface formulation, sharp interfaces are smoothed over a thin region using a continuous auxiliary variable. The motion of the interface is implicitly tracked without presumptions or prescribing the interface velocity.

2 Problem description

The system consists of a biodegradable Mg alloy in contact with physiological environments. The system domain Ω includes both the Mg alloy and the corrosive environment. A continuous phase-field parameter ϕ is introduced to distinguish different phases: $\phi = 1$ represents the solid phase (Mg alloy), $\phi = 0$ corresponds to the liquid phase (physiological fluid), and $0 < \phi < 1$ indicates the thin interfacial region between the phases (solid-liquid interface). The independent kinematic variables necessary for model description are the phase-field parameter describing the evolution of the corroding interface $\phi(\mathbf{x},t)$, the displacement vector to characterize the deformation of the solid phase $\mathbf{u}(\mathbf{x},t)$, and the normalized concentration of Mg ions $\bar{c}_{Mg}(\mathbf{x},t) = c_{Mg}/c^s_{Mg}$ with respect to the concentration in the solid phase.

The free energy functional for a heterogeneous system can be written as

$$\mathscr{F} = \int_\Omega \Big[f^{chem}(\bar{c}_{Mg},\phi) + f^{grad}(\nabla\phi) + f^{mech}(\nabla\mathbf{u},\phi) \Big]\, d\Omega, \tag{1}$$

where f^{chem} and f^{grad} are the chemical and gradient energy densities defined as [1]

$$f^{chem}(\bar{c}_{Mg},\phi) = \frac{1}{2}A\Big[\bar{c}_{Mg} - h(\phi)(\bar{c}^{s,eq}_{Mg} - \bar{c}^{l,eq}_{Mg}) - \bar{c}^{l,eq}_{Mg}\Big]^2 + \omega g(\phi); \qquad f^{grad}(\nabla\phi) = \frac{1}{2}\kappa|\nabla\phi|^2, \tag{2}$$

where $\bar{c}^{l,eq}_{Mg} = c^{l,eq}_{Mg}/c^s_{Mg}$ and $\bar{c}^{s,eq}_{Mg} = c^{s,eq}_{Mg}/c^s_{Mg}$ are the normalized equilibrium Mg concentrations in the liquid and solid phases, A is the chemical free energy density curvature parameter, $g(\phi) = 16\phi^2(1-\phi)^2$ is the double-well potential energy, $\omega = 3\Gamma/(4\ell)$ is a constant that determines the energy barrier height at $\phi = 1/2$ between the two minima at $\phi = 0$ and $\phi = 1$, $h(\phi) = \phi^3(6\phi^2 - 15\phi + 10)$ is the interpolation function, $\kappa = 3\Gamma\ell/2$ is the isotropic gradient energy coefficient, Γ is the interfacial energy, and ℓ is the interface thickness. The mechanical free energy density f^{mech} in Eq. (1) is additively decomposed into elastic f^{mech}_e and plastic components f^{mech}_p [1]

$$f^{mech}(\nabla\mathbf{u},\phi) = h(\phi)(f^{mech}_e + f^{mech}_p); \quad f^{mech}_e(\nabla\mathbf{u}) = \frac{1}{2}\boldsymbol{\varepsilon}^e : \mathbf{C} : \boldsymbol{\varepsilon}^e; \quad f^{mech}_p = \int_0^t \boldsymbol{\sigma}_0 : \dot{\boldsymbol{\varepsilon}}^p\, dt, \tag{3}$$

where $\mathbf{C}$ is the rank-four elastic stiffness tensor, $\boldsymbol{\varepsilon}^e = \boldsymbol{\varepsilon} - \boldsymbol{\varepsilon}^p$ is the elastic strain tensor obtained by subtracting the plastic strain tensor $\boldsymbol{\varepsilon}^p$ from the total strain $\boldsymbol{\varepsilon} = 1/2(\nabla\mathbf{u} + (\nabla\mathbf{u})^T)$, and $\boldsymbol{\sigma}_0$ is the Cauchy stress tensor for the intact configuration.

The following time-dependent governing equations for the independent kinematic fields $\phi(\mathbf{x},t)$, $\bar{c}_{Mg}(\mathbf{x},t)$, and $\mathbf{u}(\mathbf{x},t)$ are derived [1]

$$\frac{\partial\phi}{\partial t} = -L\Big(\frac{\partial f^{chem}}{\partial\phi} - \kappa\nabla^2\phi\Big); \quad \frac{\partial\bar{c}_{Mg}}{\partial t} = \nabla\cdot\Big[M\nabla\Big(\frac{\partial f^{chem}}{\partial\bar{c}_{Mg}}\Big)\Big]; \quad \nabla\cdot\boldsymbol{\sigma} = \mathbf{0}, \tag{4}$$

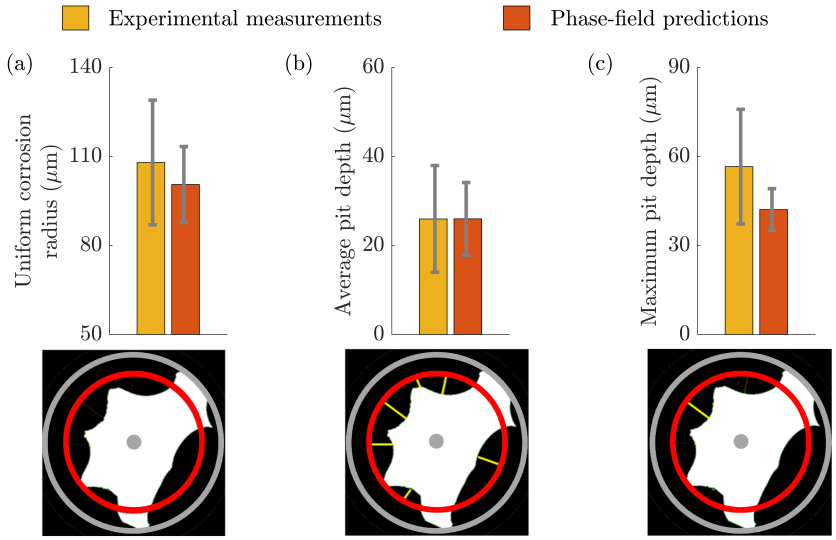

Figure 1: Comparison between experimental and simulated values for (a) uniform corrosion radius, (b) average pit depth, (c) maximum pit depth. Comparison between experimental and phase-field predictions for hydrogen gas evolution is given in [1].

where $M = D_{c_{Mg}}/(\partial^2 f^{chem}/\partial \bar{c}_{Mg}^2)$ is the mobility parameter connected to the diffusion coefficient of Mg ions $D_{c_{Mg}}$. The role of mechanical fields in enhancing corrosion kinetics is incorporated by following Gutman's theory. The mechano-chemical coupling is established through the interfacial mobility coefficient L by considering the linear relationship between L and the corrosion current density [1]

$$L = L_0\left(\frac{\varepsilon^p}{\varepsilon_y} + 1\right)\exp\left(\frac{\sigma_h V_m}{RT}\right), \tag{5}$$

where L_0 is the interfacial mobility parameter in the absence of mechanical stresses and plastic strains, ε^p is the effective plastic strain, ε_y is the initial yield strain, σ_h is the hydrostatic stress, V_m is the molar volume of the metal, R is the universal gas constant, and T is the absolute temperature.

3 Experimental and Numerical results

The constructed model is calibrated and validated against newly obtained *in vitro* corrosion data on Mg alloy wires immersed in simulated body fluid (SBF). Experimental measurements of hydrogen release over the immersion time are used to calibrate the model kinematic parameter L_0 considering uniform corrosion. The wire cross-sections measured after 24 h of immersion in SBF are compared with pitting corrosion predictions. The phase-field simulations return the same trends and accurately reproduce the experimental data for the hydrogen release and three different pitting metrics parameters: the uniform corrosion radius, the average pit depth, and the maximum pit depth, Fig. 1. The agreement between the experimental measurements and phase-field predictions indicates that the proposed model can be utilized to simulate uniform and pitting corrosion of bioabsorbable Mg alloys immersed in biological fluids.

The potential of the model is demonstrated in predicting the degradation of a bioabsorbable coronary Mg stent immersed in biological fluid. Two different case studies are considered. In the first study, the stent is mechanically loaded before immersion in the corrosive environment. It is radially expanded to a

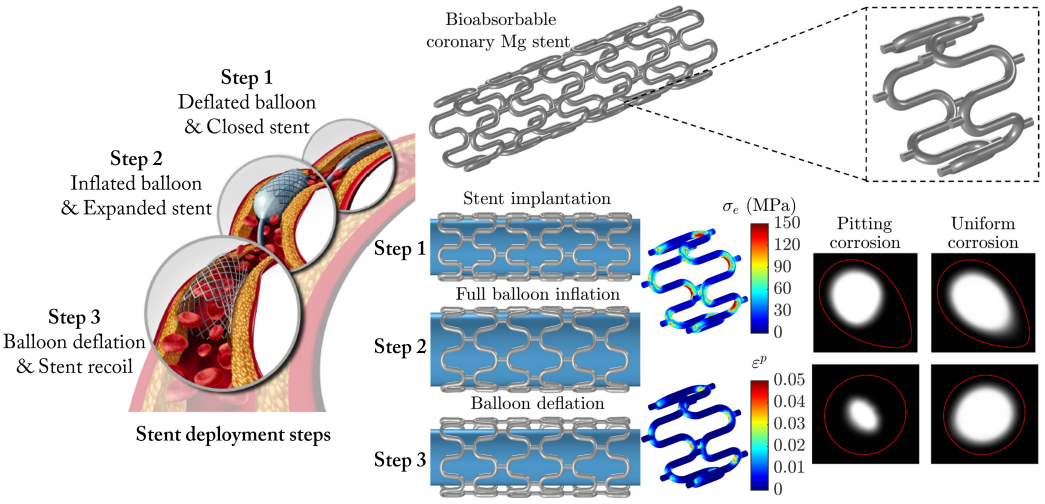

Figure 2: Bioabsorbable coronary Mg stent. Stent deployment steps, stent geometry with representative ring element, von Mises stresses σ_e and equivalent plastic strains ε^p after stent recoil.

specific outer diameter, mimicking the balloon inflation stage during deployment. This step is followed by the stent recoil, corresponding to the balloon deflation and extraction process. The stent deployment process, the stress state in terms of von Mises stresses and equivalent plastic strains for the representative ring element after stent recoil are summarized in Fig. 2. The plastic strains are incorporated into the subsequent corrosion simulation. In the second study, the as-manufactured stent is immersed in biological fluid in the absence of mechanical stresses. This case corresponds to uniform corrosion.

The results show that plastic strains are localized at the union between rings and links, providing hot spots for pitting nucleation. The dissolution rate within the pitting zone is much higher than in the remaining parts of the stent. This locally enhanced dissolution significantly reduces the thickness of the strut, as shown in two characteristic cross-sections close to the union point in Fig. 2, indicating hot spots for early stent failure. The structural integrity of the stent at these locations is severely undermined. In the case of uniform corrosion, the stent gradually dissolves with a constant dissolution rate.

4 Conclusions

A phase-field model is developed to simulate the corrosion of Mg alloys in body fluids. The model incorporates the role of mechanics in accelerating corrosion rates and promoting crack propagation. The work reveals that local plastic strains developed during stent deployment act as initiators for pitting corrosion, which proves to have more detrimental effects on stent degradation than uniform corrosion and severely compromises the structural integrity of the stent. Neglecting the mechanical effects on stent dissolution leads to unsafe design and overestimated service life predictions.

REFERENCES

[1] Kovacevic, S., Ali, W., Martínez-Pañeda, E. and Llorca, J. Phase-field modeling of pitting and mechanically-assisted corrosion of Mg alloys for biomedical applications. *Acta Biomater.* (2023) **164**:641–658.

UKACM 2024 Conference, 10-12 April 2024, Durham University, Durham, UK
https://doi.org/10.62512/conf.ukacm2024.043

AN ENRICHED PHASE-FIELD METHOD (XPFM) FOR THE EFFICIENT SIMULATION OF FRACTURE PROCESSES

Verena Curoșu[1]*, Christian Krüger[1], Stefan Loehnert[1]

[1] Institute of Mechanics and Shell Structures (IMF), Faculty of Civil Engineering, TUD Dresden University of Technology, August-Bebel-Straße 30, 01219 Dresden, Germany.
verena.curosu@tu-dresden.de
christian.krueger@tu-dresden.de, stefan.loehnert@tu-dresden.de

Abstract. Complex crack processes like crack initiation, branching, and coalescence can be simulated with the phase-field method for fracture. Here, the criterion for crack propagation is considered within the formulation of the partial differential equation. Its solution, the scalar phase-field, indicates the crack in a smeared manner. This makes the evaluation of a separate criterion for crack propagation and the tracking of the crack geometry obsolete. A challenge for the phase-field method for fracture, however, is the accurate and efficient reproduction of the phase-field, the displacement field, and their gradients. For this, the use of extremely fine meshes is often required within the standard phase-field method.
In this contribution, an enhancement of the phase-field method through the adjustment of the ansatz functions is presented. A transformation of the phase-field ansatz by embedding a quadratic ansatz into an exponential function is utilised to improve the approximation of the phase-field even with coarse meshes. The crack is not additionally restricted by the ansatz and can still develop independently of the mesh geometry.
Furthermore, the displacement ansatz is extended by a term with adjusted shape-functions carrying information about the crack geometry from the phase-field. It can reproduce the high displacement gradients across the crack. The modified shape-functions are calculated for each enriched element on a submesh by considering the local reduction of stiffness due to the phase-field. Since these shape-functions are directly coupled to the phase-field ansatz, no additional discretisation of the crack geometry is required.

Key words: *Phase-Field, XFEM, Brittle Fracture, Extended Phase-Field Method*

1 Introduction

In the phase-field method (PFM), the crack is reproduced by a scalar field, the phase-field ϕ, with $\phi = 1$ indicating the crack and $\phi = 0$ indicating the virgin material. An internal length parameter l controls the transition width between these two states. For $l \to 0$, the discrete crack is reproduced exactly.
The regarded phase-field problem is the formulation presented in [1, 2, 3] with spectral split and implicit enforcement of irreversibility using a strain energy density history field.
In the following, a discretisation technique for the PFM to reduce the need for very fine meshes is presented shortly. This extended phase-field method (XPFM) was first published in [4] and applied to fatigue fracture in [5]. For the phase-field, a quadratic LAGRANGIAN ansatz is embedded into an exponential function. This improves the accuracy of the phase-field approximation significantly even with coarse meshes. The crack is not additionally restricted by the ansatz and can develop independently of the mesh geometry. Furthermore, the standard displacement ansatz is extended by a term which can reproduce the high gradients across the crack for nearly and fully developed cracks. Here, in an improved version of the method adjusted shape-functions carrying information about the crack geometry from the

phase-field are utilised. These modified shape-functions are calculated for each enriched element with a small LAPLACIAN problem on a submesh by considering the local reduction of stiffness due to the phase-field. These shape-functions are directly coupled to the phase-field ansatz, therefore no additional discretisation of the crack geometry is required.

2 Problem description

The transformed ansatz for the phase-field ϕ in elements close to or at the crack reads

$$\phi^h(\boldsymbol{\xi}) = \exp\left(-\varsigma\Big(\sum_i N_i(\boldsymbol{\xi}) f_i / l\Big)\right) \quad \text{with} \quad \varsigma(x) = \frac{x}{\sqrt{\sqrt{x^2 + k_{reg}}}} \tag{1}$$

where $\boldsymbol{\xi}$ are the reference element coordinates, N_i are the quadratic LAGRANGIAN shape-functions associated to the element's nodes and f_i are their corresponding degrees of freedom associated to the phase-field. The square-root approximation $\varsigma(x)$ [5] with the small regularisation parameter $0 < k_{reg} << 1$ ensures differentiability of the basis function $f(\boldsymbol{\xi})$ at or below zero. Special care has to be given to the integration. An adaptive integration scheme has been presented in [5], which is similarly utilised here. The displacement field is approximated by

$$\boldsymbol{u}^h(\boldsymbol{\xi}) = \sum_i N_i(\boldsymbol{\xi}) \boldsymbol{u}_i + \sum_i N_i(\boldsymbol{\xi}_x) \boldsymbol{a}_i \tag{2}$$

with the standard degrees of freedom $\boldsymbol{u}_i$ applied at every node and the extended degrees of freedom $\boldsymbol{a}_i$, which are activated only within certain enriched elements.
In the extended ansatz, the argument $\boldsymbol{\xi}_x$ of the shape-function, carries the information about the expected displacement field. $\boldsymbol{\xi}_x$ can be interpreted as distorted reference coordinates. In Figure 1, a reference element is shown with an exemplary representation of the crack within it (orange line). The reference coordinates $\boldsymbol{\xi}$ (green) and their distorted counterparts $\boldsymbol{\xi}_x$ (blue) are depicted as functions over the element. The distortion of these coordinates $\boldsymbol{\xi}_x$ depends on the reduction of the stiffness due to the phase-field. It is calculated on a submesh over the domain of one currently considered enriched element Ω_e with the weak form of the LAPLACIAN

$$\int_{\Omega_e} g(\phi)\, \nabla\chi \cdot \nabla\delta\chi \, \mathrm{d}v = 0\,. \tag{3}$$

Here, $g(\phi)$ is the phase-field dependent stiffness degradation function, ∇ denotes the gradient operator and χ is the scalar solution field with its corresponding test function $\delta\chi$.
Equation (3) is solved for every spatial direction with different boundary conditions. Linear polynomial shape-functions are applied for the submesh used in each enriched element. The solution $\chi = \xi_x$ or $\chi = \eta_x$ is the respective component of $\boldsymbol{\xi}_x$. The mesh, on which this problem is solved, is regular with the number of nodes in each direction n_{sub}. To ensure that $\boldsymbol{\xi}_x$ exhibits coordinate-like properties within the reference element and additionally C_0-continuity is given across the element edges of the main problem, special attention has to be given to the choice of boundary conditions.
Generally, a finer submesh requires more computational effort but yields a more accurate solution. However, the computational process can be constructed to be very efficient as, due to the uniformity of the submesh, an assembly of the subproblem's global stiffness matrix and residual vector is possible before runtime. Furthermore, due to the enriched-element-wise consideration, the subproblem is very well suited for parallelisation.

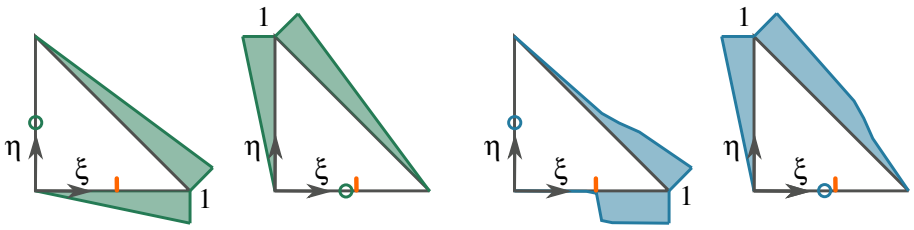

Figure 1: (from left to right) The reference element coordinates $\boldsymbol{\xi} = \{\xi, \eta\}$ and their distorted counterparts $\boldsymbol{\xi}_x = \{\xi_x, \eta_x\}$ plotted over the domain of an incipiently cracked reference element, the orange line represents approximately the location of the diffuse crack.

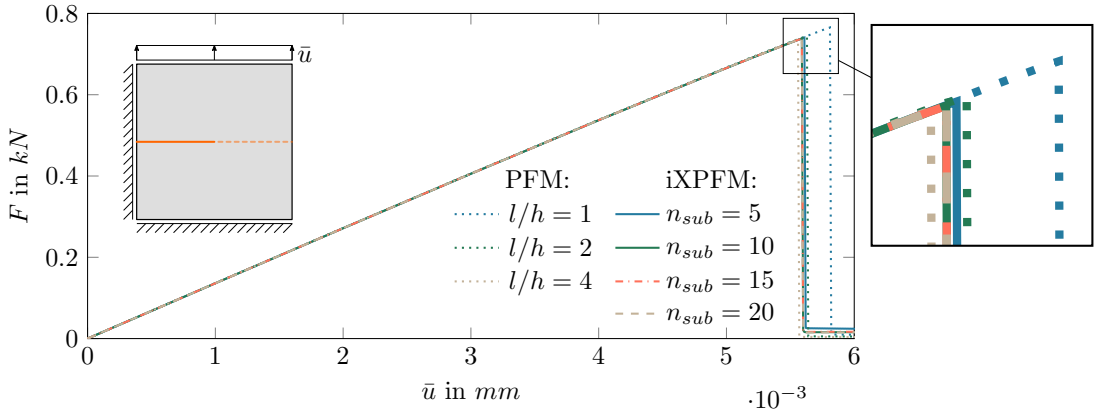

Figure 2: Load-displacement curve of a single notched tension test for PFM simulations with different mesh refinements (l/h) and XPFM simulations with $l/h = 1$ and different submesh refinements n_{sub}, the points of maximum load are magnified for better view.

3 Numerical results

To illustrate the effectiveness of the method, a single notched tension test as presented in [6] is considered. The material parameters are taken from [6] and the internal length is chosen to be $l = 0.004\,\text{mm}$. In Figure 2, the resulting force-displacement curve for different discretisations with the iXPFM and the standard PFM are shown. Furthermore, in Table 1, the resulting error of the calculated crack surface e_Γ for the same computations are listed. It can be seen, that the iXPFM simulations are able to reproduce the crack surface and the load-displacement curve accurately even though the ratio between the internal length parameter and the finite element size is $l/h = 1$. The solutions are compared to PFM simulations with a finer mesh and yield similar results. Furthermore, it can be seen that with a submesh refinement the error e_Γ decreases significantly.

Table 1: Comparison of error e_Γ for PFM and XPFM simulations for different discretizations.

PFM (no n_{sub})				iXPFM with $l/h = 1$				
l/h	1	2	4	n_{sub}	5	10	15	20
e_Γ	24.5%	11.1%	4.8%	e_Γ	15.1%	12.2%	5.2%	3.5%

4 Conclusions

A novel approach for the extension of the PFM is presented. It employs the transformed phase-field ansatz as proposed in [4, 5] and a distortion of the reference space within cracked elements for the extended displacement field ansatz. The distorted reference element coordinates are calculated on a subgrid with a phase-field dependent LAPLACIAN equation.
It was shown in a preliminary investigation, that the method holds great potential to reduce the degrees of freedom of the phase-field problem while maintaining the accuracy of the solution.
As a next step, the influence of the model parameters and the mesh/submesh refinement is to be investigated. Furthermore, the possible reduction of computational effort in comparison to the standard PFM makes the application of the method to fracture simulations in three dimensions attractive. That is why, the extension of the model to three dimensions is currently being worked on.

Acknowledgments

This project is funded by the Deutsche Forschungsgemeinschaft (DFG, German Research Foundation) - SFB/TRR280. Project-ID 417002380 as part of the Transregional Collaborative Research Center SFB/TRR280. The financial support of the German Research Foundation is gratefully acknowledged.

REFERENCES

[1] Bourdin, B. and Francfort, G.A. and Marigo, J-J. Numerical Experiments in Revisited Brittle Fracture *J. Mech. Phys. Solids* (2000) **48.4**:797–826 doi:10.1016/S0022-5096(99)00028-9.

[2] Miehe, C. and Welschinger, F. and Hofacker, M. Thermodynamically Consistent Phase-field Models of Fracture: Variational Principles and Multi-field FE Implementations *Int. J. Numer. Methods Eng.* (2010) **83.10**:1273–1311 doi:10.1002/nme.2861.

[3] Miehe, C. and Hofacker, M. and Welschinger, F. A Phase Field Model for Rate-Independent Crack Propagation: Robust Algorithmic Implementation Based on Operator Splits *Comput. Methods Appl. Mech. Eng.* (2010) **199.45-48**:2765–2778 doi:10.1016/j.cma.2010.04.011.

[4] Loehnert, S. and Krüger, C. and Klempt, V. and Munk, L. An Enriched Phase-Field Method for the Efficient Simulation of Fracture Processes *Comput. Mech.* (2023) **71.5**:1015–1039. doi:10.1007/s00466-023-02285-z.

[5] Krüger, C. and Curoșu, V. and Loehnert, S. An Extended Phase-Field Approach for the Efficient Simulation of Fatigue Fracture Processes *Int. J. Numer. Methods Eng.* (2024) Advance online publication doi:10.1002/nme.7422.

[6] Ambati, M. and Gerasimov, T. and De Lorenzis, L. A Review on Phase-Field Models of Brittle Fracture and a New Fast Hybrid Formulation *Comput. Mech.* (2015) **55.2**:383–405 doi:10.1007/s00466-014-1109-y.

UKACM 2024 Conference, 10-12 April 2024, Durham University, Durham, UK
https://doi.org/10.62512/conf.ukacm2024.045

IMMERSED TRACTION BOUNDARY CONDITIONS IN PHASE FIELD FRACTURE MODELLING

Bradley Sims[1]*, Robert E. Bird[1], William M. Coombs[1], Stefano Giani[1]

[1] Department of Engineering, Durham University, Durham, DH1 3LE, UK.
bradley.sims@durham.ac.uk
robert.e.bird@durham.ac.uk, w.m.coombs@durham.ac.uk, stefano.giani@durham.ac.uk

Abstract. Phase field approaches are an increasingly popular method for modelling complex fracture problems and have been applied to a number of real-world settings. In some applications, pressure forces, or more generally traction terms, must be considered on the crack faces. However, application of appropriate boundary conditions to represent these tractions is non-trivial, since phase field models do not include a direct description of the fracture surface due to their diffuse nature. This paper summarises one- and two-domain approaches to including immersed traction boundary conditions and states the authors' intention to implement and evaluate these methods in an *hp*-adaptive discontinuous Galerkin finite element framework.

Key words: *fracture; phase field; traction; boundary conditions; fluid-filled fractures*

1 Introduction

Phase field fracture models have gained popularity in recent years as an approach to the numerical modelling of complex fracture problems. The method evolved from Griffith's energy-based theory for fracture [1] and the subsequent re-framing of the theory as an energy minimisation problem by Francfort and Marigo [2].

Phase field fracture models are an example of a diffused fracture modelling approach. This approach can be contrasted to discrete fracture models, such as the extended finite element method (XFEM) or configurational force approach, where cracks are modelled as discontinuities in displacement, incorporated using enrichment functions in the mesh or introducing discontinuities in the mesh through mesh splitting. In the phase field approach, the fracture surfaces are represented over an approximate volume, meaning no special treatment of the mesh is required. As a result, the phase field approach is also better suited to modelling crack nucleation, and complex fracture patterns such as branching or merging.

The growing popularity of the phase field approach has led to its application to a number of real-world problems, including the modelling of calving events in ice shelves and glaciers [3–5], where large chunks of ice are lost to the ocean as a result of fractures propagating through the full thickness of the ice. These calving events are driven both by gravitational body forces in the ice, as well as fluid pressure forces from water that collects in existing fractures. However, the lack of a discrete fracture surface in phase field fracture models means that the imposition of appropriate boundary conditions, representing the fluid pressure forces, becomes challenging.

Several approaches have been taken in the existing literature, largely in the context of hydraulic fracturing, including the transformation of the fluid pressure from a surface term into a volume term through an attempt to reconstruct the fracture surface as in [6, 7], and poroelasticity approaches where the pressure term acts through the volume, controlled by the phase field value as in [3].

This paper presents these approaches and will state the authors' intention to investigate incorporating them within an *hp*-adaptive discontinuous Galerkin finite element phase field fracture code [8].

2 Phase field fracture modelling

In 1920 Alan Arnold Griffith published his energy-based theory for brittle fracture from which the field of fracture mechanics developed [1]. For an isothermal, quasi-static case, Griffith's theory states that a fracture will propagate when the release of elastic strain energy due to crack growth, is equal to or greater than the energy required to create new fracture surfaces.

Considering the arbitrary domain $\Omega \subset \mathbb{R}^\delta$ where $\delta \in \{1,2,3\}$ with the boundary $\partial\Omega \subset \mathbb{R}^{\delta-1}$ and an internal fracture $\Gamma \subset \mathbb{R}^{\delta-1}$, the work of Francfort and Marigo [2] allows Griffith's theory to be stated in variational form as an energy minimisation problem. The total energy of the system Π can be expressed using the functional

$$\Pi = \int_\Omega \Psi(\boldsymbol{\varepsilon})\,\mathrm{d}\Omega + \int_\Gamma G_c\,\mathrm{d}\Gamma - \int_\Omega \boldsymbol{f}\cdot\boldsymbol{u}\,\mathrm{d}\Omega - \int_{\partial\Omega} \boldsymbol{\tau}\cdot\boldsymbol{u}\,\mathrm{d}\partial\Omega, \tag{1}$$

where Ψ represents the strain energy density, $\boldsymbol{\varepsilon}$ the strain tensor, $\boldsymbol{f}$ the body force, $\boldsymbol{\tau}$ the surface traction and $\boldsymbol{u}$ the displacement field. G_c is known as the critical energy release rate, in other words the amount of energy required to create new fracture surfaces, per unit area of the surface.

The minimisation of Π is however challenging in its current form, due to the difficulty in integrating over an evolving discrete fracture surface Γ. A scalar field, $\phi \in [0,1]$ can therefore be introduced in order to represent the discrete surface over an approximate volume. The scalar variable ϕ is known as the phase field, and represents the transition from intact to fully damaged states, where $\phi = 0$ at an intact material point and $\phi = 1$ at a fully cracked point in space. The introduction of the phase field allows the functional to be regularised such that the problem becomes numerically tractable

$$\Pi_l = \int_\Omega [g(\phi)+\kappa]\,\Psi_0(\boldsymbol{\varepsilon})\,\mathrm{d}\Omega + G_c\int_\Omega \gamma(\phi,\nabla\phi)\,\mathrm{d}\Omega - \int_\Omega \boldsymbol{f}\cdot\boldsymbol{u}\,\mathrm{d}\Omega - \int_{\partial\Omega}\boldsymbol{\tau}\cdot\boldsymbol{u}\,\mathrm{d}\partial\Omega \tag{2}$$

where $\gamma(\phi,\nabla\phi) = \frac{1}{2l}\phi^2 + \frac{l}{2}|\nabla\phi|^2$ and the subscript 0 denotes a quantity for undamaged material. A length scale l is introduced which controls the width of the cracked region approximating the discrete fracture surface. A monotonically decreasing function, $g(\phi) = (1-\phi)^2$ is used to degrade the material stiffness with increasing damage. A small positive constant κ is used to avoid full degradation of the material stiffness, ensuring the problem remains well-posed.

The difference in crack propagation behaviour under tensile and compressive loading can be accounted for through decomposition of the strain tensor into tensile and compressive parts, which in turn allows an equivalent split of the strain energy density into positive, Ψ_0^+, and negative, Ψ_0^-, components as in [9]. A strain history term $\mathcal{H}$ can also be introduced as in [9] to prevent reversibility of damaged regions. $\mathcal{H}$ tracks the maximum tensile strain energy density where $\mathcal{H} = \max_{t\in T}(\Psi_0^+(\boldsymbol{\varepsilon},t))$ and T represents the current time.

3 Immersed traction boundary conditions

Including a pressure or traction term along crack surfaces in phase field fracture modelling is non-trivial due to the lack of discrete fracture surface in the model. As detailed in [10], the approaches taken in

existing literature to apply pressure forces to a crack surface in phase field models can be categorised into one-domain and two-domain approaches.

In a one-domain approach, the fracture is taken to be a part of a single porous domain, simply with higher porosity and permeability at the fracture location. In an example of one such approach [3], which details a phase field model for predicting fracture propagation in ice shelves, pressure forces from meltwater are incorporated in damaged regions through Biot's theory of poroelasticity. The effective stress tensor, $\boldsymbol{\sigma}$, is defined as

$$\boldsymbol{\sigma} = g(\phi)\boldsymbol{\sigma}_0 - [1 - g(\phi)]\, p\alpha \boldsymbol{I}, \tag{3}$$

where p is the fluid pressure, $\boldsymbol{\sigma}_0$ is the undamaged total stress and α is the Biot coefficient. The degradation functions in Equation (3) ensure that both the load carrying capacity is degraded with damage, but also that the pressure forces are constrained to damaged regions, with the pressure effects increasing with increased damage. This modified stress tensor is incorporated when solving for the minimum of the energy functional in Equation (2). The pressure, p, is modified based on the depth of meltwater in the crack, as detailed in [3].

By contrast, two-domain approaches attempt to reconstruct or approximate the fracture surface in some way, as a clearer interface between the solid and fluid constituents, over which a pressure can be applied. An example of this approach is given in [11]. In this approach, the work done by the pressure force on a crack surface is given by

$$\int_\Gamma p(\boldsymbol{u}^+ - \boldsymbol{u}^-) \cdot \boldsymbol{n}_\Gamma \, \mathrm{d}\Gamma, \tag{4}$$

where $\boldsymbol{u}^\pm$ denotes the displacement on the positive and negative crack faces and $\boldsymbol{n}_\Gamma$ the normal to the crack face. This expression can then be modified using the gradient of the phase field to approximate the crack volume and added to the regularised total energy functional as an additional work term. The functional then becomes

$$\Pi_l = \int_\Omega [g(\phi) + \kappa]\, \Psi_0(\boldsymbol{\varepsilon}) \, \mathrm{d}\Omega + G_c \int_\Omega \gamma(\phi, \nabla\phi) \, \mathrm{d}\Omega - \int_\Omega \boldsymbol{f} \cdot \boldsymbol{u} \, \mathrm{d}\Omega - \int_{\partial\Omega} \boldsymbol{\tau} \cdot \boldsymbol{u} \, \mathrm{d}\partial\Omega + \int_\Omega p\boldsymbol{u} \cdot \nabla\phi \, \mathrm{d}\Omega. \tag{5}$$

This approach in [11] has also been extended in [6] and [7] to include porosity. Other two-domain approaches have used level-set functions [12] and phase field contours [13] to reconstruct fracture surfaces that act as an interface over which a pressure can be imposed.

4 Observations

The inclusion of traction boundary conditions, including pressure forces, along fracture surfaces in phase field models, is challenging due to the lack of discrete fracture surface. Existing approaches fall broadly into two categories - one-domain and two-domain methods. While one-domain methods could be considered simpler to implement, particularly for porous materials where poroelasticity and immersed boundary conditions can be handled simultaneously, two-domain methods could on the other hand be interpreted as more physically representative of the mechanical processes involved, and more readily extended to general traction boundary conditions, instead of pressure forces. These different approaches will be implemented and evaluated in a discontinuous Galerkin finite element phase field model [8] and their suitability for wider applications, such as the modelling of calving events in ice shelves, considered.

Acknowledgments

This work was supported by the Engineering and Physical Sciences Research Council (Grant no.: EP/W524426/1).

References

[1] A. A. Griffith, "The phenomena of rupture and flow in solids," *Philosophical Transactions of the Royal Society of London. Series A, Containing Papers of a Mathematical or Physical Character*, vol. 221, pp. 163–198, 1921.

[2] G. A. Francfort and J. J. Marigo, "Revisiting brittle fracture as an energy minimization problem," *Journal of the Mechanics and Physics of Solids*, vol. 46, no. 8, pp. 1319–1342, 1998.

[3] T. Clayton, R. Duddu, M. Siegert, and E. Martínez-Pañeda, "A stress-based poro-damage phase field model for hydrofracturing of creeping glaciers and ice shelves," *Engineering Fracture Mechanics*, vol. 272, p. 108693, 2022.

[4] R. Sondershaus, A. Humbert, and R. Müller, "A phase field model for fractures in ice shelves," *PAMM*, vol. 22, no. 1, p. e202200256, 2023.

[5] X. Sun, R. Duddu, and Hirshikesh, "A poro-damage phase field model for hydrofracturing of glacier crevasses," *Extreme Mechanics Letters*, vol. 45, p. 101277, May 2021.

[6] K. Yoshioka and B. Bourdin, "A variational hydraulic fracturing model coupled to a reservoir simulator," *International Journal of Rock Mechanics and Mining Sciences*, vol. 88, pp. 137–150, 2016.

[7] C. Chukwudozie, B. Bourdin, and K. Yoshioka, "A variational phase-field model for hydraulic fracturing in porous media," *Computer Methods in Applied Mechanics and Engineering*, vol. 347, pp. 957–982, 2019.

[8] R. E. Bird, C. E. Augarde, W. M. Coombs, R. Duddu, S. Giani, P. T. Huynh, and B. Sims, "An hp-adaptive discontinuous Galerkin method for phase field fracture," *Computer Methods in Applied Mechanics and Engineering*, vol. 416, p. 116336, 2023.

[9] C. Miehe, M. Hofacker, and F. Welschinger, "A phase field model for rate-independent crack propagation: Robust algorithmic implementation based on operator splits," *Computer Methods in Applied Mechanics and Engineering*, vol. 199, no. 45, pp. 2765–2778, 2010.

[10] Y. Heider, "A review on phase-field modeling of hydraulic fracturing," *Engineering Fracture Mechanics*, vol. 253, p. 107881, 2021.

[11] B. Bourdin, C. Chukwudozie, and K. Yoshioka, "A Variational Approach to the Numerical Simulation of Hydraulic Fracturing," in *All Days*. San Antonio, Texas, USA: SPE, 2012, pp. SPE–159 154–MS.

[12] S. Lee, M. F. Wheeler, and T. Wick, "Iterative coupling of flow, geomechanics and adaptive phase-field fracture including level-set crack width approaches," *Journal of Computational and Applied Mathematics*, vol. 314, pp. 40–60, 2017.

[13] N. Singh, C. V. Verhoosel, and E. H. van Brummelen, "Finite element simulation of pressure-loaded phase-field fractures," *Meccanica*, vol. 53, no. 6, pp. 1513–1545, 2018.

Structural Analysis and Optimisation: Modelling, Characterisation, and Response

UKACM 2024 Conference, 10-12 April 2024, Durham University, Durham, UK
https://doi.org/10.62512/conf.ukacm2024.022

COMPUTATIONAL MODELLING OF FAILURE OF WELDED JOINTS IN HYDROGEN TRANSPORT PIPELINES

Tushar K. Mandal[1]*, Jonathan Parker[2], Michael Gagliano[2], Emilio Martinez-Paneda[1]

[1] Department of Engineering Science, University of Oxford, Oxford OX1 3PJ, UK.
tushar.mandal@eng.ox.ac.uk
[2] Electric Power Research Institute, 3420 Hillview Avenue, Palo Alto, CA 94304, USA.

Abstract. We present a computational framework that combines the welding process model and coupled deformation-diffusion-fracture model to predict the structural integrity and potential failure modes of hydrogen transport pipelines. In this study, we specifically focus on the seam welds, which are particularly vulnerable regions in pipeline infrastructure. Initially, the developed model is validated against experimentally observed R-curves of pipeline steels in hydrogen environment. Subsequently, we employ this modelling framework to investigate the mechanisms behind failure in seam welded joints, aiming to comprehend the influence of existing defects, microstructural heterogeneity, and residual stresses. Our findings reveal that the H_2 fracture pressure of the pipeline may decrease to as low as 15 MPa under realistic critical conditions. These results bring new mechanistic insight into the viability of repurposing the existing natural gas pipeline network for hydrogen transportation. Furthermore, the presented computational model enables mapping the conditions that ensure the safe transport of hydrogen.

Key words: *Hydrogen embrittlement; Multi-physics modelling; Phase field fracture; Pipeline steels; Welds*

1 Modelling framework

As sketched in Figure 1, we present a framework that combines weld process modelling and coupled deformation-diffusion-fracture simulations. The weld process model is needed to determine the residual stress/strain state of the weld (Section 1.1). Then, embrittlement simulations can be conducted and failure can be predicted as a function of the hydrogen gas pressure and relevant weld characteristics (Section 1.2).

1.1 Weld process model

We idealise the welding process as a sequential thermo-mechanical procedure. The temperature profile was obtained by solving the heat equation and is transferred to the mechanical sub-problem as an initial field, to calculate the thermal strain ε_T at each point $\mathbf{x}$ and time t given by $\varepsilon_T(\mathbf{x},t) := \alpha I(T(\mathbf{x},t) - T_0(\mathbf{x}))$, where α is the coefficient of thermal expansion, T_0 denotes the room temperature, and I is the second-order unit tensor. The temperature dependence of the thermal and mechanical material properties are considered following the ASME standard (Section II, Part D). We consider a small strain formulation and standard decomposition of strain tensor ε into thermal (ε_T), elastic (ε_e) and plastic (ε_p) components; $\varepsilon = \varepsilon_e + \varepsilon_p + \varepsilon_T$ with $\varepsilon := \frac{1}{2}\left(\nabla\mathbf{u} + (\nabla\mathbf{u})^T\right)$; here $\mathbf{u}$ presents the displacement field. A power law hardening is considered with Von Mises plasticity in the mechanical problem. The convective and radiative cooling was considered while solving the heat equation.

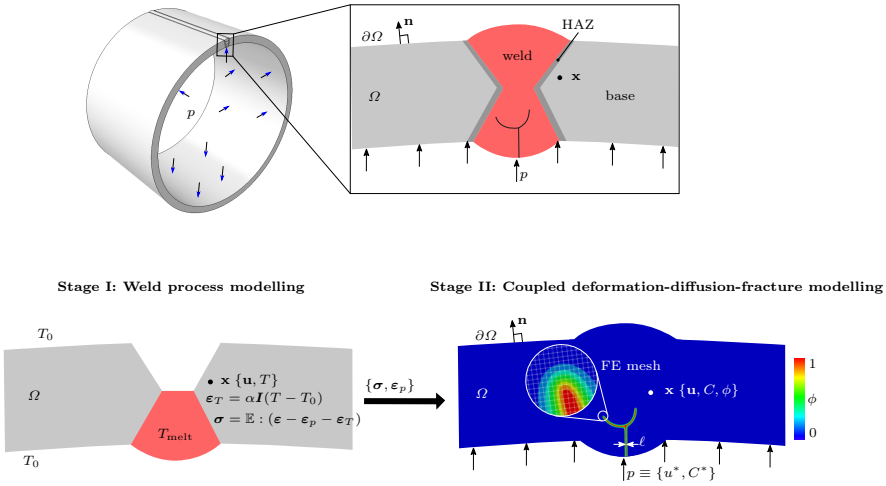

Figure 1: Schematic representation of the finite element modelling framework, aimed at predicting hydrogen-assisted failures of welded joints in pipelines subjected to an internal hydrogen pressure p.

1.2 Coupled deformation-diffusion-fracture model

We idealise the hydrogen-assisted failure of the welded joint as a coupled deformation-diffusion-fracture problem, where the evolving fracture surface is modelled using the phase field method [1]. Within the framework of the conventional phase field model [2], the total potential energy $\mathscr{E}$ of the elastoplastic solid is given by,

$$\mathscr{E} = \int_\Omega \Big(h(\phi)\psi_e(\varepsilon_e) + \bar{h}(\phi)\psi_p(\varepsilon_p) \Big) \mathrm{d}\Omega + \int_\Omega \frac{G_c(C)}{2} \left(\frac{\phi^2}{\ell} + \ell |\nabla\phi|^2 \right) \mathrm{d}\Omega, \tag{1}$$

with phase field order parameter ϕ distinguishing the intact solid ($\phi = 0$) and cracked solid ($\phi = 1$) and length scale parameter ℓ regularising a sharp crack as a diffused band of damage. The elastic and plastic part of undamaged strain energy densities, $\psi_e(\varepsilon_e)$ and $\psi_p(\varepsilon_p)$, respectively, are degraded using degradation functions $h(\phi)$ and $\bar{h}(\phi)$, respectively. We choose quadratic degradation functions as,

$$h(\phi) = (1-\phi)^2, \quad \bar{h}(\phi) := \beta h(\phi) + (1-\beta), \tag{2}$$

with $\beta = 0.1$ to ensure only 10% of the plastic work is available to create a new fracture surface following the seminal work by Taylor and Quinney [3]. The hydrogen concentration (C) dependence of the fracture energy (G_c) is considered based on a phenomenological model [4],

$$G_c(C) = \left[\frac{G_c^{\min}}{G_c(0)} + \left(1 - \frac{G_c^{\min}}{G_c(0)} \right) \exp\left(-q_1 C^{q_2}\right) \right] G_c(0), \tag{3}$$

with fracture energy of the material in the air $G_c(0)$, minimum fracture energy of the material in hydrogen $G_c^{\min}$, and the exponential fitting parameters $\{q_1, q_2\}$.

The developed fracture model (Eq. (1)) is coupled with a Fickian stress-induced diffusion equation for hydrogen as,

$$\frac{\partial C}{\partial t} = -\nabla \cdot \left(-\frac{DC}{RT} \nabla \mu \right), \quad \text{with} \quad \mu := \mu^0 + RT \ln\left(\frac{\theta_L}{1-\theta_L} \right) - \bar{V}_H \sigma_h, \tag{4}$$

with the hydrostatic stress σ_h, the reference chemical potential μ^0, effective diffusion coefficient D, ideal gas constant R, absolute temperature T, and partial molar volume of hydrogen in solid solution $\bar{V}_H$. Also, $\theta_L = C/N_L$ is the lattice occupancy with the lattice site density N_L.

2 Results and Discussions

The material properties for the base metal and the weld of the considered pipeline steels are collected from the literature. The developed model is calibrated to simulate the crack growth resistance the pipeline steels in the air and the hydrogen-containing environments [4], and the calibrated material properties for X80 steel are listed in Table 1. The calibrated model is coupled with welding process simulations [4]

	E (MPa)	ν (-)	σ_y (MPa)	n (-)	$G_c(0)$ (N/mm)	$G_c^{\min}$ (N/mm)	ℓ (mm)	D (mm^2/s)
Base	187000	0.3	660	0.10	60	7	0.17	4.5×10^{-4}
Weld	196350	0.3	726	0.05	54	6.3	0.13	3×10^{-4}

Table 1: Material parameters adopted for the weld and base metal regions of the considered X80 pipeline steel.

and used to gain insight into the structural integrity of seam (i.e., longitudinal) welds in a representative pipeline with an inner radius of 110 mm and thickness of 7.5 mm (Figure 2). Two weld configurations were employed based on images of ex-service welds from natural gas pipelines: (a) a two-pass weld of dimensions 17 x 14 mm, and (b) a three-pass weld of dimensions 21 x 13 mm. The microstructural heterogeneity of the second weld was characterised using a Vickers Hardness (VH) mapping approach.

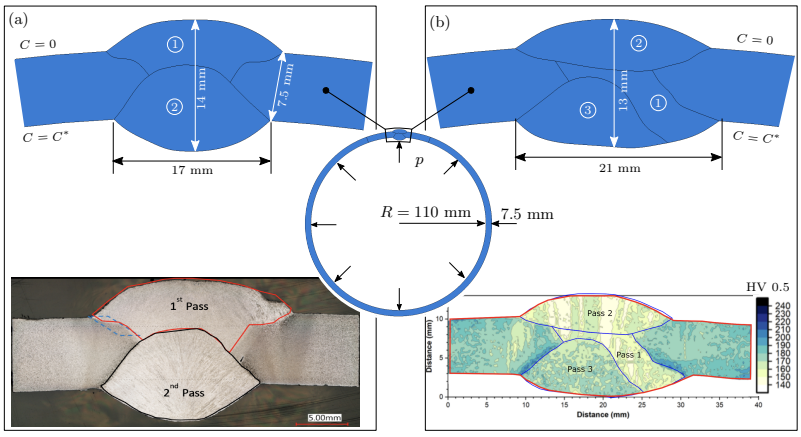

Figure 2: Schematic representation of the considered pipeline section containing a longitudinal weld.

In each case, welding residual stresses are obtained and used as an initial condition for fracture simulation where the pipe section is subjected to monotonically increasing internal hydrogen pressure p. We present our key observations below.

Effect of residual stress: In the absence of residual stresses, the X80 welded joint fails by plastic yielding, while when residual stresses are accounted for cracking is observed (Figure 3).

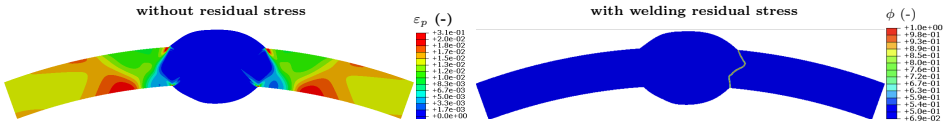

Figure 3: Investigating the role of welding residual stresses on the failure of hydrogen transport pipelines.

Sensitivity to flaws/defects: A 3 mm initial flaw at the weld-base material junction, near the HAZ region, can reduce the load capacity ($p_{\max}$) by more than 50% (Figure 4).

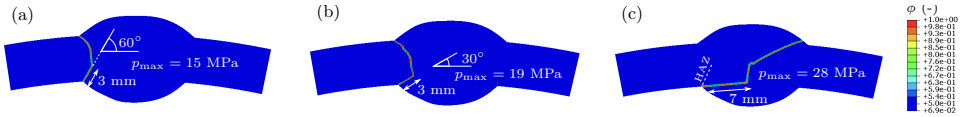

Figure 4: Investigating the role of external pre-existing defects on the failure of hydrogen transport pipelines.

Heterogeneous material properties: The failure mode of the welded joint changes from plastic yielding to cracking when microhardness map-based material properties are considered. Moreover, the load capacity reduces drastically (Figure 5).

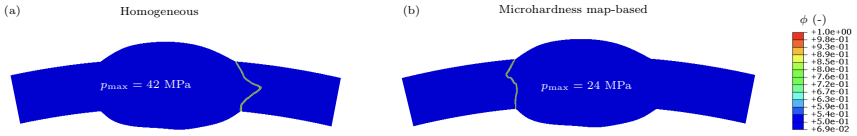

Figure 5: Investigating the role of accounting for the microstructural heterogeneity of seam welds. Three-pass weld is considered here.

Acknowledgments

The authors acknowledge financial support from EPRI through the R&D project "*Virtual Testing* of hydrogen-sensitive components". E. Martínez-Pañeda additionally acknowledges financial support from UKRI's Future Leaders Fellowship programme [grant MR/V024124/1].

References

[1] B. Bourdin, G. A. Francfort, J.-J. Marigo, Numerical experiments in revisited brittle fracture, Journal of the Mechanics and Physics of Solids 48 (4) (2000) 797–826.

[2] C. Miehe, F. Welschinger, M. Hofacker, Thermodynamically consistent phase-field models of fracture: Variational principles and multi-field FE implementations, International Journal for Numerical Methods in Engineering 83 (10) (2010) 1273–1311.

[3] G. I. Taylor, H. Quinney, The latent energy remaining in a metal after cold working, Proceedings of the Royal Society of London, Series A. 143 (849) (1933) 307–326.

[4] T. K. Mandal, J. Parker, M. Gagliano, E. Martínez-Pañeda, Computational predictions of weld structural integrity in hydrogen transport pipelines, International Journal of Hydrogen Energy (2024).

UKACM 2024 Conference, 10-12 April 2024, Durham University, Durham, UK
https://doi.org/10.62512/conf.ukacm2024.044

Characterisation of rate-dependent fracture in adhesive joints

Leo Škec[1], Giulio Alfano[2]

[1] Faculty of Civil Engineering, University of Rijeka, Radmile Matejčić 3, 51000 Rijeka, Croatia.

leo.skec@uniri.hr

[2] Deptartment of Mechanical and Aerospace Engineering, Brunel University London, Uxbridge UB8 3PH

giulio.alfano@brunel.ac.uk

ABSTRACT

For adhesive joints, several authors questioned the applicability of LEFM when the combination between the ductility of the adhesive, the stiffness of the adherents and the fracture mode leads to a relatively large process zone during crack propagation. For such cases, nonlinear fracture mechanics (NLFM) and the use of the critical value, J_c, of the J integral have been recommended. This was until it was recently showed, at least for the case of mode-I crack propagation along a thin interface, that the difference between G_c and J_c is found to be equal to the partial derivative with respect to the increase in crack length, a, of the energy dissipated in front of the crack tip. The fact that this difference is extremely small for double-cantilever-beam (DCB) specimens, together with a rigorous assessment of the accuracy entailed by the use of the equivalent-crack-length concept, were used to develop an accurate and practically effective experimental/numerical procedure to assess the rate dependence of fracture resistance in adhesive joints made of aluminium arms bonded with an epoxy adhesive. The effectiveness is the result of using simple DCB tests without the need to measure the crack length. Numerical simulations were conducted using a bespoke finite-element code tailored for DCB tests based on Timoshenko beam theory and a cohesive-zone model based on fractional viscoelasticity.

Key words: rate-dependent fracture; debonding failure; double cantilever beams; cohesive-zone model; nonlinear finite-element analysis.

1 Introduction

Linear elastic fracture mechanics (LEFM), based on Griffith's energy balance and the concept of critical energy release rate, G_c, has been shown to be valid not only for very brittle materials but also for quasi-brittle or ductile materials when the inelastic zone around the crack tip is small enough [1]. In the case of debonding of adhesive joints, damage is typically localised on a thin interface of adhesive and in many cases, either due to the ductility of the adhesive or because of the high stiffness of the substrates, the size of such inelastic zone, or cohesive zone, is considered too large for LEFM to be valid. In such cases, the critical value of the J integral, J_c, has been recommended to characterise the fracture resistance of the joints [2, 3]. In fact, the validity of any one-parameter theory has been questioned in some problems with large cohesive zones, for which multi-parameter approaches such as cohesive-zone models (CZM) have been deemed necessary [4]. The input parameter of a CZM that normally has the biggest influence on the model response is the work of separation per unit of cracked area, Ω, which is equal to the area under the traction-separation law (TSL). Interestingly, different researchers assume either that $\Omega = G_c$ or that $\Omega = J_c$ but, although the latter can be rigorously justified for homogeneous interfaces [5], the former is generally an approximation, which is normally overlooked.

On the other hand, despite the widely discussed limitations of the use of LEFM to characterise the fracture resistance of adhesive joints, all the currently approved industrial standards are based on the use of LEFM and therefore provide methods to experimentally evaluate G_c. Only few years ago has the range of validity of such approaches been rigorously assessed by Škec et al. [5], at least for the case of mode-I crack propagation on thin interfaces. This contribution is partly based on another result obtained in the same article, consisting in the rigorous derivation of the following relation between J_c and G_c, for homogeneous interfaces:

$$J_c = \Omega = G_c - \frac{\partial \Pi_D}{\partial a} \tag{1}$$

where a is the crack length and Π_D represents the energy dissipated ahead of the crack tip. As anticipated above, $\Omega = J_c$ is strictly true only for homogeneous interface, and it is worth noting that for many adhesives, the relatively random occurrence of defects across the interface results in a certain degree of variation of the fracture resistance for different values of the crack length, which can be considered equivalent to having a case of a non-homogeneous interface.

Equation (1) demonstrates that the difference between G_c and J_c is not due to the size of the process zone, or cohesive zone, but is related to how much Π_D changes during crack propagation, unlike what normally stated in the literature. In other words, if the 'damage profile' translates in a steady-state fashion with the crack tip, then $\Omega = G_c$ and, if G_c is constant, then $J_c = G_c$, regardless of the size of the cohesive zone. An example of such case is a double cantilever beam (DCB) with prescribed rotations, also known as moment-loaded DCB [4]. For the more conventional DCB with prescribed displacements, Π_D is not constant but, for most cases of interest, its variation is actually extremely small during crack propagation. An example is reported in Figure 1, which shows the difference between J_c and G_c obtained in numerical simulations of a DCB made of aluminium arms, which are bonded with an adhesive modelled via a bilinear CZM with constant properties along the interface, including constant Ω, so that $J_c = \Omega$. Different cases have been simulated with different strength, σ_{max}, of the adhesive. The smaller σ_{max}, the more ductile the adhesive, but for the most ductile case the difference between J_c and G_c is less than 2% and rapidly decreasing during crack propagation.

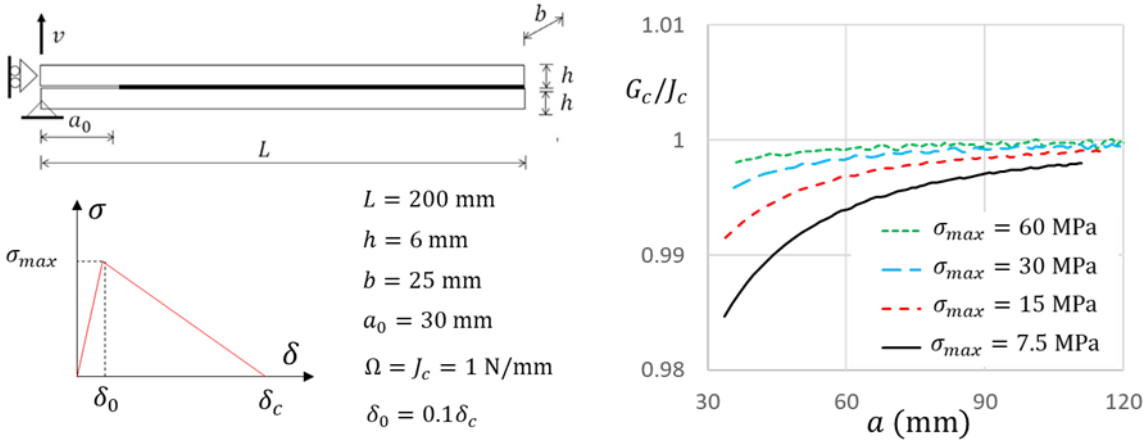

Figure 1: Relation between $J_c = \Omega$ and G_c for numerical simulations of a DCB.

Building on these results, an effective and accurate data-reduction scheme based on LEFM and the use of enhanced simple beam theory (ESBT) was proposed by the authors in Ref. [6]. The method uses the concept of equivalent crack length proposed by de Moura et al. [7], which enables the determination of the fracture resistance without measuring the crack length. The accuracy entailed by the use of the equivalent crack length concept has been rigorously assessed in Ref. [4], and its application in combination with ESBT results in a data reduction scheme that turns out to be more accurate than those available in current standards [6].

2 Rate-dependent failure of adhesive joints

The ESBT-based data reduction scheme proposed in Ref. [6] has been more recently applied to characterise the rate dependence of the failure of adhesive joints made of aluminium Al 6082-T6 substrates bonded with the epoxy adhesive Araldite® 2015 [8]. To this end, 24 DCB specimens have been tested at 5 different speeds of the prescribed cross-head displacement, ranging from a minimum of 0.1 to a maximum of 5000 mm/min. For each of these speeds, four different tests have been conducted.

Table 1. Dimensions of the DCB specimens.

Dimensions (mm)	L	d	b	a_0	c	t	l_b
Average value	250	6.35	25.4	40	60	0.25	51.7

2

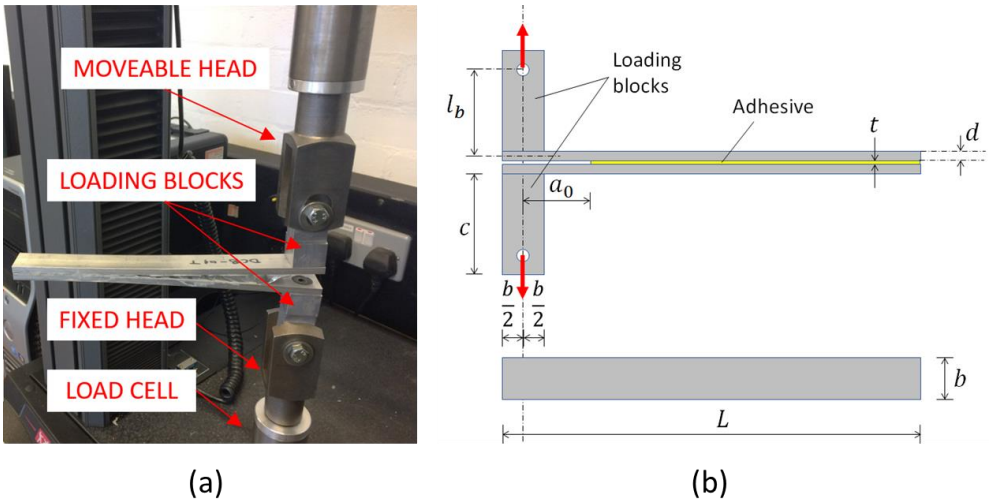

Figure 2: DCB tests: (a) experimental set up and (b) geometry of the DCB specimens.

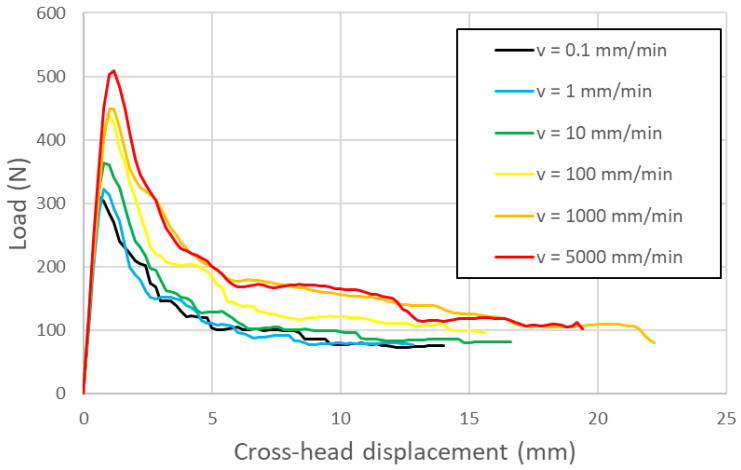

Figure 3: Average load vs cross-head displacement for each one of the tested speeds.

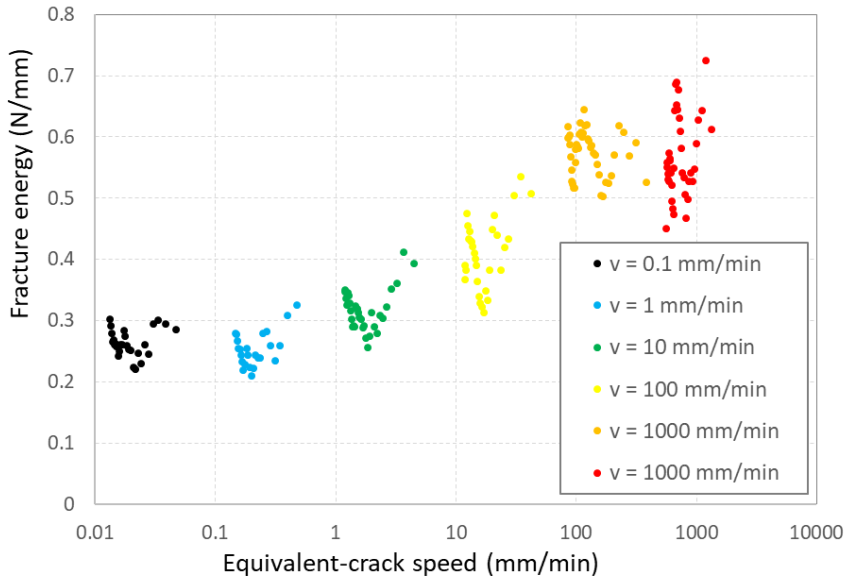

Figure 4: Fracture energy against the equivalent crack speed.

3

The geometry and the experimental set up of the DCB tests are shown in Figure 2, with the dimensions of the specimens reported in Table 1. Figure 3 plots the average load against the cross-head displacement for each one of the tested speeds. Some scatter of results for different specimens tested at the same speed and the oscillations within the load-displacement curves for each individual test (see Ref. [8] for more details) are such that a clear separation between average curves obtained at different speeds does not always occur. Nevertheless, the rate dependence of the response is evident.

The data reduction scheme adopted allowed us to determine the fracture energy against the speed of the equivalent crack length, reported in Figure 4. Although the difference between the equivalent and the actual crack lengths can be noticeable, the difference between their speed is practically negligible. Therefore, with excellent approximation, Figure 4 also shows the fracture energy against the actual crack speed and provides a clearer assessment of the rate dependence of the response. It is also interesting to note that, despite the cross-head speed is constant in each test, the crack speed decreases during crack propagation [8].

In addition to the fracture energy, the failure response of the tested specimens has also been characterised by developing a procedure to identify the input parameters of a rate-dependent CZM based on fractional viscoelasticity [9], with very good correlation between the experimental results and the numerical model, which uses bespoke finite elements combining Timoshenko beams and interface elements. These results cannot be included here due to the limited space.

3 Conclusions

On overview of the theoretical framework and a selection of results have been provided for the experimental and numerical characterisation of the rate-dependent failure of adhesive joints made of aluminium substrates bonded with an epoxy structural adhesive. The rate dependence of the response leads to values of the fracture energy up to 2.5 higher at the highest tested speeds than at the lowest speeds. The results are also characterised by noticeable scatter, which is also related to the characteristic oscillations in the load-displacement curves obtained from DCB tests not only by the present authors but also by many other researchers [8]. Current efforts are focused on investigating the root causes for this scatter and how to incorporate them in the modelling framework, so that a more accurate characterisation of the failure resistance of adhesive joint can be achieved.

Acknowledgments

This research has been funded by the European Union as a Marie Sklodowska-Curie Action, under the Horizon 2020 Research and Innovation Programme (grant agreement No. 701032).

References

[1] T.L. Anderson, (2017). Fracture mechanics: fundamentals and applications. *CRC Press*, Boca Raton.
[2] C. Sarrado, A. Turon, J. Costa, J. Renart. (2016). On the validity of linear elastic fracture mechanics methods to measure the fracture toughness of adhesive joints. *International Journal of Solids and Structures* 81, 110–116.
[3] R. Campilho, D. Moura, M. Banea, L. da Silva, (2015). Adhesive thickness effects of a ductile adhesive by optical measurement techniques, *International Journal of Adhesion and Adhesives*, 57, 125–132.
[4] B.F. Sørensen, T.K. Jacobsen, (2003). Determination of cohesive laws by the J integral approach. *Engineering Fracture Mechanics* 70, 1841–1858.
[5] L. Škec, G. Alfano, G. Jelenić, (2018). On G_c, J_c and the characterisation of the mode-I fracture resistance in delamination or adhesive debonding. *International Journal of Solids and Structures* 144-145:100-122.
[6] L. Škec, G. Alfano, G. Jelenić, (2019). Enhanced simple beam theory for characterising mode-I fracture resistance via a double cantilever beam test. *Composites Part B* 167:250-262.
[7] M.F.S.F. de Moura, R.D.S.G. Campilho, J.P.M. Gonçalves, (2008). Crack Equivalent Concept Applied to the Fracture Characterization of Bonded Joints under Pure Mode I Loading. *Composites Science Technology*, 68(10–11), 2224–2230.
[8] L. Škec, G. Alfano, (2023). Experimental and numerical study of rate-dependent mode-I failure of a structural adhesive, *The Journal of Adhesion* 99(8): 1323-1355.
[9] M. Musto, G. Alfano, (2015). A fractional rate-dependent cohesive-zone model. *International Journal for Numerical Methods in Engineering* 103(5): 313-341.

UKACM 2024 Conference, 10-12 April 2024, Durham University, Durham, UK
https://doi.org/10.62512/conf.ukacm2024.061

ROBUST TOPOLOGY OPTIMISATION OF LATTICE STRUCTURES WITH SPATIALLY CORRELATED UNCERTAINTIES

Ahmet Oguzhan Yuksel[1], Ismael Ben-Yelun[1,2] and Fehmi Cirak[1]

[1] Department of Engineering, University of Cambridge, Trumpington Street, Cambridge, CB2 1PZ, UK, aoy21@cam.ac.uk and fc286@cam.ac.uk.

[2] E.T.S. de Ingeniería Aeronáutica y del Espacio, Universidad Politécnica de Madrid, Pza. Cardenal Cisneros 3, Madrid, 28040, Spain, i.binsenser@upm.es.

Abstract. The uncertainties in material and other properties of structures are often spatially correlated. We introduce an efficient technique for representing and processing spatially correlated random fields in robust topology optimisation of lattice structures. Robust optimisation takes into account the statistics of the structural response to obtain a design whose performance is less sensitive to the specific realisation of the random field. We represent Gaussian random fields on lattices by leveraging the established link between random fields and stochastic partial differential equations (SPDEs). The precision matrix, i.e. the inverse of the covariance matrix, of a random field with Matérn covariance is equal to the finite element stiffness matrix of a possibly fractional PDE with a second-order elliptic operator. We consider the discretisation of the PDE on the lattice to obtain a random field which, by design, takes into account its geometry and connectivity. The so-obtained random field can be interpreted as a physics-informed prior by the hypothesis that the elliptic PDE models the physical processes occurring during manufacturing, like heat and mass diffusion. Although the proposed approach is general, we demonstrate its application to lattices modelled as pin-jointed trusses with uncertainties in member Young's moduli. We consider as a cost function the weighted sum of the expectation and standard deviation of the structural compliance. To compute the expectation and standard deviation and their gradients with respect to member cross-sections we use a first-order Taylor series approximation. The cost function and its gradient are computed using only sparse matrix operations. We demonstrate the efficiency of the proposed approach using several lattice examples with isotropic, anisotropic and non-stationary random fields and up to eighty thousand random and optimisation variables.

Key words: *robust optimisation, random fields, lattice structures, topology optimisation*

1 Introduction

In robust optimisation, uncertainties in material, geometry, loading, and manufacturing are taken into account by considering a cost function consisting of the weighted sum of the expectation and standard deviation of standard cost functions used in deterministic optimisation. As a result, robust optimisation yields a structure which is optimal with respect to a chosen cost function and is less sensitive to the uncertain properties of the actual structure. We introduce an efficient topology optimisation approach [1] for large lattice structures with spatially correlated random material properties, see Figure 1.

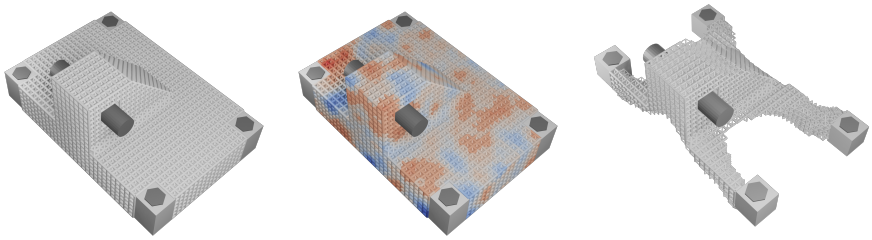

(a) Original design (b) Sample (c) Optimised design

Figure 1: Robust topology optimisation of a bracket consisting of body-centred cubic unit cells. The bracket is fixed at the four corners of the base plate and an external load is applied at the horizontal shaft attached to the vertical plate. The ground structure (a), a sample depicting the Young's moduli variation (b), and the optimised lattice structure (c).

2 Perturbation Approximation

The first-order series expansion of the random displacement vector $\boldsymbol{u}(\boldsymbol{s},\boldsymbol{r})$ around the expected value $\overline{\boldsymbol{r}}$ of the random vector is given by

$$\boldsymbol{u}(\boldsymbol{s},\boldsymbol{r}) \approx \boldsymbol{u}(\boldsymbol{s},\overline{\boldsymbol{r}}) + \frac{\partial \boldsymbol{u}(\boldsymbol{s},\overline{\boldsymbol{r}})}{\partial \boldsymbol{r}} \left(\boldsymbol{r}-\overline{\boldsymbol{r}}\right) . \tag{1}$$

The gradient of the solution is derived by differentiating the equilibrium equation yielding

$$\frac{\partial \boldsymbol{u}(\boldsymbol{s},\overline{\boldsymbol{r}})}{\partial \boldsymbol{r}} = -\boldsymbol{K}(\boldsymbol{s},\overline{\boldsymbol{r}})^{-1} \frac{\partial \boldsymbol{K}(\boldsymbol{s},\overline{\boldsymbol{r}})}{\partial \boldsymbol{r}} \boldsymbol{u}(\boldsymbol{s},\overline{\boldsymbol{r}}) . \tag{2}$$

Hence, the probability density of the displacement vector is also a Gaussian,

$$p\left(\boldsymbol{u}(\boldsymbol{s})\right) = \mathcal{N}\left(\overline{\boldsymbol{u}}(\boldsymbol{s}), \boldsymbol{C}_u(\boldsymbol{s})\right) . \tag{3}$$

Given the series expansion (1), we obtain for the expected value and for the covariance

$$\overline{\boldsymbol{u}}(\boldsymbol{s}) = \boldsymbol{u}\left(\boldsymbol{s},\overline{\boldsymbol{r}}\right), \quad \boldsymbol{C}_u(\boldsymbol{s}) = \frac{\partial \boldsymbol{u}(\boldsymbol{s},\overline{\boldsymbol{r}})}{\partial \boldsymbol{r}} \boldsymbol{C}_r \left(\frac{\partial \boldsymbol{u}(\boldsymbol{s},\overline{\boldsymbol{r}})}{\partial \boldsymbol{r}}\right)^{\mathsf{T}} . \tag{4}$$

We arrive at the probability density of the compliance

$$p(J) = \mathcal{N}\left(\overline{J}(\boldsymbol{s}), \sigma_J(\boldsymbol{s})^2\right) , \tag{5a}$$

with the mean and variance

$$\overline{J}(\boldsymbol{s}) = \boldsymbol{f} \cdot \overline{\boldsymbol{u}}(\boldsymbol{s}), \quad \sigma_J(\boldsymbol{s})^2 = \boldsymbol{f} \cdot \boldsymbol{C}_{\boldsymbol{u}}(\boldsymbol{s},\overline{\boldsymbol{r}})\boldsymbol{f} . \tag{5b}$$

3 Spatial Random Fields

We consider in $\mathbb{R}^d$, $d \in \{1, 2, 3\}$, a zero-mean Gaussian random field,

$$r(\boldsymbol{x}) \sim \mathcal{GP}\left(0, c_r\left(\boldsymbol{x}, \boldsymbol{x}'\right)\right) , \tag{6}$$

with the Matérn covariance function $c_r(\boldsymbol{x}, \boldsymbol{x}')$ defined as

$$c_r(\boldsymbol{x}, \boldsymbol{x}') = \mathbb{E}[r(\boldsymbol{x})r(\boldsymbol{x}')] = \frac{\sigma^2}{2^{\nu-1}\Gamma(\nu)} \left(\kappa\|\boldsymbol{x} - \boldsymbol{x}'\|\right)^{\nu} K_{\nu}\left(\kappa\|\boldsymbol{x} - \boldsymbol{x}'\|\right) , \tag{7}$$

with $\sigma \in \mathbb{R}^+$ being the standard deviation, $\nu \in \mathbb{R}^+$ the smoothness parameter, $\ell \in \mathbb{R}^+$ the length-scale parameter, Γ the Gamma function and K_ν the modified Bessel function of the second kind of order ν. The parameter κ is $\kappa = \sqrt{2\nu}/\ell$. Stated in [2] and [3], the random field $r(\boldsymbol{x})$ is the solution of the stochastic partial differential equation (SPDE)

$$\left(\kappa^2 - \Delta\right)^{\beta} r(\boldsymbol{x}) = \frac{1}{\tau} g(\boldsymbol{x}) , \tag{8}$$

where Δ is the Laplace operator, $g(\boldsymbol{x})$ a Gaussian white noise process

$$g(\boldsymbol{x}) \sim \mathcal{GP}(0,\ \delta(\boldsymbol{x} - \boldsymbol{x}')) , \tag{9}$$

and the remaining two parameters are defined as

$$\beta = \frac{\nu}{2} + \frac{d}{4},\ \ \tau^2 = \frac{\Gamma(\nu)}{\sigma^2\Gamma(\nu + d/2)(4\pi)^{d/2}\,\kappa^{2\nu}}. \tag{10}$$

A straightforward finite element discretisation of the PDEs in the recursion yields

$$\left(\kappa^2\boldsymbol{M} + \boldsymbol{A}\right)\boldsymbol{r}^{(1)} = \frac{1}{\tau}\boldsymbol{g} , \tag{11a}$$

$$\left(\kappa^2\boldsymbol{M} + \boldsymbol{A}\right)\boldsymbol{r}^{(k)} = \boldsymbol{M}\boldsymbol{r}^{(k-1)} , \tag{11b}$$

where $\boldsymbol{M}$ is the (lumped) mass matrix, $\boldsymbol{A}$ the stiffness matrix and $\boldsymbol{g}$ a Gaussian white noise vector with the density

$$\boldsymbol{g} \sim \mathcal{N}(\boldsymbol{0}, \boldsymbol{M}) ; \tag{12}$$

see [4]. The solution vector $\boldsymbol{r}$ is a Gaussian and has the probability density

$$\boldsymbol{r} \sim \mathcal{N}\left(\boldsymbol{0}, \boldsymbol{C}_r\right) = \mathcal{N}\left(\boldsymbol{0}, \boldsymbol{Q}_r^{-1}\right) , \tag{13}$$

with the precision matrix

$$\boldsymbol{Q}_r = \tau^2\sqrt{\boldsymbol{M}}\left(\kappa^2\boldsymbol{I} + \sqrt{\boldsymbol{M}^{-1}}\boldsymbol{A}\sqrt{\boldsymbol{M}^{-1}}\right)^{2\beta}\sqrt{\boldsymbol{M}} . \tag{14}$$

4 Numerical results

Figure 2 shows two optimisation results obtained by optimising the engine bracket given in Figure 1a. One can see that the material is more dispersed when the optimisation is carried out with cost function consisting only the standard deviation. Therefore, the optimised structure can handle the prescribed load better under the influence of material uncertainty.

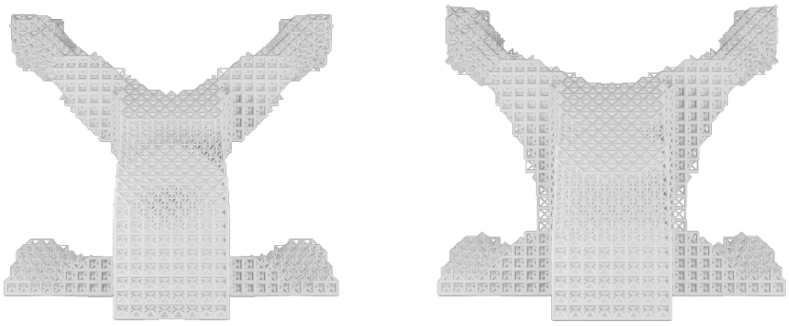

(a) Optimised $\overline{J}$ (b) Optimised $\sigma_J(\boldsymbol{s})$

Figure 2: Engine bracket. Comparison of the optimised engine bracket for the cost function consists only of $\overline{J}$ (a), and for the right only of $\sigma_J(\boldsymbol{s})$ of the compliance (b).

5 Conclusions

We hypothesise that the SPDE models the unaccounted physical diffusion processes occurring during the manufacturing of the lattice structure and, hence, is an effective approach to constructing physics-informed random fields with an extension to non-stationary and anisotropic random fields. To optimise the cross-sectional areas of the members, we compute the required mean and standard deviation of the compliance and constraint functions, obtaining optimised structures more robust against variations in material properties. The efficiency of the series expansion combined with the sparsity of the precision matrix of the random field allows us to optimise large lattice structures with eighty thousand members with random Young's moduli.

Acknowledgments

I.B-Y. was supported by the European Union's Horizon 2020 research and innovation programme under the Marie Sklodowska-Curie Grant Agreement No. 101007815. A.O.Y. was supported by a fellowship of the Ministry of National Education of the Republic of Turkey. F. C. was supported by Wave 1 of The UKRI Strategic Priorities Fund under the EPSRC Grant EP/T001569/1 and The Alan Turing Institute.

REFERENCES

[1] Ben-Yelun I, Yuksel AO, Cirak F (2023) *Robust topology optimisation of lattice structures with spatially correlated uncertainties.* Structural and Multidisciplinary Optimization 67, 16 (2024).

[2] Whittle P (1954) *On stationary processes in the plane.* Biometrika pp 434–449.

[3] Lindgren F, Rue H, Lindström J (2011) *An explicit link between Gaussian fields and Gaussian Markov random fields: the stochastic partial differential equation approach.* Journal of the Royal Statistical Society: Series B (Statistical Methodology) 73:423–498.

[4] Koh KJ, Cirak F (2023) *Stochastic PDE representation of random fields for large-scale Gaussian process regression and statistical finite element analysis.* Computer Methods in AppliedMechanics and Engineering 417:116358.

UKACM 2024 Conference, 10-12 April 2024, Durham University, Durham, UK
https://doi.org/10.62512/conf.ukacm2024.064

Bayesian optimisation of buckling loads of trusses with random imperfections

Tianyi Liu[1*], Fehmi Cirak[1]

[1] Department of Engineering, University of Cambridge, Cambridge CB2 1TN, UK.
tl499@cam.ac.uk, f.cirak@eng.cam.ac.uk

Abstract

Optimisation of linear structures is a well-developed and highly relevant research field. In particular, for linear problems with differentiable objective functions, gradient-based methods are well suited. In engineering practice, structural nonlinear behaviour and imperfections different from ideal design often need to be considered. Optimised lightweight structures, such as long-span bridges and stadium roofs, are more sensitive to sudden failure through buckling. Imperfections or perturbations in geometry and loading can drastically reduce the buckling load of a structure compared to that of a perfect structure. It is, however, computationally expensive to analyse structural problems with nonlinearities and imperfections and to compute the derivatives of the respective objective functions, rendering gradient-based methods unsuitable.

In the present work, we use a Bayesian optimisation technique with a Gaussian process as the surrogate model for the described structural problems with random imperfections. Bayesian optimisation is exceptionally well suited for expensive black-box objective functions with no analytical expressions. To rapidly determine the random buckling loads, we consider an extended system of equilibrium equations for directly computing the buckling loads, i.e. bifurcation and snap-through points on the load-displacement path. This approach is exceedingly efficient for repeatedly computing buckling loads for different imperfections. We use the complex-step derivative approximation to determine the required directional derivatives of matrices. A low discrepancy sequence, Sobol sequence, is adopted for sampling from imperfections.

Key words: *Geometric nonlinear analysis; Structural imperfections; Bayesian optimisation; Gaussian process; Finite elements; Sobol sequence*

1 Introduction

A lot of structures, especially optimised structures, are imperfection-sensitive. The initial geometric imperfections induced during construction could change the response path and stability behaviour of the structure drastically. Therefore, we perform a robust structural optimisation with the consideration of random imperfections. The imperfections are assumed to be a normal distribution. We use the direct computation method and quasi-Monte Carlo sampling to obtain the probability distribution of buckling loads. Then, the parameters of the buckling load distribution, like mean and variance, are included in the objective function of structural optimisation.

2 Problem description

We propose an algorithm for obtaining the probability distribution of buckling loads. It involves the direct computation of stability point, extended system method, and a quasi-Monte Carlo sequence, Sobol sequence. It starts with performing the traditional nonlinear analysis using the displacement control method of a perfect structure. The imperfection samples are generated by the Sobol sequence. They are separated into positive and negative and sorted in ascending order. Then, we iterative through each imperfection, where the extended system method is adopted to directly compute the buckling loads. The following figures illustrate the proposed algorithm.

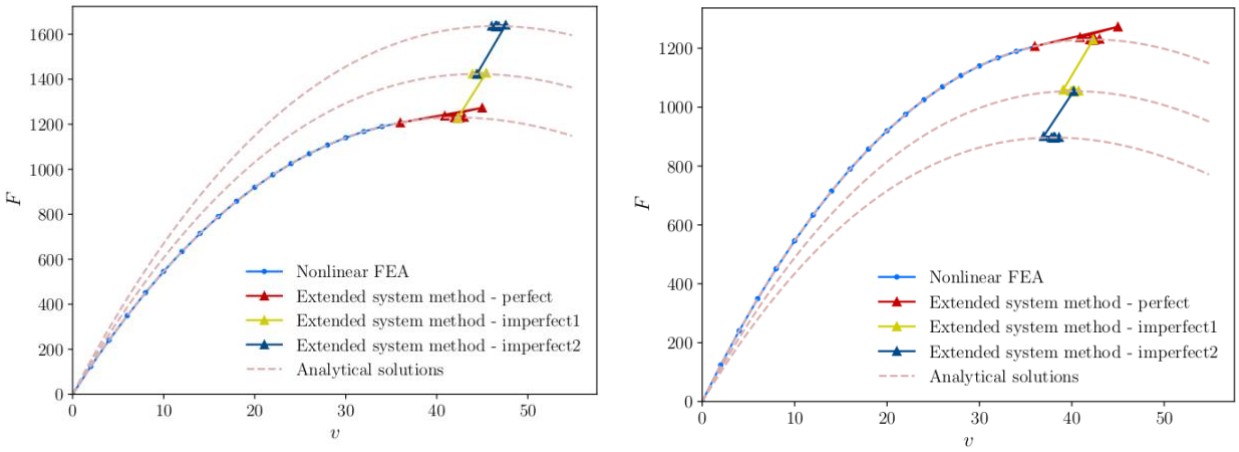

Figure 1: The illustration of the algorithm of computing imperfect buckling load distribution.

We consider the sizing optimisation of the buckling loads of random imperfect trusses. The total volume is fixed. The aim is to increase the mean of buckling load and decrease the standard deviation. A trade-off parameter is introduced to balance the mean and standard deviation of buckling load distribution. The objective function is given by

$$g(a) = \alpha \frac{\overline{F_c}(a)}{\overline{F_c^*}} - (1-\alpha)\frac{\sigma_{F_c}(a)}{\sigma_{F_c}^*(a)} \tag{1}$$

where α is the trade-off parameter, $\overline{F_c}$ is the mean of buckling loads and σ_{F_c} is the standard deviation of buckling loads. The mean and standard deviation are normalised between [0,1]. The Bayesian optimisation with the Gaussian process as the surrogate model is employed to maximise the above equation.

3 Numerical results

Consider a Von Mises truss as an example to demonstrate the proposed algorithm. The buckling load distribution of random imperfect structures are

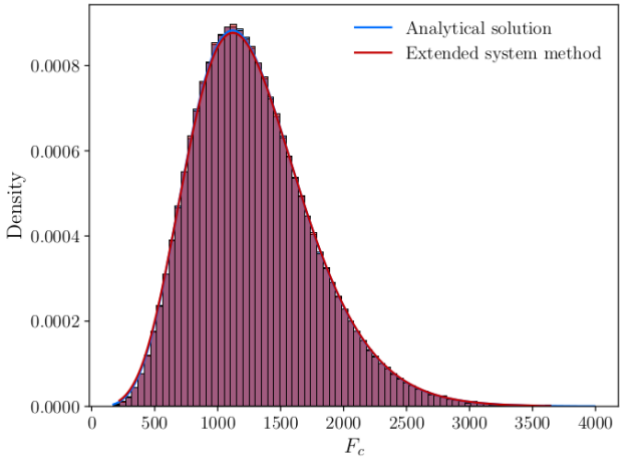

Figure 2: The probability distribution of buckling loads of Von Mises truss.

With more Sobol sets, the results of the proposed algorithm are closer to the analytical solutions. The convergence of mean and standard deviation are

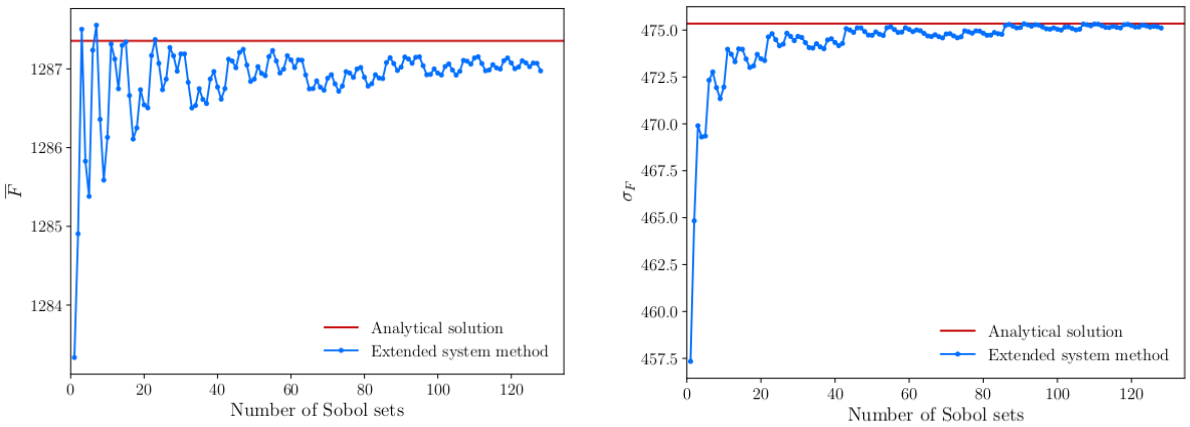

Figure 3: The convergence of mean and standard deviation of buckling load distribution.

We consider a 3D star dome truss for the Bayesian optimisation. The robust optimisation yields different results with the choices of the trade-off parameter α. The solution points with different α forms a Pareto front as

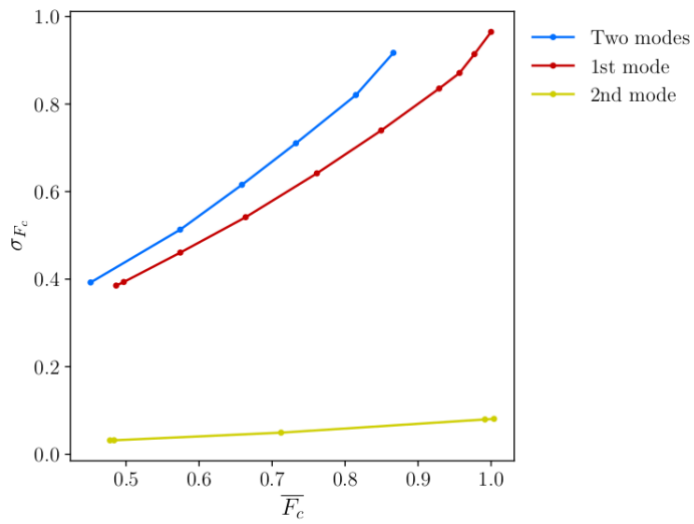

Figure 4: The Pareto fronts of the robust optimisation of star dome truss.

The optimised trusses with different α have different shapes. Three results with $\alpha = 0.0$, $\alpha = 0.52$ and $\alpha = 1.0$ are compared in the following figure. All trusses are drawn in top views for easy comparison.

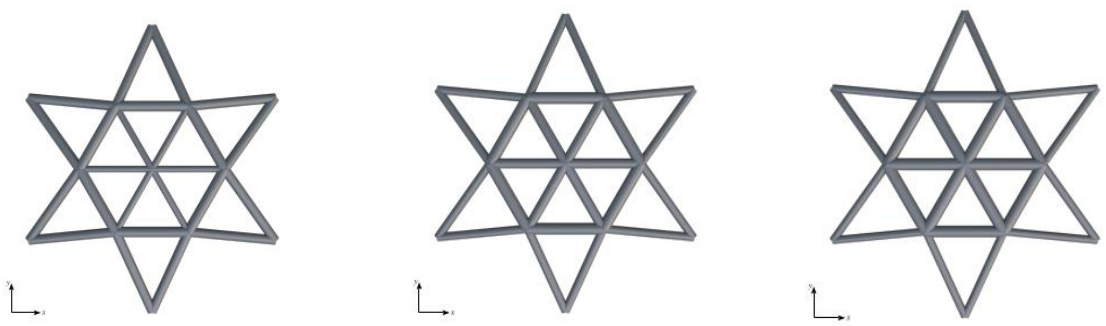

Figure 5: Comparison of optimised star dome trusses using different α.

4 Conclusions

The proposed algorithm using extended system method and Sobol sequence could compute the buckling load distribution effectively and accurately. It is important to consider the random imperfections since the results are very sensitive to those imperfections. In robust optimisation, the desired result with maximum mean and minimum standard deviation can not be achieved at the same time. The trade-off parameter should be chosen carefully to balance the buckling load mean and robustness of the optimisation result. Different values of trade-off parameters lead to different results. This approach provides engineers an opportunity to robustly design the structure from case to case.

References

[1] J. Bonet & R. D. Wood, (1997). Nonlinear Continuum Mechanics for Finite Element Analysis, *Cambridge University Press*, 63–88.
[2] P. I. Frazier, (2018). A Tutorial on Bayesian Optimization, *arXiv*, arXiv:1807.02811.
[3] C. E. Rasmussen & C. K. I. Williams, (2006). Gaussian Processes for Machine Learning, *The MIT Press*, 7–31.
[4] P. Wriggers, (2008). Nonlinear Finite Element Methods, *Springer*, 255–271.
[5] P. Wriggers & J. C. Simo, (1990). A general procedure for the direct computation of turning and bifurcation points, *International Journal for Numerical Methods in Engineering*, 30(1), 155–176.
[6] P. Wriggers, W. Wagner & C. Miehe, (1988). A quadratically convergent procedure for the calculation of stability points in finite element analysis, *Computer Methods in Applied Mechanics and Engineering*, 70(3), 329–347.
[7] Sobol', I. Y. M. (1967). On the distribution of points in a cube and the approximate evaluation of integrals, *USSR Computational Mathematics and Mathematical Physics*, 7(4), 86-112.

UKACM 2024 Conference, 10-12 April 2024, Durham University, Durham, UK
https://doi.org/10.62512/conf.ukacm2024.065

An analysis of stress and strain state of notched solid beams undergoing static loading

Michael T White[1,2], Dr Kasra Sotoudeh[3], Dr Marius Gintalas[1], Dr Nenad Djordjevic[1]

[1] College of Engineering, Design and Physical Sciences, Brunel University, London, UB8 3PH, UK.
[2] NSIRC, TWI Ltd, Granta Park, Great Abington, Cambridge, CB21 6AL, UK
M.white@affiliate.twi.ac.uk
[3] TWI Ltd, Granta Park, Great Abington, Cambridge, CB21 6AL, UK
Kasra.sotoudeh@twi.co.uk, Marius.gintalas@brunel.ac.uk, Nenad.Djordjevic@brunel.ac.uk

Abstract

Fracture testing is a common testing method for the assessment of mechanism of fracture. Single edged notched bending (SENB), single edged notched tension (SENT), or compact tension (CT) specimens are often utilised to analyse stress/strain state and for fracture analysis [1], [2]. However, when SENB and SENT specimens are not appropriate for the strain field required, a variety of notch geometries are used. Different notch geometries can create a variety of different strain fields, for example the use of V-notches to represent the stress/strain state in weld defects or the use of U notches to simulate geometrical change, both creating different levels of stress concentration [3]. This variety of strain fields, created around different stress raiser geometries, requires an investigation into different stress raiser geometries and their effects on strain field. The Ramberg-Osgood model is used on a variety of different notch geometries, to assess the stress/strain state created and the effects of altering notch geometry to inform their use for stress/strain analysis. The stress and strain field will be assessed through use of J-integral, stress intensity factor, stress concentration factor and T-stress, obtained numerically by using FEM solver Abaqus.

Key words: Fracture mechanics, Toughness, Notches, J-integral, Stress triaxiality

1 Introduction

Fracture testing is an important field of testing, used to assess mechanisms of fracture, stress and strain state involved during fracture, assessment of crack propagation and determining the origin of fracture for a specimen [4].

Material fracture often initiates from points of stress concentration [5], [6] These points of stress concentration can include any notches, groves, cracks, holes and other features which can affect the local stress distribution in a material [7]. Component defects, whether by design or inherently present, act as stress concentrators, leading to fracture as the defects expand. When conducting fracture testing on metals, the fracture strength is often shown to be lower than the predicted result, likely due to the localised stress concentrations caused by defects[8]. As a result, fracture testing, such as 3-point bending testing, must involve the use of a stress raisers to simulate the stress concentrations caused by innate cracks during material use.

Common fracture testing methods often include use of SENB and SENT specimens, for the assessment of material resistance to fracture. SENT and SENB specimens are designed to induce a different constraint levels and the different strain fields applicable/of interest across a range of industries [1], [2]. These standardised tests include the use of a fatigue pre-crack to measure the progression of crack extension. These tests however, aimed at the measurement of crack propagation, cannot be used to assess the onset of crack initiation, a key testing parameter when assessing material integrity and resistance to fracture of high-performance alloys and engineering structures. This is particularly important when assessing materials undergoing environmentally assisted cracking, including hydrogen embrittlement [9].

The necessity to measure the onset of crack initiation, for fracture analysis, requires an investigation into alternative test methods besides the use of standardised fracture toughness testing methodologies. This paper aims to assess the stress and strain state created by a range of different notch geometries, for use in assessing fracture initiation, utilising finite element analysis (FEA) to simulate the strain behaviour of a beam in 3-point bending.

2 Problem description

One challenge, concerning the use of SENB, SENT and CT specimens, is that standard specimens used in fracture mechanics for assessment of the material toughness, i.e. resistance to fracture, do not necessarily undergo the stress states observed in the real-world structures [8], which is why the design is typically conservative. Depending on the situation being simulated during testing, different stress raiser geometries will be required [3]. Particularly, when the assessment of fracture initiation is required, pre-cracked specimens are not sufficient [9]. Therefore, an alternative testing method is required, utilising specimens without a pre-crack. Utilising notch geometry, for component design, requires a keen understanding of the stress/strain state created by different notch geometries. This requirement, for stress/strain analysis has been conducted utilising Abaqus FEM solver, utilising a 3D deformable model of duplex stainless steel UNS: S31803. A range of different notch geometries have been selected, for modelling, displayed in table 1 which includes crack ligament ratio defined as notch depth over specimen width [10].

Specimen	Crack ligament ratio (a/w)	Notch depth (mm)	Notch tip diameter (mm)	Notch type
1	0.5	6	0.2	U-notch
2	0.5	6	0.4	U-notch
3	0.5	6	0.6	U-notch
10	0.5	6	0	Sharp crack
11	0.5	6	0.1	U-notch

Table 1 - Modelling geometries

The numerical models shown in table 1 utilise the Ramberg-Osgood model of deformation plasticity, using Abaqus FEM software, for plastic simulations of ductile materials, ideal for use on duplex stainless steels. The Ramberg-Osgood model utilises Young's modulus (E), hardening exponent (n) and yield offset (α) to describe the relationship between stress (σ) and strain (ε), for a given material, as shown in equation 1 [11].

$$E\epsilon = \sigma + \alpha\left(\frac{|\sigma|}{\sigma_0}\right)^{n-1} \tag{1}$$

The relationship between stress and strain, provided by the Ramberg-Osgood model, can be used to compare the stress and strain state created by each different notch geometry. From the subsequent models generated, a number of stress and strain parameters will be assessed including j-integral, stress intensity factor, stress concentration factor and T-stress.

3 Numerical results

Geometry of one model of a three-point bend test developed in Abaqus is shown in Figure 1. Due to the symmetry of the problem, only one half of the model is used in the analysis with appropriate boundary conditions [12].

0.1mm EDM Notch (Specimen 11)								
Notch width (mm)	Notch a/w ratio	Load (N)	Elastic J-integral (N/mm)	Elastic-plastic J-integral (N/mm)	Stress intensity factor (MPa·√mm)	T stress (MPa)	Stress concentration factor	Normalised T stress - β
0.1	0.5	1611.75	12.74	17.72	1676	56.09	8.29	10.087

Table 2 - specimen 11 parameters

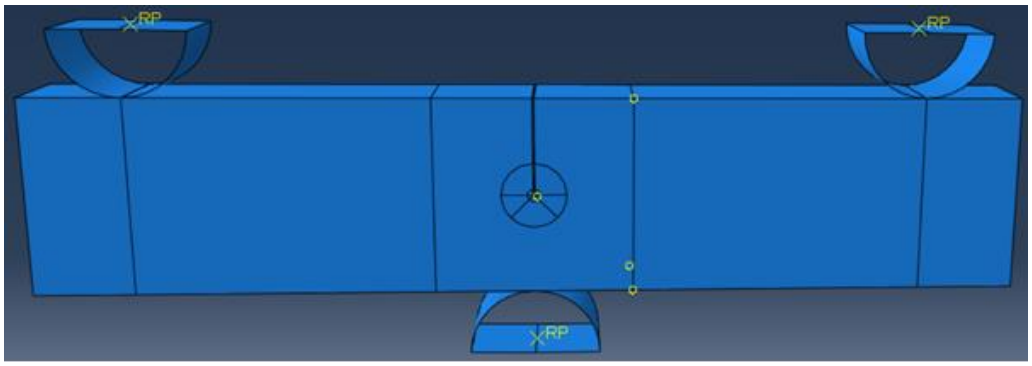

Figure 1 - Specimen 11 geometry

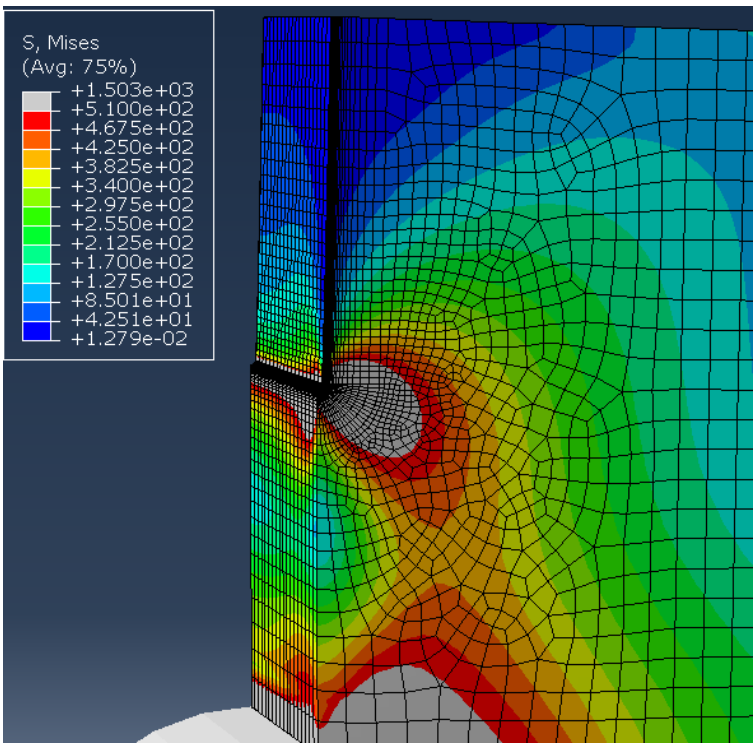

Figure 2 - Plastic deformation - von mises stress

Numerical solutions obtained in elastic-plastic analysis of specimen 11 are given in **Error! Reference source not found.**, whilst the distribution of the effective stress in the vicinity of the notch tip is shown in **Error! Reference source not found.**. The grey zone in figure 2 represents the area of plastic deformation created by this notch geometry. Table 1 displays the applied load, as well as the parameters used to evaluate and compare stress concentration, fracture strength and stress triaxiality created by the different notch geometries.

4 Conclusions

Our observations show that:

- FEA modelling can be utilised to analyse the strain field created by different stress raiser geometries
- Altering notch geometry has a significant effect on stress concentration, resistance to fracture and stress triaxiality at the notch tip.
    - For example, the increasing notch radius is shown to increase both J – integral and stress intensity factor, representing an increase in fracture resistance and a decrease in stress concentration at the notch tip.
    - Increasing notch radius decreases T-stress, which indicates a decrease in stress triaxiality (constraint) at the notch tip. Decreasing stress triaxiality effects the strain field at the notch tip and increases resistance to fracture.

Acknowledgments

This publication was made possible by the sponsorship and support of LRF. The work was enabled through, and undertaken at, the National Structural Integrity Research Centre (NSIRC), a postgraduate engineering facility for industry-led research into structural integrity established and managed by TWI through a network of both national and international Universities.

References

[1] K. A. Macdonald, E. Østby, and B. Nyhus, "Constraint fracture mechanics: test methods," in *Fracture and Fatigue of Welded Joints and Structures*, Elsevier, 2011, pp. 31–59. doi: 10.1533/9780857092502.1.31.

[2] B. Nyhus, M. L. Polanco, and O. Ørjasæther, "SENT Specimens an Alternative to SENB Specimens for Fracture Mechanics Testing of Pipelines," *Proceedings of the International Conference on Offshore Mechanics and Arctic Engineering - OMAE*, vol. 3, pp. 259–266, Jan. 2009, doi: 10.1115/OMAE2003-37370.

[3] M. Solnørdal, S. Wästberg, G. Heiberg, and O. Hauås-Eide, "Hydrogen Induced Stress Cracking (HISC) and DNV-RP-F112," *Measurement and Control*, vol. 42, no. 5, pp. 145–148, Jun. 2009, doi: 10.1177/002029400904200504.

[4] R. Allaire, "Fracture Analysis, a Basic Tool to Solve Breakage Issues," 2004.

[5] A. Moftakhar, A. Buczynski, and G. Glinka, "Calculation of elasto-plastic strains and stresses in notches under multiaxial loading," *Int J Fract*, vol. 70, no. 4, pp. 357–373, Dec. 1994, doi: 10.1007/BF00032453/METRICS.

[6] G. Pluvinage, "Fracture and Fatigue Emanating from Stress Concentrators," *Fracture and Fatigue Emanating from Stress Concentrators*, 2004, doi: 10.1007/1-4020-2612-9.

[7] W. D. Pilkey and D. F. Pilkey, "Peterson's Stress Concentration Factors, Third Edition," *Peterson's Stress Concentration Factors, Third Edition*, pp. 1–522, Apr. 2008, doi: 10.1002/9780470211106.

[8] J. F. (John F. Knott, "Fundamentals of fracture mechanics," 1973.

[9] L. Blanchard, H. Dong, and K. Sotoudeh, "Environmental Testing of Rolled and Hot Isostatically-Pressed Duplex Stainless Steels." OnePetro, Apr. 15, 2018. Accessed: Jul. 13, 2023. [Online]. Available: https://dx.doi.org/

[10] D. Moon, J. Park, and M. Kim, "Effects of the Crack Tip Constraint on the Fracture Assessment of an Al 5083-O Weldment for Low Temperature Applications," *Materials*, vol. 10, no. 7, p. 815, Jul. 2017, doi: 10.3390/ma10070815.

[11] R. Giardina, "On The Ramberg-Osgood Stress-Strain Model And Large Deformations of Cantilever Beams," 2017. Accessed: Dec. 05, 2023. [Online]. Available: https://scholarworks.uno.edu/td/2377

[12] I. Koutromanos, J. McClure, and C. J. Roy, *Fundamentals of finite element analysis : linear finite element analysis*. 2018. Accessed: May 18, 2023. [Online]. Available: https://www.wiley.com/en-us/Fundamentals+of+Finite+Element+Analysis%3A+Linear+Finite+Element+Analysis-p-9781119260080

UKACM 2024 Conference, 10-12 April 2024, Durham University, Durham, UK
https://doi.org/10.62512/conf.ukacm2024.076

RESPONSE OF A SLENDER STRUCTURE SUBJECT TO STOCHASTIC GROUND MOTION

Lukman O. Olawale[1*], Erwin George[1], Tao Gao[2], Choi-Hong Lai[1]

[1] School of Computing and Mathematical Sciences, Faculty of Engineering and Science, University of Greenwich, London, SE10 9LS, UK. l.o.olawale@greenwich.ac.uk
[2] School of Mathematics, Statistics and Actuarial Science, University of Essex, Colchester CO4 3SQ, UK. t.gao@essex.ac.uk

Abstract. The stochastic analysis of the deflection behaviour of an idealised slender structure subject to stochastic disturbance is studied. In a previous work by the authors, the response of an Euler-Bernoulli beam subject to stochastic disturbance was studied. The current work extends the same techniques to a modified Euler-Bernoulli beam with both flexural beam and shear properties. The beam is subjected to a stochastic ground motion in the form of periodic motion with disturbance in the amplitude of the motion. The disturbance is in the form of Gaussian white noise. This results in a Stochastic Partial Differential Equation (SPDE) version of the modified Euler-Bernoulli beam equation. The stochastic analysis was then conducted by numerical methods using a combination of a finite difference scheme and Monte-Carlo Simulation. Given that the input force is Gaussian, it is also observed that the response of the system is a Gaussian process.

Key words: *Euler-Bernoulli beam; Stochastic PDE; White noise; Uncertainty quantification; Implicit numerical scheme; Monte carlo method.*

1 Introduction

Stochastic modelling is important for problems with inputs containing uncertainties as is it helps in capturing the uncertainties in the system. For example, one can describe the system response when one is able to obtain the response distribution function either numerically or in closed form where possible. As a follow up to the work of the author (see [1]), in this work we examine the effect of both stochastic body forces and ground motion by examining such forces as the input of a modified Euler-Bernoulli beam equation [2]. For a uniform mass, uniform stiffness and undamped vibration, the modified Partial Differential Equation (PDE) is given by

$$EI\frac{\partial^4 w}{\partial y^4}+\mu\frac{\partial^2 w}{\partial t^2}-GA\frac{\partial^2 w}{\partial y^2}=Q(y,t) \tag{1}$$

where w is the lateral deflection, y is the longitudinal spatial variable, t is the time variable, Q is the input load, μ is the mass per unit length, E is the Young's modulus, I is the second moment of the area of the beam's cross section. The product EI is known as the flexural rigidity that measures the force required to bend the beam. GA is the shear rigidity of the beam, where G is the shear modulus and A is the cross-section area of the beam. As in the related paper [1], in this study, we consider a stochastic force of the form

$$Q(y,t)\propto\xi(y,t)\,, \tag{2}$$

where $\xi(y,t)$ is a Gaussian white noise giving rise to a Stochastic Partial Differential Equation (SPDE).

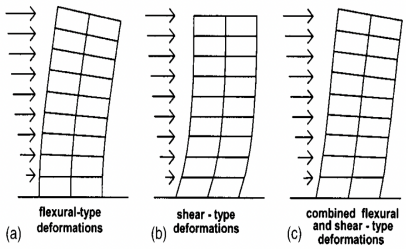

Figure 1: Lateral deformations of the beam [2]

2 Formulation

A beam of length h with uniform density, flexural rigidity and shear rigidity subject to undamped vibration caused by ground acceleration is considered. Its lower end is assumed fixed at the foundation forming a cantilever structure. The beam is assumed to have both flexural and shear properties, thus, able to deform in both bending and shear configurations. The response of such a beam, illustrated in Figure 1, subjected to a sinusoidal ground motion is governed by a modified Euler-Bernoulli equation as

$$\frac{\partial^4 w}{\partial y^4} + \frac{\mu}{EI}\frac{\partial^2 w}{\partial t^2} - \frac{GA}{EI}\frac{\partial^2 w}{\partial y^2} = -\frac{\mu}{EI}\frac{\partial^2}{\partial t^2}\big(\alpha \sin(\omega t)\big). \tag{3}$$

The problem is formulated in a two-dimensional Cartesian coordinate system with origin at the fixed end of the beam. The pressure load acts along the x-axis thus the displacement of the beam is denoted by $x = w(y;t)$. By the process of non-dimensionalisation we can re-scale equation (1) as

$$w'''' + \ddot{w} - \beta^2 w'' = \alpha \sin \omega t\,, \tag{4}$$

by choosing h, $\sqrt{\mu h^4/EI}$, EI/h^4, *and* $\sqrt{EI/\mu h^4}$ as the reference length, time, pressure respectively and angular frequency respectively. For ease of notations, a prime $'$ is used to denote the partial derivative of the displacement with respect to y, and a dot $\cdot$ is used to denote the partial derivative of the displacement with respect to t; w and α are the scaled deflection and amplitude; y and t are the spatial and temporal variable respectively and $\beta = h\sqrt{\frac{GA}{EI}}$ is the parameter that controls the overall shear and flexural behaviour of the beam. The boundary conditions for the cantilever beam are

$$w(0,t) = w'(0,t) = w''(1,t) = w'''(1,t) - \beta^2 w'(1,t) = 0\,. \tag{5}$$

For an initial value problem (IVP), the beam is assumed to be initially at rest, so

$$w(y,0) = \dot{w}(y,0) = 0\,. \tag{6}$$

By considering a disturbance in the amplitude of the period ground motion we obtain the stochastic PDE of the form

$$w'''' + \ddot{w} - \beta^2 w'' = (\alpha + \sigma\xi)\sin \omega t \tag{7}$$

where σ^2 is the variance of the stochastic process. The white noise (ξ), see [3], is defined as the time derivative of standard Wiener process W

$$\xi(y,t) = \dot{W}(y,t). \tag{8}$$

2.1 Numerical Scheme

In this study, we will analyse the stochastic process of the system via a numerical approach. To this end we employ an implicit finite difference scheme to ensure the stability of the computation. The domain of the problem is uniformly discretised into N grid points $y_j = \frac{j}{N}$, for $j = 1,2,...,N$, with step size $\Delta y = 1/N$ and $w_j \approx w(y_j)$ for $j = 1,2,...,N$. By imposing a second order finite difference scheme on the boundary conditions in (5) a finite difference formula for the ghost points can be derived then a matrix of the finite difference scheme for w over $\{y_j\}_{j=1,2,...,N}$ can be written.

If one introduces an artificial variable $v = \dot{w}$ which is second order in time, equation (7) can be rewritten as a system of two coupled PDEs of the first order

$$\frac{\partial U}{\partial t} = \left(\mathcal{M}_1 + \beta^2 \mathcal{M}_2\right) U + F\,, \tag{9}$$

where $U = \begin{pmatrix} w \\ v \end{pmatrix}, \mathcal{M}_1 = \begin{pmatrix} 0 & 1 \\ -D^4 & 0 \end{pmatrix}, \mathcal{M}_2 = \begin{pmatrix} 0 & 0 \\ D^2 & 0 \end{pmatrix}, F = \begin{pmatrix} 0 \\ q \end{pmatrix}$, D^4 and D^2 is fourth-order and second-order finite difference scheme respectively. The time domain $[0,T]$ is divided into n steps with $\Delta t = T/n$, where T is the final time. By discretising spatially in y and temporally in t the discretised variables are

$$U_j^k = \begin{pmatrix} w_j \\ v_j \end{pmatrix} \text{ at } t = t_k = k\Delta t. \tag{10}$$

The backward Euler scheme can then be written in the matrix form

$$\begin{bmatrix} I_N & -\Delta t I_N \\ \Delta t\left(\mathbf{M}_1 + \beta^2 \mathbf{M}_2\right) & I_N \end{bmatrix} \begin{bmatrix} W \\ V \end{bmatrix}^{k+1} = \begin{bmatrix} W \\ V \end{bmatrix}^{k} + \begin{bmatrix} 0 \\ \Delta t Q \end{bmatrix}, \tag{11}$$

where I_N is the identity matrix and $\mathbf{M}_1$ and $\mathbf{M}_2$ are the matrix replacement of the fourth-order and second-order finite difference scheme for D^4 and D^2 respectively, $W = [w_1, w_2, \ldots, w_N]^T$, $V = [v_1, v_2, \ldots, v_N]^T$ and the discretised load, $Q = [q_1, q_2, \ldots, q_N]^T$, where $q_i = (1 + \sigma\zeta)\sin\omega t_k$ and $\zeta = dW/dt \approx N(0,1)/\sqrt{\Delta t}$, where $N(0,1)$ is a normally distributed random variable with zero mean and unit variance. Equation (11) is used to conduct Monte Carlo (MC) simulations to obtain data for analysis. For good accuracy, $\Delta y = 0.002$ and $\Delta t = 0.1s$ were chosen for 10,000 simulations and the standard deviation of the stochastic process is chosen as $\sigma = 0.01$.

3 Results

The snapshot of the deflection profile of the MC simulation at time T is shown in Figure 2a where we see a cluster of the deflection about a region. The Expectation $\mathbb{E}[w]$ shown in Figure 2b seemed to be the region about which the cluster is formed which is what is expected due to the fact that the input force is Gaussian. The resulting output is also a Gaussian process as can be confirmed by the distribution of the deflection at the top of the beam shown in Figure 3.

4 Conclusions

The stochastic analysis of a beam that can deformed by a combination of flexural and shear deformation is conducted. The beam is subjected to stochastic ground motion in the form of periodic motion with disturbance in the amplitude of the motion. The deformation of the beam is governed by a modified form

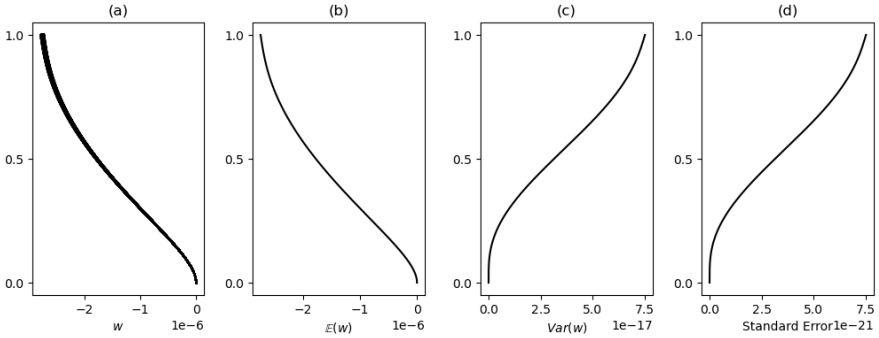

Figure 2: (a) Snapshots of w due to stochastic load in (7) using Monte-Carlo method at time T (b) Expectation $\mathbb{E}(w)$ of the stochastic process at T along the beam (c) Variance of the stochastic process at T along the beam (d) Standard error of the Monte Carlo method at T along the beam

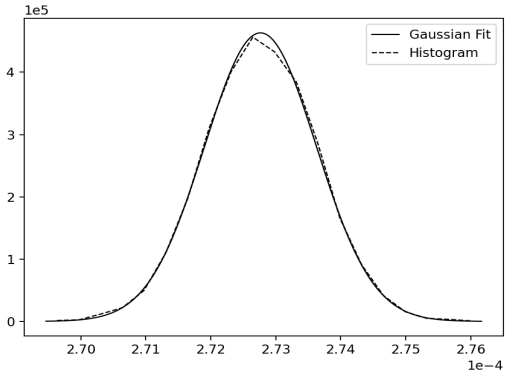

Figure 3: Histogram of the deflection data, w_1, from time T and distribution fitted to the data.

of Euler-Bernoulli beam equation. The stochastic analysis was conducted by numerical methods using a combination of a finite difference scheme and Monte-Carlo Simulation. Given that the input force is Gaussian, it is also observed that the response of the system is a Gaussian process.

REFERENCES

[1] Olawale L., Gao T., George E., Lai C-H. (2023), Response of an Euler-Bernoulli beam subject to a stochastic disturbance. *Eng Comput*. https://doi.org/10.1007/s00366-023-01917-5.

[2] Miranda, E., and Taghavi, S. (2005),Approximate floor acceleration demands in multi-story buildings. I: Formulation." *J. Struct. Eng.*, 131(2), 203–211.

[3] Higham D. J. (2001) An algorithmic introduction to numerical simulation of stochastic differential equations. SIAM review, 43(3), 525–546.